UNIVERSITY OF CALIFORNIA, MERCED

# Tunable Microwave Cavities for Macroscopic Cavity Optomechanics

A dissertation submitted in partial fulfillment of the
requirements for the degree of
Doctor of Philosophy
in

Physics

by

Jacob Michael Pate
May 2020

Tunable Microwave Cavities for Macroscopic Cavity Optomechanics

The dissertation of Jacob Michael Pate, titled Tunable Microwave Cavities for Macroscopic Cavity Optomechanics, is approved, and it is acceptable in quality and form for publication.

| | |
|---|---|
| (Dr. Jay Sharping) Principal Advisor | Date |
| (Dr. Michael Scheibner) Committee Chair | Date |
| (Dr. Raymond Chiao) Committee Member | Date |
| (Dr. Lin Tian) Committee Member | Date |

University of California, Merced
2020

This work is dedicated to my Lord and Savior Jesus Christ, my wife Marissa, and my son Mason for their encouragement and support of my education and the exciting journeys along the way.

# Acknowledgments

I want to first thank my advisor, Dr. Jay Sharping, for allowing me to pursue the research projects which have interested me the most. Jay brought me into the lab and assigned me to a project originally dealing with squeezed microwave fields in superconducting cavities. Throughout my learning experience you have allowed me to venture off and test new ideas, seek out collaborative efforts, and fail many times while remaining patient. Thank you for helping support my three-month stay at the University of Western Australia (UWA). Jay, you have always supported me on my educational adventures and I'm especially thankful for you.

I want to thank Dr. Raymond Chiao, a co-advisor to me, who taught me about pursuing big ideas for big returns. You had an especially curious mind that continues to amaze me. Your ability to write nearly one new research idea every week within your memos is astounding! I have no question that there are many buried treasures waiting to be found within your fascinating memos.

My extensive time in the machine shop has led me to be incredibly grateful for two men, Brian Zimmermann and Keith Blackburn, who helped me develop the machine shop skills I desperately needed. Brian and Keith, you both had patience with me in the beginning stages of my familiarity with the machine shop as well as the silly mistakes I made in the years throughout. Thank you for all of your help!

To Dr. Keith Schwab, who was my first mentor outside of UC Merced and, after a single email asking for advice on a particular issue, he took time from his busy schedule to aid me in the development of the artificial, external capacitor for tunable cavities that was instrumental to my subsequent projects. Everything from the design of the external electrodes to the low-noise pre-amplifiers was a gift from Keith. I have always appreciated his simplistic, yet powerful approach to solving practical problems. Through Keith's influence and guidance, I took the tunable system I developed and applied it to the highly sensitive re-entrant cavities.

About a year went by after my collaborative effort with Dr. Keith Schwab when I met Dr. Michael Tobar. I was intrigued and fascinated by the similar works of Dr. Tobar at UWA. A single email eventually led to a connection, which compelled me to visit UWA for one week. After witnessing the amazing quality of the research laboratory and warm, friendly environment, I was left wanting more. Not only did

you invite me into your lab, but you graciously provided housing accommodations for my visit. At the end of my brief stay Dr. Tobar invited me to come back for an additional three months to continue work. Out of your own research budget you paid for the flights of my family to visit UWA once again. Your knowledge and guidance proved priceless for my career, yet, perhaps more importantly, I will never forget your caring nature to aid and advance a foreign student.

To my former lab mates who put up with me in the lab Luis, Al, Johnathon, Jeff, and Nabin, those whom I have worked most closely with, thank you for efforts of either helping me in my studies or listening to some of my ridiculous ideas. I hope through our interactions you were able to learn as much from me as I have from you all.

I am especially thankful for all my friends and family (including our recent friends in Australia through school and church) who have encouraged and supported me in my studies! Either through prayer or meeting together in person to talk, every amount that you all have invested into me has made a tremendous impact on my personal life and educational career!

I am extremely grateful for my wife and son (Marissa and Mason) who have supported me in all the adventures over the past several years. To my wife, the amazing woman who supported me in every endeavor including, but not limited to, moving to Western Australia for three months and home schooling Mason. Not only did she support my decisions, she shared enthusiasm and encouragement with every project I attempted to tackle. In the midst of her own full-time schoolwork, parenting, and keeping the chaos, she managed to make time to encourage and uplift me when times were difficult. She brings order and beauty to my life.

My son, Mason, has given me incredible encouragement and cheers me on when the going gets tough. He also constantly reminds me of the priceless values of faith, curiosity, and excitement adults seem to lose in the process of "growing up." As a parent, I see how dependent and trusting a child is towards a parent and it reminds me of how I should handle my own faith. A child often exemplifies curiosity better than a seasoned scientist. There is no limit to the amount of questions or thoughts children have when perplexed by a topic and are consequently driven towards discovery. Lastly, children have a unique and incredibly expressive way of showing excitement. I especially believe adults should likewise seek passion in their careers because it is passion that drives individuals towards extraordinary.

Lastly, it is my belief that Christians should be the most scientifically curious individuals, learning and applying from what has been, towards what will be. Therefore, I want to give all credit to my Lord and Savior, Jesus Christ, who has opened unbelievable doors in my career and gives me passion and motivation in this exciting journey.

# Dr. Jacob Pate

Enthusiastic and Motivated Applied Physicist!

*To excel at a job that challenges, motivates, and inspires me to grow in my passion for applied physics and technology!*

Willing to relocate: Anywhere
Authorized to work in the US for any employer

## Work Experience

### Visiting Researcher

Australian Centre of Excellence for Engineered Quantum Systems (EQUS) at University of Western Australia – Perth, WA
September 2019 – March 2020
2nd Visit:

- Experimental setup for the next-generation Casimir experiments to investigate the potential impact and increased sensitivity with mechanical resonators and microwave re-entrant cavities.
- Traveled to Perth, Australia to establish the experiment, procedures, and guidance for the incoming graduate students to continue my graduate work involving the Casimir effect and arbitrary manipulation of metallic silicon nitride membranes.

1st Visit:

- Investigation and observation of the thermal Casimir force and its effect and applications on macroscopic mechanical oscillators in microwave re-entrant cavities.
- Introduction to bulk acoustic wave (BAW) quartz resonators within microwave cavities for precision measurements in optomechanical experiments.
- Experience within a world-class research laboratory and research guidance under Dr. Michael Tobar and lessons on microwave interferometry by Dr. Eugene Ivanov.

### Graduate Student / Teaching Assistant

University of California, Merced – Merced, CA
August 2014 – February 2020
Studied the interactions between light and matter (optomechanics) through high-Q and strongly-coupled microwave superconducting radio frequency cavities. Investigations have focused upon cavities with the following geometries: cylindrical, coaxial $\lambda/4$, and re-entrant designs — all designed, built, and tested by myself.

- Experience supervising a lab and working with cryogenic systems and dilution refrigerators.
- Extensive machine shop training and use (> two years) on campus to build and test 3-D resonant microwave cavities.
- Obtained training with a scanning electron microscope (FEG-SEM).
- Taught calculus I and II sections as well as introductory physics labs and discussion sections as a teaching assistant over a period of several years.
- Great programming experience in MATLAB, LabVIEW, Fusion 360 CAD software (Autodesk), COMSOL Multiphysics, and LaTeX with familiarity in Python, Mathematica.

Posters / Talks Given:

- Frequency Control for Double Cavity Parametric Amplifier - poster presented at UC Merced in Spring 2016
- Measurement Scheme for Microwave SRF Double Cavity - poster presented at UC Merced in Spring 2016
- Macroscopic Optomechanically-Induced Transparency - talk presented at APS March Meeting Spring 2017 - New Orleans
- Towards Macroscopic Cavity Optomechanics - poster presented at APS Far West Fall 2017 - UC Merced
- Noise Thermometry for Macroscopic Cavity Optomechanics - talk at APS March Meeting - Los Angeles
- Capacitive Tuning of an SRF Cavity Incorporating a Flexible Silicon-Nitride Membrane - poster presented at Applied Superconductivity Conference Fall 2018 – Seattle
- Invited talk and visit at the University of Western Australia - Spring 2019
- Field-cooled magnetic levitation of a neodymium magnet within a superconducting radio frequency cavity - Co-author presentation at ASC Tampa 2020

Published Papers:

- Electrostatic tuning of mechanical and microwave resonances in 3D superconducting radio frequency cavities - AIP Advances
- A parametric oscillator for classroom demonstration or student laboratory - European Journal of Physics
- Normal-mode splitting in coupled high-Q microwave cavities - Journal of Applied Physics
- Casimir spring and dilution in macroscopic cavity optomechanics - Submitted to Nature Physics
- High-Q SRF 3D Cavities for RF Optomechanics - In Progress
- Field-cooled magnetic levitation of a neodymium magnet within a superconducting radio frequency cavity - In Progress

## Summer Intern / Student Engineer

Jet Propulsion Laboratory – Pasadena, CA
Summers June 2011 – August 2015
During my five years of summer internships, I gained the experience and knowledge of working with optics, heterodyne interferometry, lasers, metrology, LabVIEW (interfacing with data acquisition instruments), and MATLAB programming. As a member of a group in the metrology and interferometry section, I developed practical skills such as teamwork, mentoring, working under a deadline, and data analysis.

## Student Observatory Technician

California State University, San Bernardino – San Bernardino, CA
September 2011 – March 2014
During my time at the Murillo Family Observatory, I helped operate the newly built observatory on campus doing tasks such as building cables, working on software communications between the telescopes and computers, installing hardware for the telescope, and imaging the sky. I have given a presentation at the American Association of Physics Teachers (AAPT) as well as assisted with outreach opportunities for people of all ages ranging from elementary students to CSUSB alumni to formal dinners with generous benefactors.

## Thousand Pines Christian Camp and Conference Center

Crestline, CA
June 2001 – September 2011
I helped supervise and run recreational activities (such as paintball, climbing wall, zip line, mountain bikes, skate park, etc.) for guests of all ages. Before being a recreation assistant, I worked in the kitchen and malt shop making and serving food for the guests.

## Education

### PhD in Physics
University of California, Merced – Merced, CA (August 2014 – February 2020)
Cumulative GPA: 3.85

### BS and BS Applied in Physics
California State University, San Bernardino – San Bernardino, CA (September 2009 – March 2014)
Cumulative GPA: 3.5

### High School Diploma
Rim of the World High School – Lake Arrowhead, CA (August 2006 – June 2009)
Cumulative GPA: 4.05

## Skills

- Calculus
- MATLAB
- LabVIEW
- Geometry
- Tutoring
- CAD
- Physics
- Stock Trading
- Data Analysis
- LaTeX
- Public Speaking
- Critical Thinking
- Presentation Skills
- Photonics
- Data Acquisition
- Instrumentation
- Engineering
- PowerPoint
- Trading
- Research and Development
- Research Laboratory Experience
- Illustration
- COMSOL Multiphysics
- Machine Shop Skills

## Links

LinkedIn Profile: https://www.linkedin.com/in/positivejake/

## Awards

### Physics Graduate Student Summer Fellowship
Summers 2017 – 2019

### Dean's List
Every quarter from 2009 – 2013

### Charles Fred Kellers Scholarship Recipient
September 2012

### NSF S-STEM Scholarship
September 2011

### Mathematics and Science Scholarship Recipient
September 2009

## Publications

**Electrostatic tuning of mechanical and microwave resonances in 3D superconducting radio frequency cavities**
https://doi.org/10.1063/1.5055887
November 2018

**Normal-mode splitting in coupled high-Q microwave cavities**
https://doi.org/10.1063/1.5110611
November 2019

**A parametric oscillator for classroom demonstration or student laboratory**
https://iopscience.iop.org/article/10.1088/1361-6404/ab2fe9
September 2019

**Casimir spring and dilution in macroscopic cavity optomechanics**
*Submitted and under review at Nature Physics*
https://arxiv.org/abs/2004.05983
April 2020

**High-Q SRF 3D Cavities for RF Optomechanics**
*In preparation*

**Field-cooled magnetic levitation of a neodymium magnetic within a superconducting radio frequency cavity**
*In preparation*

**Abstract**

This thesis begins with the introduction of optomechanics, the study of the interaction between light (photons) and mechanical oscillations (phonons) using bulk 3-D cavities. The description of 3-D microwave cavities is introduced as the boundary of the electromagnetic field and the mathematics are developed for the interaction between the electromagnetic field and a fluctuating boundary (mechanical oscillator). This work was established in pursuit of observing optomechanical effects within macroscopic 3-D cavity systems.

Three main microwave 3-D cavity geometries were used for this work: cylindrical, re-entrant, and coaxial quarter-wave ($\lambda/4$) cavities. A large number of cavities were made by the author in a machine shop in an attempt to develop strongly-coupled optomechanical systems. The pursuit of this goal led to the first observation of strain engineering, or dissipation dilution, via the thermal Casimir effect and its exciting potential applications.

The noteworthy projects that saw success in this work were the development of tunable, superconducting microwave cavities using a lossless, non-contacting fashion in addition to the ground-up progression of re-entrant cavities that led to the first observation of the thermal Casimir spring and dilution effect at room temperature. The outcome of this work opens the doorway for the development of "*in situ*" arbitrary, topological resonators with the added benefit of an increased mechanical quality factor $Q_m$ due to heightened strain.

# Contents

# List of Figures

# List of Symbols

| Symbol | Meaning |
|---|---|
| $\omega_0, \omega_c$ | Microwave cavity resonance frequency |
| $\omega_l$ | Laser or microwave pump frequency |
| $\Omega_m$ | Mechanical oscillator resonance frequency |
| $\Delta$ | Detuning from the cavity frequency, $\Delta = \omega_l - \omega_0$ |
| $\kappa_{i,0}$ | Intrinsic loss rate of the cavity to the environment |
| $\kappa_e$ | External loss rate arising from coupling the cavity to a waveguide |
| $\kappa$ | Total cavity loss rate, $\kappa = \sum_i \kappa_i$ |
| $\Gamma_m$ | Intrinsic mechanical loss rate (damping) |
| $Q_0(Q_L)$ | Intrinsic (loaded) quality factor of a resonator $Q_0 = \omega/\kappa_0$ |
| $\beta$ | Waveguide coupling (max value $= \infty$), $\beta = \kappa_e/\kappa_0$ |
| $\eta$ | Coupling efficiency (max value $= 1$), $\eta = \kappa_e/\kappa$ |
| $G$ | Optomechanical coupling rate, $G = -d\omega/dL$ |
| $x_{\mathrm{zpf}}$ | Mechanical amplitude of zero-point fluctuations, $x_{\mathrm{zpf}} = \sqrt{\hbar/(2m_{\mathrm{eff}}\Omega_m)}$ |
| $g_0$ | Vacuum optomechanical single photon coupling rate, $g_0 = Gx_{\mathrm{zpf}}$ |
| $\hat{a}$ | Microwave field amplitude |
| $\bar{n}, n_{\mathrm{cav}}$ | Cavity occupation (photon) number, $\bar{n} = \hat{a}^\dagger \hat{a}$ |
| $n_{\mathrm{th}}, n_m$ | Mechanical occupation (phonon) number, $n_{\mathrm{th}} = (e^{\hbar\Omega_m/k_BT} - 1)^{-1} \approx k_BT/\hbar\Omega_m$ |
| $g$ | Multiphoton vacuum optomechanical coupling rate, $g = g_0\sqrt{\bar{n}}$ |
| $\chi_m$ | Mechanical susceptibility, $\chi_m = (m_{\mathrm{eff}}(\Omega_m^2 - \Omega^2 - i\Omega\Gamma_m))^{-1}$ |
| $\Omega_{\mathrm{eff}}$ | Effective mechanical frequency accounting for dynamical backaction |
| $\Gamma_{\mathrm{eff}}$ | Effective optomechanical damping accounting for dynamical backaction |
| $S_{OO}$ | Double-sided power spectral density, $S_{OO}(\Omega) = \int_{-\infty}^{\infty} \langle O(\tau)O(t+\tau)\rangle\, e^{i\Omega\tau} d\tau$ |
| $\bar{S}_{OO}$ | Symmetrized power spectral density, $\bar{S}_{OO}(\Omega) = (S_{OO}(\Omega) + S_{OO}(-\Omega))/2$ |
| $S_O$ | Single-sided power spectral density, $S_O(\Omega) = 2\bar{S}_{OO}(\Omega)$ |
| $\mathcal{C}_0$ | Single-photon cooperativity, $\mathcal{C}_0 = 4g_0^2/(\kappa\Gamma_m)$ |
| $C$ | Parallel-plate capacitance, $C = \epsilon A/d$ |
| $\Gamma$ | Reflection coefficient, equivalent to $S_{11}$ measurement |
| $V_{\mathrm{DC}}$ | DC bias voltage on sensing electrode |

# Chapter 1

# Introduction

*"Your personal philosophy is the major determining factor in how your life works out."* – *Jim Rohn*

The concept of light, or radiation, applying pressure on an object dates back to Kepler's observation of a comet in which he noted the comet's tail always pointed away from the Sun [1]. It wasn't until the 1800s when the concept of radiation was brought to light with James Clerk Maxwell. He formulated the classical theory of electromagnetism in which the wave-like properties of electric and magnetic fields traveling at the speed of light were mathematically discovered. His work on electromagnetic waves has led to the birth of every form of modern-day communication technology.

Fast forward sixty years through the development of blackbody radiation, special relativity, superconductivity, and quantum mechanics to 1945 in which electromagnetic waves were used during WWII as detectors for foreign objects (radar). A large wooden gift was given to the United States Ambassador to the Soviet Union Averell Harriman on behalf of the Soviet Union as a gesture of kindness [2]. A brilliant scientist named Léon Theremin hid a passive listening spy device called "The Thing" within the Great Seal on the front.

The device was composed of a microwave cavity, an antenna, and a flexible diaphragm that modulated the microwave resonance frequency. A radio signal would remotely "power" the device while acoustic waves modulated the microwave resonance and the reflected radio waves were subsequently down-converted to audio frequencies. The device had no active power supply and went unnoticed for seven years. The concept behind "The Thing" is actively used today throughout society (e.g. RFID technology) [3] and in the field of cavity optomechanics.

A coupled of decades following WWII and the ground-breaking work of Dr. Vladimir Braginksy on the interactions of radiation pressure and mechanical oscillators is introduced that led to the birth of contemporary cavity optomechanics. Dr. Braginsky investigated the ponderomotive effects of radiation pressure, that is, the ability to cool and amplify mechanical motion. The field of cavity optomechanics investigates the interactions of light and matter within an enclosed volume wherein the matter, a mechanical oscillator, is manipulated by the incident light, an electromagnetic cavity. The truly macroscopic scale of such an experiment is the Laser Interferometer Gravitational-Wave Observatory (LIGO), which reported the first-ever observation of a binary black-hole merger in 2016 [4]. The light, or photons within the cavity, can possess long lifetimes and therefore interact with the mechanical resonator multiple times before decaying. The long lifetime of the cavity enables the minuscule radiation pressure to become noticeable after many round-trip interactions with the mechanical oscillator. Such interplay between the electromagnetic field and mechanical resonator has led to interesting experimental observations such as optical cooling [5], optical amplification [6], optomechanically-induced transparency [7], frequency conversion between microwave and optical domains [8, 9], and optomechanical devices such as amplifiers and circulators [10, 11].

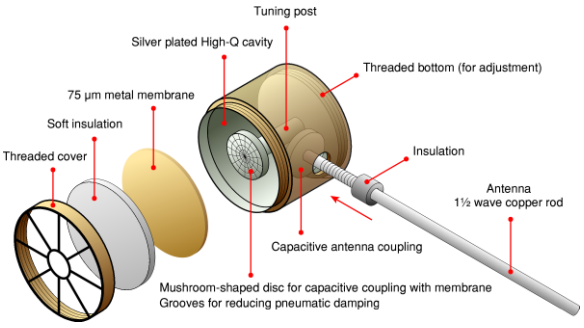


Figure 1.1: "The Thing" listening device by Léon Theremin for spying on the US Ambassador during the Cold War [2].

The decades-long development of micro-electromechanical systems (MEMS) paved the way for the capability to create exquisite nano- and micro-mechanical oscillators. Some of the major advantages of creating such small oscillators are the low mass and volume, which means that microwave circuits and mechanical structures are now able to "feel" the effects of radiation pressure, even the very act of measuring the device! The capability to miniaturize the microwave field volume and mechanical resonator naturally leads to incredibly strong coupling from the localized microwave field. In the event that the mechanics are strongly coupled to the incident light, one is able to study the very nature of quantum light or quantum mechanics.

Generally speaking, the actual mechanical device is quite simple and the complexity arises in the methods to measure the mechanical object. Over the past few decades, the ability to manufacture MEMS and NEMS has become cheaper and easier. For example, a simple SiN square membrane acting as a mechanical oscillator 1 mm in length and thickness 50 nm has been shown to demonstrate quality factors at

room temperature above $Q_m > 1$ million and is used in quantum experiments [13,14]. The cost of the bare quantum membrane device — only two cups of coffee! Of course, the cost of actual research emerges in the measurement apparatus, techniques used and methods to manipulate the membrane structure; however, it is absolutely remarkable the rapid development of technology that has given rise to cost-effective quantum devices.

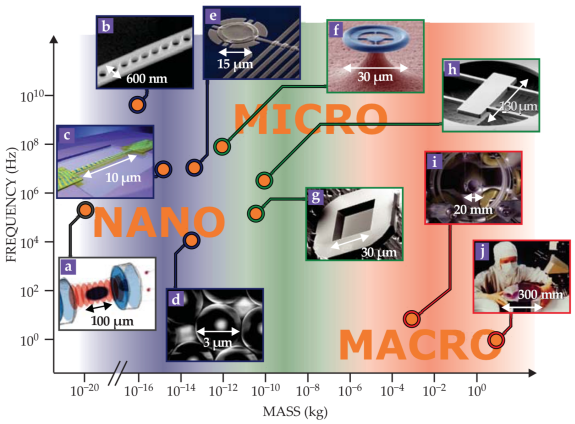


Figure 1.2: Image adapted from *Quantum Optomechanics* [12] showing past optomechanical devices with their respective masses and resonant frequencies.

Cavity optomechanics has proven to be an exciting platform for quantum information technology [15], metrology, sensing, and quantum science [16–20] with a promising future in commercial devices [21]. Today, superconducting radio frequency cavities have quality factors that exceed $Q > 10^{11}$ [22–25]. Optomechanical devices have achieved sensitivities surpassing the standard quantum limit (SQL). Silicon nitride mechanical resonators have achieved ultrastrong cooperativity and coupling to the electromagnetic field [13, 14, 26]. Mechanical resonators have been designed using dissipation engineering in which the coherence times have been drastically enhanced from environmental decoupling and increased strain [27, 28]. Bulk 3-D cavities are being developed to enhance the lifetimes of "flying qubits" for the anticipated future of quantum computing [15]. Lastly, hybrid optomechanical architectures are being developed for efficient and reliable transducers between vastly different frequency regimes using mechanical oscillators [8, 9].

The vast majority of this work was focused on trying to observe optomechanical effects within macroscopic oscillators — effects such optomechanically-induced transparency (OMIT), optomechanical damping, and mechanical frequency shifts which are all much more easily observed for nano- and micro-mechanical oscillators due to the lower mass and higher frequency. The combination of these two criteria allow stronger coupling to the electromagnetic field and the feasibility of the "resolved sideband regime" in which there is an increased asymmetry of the scattered modes and the optomechanical effects are easier to observe. As such, much of the optomechanical theory is introduced and derived even though we were not successful in observing some of the phenomena. However, as a result of trying to make more strongly-coupled optomechanical systems we discovered a unique physical effect at short length scales,

known as the thermal Casimir force, that was not observed previously in optomechanical systems. We also demonstrate some interesting characteristics of this effect such as the static Casimir spring and Casimir dilution. The latter has never been observed before and also shows great promise towards the future of developing re-configurable "*in situ*" mechanical oscillators using the Casimir force.

The extensive field of optomechanics has studied mechanical resonators in the predominantly nano- and micrometer scale (often coined the mesoscopic regime) and the question of where the boundary between classical and quantum mechanics lies remains an intriguing and captivating pursuit to this day. The overarching goal of this thesis work was to aim and construct a macroscopic platform for observing cavity optomechanical phenomena [5, 16, 20, 29–32].

In the subsequent chapters we begin with the introduction of microwave cavities, the construction of a cylindrical geometry and the modes that resonate inside the metallic structure. Afterwards, the mechanical element is brought into the scope of discussion that gives rise to the field of cavity optomechanics. The mechanical resonator acts as a variable boundary to the microwave geometry and therefore couples directly to the microwave field. The interaction between the microwaves and mechanical oscillator leads to modifications in the dynamic membrane response such as frequency, quality factor, and occupation number. Next, we discuss the experimental approach in developing the tunable macroscopic optomechanical device and operation in a dilution refrigerator to enable the superconductivity properties of the microwave cavity. Lastly, we finish the thesis under the discussion and creation of a tunable narrow gap between the mechanical oscillator and a re-entrant microwave cavity, which resulted in the observation of the thermal Casimir force. This unexpected observation has exciting future applications in the dynamic manipulation of mechanical oscillators!

# Chapter 2

# Microwave Cavities

*"Success is walking from failure to failure with no loss in enthusiasm."* – *Winston Churchill*

Metallic microwave cavities form the basis of the electromagnetic resonators that we have used and created for this doctoral work. However, the reader may be interested to know that metallic cavities are certainly not the only electromagnetic resonators as there are a variety of resonator types (metallic and dielectric) and materials operating in the microwave regime such as sapphire whispering gallery modes, Bragg reflectors, etc. A discussion and introduction of the main microwave cavities we used are presented below. A view of most of the cavities constructed during this thesis work can be seen in Fig. 2.1. Most of the cavities have undergone at least one and often multiple design/machining revisions to conserve the metal supply.

## 2.1 Cylindrical Cavities

The cylindrical and rectangular geometries are among the most well understood microwave cavities with convenient analytical solutions. In the beginning years of this research cylindrical cavities were mainly used for their simplicity of construction and general understanding of microwave cavities. We will derive the equations for a cylindrical cavity starting from a general model of an arbitrary waveguide, transforming to a circular waveguide, and then ending with the cylindrical cavity. The following derivation has been adapted from *Microwave Engineering* by David Pozar [33]. We begin with the cylindrical coordinates for a circular waveguide and consider Maxwell's

Figure 2.1: A view of the (mostly) chronological development of microwave cavities used in this thesis work.

equations in a source-free, linear, isotropic, homogenous region:

$$\nabla \times \vec{E} = -j\omega\mu\vec{H}, \tag{2.1}$$

$$\nabla \times \vec{H} = j\omega\epsilon\vec{E}, \tag{2.2}$$

where $\vec{E}$ is the electric field, $\vec{H}$ is the magnetic field, $\mu$ is the relative permeability, $\epsilon$ is the relative permittivity, and $\omega$ is the angular frequency of the wave. From these two equations we can write down the Helmholtz wave equation, which we will use later. Insert Eq. 2.2 into Eq. 2.1 and consider that $\nabla \cdot E = 0$ in a source-free region[1]. From this point we immediately write down

$$\nabla^2 E + k^2 E = 0, \tag{2.3}$$

[1] $\nabla \times \nabla \times A = \nabla(\nabla \cdot A) - \nabla^2 A$

where $k = \omega\sqrt{\mu\epsilon}$. In cylindrical coordinates we assume solutions of the form

$$\vec{E}(\rho,\phi,z) = [\vec{e}(\rho,\phi) + \hat{z}e_z(\rho,\phi)]e^{-j\beta z}, \tag{2.4}$$

$$\vec{H}(\rho,\phi,z) = [\vec{h}(\rho,\phi) + \hat{z}h_z(\rho,\phi)]e^{-j\beta z}, \tag{2.5}$$

where we have introduced the propagation constant $\beta$ of the traveling wave. These equations consider forwards propagation; for backwards traveling waves replace $\beta \to -\beta$. Assuming the above solution for $H_z$ and analogously for $E_z$ we expand the Helmholtz wave equation to give us six equations[2]:

$$\nabla \times \vec{E} = \underbrace{\hat{\rho}\left(\frac{1}{\rho}\frac{\partial E_z}{\partial \phi} + j\beta E_\phi\right)}_{=-j\omega\mu H_\rho} + \underbrace{\hat{\phi}\left(-j\beta E_\rho - \frac{\partial E_z}{\partial \rho}\right)}_{=-j\omega\mu H_\phi} + \underbrace{\hat{z}\frac{1}{\rho}\left(\frac{\partial(\rho E_\phi)}{\partial \rho} + \frac{\partial E_\rho}{\partial \phi}\right)}_{=-j\omega\mu H_z}, \tag{2.6}$$

$$\nabla \times \vec{H} = \underbrace{\hat{\rho}\left(\frac{1}{\rho}\frac{\partial H_z}{\partial \phi} + j\beta H_\phi\right)}_{=j\omega\epsilon E_\rho} + \underbrace{\hat{\phi}\left(-j\beta H_\rho - \frac{\partial H_z}{\partial \rho}\right)}_{=j\omega\epsilon E_\phi} + \underbrace{\hat{z}\frac{1}{\rho}\left(\frac{\partial(\rho H_\phi)}{\partial \rho} + \frac{\partial H_\rho}{\partial \phi}\right)}_{=j\omega\epsilon E_z}. \tag{2.7}$$

Now, we want to solve for the transverse field components from the longitudinal components. The idea to separate these equations is to isolate a single component and eliminate it with another equation. For example, we can solve for the $H_\rho$ component:

$$\begin{aligned} \frac{1}{\rho}\frac{\partial E_z}{\partial \phi} + j\beta E_\phi = -j\omega\mu H_\rho \quad &\to \quad E_\phi = \frac{1}{j\beta}\left(-j\omega\mu H_\rho - \frac{1}{\rho}\frac{\partial E_z}{\partial \phi}\right), \\ -j\beta H_\rho - \frac{\partial H_z}{\partial \rho} = j\omega\epsilon E_\phi \quad &\to \quad E_\phi = \frac{1}{j\omega\epsilon}\left(-j\beta H_\rho - \frac{\partial H_z}{\partial \rho}\right). \end{aligned}$$

Subtracting these two equations and solving for $H_\rho$ yields

$$H_\rho = \frac{j}{k_c^2}\left(\frac{\omega\epsilon}{\rho}\frac{\partial E_z}{\partial \phi} - \beta\frac{\partial H_z}{\partial \rho}\right), \tag{2.8}$$

where we have introduced some new, useful notation. Recall that $k = \omega\sqrt{\mu\epsilon}$ and now we have defined the cutoff wavenumber

$$k_c^2 = k^2 - \beta^2. \tag{2.9}$$

[2]In cylindrical coordinates the vector curl is written as $\nabla \times \vec{A} = \hat{\rho}\left(\frac{1}{\rho}\frac{\partial A_z}{\partial \phi} - \frac{\partial A_\phi}{\partial z}\right) + \hat{\phi}\left(\frac{\partial A_\rho}{\partial z} - \frac{\partial A_z}{\partial \rho}\right) + \hat{z}\frac{1}{\rho}\left(\frac{\partial(\rho A_\phi)}{\partial \rho} - \frac{\partial A_\rho}{\partial \phi}\right)$

Therefore, the other transverse field components are solved in the same fashion as we did for $H_\rho$ and are written for completeness as

$$E_\rho = -\frac{j}{k_c^2}\left(\beta\frac{\partial E_z}{\partial \rho} + \frac{\omega\mu}{\rho}\frac{\partial H_z}{\partial \phi}\right), \tag{2.10a}$$

$$E_\phi = -\frac{j}{k_c^2}\left(\frac{\beta}{\rho}\frac{\partial E_z}{\partial \phi} - \omega\mu\frac{\partial H_z}{\partial \rho}\right), \tag{2.10b}$$

$$H_\rho = \frac{j}{k_c^2}\left(\frac{\omega\epsilon}{\rho}\frac{\partial E_z}{\partial \phi} - \beta\frac{\partial H_z}{\partial \rho}\right), \tag{2.10c}$$

$$H_\phi = -\frac{j}{k_c^2}\left(\omega\epsilon\frac{\partial E_z}{\partial \rho} + \frac{\beta}{\rho}\frac{\partial H_z}{\partial \phi}\right). \tag{2.10d}$$

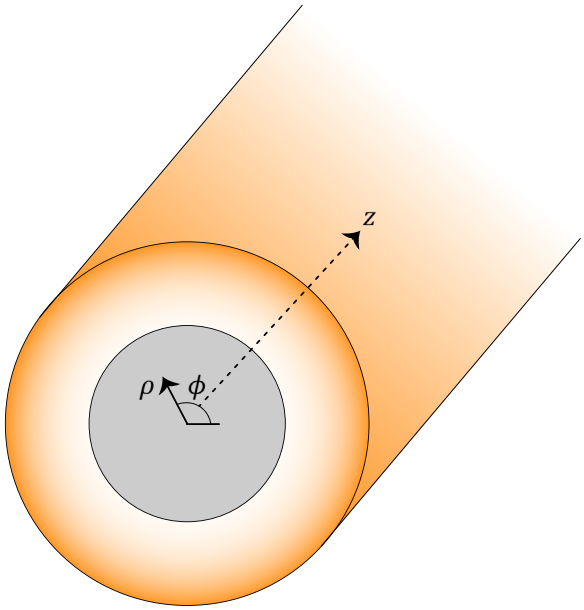


Figure 2.2: The cross-section of a circular waveguide represented by cylindrical coordinates.

These equations are general relations for the transverse field components for a propagating wave within an arbitrary waveguide geometry and will therefore be used later for the development of the cylindrical cavity. We shall now consider more specifically the circular waveguide (shown in Fig. 2.2) and solve for the transverse electric (TE) modes of the waveguide. TE modes are described by $E_z = 0, H_z \neq 0$ within the waveguide. Therefore, we can start by focusing on the $z$-component of the

magnetic field from Eq. 2.5, $H_z = h_z(\rho,\phi)e^{-j\beta z}$, for the Helmholtz wave equation[3]:

$$\nabla^2 H_z + k^2 H_z = 0,$$
$$\left(\frac{1}{\rho}\frac{\partial^2}{\partial\rho^2} + \frac{1}{\rho}\frac{\partial}{\partial\rho} + \frac{1}{\rho^2}\frac{\partial^2}{\partial\phi^2} - \beta^2 + k^2\right) h_z(\rho,\phi) = 0,$$
$$\left(\frac{1}{\rho}\frac{\partial^2}{\partial\rho^2} + \frac{1}{\rho}\frac{\partial}{\partial\rho} + \frac{1}{\rho^2}\frac{\partial^2}{\partial\phi^2}k_c^2\right) h_z(\rho,\phi) = 0.$$

At this point we want to apply the method of separation of variables. This technique allows us to separate the equations with their respective coordinates. We assume a solution of the form $h_z = R(\rho)P(\phi)$ and substitute[4]:

$$\frac{\rho}{R}\frac{\partial^2 R}{\partial\rho^2} + \frac{\rho}{R}\frac{\partial R}{\partial\rho} + \rho^2 k_c^2 = -\frac{1}{P}\frac{\partial^2 P}{\partial\phi^2}, \tag{2.11}$$

where we have multiplied through by $\rho^2$ and divided through by $h_z = R(\rho)P(\phi)$. Since both sides are dependent upon differing variables and this equation must hold for all possible values, both sides must be equal to a constant. Considering the right hand side with the coordinate $\phi$,

$$-\frac{1}{P}\frac{d^2 P}{d\phi^2} = k_\phi^2,$$
$$\frac{d^2 P}{d\phi^2} + P k_\phi^2 = 0$$

and has a general solution $P(\phi) = A\sin k_\phi\phi + B\cos k_\phi\phi$. This solution must be periodic in $\phi$ such that $h_z(\phi) = h_z(\phi \pm 2\pi)$, which requires that $k_\phi$ be an integer:

$$P(\phi) = A\sin n\phi + B\cos n\phi. \tag{2.12}$$

Now we can look at the left hand side of Eq. 2.11 with coordinate $\rho$:

$$\frac{\rho}{R}\frac{d^2 R}{d\rho^2} + \frac{\rho}{R}\frac{dR}{d\rho} + \rho^2 k_c^2 = k_\phi^2, \tag{2.13}$$
$$\rho^2\frac{d^2 R}{d\rho^2} + \rho\frac{dR}{d\rho} + \left(\rho^2 k_c^2 - n^2\right) R = 0. \tag{2.14}$$

[3]The Laplacian, or divergence of the gradient, is (in cylindrical coordinates): $\nabla\cdot\nabla f = \nabla^2 f = \frac{1}{\rho}\frac{\partial}{\partial\rho}\left(\rho\frac{\partial f}{\partial\rho}\right) + \frac{1}{\rho^2}\frac{\partial^2 f}{\partial\phi^2} + \frac{\partial^2 f}{\partial z^2}$.

[4]As an example of variable separation, $\frac{\partial h_z(\rho,\phi))}{\partial\rho} = \frac{\partial}{\partial\rho}\left[R(\rho)P(\phi)\right] = P(\phi)\frac{\partial}{\partial\rho}\left[R(\rho)\right]$.

Equation 2.14 is known as Bessel's differential equation and has the following solution:

$$R(\rho) = CJ_n(k_c\rho) + DY_n(k_c\rho), \tag{2.15}$$

where $J_n, Y_n$ are the Bessel functions of the first and second kinds, respectively. This solution is simplified, however, by considering that $Y_n(x) \to \infty$ as $x \to 0$ and is therefore unphysical, which requires $D = 0$. Let us recall the solution we have thus far for the magnetic field

$$H_z(\rho, \phi, z) = (A \sin n\phi + B \cos n\phi)\, J_n(k_c\rho)e^{-j\beta z} \tag{2.16}$$

and we have absorbed the constant $C$ into $A$ and $B$. This equation is not yet useful since we have too many unknowns. Let us consider the boundary condition that the tangential electric field is zero at the very edge of the waveguide wall, $E_\phi(\rho = a, \phi) = 0$. In this case $a$ is the radius of the waveguide. We need to solve $E_\phi$ from Eq. 2.10a before we apply the boundary:

$$E_\phi(\phi, \rho, z) = \frac{j\omega\mu k_c}{k_c^2}\,(A \sin n\phi + B \cos n\phi)\, J_n'(k_c\rho)e^{-j\beta z}.$$

In order to make $E_\phi(\rho = a, \phi) \to 0$ we must have $J_n'(p_{nm}') = J_n'(k_c a) = 0$ where $p_{nm}'$ is the $m^{\text{th}}$ root of $J_n'$. These evaluations are referred to as the zeros of the Bessel function and easily referenced in tables. These definitions lead to the cutoff wavenumber for the TE modes in a circular waveguide:

$$k_{c_{nm}} = \frac{p_{nm}'}{a}. \tag{2.17}$$

We will now go through a similar, but abbreviated, derivation for the TM modes to obtain the cutoff wavenumber. Recall that the nomenclature of TM modes requires $E_z \neq 0, H_z = 0$ and that we have the solution $E_z = e_z(\rho, \phi)e^{-j\beta z}$. Repeating the steps above with $\nabla^2 e_z + k^2 e_z = 0$ will result in the solution,

$$E_z(\rho, \phi, z) = (A \sin n\phi + B \cos n\phi)\, J_n(k_c\rho)e^{-j\beta z}.$$

We apply the boundary condition $E_\phi(\rho = a, \phi) = 0$, but this step is now easier than before because we can evaluate the condition directly. This means we identify that $J_n(p_{nm)=0}$ resulting in the cutoff wavenumber for the TM mode in a circular waveguide:

$$k_c = \frac{p_{nm}}{a}. \tag{2.18}$$

Remember that before we had $E_\phi \propto \frac{\partial H_z}{\partial \rho}$ which was what led to the derivative of the

Bessel function.

Finally we arrive at the geometry for the cylindrical cavity. The expressions for the TE and TM modes of a circular waveguide were derived because of the intuitive transition from the waveguide to the cavity. The cylindrical cavity can be thought of as a section of circular waveguide shorted at both ends. We can also include forward and backward traveling waves in the cavity and express the transverse electric fields $(E_\rho, E_\phi)$ of either $\mathrm{TE_{nm}}$ or $\mathrm{TM_{nm}}$ waveguide modes as $\vec{E}_t(\rho,\phi,z) = \vec{e}(\rho,\phi)\left(A^+e^{-j\beta_{nm}z} + A^-e^{j\beta_{nm}z}\right)$ where $A^+, A^-$ are the forward and backward traveling wave amplitudes, respectively. The transverse electric field vanishes for the shorted ends of the cavity allowing,

$$\vec{E}_t = 0 = \begin{cases} \vec{e}(\rho,\phi)\left(A^+ + A^-\right), & z = 0, \\ \vec{e}(\rho,\phi)\left(A^+e^{-j\beta_{nm}d} + A^-e^{j\beta_{nm}d}\right), & z = d. \end{cases} \tag{2.19}$$

The first boundary condition above results in $A^+ = -A^-$ and can be used to rewrite the second as $0 = \vec{e}(\rho,\phi)\left(A^+e^{-j\beta_{nm}d} - A^+e^{j\beta_{nm}d}\right) \rightarrow \vec{e}(\rho,\phi)(-2jA^+\sin\beta_{nm}d)$. For this equation to be zero, it must be that $\beta_{nm}d = 0, \pi, 2\pi, \cdots = l\pi$. Remember the relationship between the cutoff wavenumber and the propagation constant $k_c^2 = k^2 - \beta_{nm}^2$. From this information we can write down the resonant frequencies of the $\mathrm{TE}_{nml}$ modes as,

$$k^2 = k_c^2 + \beta_{nm}^2, \tag{2.20}$$

$$\omega = \frac{1}{\mu\epsilon}\left(k_c^2 + \beta_{nm}^2\right), \tag{2.21}$$

$$\Rightarrow f_{nml} = \frac{c}{2\pi\sqrt{\mu_r\epsilon_r}}\sqrt{\left(\frac{p'_{nm}}{a}\right)^2 + \left(\frac{l\pi}{d}\right)^2}, \tag{2.22}$$

where $c = \frac{1}{\sqrt{\mu_0\epsilon_0}}$ has been introduced as the speed of light constant[5]. Likewise, we can do the same for the TM modes, only the cutoff wavenumber changes to what we obtained in Eq. 2.18. The resonant frequencies of the $\mathrm{TM}_{nml}$ mode are:

$$f_{nml} = \frac{c}{2\pi\sqrt{\mu_r\epsilon_r}}\sqrt{\left(\frac{p_{nm}}{a}\right)^2 + \left(\frac{l\pi}{d}\right)^2}. \tag{2.23}$$

Lastly, the field equations for the $\mathrm{TE}_{nml}$ mode are derived and this formulation can be extended for the $\mathrm{TM}_{nml}$ modes, but is not included here. Using our previous result

[5]Perhaps it is useful to note that the permittivity can be written as $\epsilon = \epsilon' = \epsilon_0\epsilon_r$, whereas in the presence of a dielectric the permittivity is modified to $\epsilon = \epsilon' - j\epsilon'' = \epsilon_0\epsilon_r(1 - j\tan\delta)$ where $\tan\delta$ is the loss tangent of the material.

that $A^+ = -A^-$ we express the $z$-component of the magnetic field (remember TE mode $E_z = 0, H_z \neq 0$) as:

$$\begin{aligned} H_z &= (A \sin n\phi + B \cos n\phi)\, J_n \left(\frac{p'_{nm}}{a} p\right) \left(-2jA^+ \sin \frac{\pi l z}{d}\right), \\ &= H_0 J_n \left(\frac{p'_{nm}}{a} p\right) \cos n\phi \sin \frac{\pi l z}{d}, \end{aligned}$$

where $H_0 = -2jA^+$ and we have rotated the coordinate system about the $z$-axis[6]. The complete set of components for the $\mathrm{TE}_{nml}$ can be solved using the previous expression for $H_z$ as well as Eqns. 2.10a-2.10d and $E_z = 0$:

$$\begin{aligned} H_z &= H_0 J_n \left(\frac{p'_{nm}}{a} p\right) \cos n\phi \sin \frac{\pi l z}{d}, \\ H_\rho &= \frac{\beta a H_0}{p'_{nm}} J'n \left(\frac{p'_{nm}}{a} p\right) \cos n\phi \cos \frac{\pi l z}{d}, \\ H_\phi &= -\frac{\beta a^2 n H_0}{(p'_{nm})^2 \rho} J'n \left(\frac{p'_{nm}}{a} p\right) \sin n\phi \cos \frac{\pi l z}{d}, \\ E_\rho &= \frac{jk\eta a^2 n H_0}{(p'_{nm})^2 \rho} J'n \left(\frac{p'_{nm}}{a} p\right) \sin n\phi \sin \frac{\pi l z}{d}, \\ E_\phi &= \frac{jk\eta a H_0}{p'_{nm}} J'n \left(\frac{p'_{nm}}{a} p\right) \cos n\phi \sin \frac{\pi l z}{d}, \\ E_z &= 0, \end{aligned}$$

where $\eta = \sqrt{\mu/\epsilon}$.

The introduction of the cavity and its theoretical construction is now finished, but now we shall discuss the application of the microwave cavity and its usefulness, in particular the quality factor of the microwave cavity. The quality factor, $Q$, is ubiquitous throughout most of the world of physics and takes two main meanings. The first definition is that the quality factor represents the number of coherent oscillations before decaying to 37% ($e^{-1}$) of its initial energy. The second definition, and often more useful for microwave applications, is the relationship between the stored energy and dissipated power. A cavity with $Q > 1$ allows more energy to "build up" than is dissipated. For a microwave cavity, the stored energy is the microwave field and the dissipated power is due to the surface current in the conducting walls of the cavity. The latter definition will be discussed theoretically. The quality factor can be restated

[6] As explained further in *Microwave Engineering*, the coordinates can be rotated about the $z$-axis to yield either $A = 0$ or $B = 0$.

in the following manner [34]:

$$Q = \frac{\text{Oscillator Rate} \times \text{Energy Stored}}{\text{Power Dissipated}},$$

where the stored energy is written as

$$U = \frac{\mu_0}{2}\int_V |\vec{H}|^2 dV = \frac{\epsilon_0}{2}\int_V |\vec{E}|^2 dV$$

and the dissipated power as

$$P_{\text{diss}} = \frac{R_s}{2}\int_S |\vec{H}|^2 dS,$$

with $R_s$ as the surface resistance of the conducting walls and is given by

$$R_s = \sqrt{\frac{\omega\mu}{2\sigma}} = \frac{1}{\delta_s \sigma}, \tag{2.24}$$

where $\sigma$ is the conductivity and $\delta_s = \sqrt{\frac{2}{\omega\mu\sigma}}$ is the skin depth, or the amount of microwave penetration into a conductor. The skin depth is the region at which the large majority of the electric field flows within the conductor and decays exponentially into the material. By identifying the integral types above it becomes clear that maximizing the volume to surface area results in higher $Q$ because there is less dissipated power in the conducting walls. Therefore, in relation to energy and power, the quality factor is

$$Q = \frac{\omega_0\mu_0 \int_V |\vec{H}|^2 dV}{R_s \int_S |\vec{H}|^2 dS} = \frac{G}{R_s}, \tag{2.25}$$

where $G$ is known as the geometry factor. This notation will typically be avoided as it becomes confusing later when referring to the frequency-pull parameter also designated as $G$. A much more useful notation, however, is stated in reference to losses or a rate of energy loss,

$$Q = \frac{\omega_0}{\kappa} = \omega_0 \tau, \tag{2.26}$$

where $\kappa$ is the energy loss rate (in Hz) and $\tau$ is the decay time. In the frequency domain, $\kappa$ is the full width at half maximum (FWHM) of the resonance response. The resonance response is often fit to a Lorentzian to obtain $\kappa$ or is frequently estimated by taking the width of the spectral resonance at 3 dB below the maximum (half-maximum) for transmission or 3 dB above the minimum for reflection. The reason that a Lorentzian is used to fit the spectral response of an oscillator is because the

Fourier transform of a decaying, oscillating exponential function has a Lorentzian line-shape. Until this point the losses have been lumped together into a single term $\kappa$, however, they are most often expressed as separate entities where

$$\kappa = \sum_i \kappa_i.$$

For a cavity the losses are usually expressed as $\kappa = \kappa_0 + \kappa_e$ with $\kappa_0$ as the intrinsic loss of the cavity and $\kappa_e$ is the external loss of the cavity, or the method in which the cavity couples to the outside environment. This is a fancy method of saying $\kappa_e$ is introduced by attaching cables (waveguides) to the cavity and therefore adds some energy loss. For a double-sided cavity (i.e. transmission measurement), each coupled side takes the form $\kappa_{\text{ex}} = \kappa_e/2$ (with each port identical) whereas it is only $\kappa_{\text{ex}} = \kappa_e$ for a single port cavity in reflection. To be clear, $\kappa$ represents the FWHM of the power in the frequency domain [35]. The amplitude decays with a rate $\frac{1}{2\tau}$ whereas the power decays with $\frac{1}{\tau}$. Because the losses add linearly, the quality factors add inversely

$$\frac{1}{Q_L} = \frac{1}{Q_0} + \frac{1}{Q_{ex,1}} + \frac{1}{Q_{ex,2}} + \cdots.$$

Intuitively this should make sense because the loaded quality factor $Q_L$ is limited to the most "lossy" mechanism. This is also the same method that parallel resistances add in a circuit. The decay time $\tau_L$ of the microwave cavity is often measured and the intrinsic $Q$ can be found via

$$Q_0 = \underbrace{\omega_0 \tau_L}_{Q_L}(1 + \beta_1 + \beta_2 + \cdots), \tag{2.27}$$

where $\beta_i$ is referred as the coupling coefficient of the $i^{\text{th}}$ coupled port and is related to the decay rates by $\beta_i = \kappa_{e,i}/\kappa_0$. Under-coupled ports occur for $\beta_i < 1$, critically-coupled ports have $\beta_i = 1$, and over-coupled ports occur for $\beta_i > 1$. A time-saving and useful technique to obtain critically coupled cavities is to know that $\beta/Q$ stays roughly constant. In other words, if one expects the cavity $Q$ to increase three orders of magnitude and be critically coupled at cryogenic temperatures, the couplers should be under coupled to roughly $\beta = 0.001$ at room temperature. The coupling coefficient can be calculated via

$$\beta = \frac{1 - \sqrt{\frac{P_{\text{on}}}{P_{\text{off}}}}}{1 + \sqrt{\frac{P_{\text{on}}}{P_{\text{off}}}}}, \tag{2.28}$$

where $P_{\text{on}}, P_{\text{off}}$ is the power on/off resonance, respectively.

Going back to specific geometries, the quality factor of the cylindrical geometry

with finite conducting walls can be expressed as

$$Q_0 = \frac{(ka)^3 \eta a d}{4(p'_{nm})^2 R_s} \frac{1 - \left(\frac{n}{p'_{nm}}\right)^2}{\left\{\frac{ad}{2}\left[1 + \left(\frac{\beta a n}{(p'_{nm})^2}\right)^2\right] + \left(\frac{\beta a^2}{p'_{nm}}\right)^2 \left(1 - \frac{n^2}{(p'_{nm})^2}\right)\right\}}. \tag{2.29}$$

Figure 2.3 shows $Q_0$ for a few different TE modes. In practice, we witnessed the room temperature quality factors of some copper cavities range between $Q_0 = 5 \times 10^3 - 13 \times 10^3$. The cavity length was chosen to be $d = 38.1$ mm for the calculations, which was typical for our experiments. Contrary to the graph, we typically coupled to the $TE_{011}$ mode. The $TE_{011}$ mode for a cylindrical cavity is graphically shown in Fig. 2.4. If we consider the discussion of superconductivity and assembly of the real cavity device, the choice of the $TE_{011}$ mode becomes easier to understand even though numerically there are other higher-$Q$ modes. Equation 2.29 does not consider the seams or gaps in the device, but rather the walls themselves as if the cavity was completely and perfectly enclosed. In reality, there must be at least one joint seam where an end-cap seals the cavity after the machining process. Note that this is not true for 3-D printed cavities (an active area of research to reduce costs and increase performance [36]). Therefore, the $TE_{011}$ mode is chosen because it has the lowest amount of field present at the seams for both electric and magnetic fields.

This issue of surface conductivity at the seams becomes even more crucial if we discuss the idea of superconductivity. Superconductivity is a phenomenon in which a material is cooled to the point that the surface resistance drops to (nearly) zero. Ideally, a current would flow forever with zero resistance, however, there is always some residual resistance (typically on the order of a few nano-Ohms) and this is an active investigation that the accelerator community continues to tackle [24]. The majority of superconducting materials have been successfully explained (except in the case of high-temperature superconductors) by the Bardeen, Cooper, and Schrieffer (BCS) theory that explains the interesting effect as a superfluid of Cooper pairs, that is, electrons coupled together that are mediated through phonons [37]. Therefore, for the cylindrical cavity design, the surface current must "jump" over the discontinuity between the two objects (cavity body and boundary), which in turn reduces the microwave $Q$.

To cool the microwave resonators into a superconducting state we used dilution refrigerators (a real picture of a cavity at the base plate is seen in Fig. 2.5). The fridge can cool to a temperature of $T = 4$ K using a pulse-tube cryocooler before a mixture of $^3$He and $^4$He takes place in a mixing cycle to reach a base temperature around $T = 60$ mK. The refrigerator had a cooling power of roughly 200 $\mu$W at the 4 K stage. Niobium has a superconducting transition temperature of $T = 9.3$ K whereas aluminum is $T = 1.2$ K. In light of this, the cost of instrumentation to

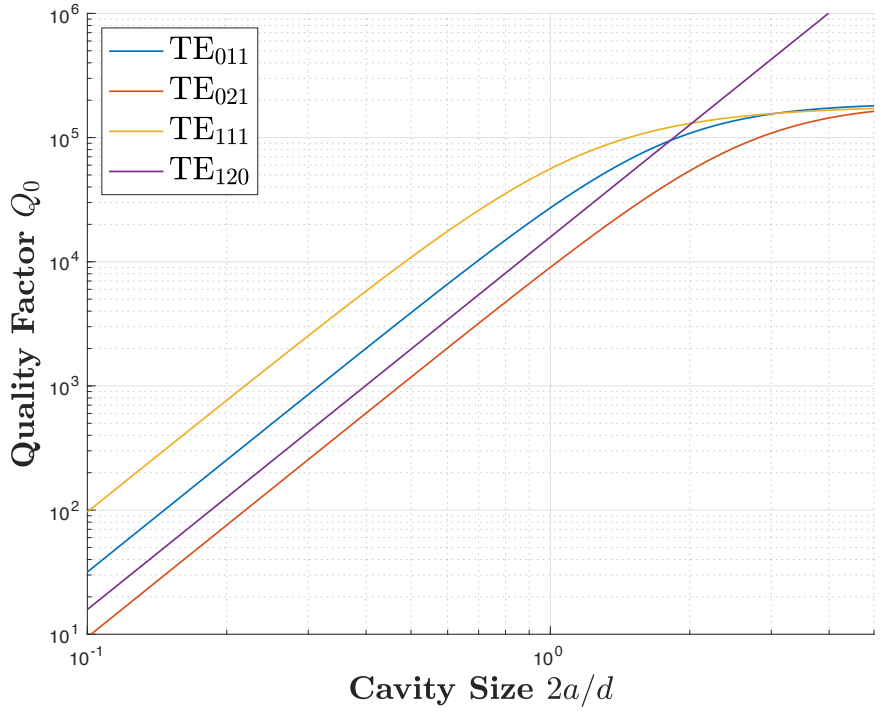


Figure 2.3: The unloaded quality factor $Q_0$ of a copper cylindrical cavity is plotted for several TE modes using Eq. 2.29 as a function of cavity diameter $2a$ to length $d$.

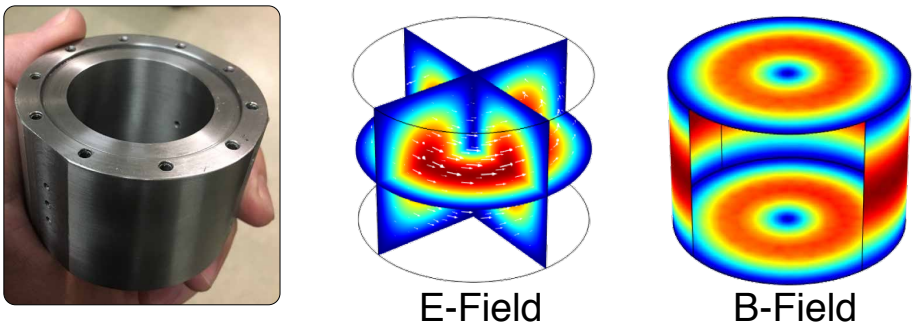


Figure 2.4: Normal niobium cylindrical cavity (left) with the $TE_{011}$ mode for this geometry showing both electric and magnetic field patterns.

achieve a superconducting state is much cheaper for niobium than aluminum because there is no need for a dilution refrigerator for niobium; one can use a much cheaper 4 K cryocooler. A graphic of the various stages and amplifiers can be seen in Fig. 2.6.

A major hurdle to our experiments was the noise introduced by the pulse-tube cryocooler typically in the range of 3-10 kHz. Our large circular mechanical oscillators

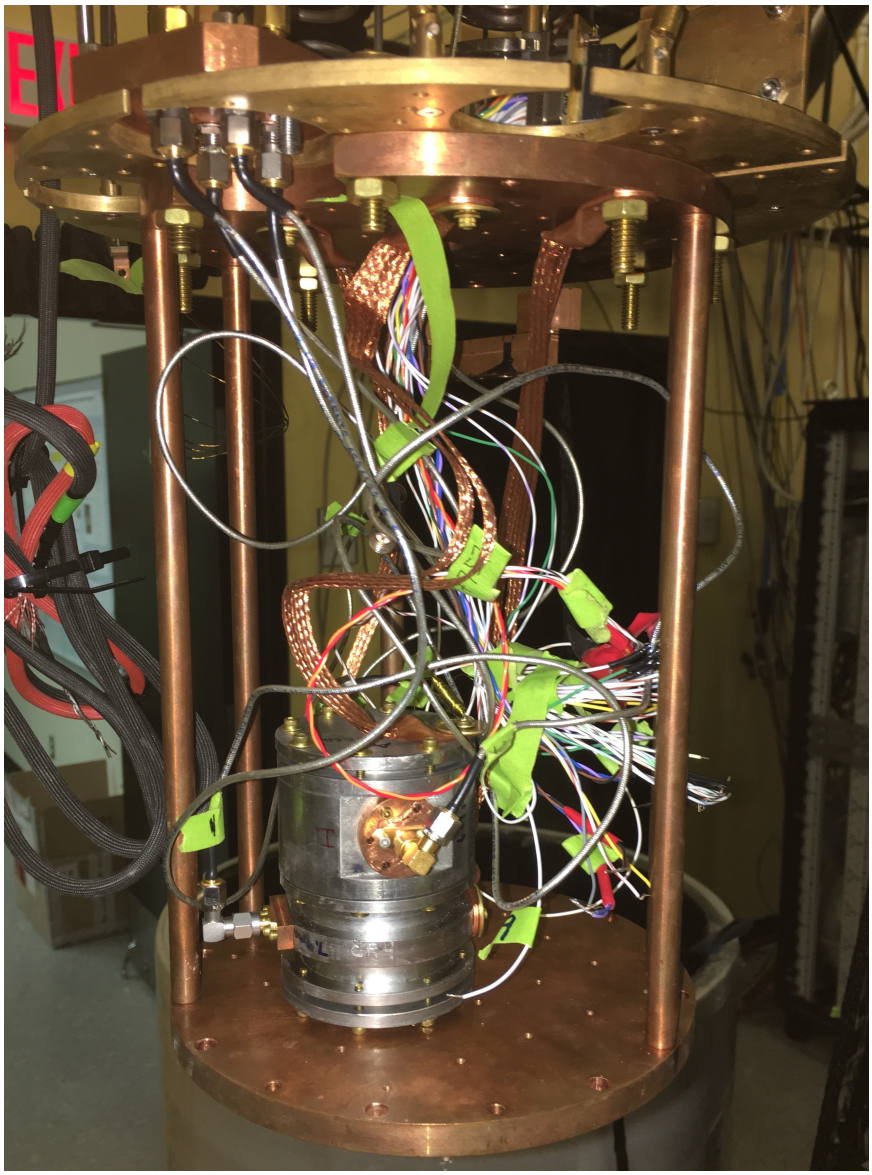

Figure 2.5: A cavity is placed at the mixing chamber plate of the dilution refrigerator. The SMA cables are connected to the cavities for transmission and reflection measurements with the amplifiers, circulators, and attenuators placed above this plate.

(discussed later) also had resonance frequencies on the order of 2.5-10 kHz, creating a challenging problem of detecting the resonance. While this continues to remain a challenge for the low-frequency oscillators, we made good progress on reducing the pulse-tube noise at the mixing chamber plate by physically separating the coaxial cable assembly from the fridge plates using felt. The felt helps prevent high-frequency

acoustic noise from traveling down the SMA microwave cables. The cables, however, still needed to be thermally anchored to the fridge plates so we used copper-braided wire and aluminum tape. These implementations resulted in a noise reduction up to a factor of 40 shown in Fig. 2.7.

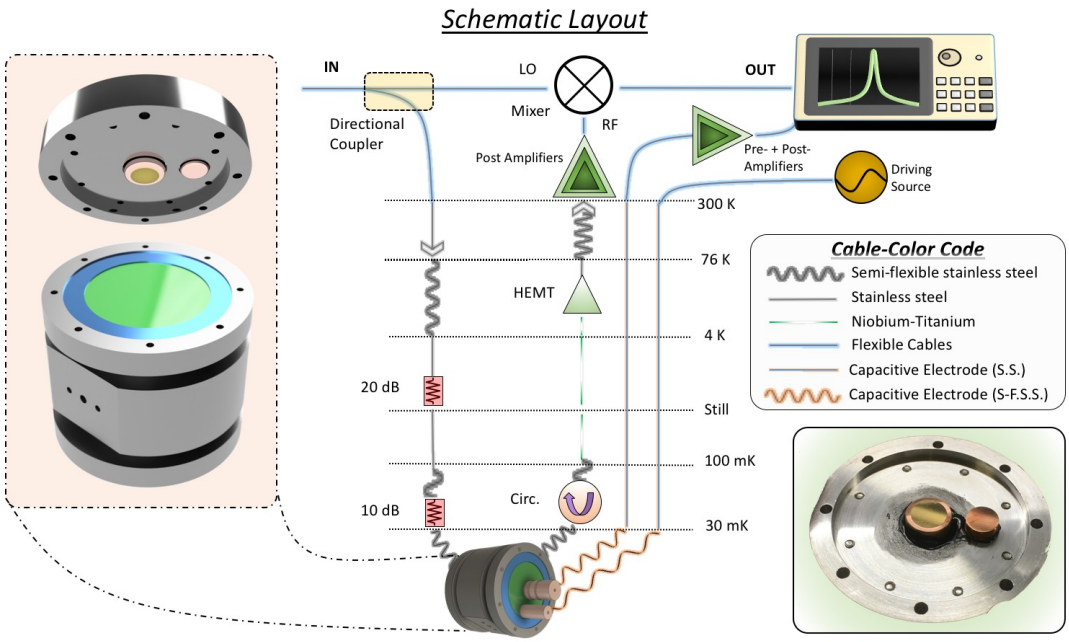


Figure 2.6: This is the general layout of the dilution refrigerator, cables, and measurement setup regarding the microwave cavities. Most of the time a mixer was not used and the measurement was simply a transmission of the cavity. The membranes forming the cavity boundary will be discussed later.

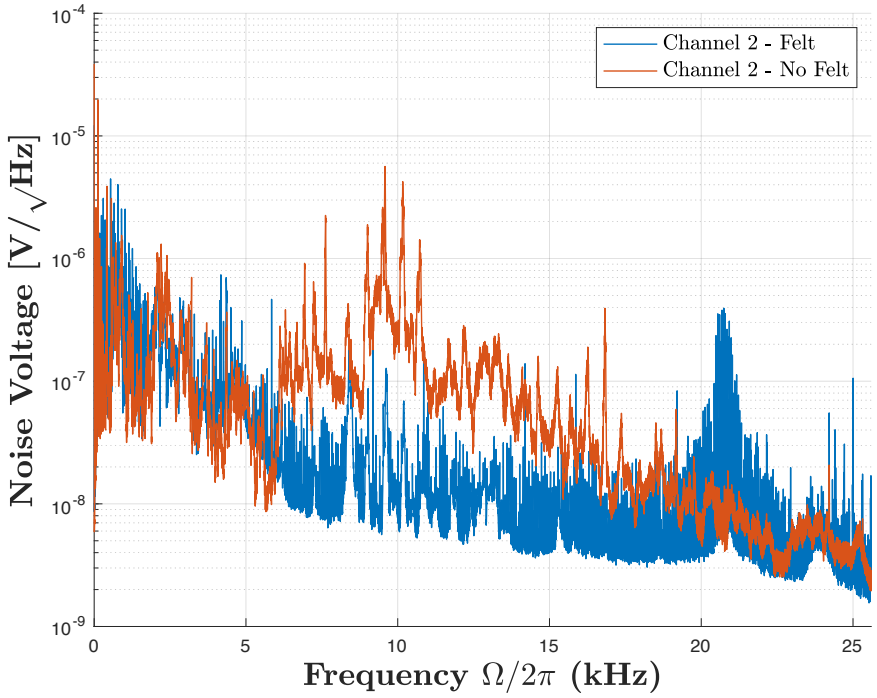


Figure 2.7: This data shows a reduction factor of about 40 for noise between 5 and 10 kHz arising from the pulse tube cooler.

## 2.2 $\lambda/4$ Coaxial "Stub" Cavities

The SRF group at UC Merced has discovered the importance of maintaining good electrical contact between adjoining cavity segments for high electrical quality factor ($Q > 10^8$). This was not the focus of this research, however, it is important to mention because this highlights a shift in cavity designs. The cylindrical cavity requires at least one seam, or point of contact between two boundaries, to form the electromagnetic resonator. As a result, there is a discontinuous "jump" in the surface current of the resonator that was shown to be very difficult to compensate for in order to achieve a large quality factor. The postdoc in our lab at the time, Dr. Luis Martinez, was able to manufacture a cavity with a quality factor of $Q_0 = 3 \times 10^8$ before annealing after years of working on the process. In contrast, the stub cavity as explained below, realized a quality factor of $Q_0 = 1.6 \times 10^9$ on the first attempt (with etching and annealing).

One of the remarkable features of the "stub" cavities is the lack of a seam to assemble the cavity. This one feature was a major detriment to the previous cylindrical cavity designs. The stub cavity is sometimes referred to as a vacuum-terminated

coaxial stub cavity since there is no apparent metallic boundary. Instead, the cavity remains open at one end. The long tube of this cavity permits high-$Q$ because the electric field decays exponentially away from the stub while the magnetic field remains at the base of the cavity [15]. The resonance frequency is approximately determined by the length of the stub. The other elements such as stub diameter and distance-to-wall also affect the frequency, though not quite as much as the height of the stub. As it turns out, there are no analytical solutions to the stub cavity and one roughly approximates the frequency by solving a transcendental equation. For these reasons, this approach was never used and, instead, a finite element analysis approach with COMSOL was used that gave accuracies within a couple of percent of the actual machined device.

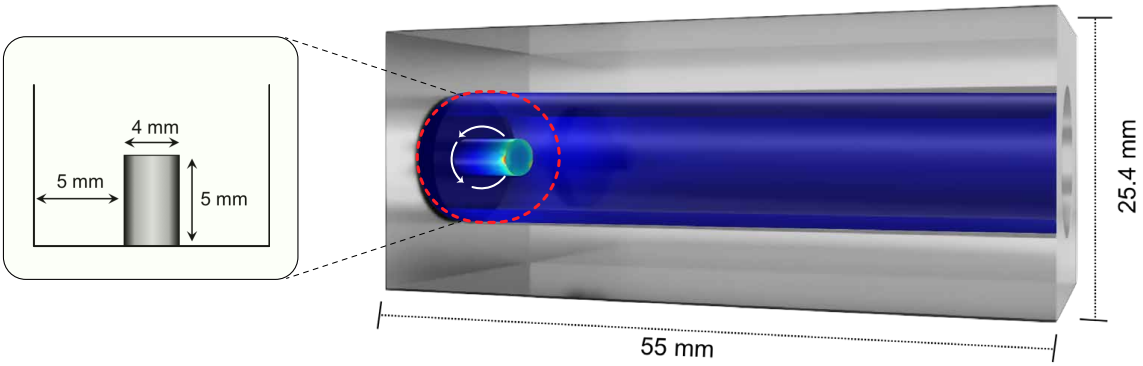


Figure 2.8: Here is a coaxial $\lambda/4$ stub cavity with the electric field overlayed as a heat map and modeled by COMSOL. Rather than a traditional cylindrical cavity with two boundaries, the open end is often coined "vacuum-terminated." The magnetic field is illustrated with white arrows and circles around the stub with the largest field amplitude at the base of the stub.

Cavities were machined from stock 6061 (alloy) aluminum, 101 copper, and reactor-grade niobium. The main difficulty in machining these cavities, apart from the challenge of machining niobium, is attempting to create a smooth surface at the base of the stub. An extended 1/8" end-mill was typically used for milling out the stub and then some Scotch-Brite$^{TM}$ pads are pushed into the cavity while on a lathe to smooth out the machine marks.

## 2.3 Re-entrant Cavities

Near the end of this research work, while attempting to increase coupling between the mechanical resonator and the cavity, the cavity designs changed from empty cylindrical cavities to $\lambda/4$ coaxial stub cavities to a combination of the two together, called re-entrant cavities. This was a great confirmation of the direction we took in cavity design for increasing sensitivity based upon trial and error prototype cavities. We became familiar with Dr. Michael Tobar's work and discovered the decades-long progress of re-entrant cavities and their remarkable sensitivity based upon small gap sizes within microwave cavities. This section will discuss these types of microwave cavities.

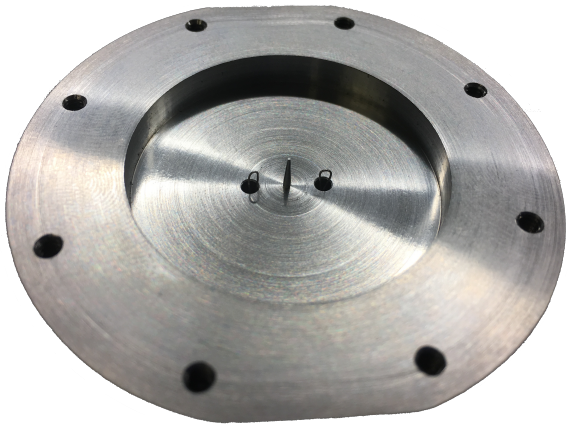

Figure 2.9: This is one of the re-entrant cavities with the loop antennas shown for magnetic field coupling. This cavity has a cone angle of 3°. The spacing set between the cone and boundary (not shown) is ideally made to be as small as possible for the highest sensitivity. For some of the cavities, the gap became as small as $< 1$ $\mu$m.

The re-entrant cavity is a unique microwave oscillator because it allows the existence of microwave frequencies within a sub-wavelength gap spacing ($x$). In its simplest understanding, the gap between the post and the boundary behaves like a capacitor and the post acts like an inductor. The re-entrant cavity is frequently considered to behave as a lumped model with the spatial separation of $E$ and $B$ fields as is the case for an LC circuit. The electric field $E = E_0 e^{i\omega t}$ is concentrated between the post while the magnetic field $B = B_0 e^{i\omega t}$ circles around the post [38, 39]. The microwave frequency for the re-entrant cavity with a frustum is approximated as a

lumped LC model [40] with the geometric parameters illustrated in Fig. 2.10:

$$r_0 = \bar{r_0} - \frac{x}{\tan\alpha}, \tag{2.30a}$$

$$L = \frac{\mu_0 h}{2\pi}\left(\ln\frac{e r_2}{r_1} - \frac{r_0}{r_1 - r_0}\ln\frac{r_1}{r_0}\right), \tag{2.30b}$$

$$l_m = \frac{1}{3}\frac{\sqrt{\{2(r_1-r_0)^2 + 3(r_2-r_1)(r_1+r_2-2r_0)\}^2 + h^2(3r_2-2r_1-r_0)^2}}{2r_2 - r_1 - r_0}, \tag{2.30c}$$

$$C_0 = \frac{\pi\epsilon_0\bar{r}_0^2}{x}, \tag{2.30d}$$

$$C_1 = \frac{\pi\epsilon_0(r_0^2 - \bar{r}_0^2)}{x} + \frac{2\pi\epsilon_0}{\alpha}\left[r_0 \ln\frac{e l_m \sin\alpha}{x} + \frac{x\cot\alpha}{2}\ln\frac{\sqrt{e} l_m \sin\alpha}{x}\right]. \tag{2.30e}$$

Based upon these geometric definitions the resonance frequency is expressed with

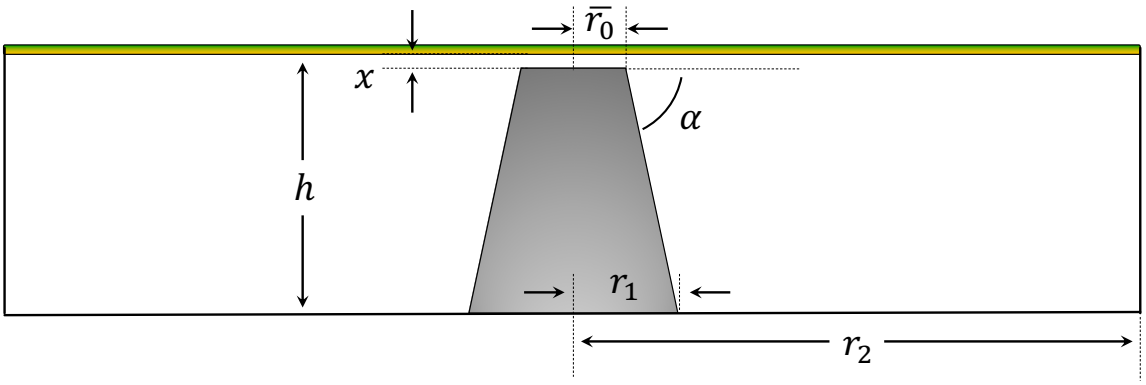


Figure 2.10: The re-entrant cavity parameters for determining the resonance frequency and its relation to gap size $x$.

the familiar equation for an LC oscillator:

$$f = \frac{1}{2\pi\sqrt{L(C_0 + C_1)}}. \tag{2.31}$$

In other words, $C_0$ is the "bare capacitance" while $C_1$ can be described as a "fringing capacitance" that accounts for the walls of the post. The cavity height $h$ is the sum of the re-entrant post height and the gap size $h = h_p + x$. The final geometry of the most sensitive cavity we created had the following parameters: $h_p = 4.25 \times 10^{-3}$ m, $\bar{r}_0 = 1.85 \times 10^{-4}$ m, $\alpha = 87$ degrees, $r_1 = 3.5 \times 10^{-4}$ m, and $r_2 = 19.05 \times 10^{-3}$ m. The smallest gap we achieved was $x = 585$ nm, although this is not the most sensitive cavity as we found another mechanism that limited the sensitivity of the cavity and is discussed in later chapters.

For a re-entrant cavity with a straight-post, which seems to be more typical in the literature, the expression is simpler and more intuitive:

$$L = \mu_0 \frac{h}{2\pi} \ln\left(\frac{r_{\text{cav}}}{r_{\text{post}}}\right), \tag{2.32a}$$

$$C_0 = \epsilon_0 \frac{\pi r_{\text{post}}^2}{x}, \tag{2.32b}$$

$$C_1 = 4\epsilon_0 r_{\text{post}} \ln\left(\frac{e\sqrt{(r_{\text{cav}} - r_{\text{post}})^2 + h^2}}{2x}\right). \tag{2.32c}$$

The final resonance frequency is again identical to Eq. 2.31.

## 2.4 Reflection and Transmission of a Double-Sided Cavity

Let us consider the cavity coupling at this point and how it interacts with the microwave response. Perhaps it is convenient to mention that a Lorentzian can be explained by the frequency response given to a decaying, oscillatory function. If one were to Fourier-transform the time domain response of a decaying oscillator they would arrive at the Lorentzian-shaped profile in the frequency domain. A slight modification to this is the Fano-like line shape, which is the asymmetric Lorentzian. We begin with the formulation of input-output theory. The best reference for this work is by Li et al. [41] which deals with multiple cavity schemes (including coupled double cavities), but for simplicity, we will cover the cavity most frequently used in this work: the double-sided cavity is known as an S2 configuration from the referenced paper and shown in Fig. 2.13.

Let us first solve for the reflection signal for the resonator. Using some input-output theory, the output signal is written as

$$\hat{a}_{\text{out}} = \hat{a}_{\text{in}} - \sqrt{\kappa_{\text{ex}}}\hat{a}, \tag{2.33}$$

where $\hat{a}$ is the microwave field amplitude operator using the language of quantum optics. However, it should be clear that even though these equations use the quantum language, this does not imply the underlying mechanism is quantum. After all, we are discussing a classical signal interacting with a classical resonator. For simplicity we drop the hats on the operators. The field amplitude in the resonator is expressed as an equation of motion and is derived in detail later in Ch. 3:

$$\dot{a} = (j\omega_0 - \kappa/2)a + \sqrt{\kappa_{\text{ex}}}a_{\text{in}}. \tag{2.34}$$

This can be simplified in the time domain (or frequency domain) using $a(t) = ae^{j\omega_\ell t}$. It is important to note that the meaning of $\kappa_{\text{ex}}$ will change depending on the coupling configuration, but the overall definition of the decay rate $\kappa = \kappa_0 + \kappa_e$ will not change. Let the reader be aware that we try to keep notation the same through this work, yet sometimes we may inadvertently use the subscript $i$ for intrinsic instead of 0 (i.e. $\kappa_i \equiv \kappa_0$). For the double-sided configuration presented, $\kappa_{\text{ex}} = \kappa_e/2$. For single-port cavities, $\kappa_{\text{ex}} = \kappa_e$,

$$i\omega_\ell a = (j\omega_0 - \kappa/2)a + \sqrt{\kappa_{\text{ex}}}a_{\text{in}}, \tag{2.35}$$

$$\rightarrow \qquad a = \frac{\sqrt{\frac{\kappa_e}{2}}a_{\text{in}}}{-j\Delta + \kappa/2}, \tag{2.36}$$

where we have introduced $\Delta = \omega_l - \omega_0$ as a convenient method for identifying detuning from the cavity resonance.

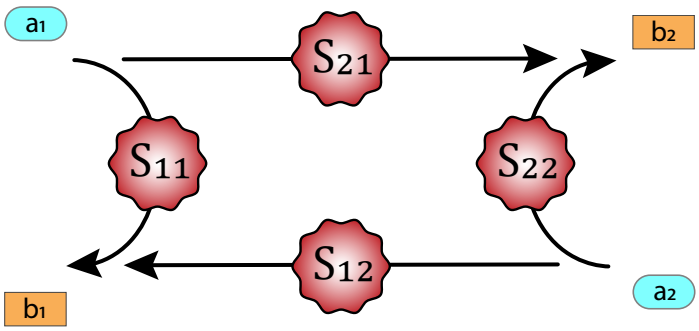


Figure 2.11: This is a method for visualizing the S-parameters in the context of transmitted and reflected waves. The $a$-ports (ovals) represent inputs and the $b$-ports (squares) are outputs. The relationship between the input and output ports are the S-parameters.

From Fig. 2.11, we can consider an example of a reflection measurement. The reflection voltage (amplitude) signal can be written down from the diagram as $b_1 = S_{11}a_1$, therefore we can write the reflection S-parameter $S_{11} = \frac{b_1}{a_1}$. Generalizing for a two-port network leads to

$$S_{ij} \equiv \frac{\text{Output}}{\text{Input}} = \frac{b_i}{a_j}. \tag{2.37}$$

In decibels (as is typically represented on the network analyzer) we can write $S_{ij}(\text{dB}) = 20\log|S_{ij}|$. Another thought regarding the decibel scale: the half-power bandwidth is often considered as a characteristic of the device under test (DUT). For instance, if we want to measure the half-power this implies,

$$\left|\frac{V_{\text{out}}}{V_{\text{in}}}\right| = \frac{1}{\sqrt{2}},$$
$$\text{dB} = 20\log_{10}\left(\frac{1}{\sqrt{2}}\right) = -3\text{dB}.$$

Equation 2.37 can be written in matrix form with the knowledge that injecting a signal into port one means no signal is injected into port two ($a_2 = 0$) and vice versa:

$$\begin{bmatrix} b_1 \\ b_2 \end{bmatrix} = \begin{bmatrix} S_{11} & S_{12} \\ S_{21} & S_{22} \end{bmatrix} \times \begin{bmatrix} a_1 \\ a_2 \end{bmatrix}. \tag{2.38}$$

Now, using this information we turn to the similar formulation for the reflection of a microwave cavity using input-output theory. Referring to Fig. 2.13, the reflection coefficient is defined by $S_{11} \equiv \frac{a_r}{a_{\text{in}}}$. If we let $a_r = a_{\text{out}}$, then we have (ignoring phase shifts):

$$S_{11} \equiv \frac{a_r}{a_{\text{in}}} = 1 - \frac{\sqrt{\frac{\kappa_e}{2}}a}{a_{\text{in}}}, \tag{2.39}$$
$$= 1 - \frac{\frac{\kappa_e}{2}}{-j\Delta + \kappa/2}, \tag{2.40}$$
$$= \frac{j\Delta + \kappa_0/2}{-j\Delta + \kappa/2}. \tag{2.41}$$

The normalized detected reflection signal is written as a power ($P_{\text{ref}}/P_{\text{inc}} = |S_{11}|^2$),

$$R \equiv |S_{11}|^2 = \frac{4\Delta^2 + \kappa_0^2}{4\Delta^2 + \kappa^2}.$$

When probing on resonance (maximum amplitude), the expression reduces to a very

simple equation,

$$R = \left(\frac{\kappa_0}{\kappa}\right)^2.$$

Let us now turn our attention to the transmission of the cavity. It would be misleading to use the same approach above with input-output theory by identifying $a_t = a_{\text{out}}$ and then continuing because one would arrive at the same expression as the reflection signal, which must be false. Likewise, the transmission signal will be greatest when probing on resonance. As an aside, a standing wave cavity that is equally coupled to both waveguides has no preferential loss direction and decays equally into both waveguides, which leads us to write for the transmission signal:

$$a_t = \sqrt{\kappa_{\text{ex}}}a$$

since $a_{\text{in}} = 0$ for the opposing waveguide. Same as before, the input decay is half of the total external decay rate $\kappa_{\text{ex}} = \kappa_e/2$. The amplitude of transmission can be written as:

$$S_{21} \equiv \frac{a_t}{a_{\text{in}}} = \frac{\frac{\kappa_e}{2}}{-j\Delta + \kappa/2}. \tag{2.42}$$

The detected power signal on the transmission port follows straightforwardly

$$T \equiv |S_{21}|^2 = \frac{\kappa_e^2}{4\Delta^2 + \kappa^2}. \tag{2.43}$$

When probing on resonance we see that

$$T = \left(\frac{\kappa_e}{\kappa}\right)^2.$$

The power dissipated in the resonator can also be expressed in terms of energy conservation. We must have $1 = D + T + R$, which implies the dissipated power in the resonator is

$$D = 1 - (T + R), \tag{2.44}$$

$$D = \frac{2\kappa_e\kappa_0}{4\Delta^2 + \kappa^2}. \tag{2.45}$$

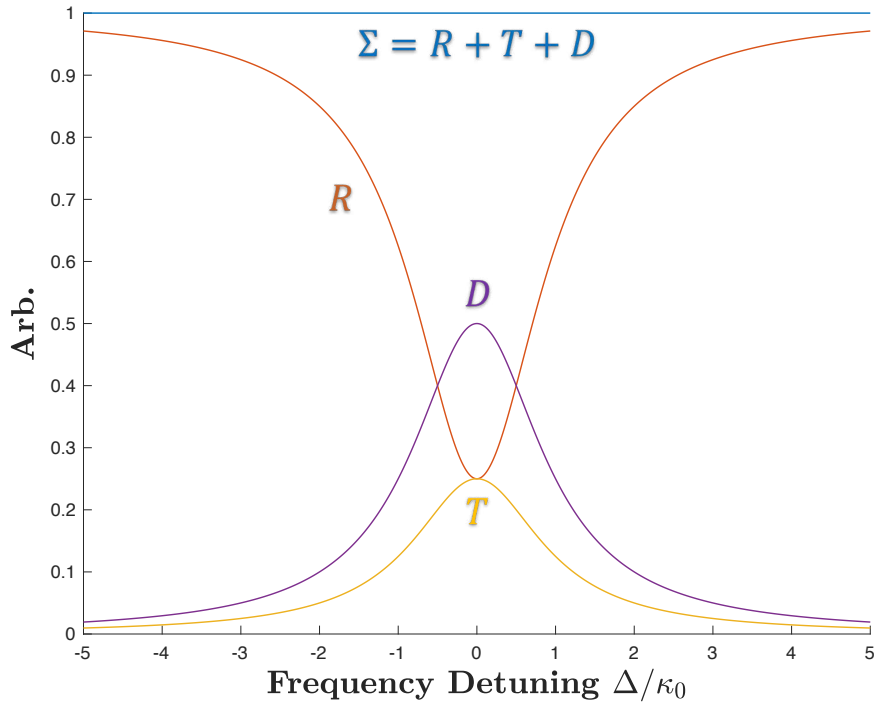


Figure 2.12: This representation shows the relationships between reflected power (Eq. 2.4), transmitted power (Eq. 2.43), and dissipated power in the resonator (Eq. 2.45).

These relationships are graphically displayed in Fig. 2.12. For completeness the transmitted power through the resonator is expressed as $P_{\text{out}} = |S_{21}|^2 P_{\text{inc}}$, where $P_{\text{inc}}$ is the incident power acting on the resonator. We shall become more familiar with this concept later, but it is good to mention the occupation number of the microwave cavity in photons. The occupation number is written as $\bar{n} = \langle \hat{a}^\dagger \hat{a} \rangle = |a|^2$ for fields with large mean value amplitudes to be considered classical. This is related to the semi-classical approach used in quantum optics. The power is related by $P = \hbar\omega|a|^2 = \hbar\omega\bar{n}$. Therefore, using Eq. 3.3c we can write the occupation number of the double-sided cavity as:

$$\bar{n} = \frac{2k_{\text{in}}}{4\Delta^2 + \kappa^2} \frac{P_{\text{inc}}}{\hbar\omega_d}, \tag{2.46}$$

where $\omega_d$ is the drive frequency and $|a_{\text{in}}|^2$ has been replaced according to $P_{\text{inc}} = \hbar\omega_d|a_{\text{in}}|^2$. Remember that the expression for $\kappa_{\text{ex}}$ in relation to $\kappa_{\text{e,in}}$ will change depending upon the coupling configuration.

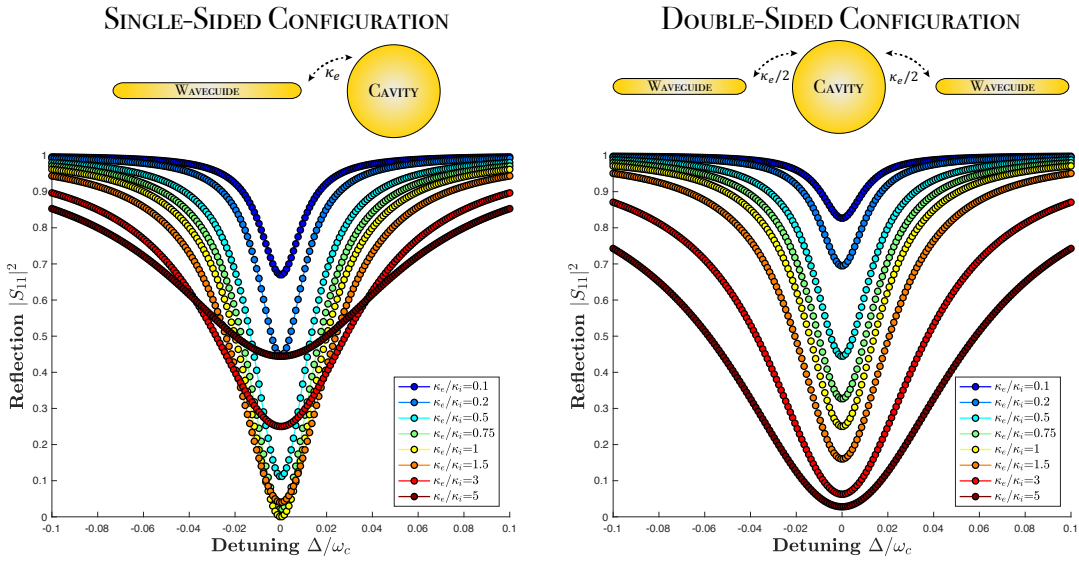


Figure 2.13: Here is the single-sided vs double-sided cavity reflection response for a cavity with $Q_0 = 50$. The over-coupled ports bring down the loaded quality factor to $Q_L = 8$. Notice that for a single-sided cavity the strength of the reflected dip is reduced for increased coupling beyond critical coupling ($\kappa_e = \kappa_i$). The dots are not data here, but only shown for clarity.

## 2.5 Ring-Down Measurement

To measure a real cavity we must connect it to a measurement device, which is done using SMA microwave cables. The energy is coupled into and out of the cavity using antenna loop couplers where a flux of magnetic field generates a current, or probe antennas that couple to the electric field. In the case of high-$Q$ cavities where the quality factor greatly exceeds $10^4$, our network analyzer (HP 8720C) proved to be insufficient to accurately measure the response of the cavity. The smallest bin size on the network analyzer was 100 kHz per point. For a microwave cavity with $\omega_0/2\pi$ =10 GHz and $Q = 1\times10^5$, this yields an intrinsic bandwidth of $\kappa/2\pi$ =100 kHz. Therefore, we typically measured the response of the high-$Q$ cavity through a pulse-ringdown technique.

To make the microwave couplers sufficiently under-coupled for high-$Q$ measurements, the resonance could not be measured at room temperature. Room-temperature couplers were made specifically for this purpose and the cryogenic resonance was later found by searching around the room-temperature resonance. For the cylindrical and stub cavity designs, thermal contraction and a superconducting state typically shift the cavity no more than 50 MHz from the room temperature resonance.

To determine the actual $Q$ of the cavity using a ringdown technique, a reflection

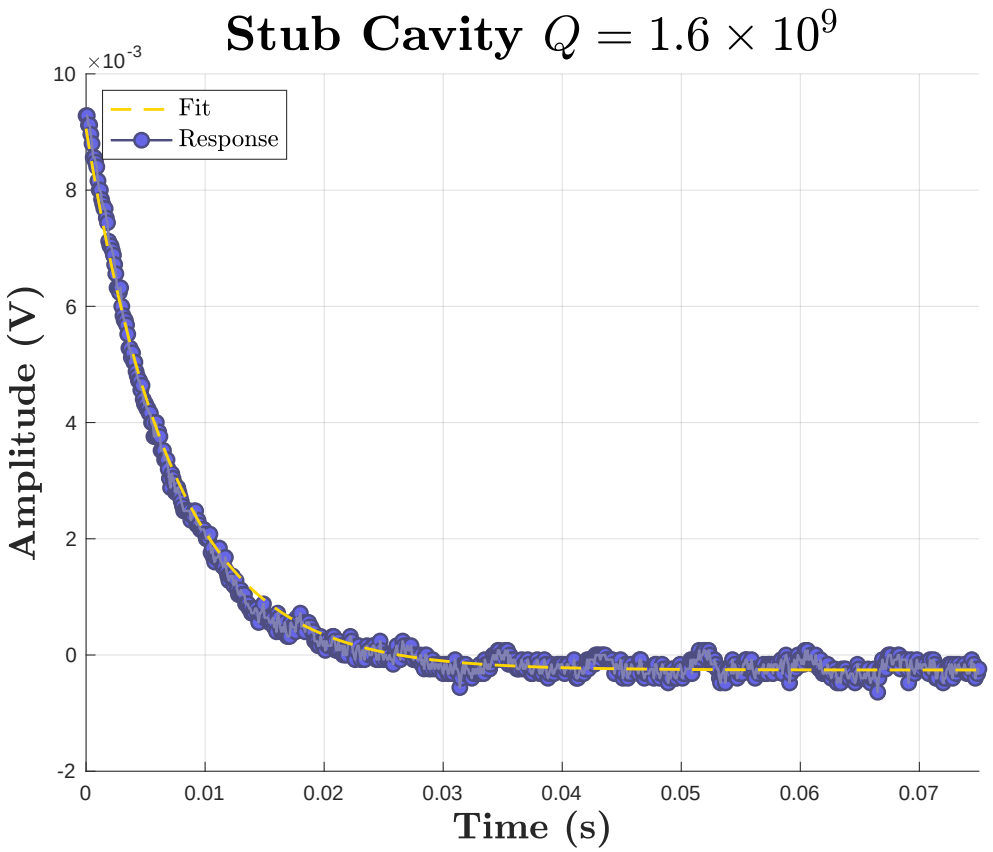


Figure 2.14: This is the best quality factor our group has achieved to date. The measured quality factor here was $Q_0 = 1.6 \times 10^9$, corresponding to an intrinsic time decay constant of $\tau_0$ =25 ms. Shown is the loaded time decay constant with a single coupled port and $\beta = 2.2$.

pulse is sent from the signal generator (Agilent N1853A) and a double-peak feature is observed on the triggered oscilloscope [34]. A ratio of the two peaks can be used to give a measure of the coupling coefficient $\beta$:

$$\beta = \frac{1}{2\sqrt{\frac{P_f}{P_e}} - 1}, \tag{2.47}$$

where $P_f$ is the first peak amplitude and $P_e$ is the second peak amplitude. Provided the amplitude of the Schottky-diode is low enough, the voltage is a measure of power and the decaying amplitude is fit according to

$$V = Ae^{-\frac{t}{\tau_L}} + c.$$

The reader may notice the lack of the factor of "2" next to $\tau_L$ and this is a reminder that we are measuring power on the oscilloscope, not amplitude due to the Schottky diode. The intrinsic (unloaded) $Q_0$ of the cavity can be found via Eq. 2.27.

A new cavity *with a membrane* was designed around minimizing the seam losses to increase the cavity quality factor $Q$. Previous designs with both aluminum and niobium cavities resulted in a saturated $Q$ with a membrane of about $Q \approx$ 1-2 million. The newly designed cavity featured a vacuum gap that pushed the point of electrical contact further from the cavity axis. The idea was to reduce the field amplitude of the $TE_{011}$ mode even lower so that there was negligible current crossing the discontinuous region between the membrane and the cavity. A second difference was that the cavity was machined from a single piece of Nb rather than creating two separate end-caps. These implementations led to a cavity with $Q \approx 17$ million about an order of magnitude improvement before any chemical etching or heat treatment.

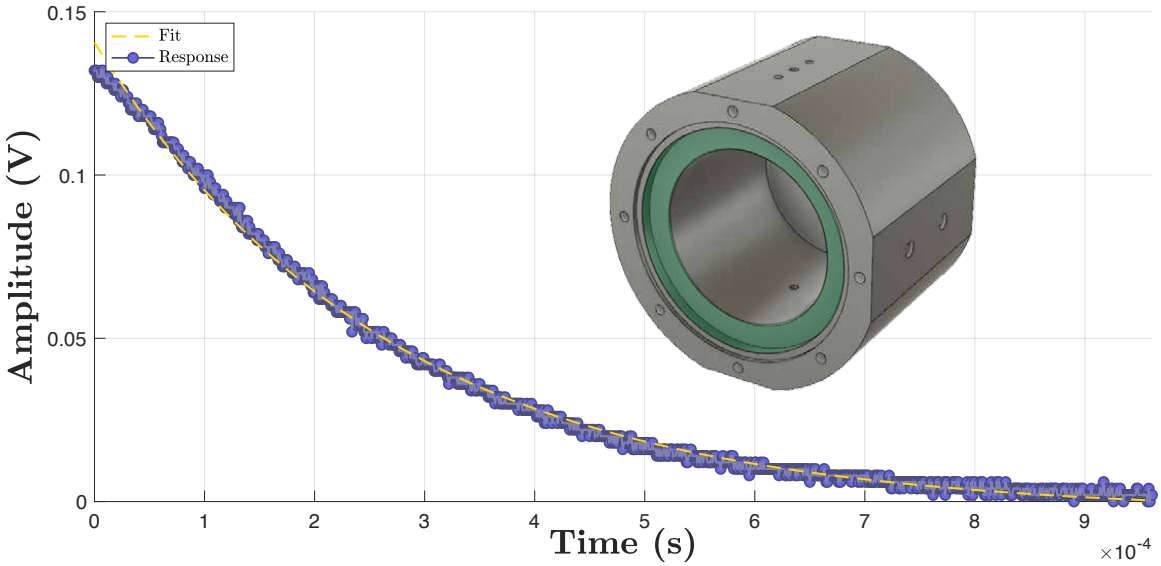


Figure 2.15: The pulsed-ringdown response for the cylindrical cavity with an increased radius at the point of electrical contact. The quality factor rose to $Q = 17$ million (above) after these changes in addition to having only one boundary seam. The highlighted green ring is the vacuum gap and the membrane would rest on the thin ledge above that.

Let us summarize a couple characteristics of the three main cavity types used (see Fig. 2.16 for example transmission responses). The re-entrant microwave cavity has a lower, fundamental resonance frequency because the resonance is confined to a sub-wavelength gap size, however this comes at the sacrifice of $Q$ since the geometry factor is smaller (smaller mode volume). The coaxial $\lambda/4$ cavity has a higher quality

factor, but there is only one resonance (for our geometries) between 0 and 20 GHz. One difficulty with this design is an experimental effort in trying to couple a second, mechanical resonator deep inside the metallic structure. The cylindrical cavity has multiple high-$Q$ resonances and the incorporation of a mechanical element is fairly straightforward. At superconducting temperatures, however, the $Q$ is much more difficult to increase to that of the coaxial $\lambda/4$ cavity because of the seam to seal the cavity.

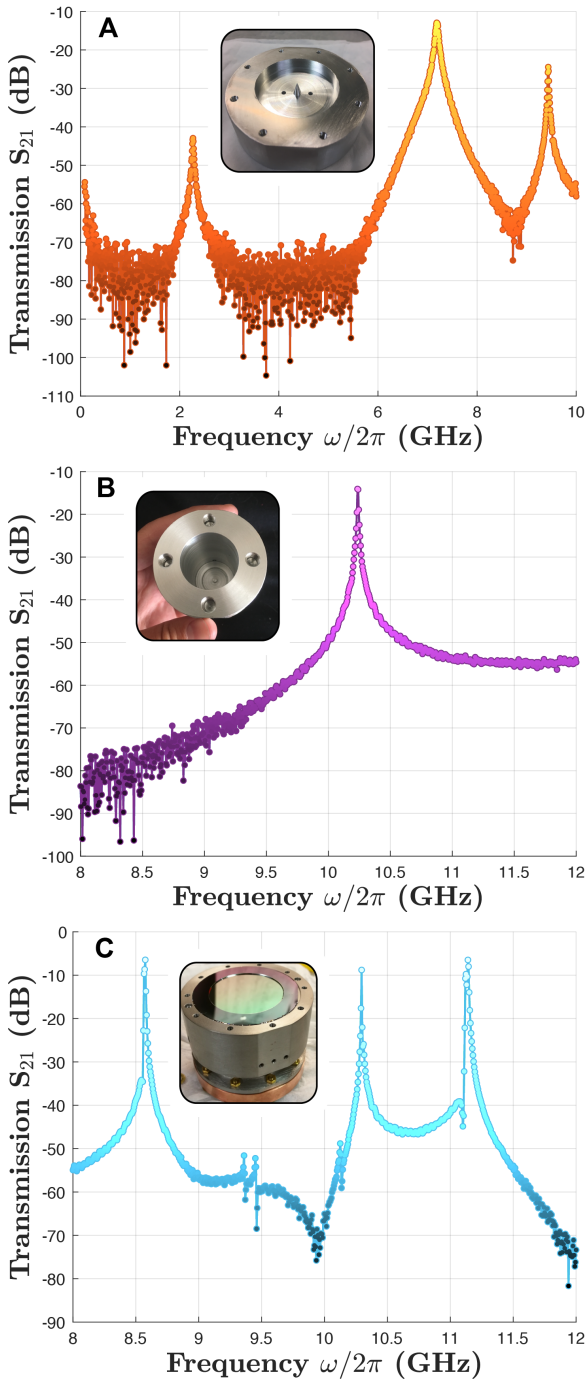


Figure 2.16: A comparison of different transmission responses for the main cavity geometries used in this work. (**A**) The re-entrant cavity, (**B**) the coaxial $\lambda/4$ stub cavity, and (**C**) the cylindrical cavity.

# Chapter 3

# Cavity Optomechanics

*"The greater danger for most of us is not that our aim is too high and we miss it, but that it is too low and we reach it."* – *Michelangelo*

The introduction of microwave cavities, their characteristics, and the method of measurement has been discussed up until this point. We consider the effect of a moveable boundary condition, more specifically one that can oscillate. The mechanical motion of the boundary couples to the electromagnetic field within a cavity, giving rise to the subject of this chapter: cavity optomechanics [30, 35, 42].

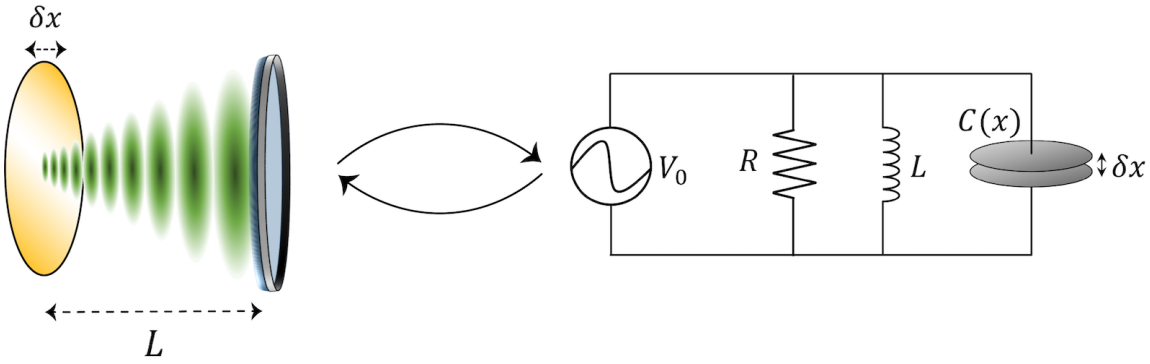


Figure 3.1: Both optical and electrical models are shown displaying the similarities between optical and electrical cavities. Both systems are ubiquitously used in optomechanics. In either case, the resonance frequency is shifted by the movement of a mechanical oscillator, whether it be a moveable mirror or variable capacitor.

The following derivation is identical for both microwave and optical frequencies. To start, let's consider the images in Fig. 3.1: a moveable membrane exists within a general cavity (say optical) and interacts with the incident radiation. Due to the extremely isolated and controlled environment, the radiation is capable of *manipulating* the membrane (a mechanical oscillator). As the membrane is displaced, a phase-shift is imprinted onto the optical *and* at the same time the intensity changes as a result of the optical delay. The resonance frequency is determined by the length $L$ of the cavity, which is now a variable quantity as a result of the mechanical oscillator. So, the resonance frequency can be expanded in a Taylor series:

$$\omega(x) = \omega_0 + \hat{x}\frac{d\omega}{dL} + \cdots .$$

The quantity $d\omega/dL$ is commonly referred to as the frequency-pull parameter $G \equiv -\frac{d\omega}{dL}$ ($\approx \omega/L$ for a Fabry-Pérot cavity) and dictates the amount of frequency shift per unit length change of the cavity. As a side note, a negative sign appears because an increase in the cavity length ($x > 0$) results in a decrease of the frequency ($G > 0$) [30]. The position coordinate $\hat{x}$ is written in terms of the phonon creation and annihilation operators $\hat{x} = x_{\text{zpf}}(\hat{b}^\dagger + \hat{b})$, where $x_{\text{zpf}} \equiv \sqrt{\frac{\hbar}{2m_{\text{eff}}\Omega_m}}$ is the zero-point fluctuations of the mechanical oscillator. If one defines one more quantity $g_0 \equiv Gx_{\text{zpf}}$ as the single photon vacuum optomechanical coupling rate, the expansion now reads:

$$\omega(x) = \omega_0 - G\hat{x} + \cdots .$$

Up until this point, the concept of the mechanical resonator has been slightly vague other than it acts as an oscillator. Figure 3.2 shows a picture of the real membrane (purchased from Norcada) sitting atop a microwave copper re-entrant cavity. Nearly all of the membranes had dimensions: 38.1 mm diameter window, 50.8 mm diameter frame, 300 nm Au or Nb, 500 nm SiN, and 500 $\mu$m thick frame. There was also a thin chromium adhesion layer to allow the metallic coating to stick to the silicon nitride layer.

## 3.1 Heisenberg-Langevin Approach

The Hamiltonian of the optomechanical system incorporates terms from the following: the cavity (system) with photons, the mechanical oscillator (bath), the coupling between the system and bath (interaction), and the driving microwave or optical field

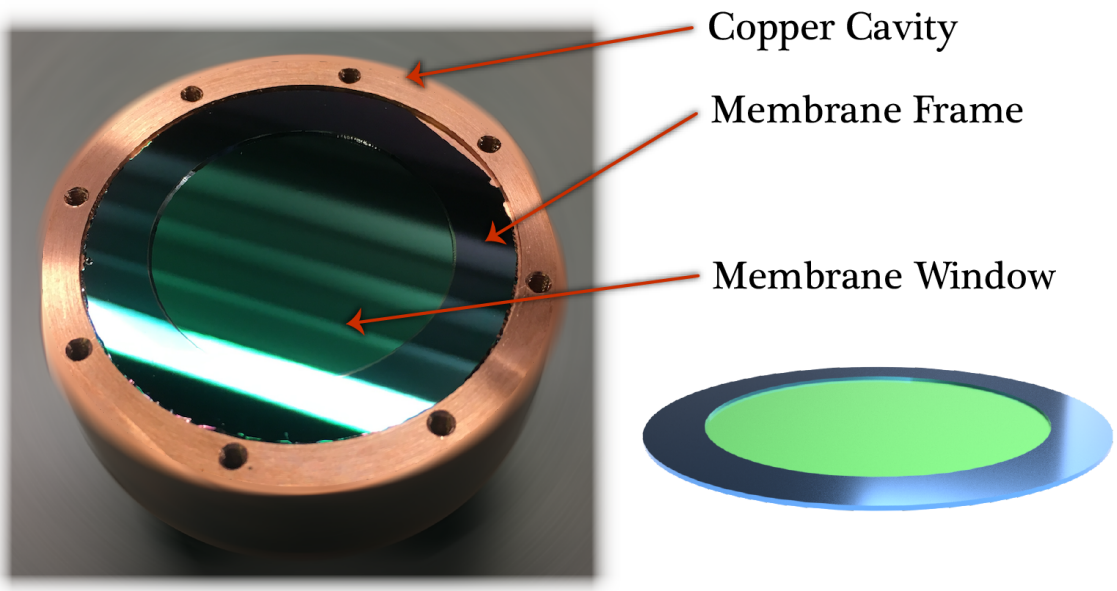


Figure 3.2: This is the mechanical oscillator most typically used in the experiments with a silicon frame and silicon nitride membrane. The coating to the membrane (gold or niobium) was deposited on the underside facing inwards to the cavity (not shown).

(see Fig. 3.3). Thus, the Hamiltonian is written down as follows:

$$\hat{H} = H_{\text{mech}} + \hat{H}_{\text{opt}} + \hat{H}_{\text{int}} + \hat{H}_{\text{drive}}, \tag{3.1a}$$

$$\hat{H}_{\text{mech}} = \frac{\hat{p}^2}{2m_{\text{eff}}} + \frac{1}{2} m_{\text{eff}} \Omega_m^2 \hat{x}^2, \tag{3.1b}$$

$$\hat{H}_{\text{opt}} = \hbar\omega_c \left( \hat{a}^\dagger \hat{a} + \frac{1}{2} \right), \tag{3.1c}$$

$$\hat{H}_{\text{int}} = -\hbar G \hat{x} \hat{a}^\dagger \hat{a}, \tag{3.1d}$$

$$\hat{H}_{\text{drive}} = i\hbar\sqrt{\kappa_e} \Big( a_{\text{in}}(t) \hat{a}^\dagger - a_{\text{in}}^*(t) \hat{a} \Big). \tag{3.1e}$$

The mechanical Hamiltonian can be re-expressed in terms of the phonon creation and annihilation operators as

$$\hat{H}_{\text{mech}} = \hbar\Omega_m \left( \hat{b}^\dagger \hat{b} + \frac{1}{2} \right).$$

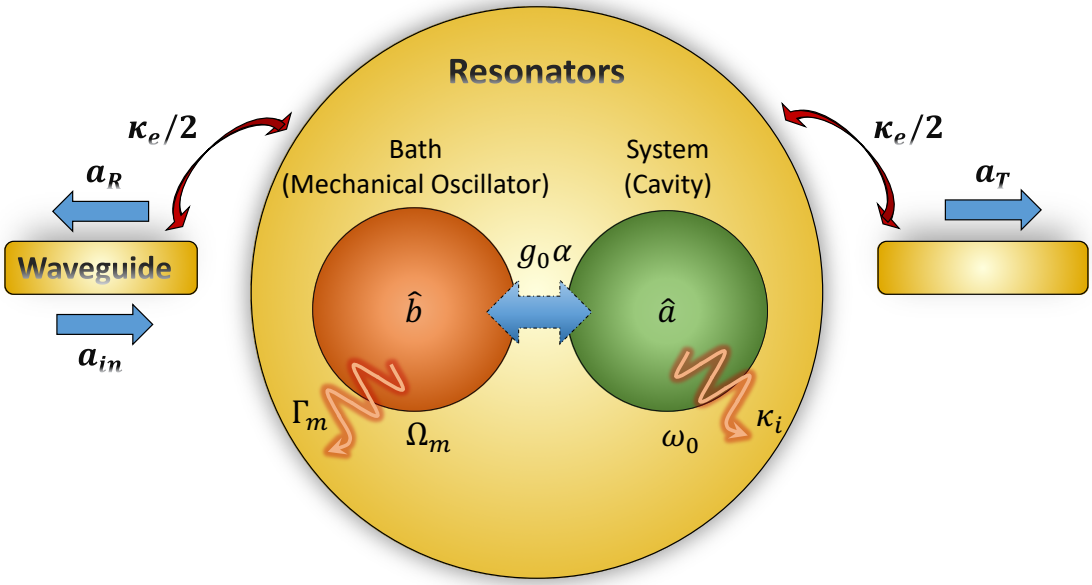


Figure 3.3: This optomechanical cavity configuration is known as a double-sided, standing-wave cavity and is primarily used in the majority of the work. Often times the second port for transmission is not incorporated.

At this point the Hamiltonian can be written (in the rotating frame and ignoring the vacuum energy of $\hbar\omega/2$) as

$$\hat{H} = -\hbar\Delta\hat{a}^\dagger\hat{a} + \hbar\Omega_m\hat{b}^\dagger\hat{b} - \hbar g_0\hat{a}^\dagger\hat{a}(\hat{b}^\dagger + \hat{b}) + H_{\text{drive}} + \cdots, \tag{3.2}$$

where the detuning term $\Delta \equiv \omega_l - \omega_c$ has been introduced. Positive $\Delta$ implies the laser has a higher frequency than the cavity resonance and vice-versa. Notice that the radiation pressure force can be written down as $\hat{F}_{\text{rp}} = -\frac{dH_{\text{int}}}{d\hat{x}} = \hbar G\hat{a}^\dagger\hat{a} = \hbar G\bar{n}$. Ignoring the effect of dissipation and loss, the equation of motion for the amplitude of the intracavity field can be written in the Heisenberg picture as[1]:

$$\begin{aligned}\dot{\hat{a}} = -\frac{i}{\hbar}[\hat{a}, \hat{H}] &= -\frac{i}{\hbar}\left\{[\hat{a}, \hat{H}_{\text{opt}}] + [\hat{a}, \hat{H}_{\text{int}}]\right\}, \\ &= -\frac{i}{\hbar}(-\hbar\Delta\hat{a} - \hbar g_0(\hat{b}^\dagger + \hat{b})\hat{a}), \\ &= i(\Delta + G\hat{x})\hat{a}.\end{aligned}$$

[1]Remember the commutation relations $[\hat{a}, \hat{a}^\dagger] = 1$ and $[\hat{a}, \hat{a}] = 0$ as well as $[\hat{a}, \hat{b}] = [\hat{a}, \hat{b}^\dagger] = 0$.

If one now looks at all the equations of motion and incorporates dissipation (nearly always done *ad hoc*) using the Heisenberg-Langevin equations (recall $[x, p] = i\hbar$ for deriving),

$$\frac{d}{dt}\hat{x}(t) = \frac{\hat{p}(t)}{m_{\text{eff}}}, \tag{3.3a}$$

$$\frac{d^2}{dt^2}\hat{x}(t) = -\Omega_m^2\hat{x}(t) - \Gamma_m\frac{d}{dt}\hat{x}(t) + \frac{\hbar G}{m_{\text{eff}}}\hat{a}^\dagger\hat{a} + \sqrt{\Gamma_m}\hat{\xi}_{th}(t), \tag{3.3b}$$

$$\frac{d}{dt}\hat{a}(t) = i(\Delta + G\hat{x})\hat{a}(t) - \frac{\kappa}{2}\hat{a}(t) + \sqrt{\kappa_e}\hat{a}_{\text{in}}(t) + \sqrt{\kappa_0}\hat{a}_{\text{vac}}(t). \tag{3.3c}$$

The last two quantities on the end line correspond to the intrinsic noise of the cavity vacuum as well as the external laser noise. The second line was introduced from the classical driven, damped, harmonic oscillator with the force arising from radiation pressure and fluctuating thermal noise (Brownian motion of the mechanical resonator) in vacuum. The Brownian displacement amplitude can be found by considering the equipartition theorem where each mode has an average of $\frac{1}{2}k_BT$ of energy. Therefore, the rms displacement can be found via $m_{\text{eff}}\Omega_m^2\left\langle\delta\hat{x}_{\text{rms}}^2\right\rangle = k_BT$. To solve the equations of motion, the following guessed solutions are used:

$$\hat{a}(t) = \bar{a} + \delta\hat{a}(t), \tag{3.4a}$$

$$\hat{x}(t) = \bar{x} + \delta\hat{x}(t), \tag{3.4b}$$

$$\hat{a}_{\text{in}}(t) = \bar{a}_{\text{in}} + \delta\hat{a}_{\text{in}}(t). \tag{3.4c}$$

In a sense these solutions are testing for first order perturbations to the average signal. First, we consider the static case and solve for those solutions. The approach here is frequently denoted a mean-field approximation. This means that derivatives vanish in time (i.e. $\dot{\bar{x}} = 0$). Therefore, the average static displacement of the oscillator is:

$$0 = -m_{\text{eff}}\Omega_m^2\bar{x} + \hbar G\bar{a}^2,$$

$$\bar{x} = \frac{\hbar G\bar{n}}{m_{\text{eff}}\Omega_m^2}.$$

This equation shows the mean position of the oscillator is proportionally displaced by some amount of radiation pressure. For the intracavity field equation of motion we have:

$$0 = i(\Delta + G\bar{x})\bar{a} - \frac{\kappa}{2}\bar{a} + \sqrt{\kappa_e}\bar{a}_{\text{in}},$$

$$\bar{a} = \frac{\sqrt{\kappa_e}\bar{a}_{\text{in}}}{-i(\Delta + G\bar{x}) + \kappa/2}.$$

Since only the dynamics of the system are considered, the static displacement can be lumped into the detuning

$$\bar{\Delta} \equiv \Delta + G\bar{x}. \tag{3.5}$$

Now, we return to the previously assumed solutions to analyze the system about equilibrium positions. Therefore inserting the full solution now (and $\bar{a}^* = \bar{a}$ since it is a real quantity),

$$\begin{aligned}
\frac{d^2}{dt^2}\delta\hat{x}(t) &= -\Omega_m^2(\bar{x} + \delta\hat{x}(t)) + \frac{\hbar G}{m_{\text{eff}}}(\bar{a} + \delta\hat{a}^\dagger(t))(\bar{a} + \delta\hat{a}(t)) - \Gamma_m\frac{d}{dt}\delta\hat{x}(t) + \sqrt{\Gamma_m}\hat{\xi}(t), \\
\frac{d^2}{dt^2}\delta\hat{x}(t) &= -\Omega_m^2\delta\hat{x}(t) + \frac{\hbar G}{m_{\text{eff}}}\left(\bar{a}\delta\hat{a}(t) + \bar{a}\delta\hat{a}^\dagger(t) + \delta\hat{a}^\dagger(t)\delta\hat{a}(t)\right) - \Gamma_m\frac{d}{dt}\delta\hat{x}(t) + \sqrt{\Gamma_m}\hat{\xi}(t), \\
\frac{d^2}{dt^2}\delta\hat{x}(t) &+ \Gamma_m\frac{d}{dt}\delta\hat{x}(t) + \Omega_m^2\delta\hat{x}(t) = \frac{\hbar G}{m_{\text{eff}}}\bar{a}\left(\delta\hat{a}(t) + \delta\hat{a}^\dagger(t)\right) + \sqrt{\Gamma_m}\hat{\xi}(t).
\end{aligned}$$

The last equation represents the classical damped harmonic oscillator on the LHS with the external driving terms (radiation pressure force and thermal motion) on the RHS. The term $\propto \delta\hat{a}^\dagger(t)\delta\hat{a}(t)$ was removed due to its extremely small significance. The other dynamic equations of motion are:

$$\begin{aligned}
\delta\dot{\hat{a}}(t) &= i\Delta\delta\hat{a}(t) - \frac{\kappa}{2}\delta\hat{a}(t) + iG(\bar{x} + \delta\hat{x}(t))(\bar{a} + \delta\hat{a}(t)) + \sqrt{\kappa_e}\delta\hat{a}_{\text{in}}(t) + \sqrt{\kappa_0}\delta\hat{a}_{\text{vac}}(t), \\
&= i\Delta\delta\hat{a}(t) - \frac{\kappa}{2}\delta\hat{a}(t) + iG\bar{x}\delta\hat{a}(t) + iG\bar{a}\delta\hat{x}(t) + \sqrt{\kappa_e}\delta\hat{a}_{\text{in}}(t) + \sqrt{\kappa_0}\delta\hat{a}_{\text{vac}}(t), \\
\frac{d}{dt}\delta\hat{a}(t) &= \left(i\bar{\Delta} - \frac{\kappa}{2}\right)\delta\hat{a}(t) + iG\bar{a}\delta\hat{x}(t) + \sqrt{\kappa_e}\delta\hat{a}_{\text{in}}(t) + \sqrt{\kappa_0}\delta\hat{a}_{\text{vac}}(t), \\
\Rightarrow \frac{d}{dt}\delta\hat{a}^\dagger &= \left(-i\bar{\Delta} - \frac{\kappa}{2}\right)\delta\hat{a}^\dagger(t) - iG\bar{a}\delta\hat{x}^\dagger(t) + \sqrt{\kappa_e}\delta\hat{a}_{\text{in}}^\dagger(t) + \sqrt{\kappa_0}\delta\hat{a}_{\text{vac}}^\dagger(t).
\end{aligned}$$

One may notice in the middle of the expansion that the term $\propto \bar{x}\bar{a}$ was omitted; this is due to the lack of time dependence and therefore does not contribute to the dynamic solution. The easiest way to get rid of these derivatives is to look at the solution in the frequency domain ($\delta\hat{x}^\dagger(\Omega) = \delta\hat{x}(\Omega)$ for the Hermitian operator), so we Fourier transform the equations[2]. A quick sidetone for the reader: at this point the analysis is carried forward with the aim of theoretically investigating dynamical sideband cooling. The approach for optomechanically induced transparency (OMIT)

[2]The Fourier transform is taken here to be $f(\Omega) \equiv \int_{-\infty}^{\infty} f(t)e^{+i\Omega t}dt$. In addition, it is useful to note the property $\delta\hat{a}^\dagger(\Omega) = (\delta\hat{a}(-\Omega))^\dagger$. Using these properties, one can show that $F\left[\frac{d}{dt}f(t)\right] = -i\Omega f(\Omega)$ using the transform in reverse. If $f(t) = \frac{1}{2\pi}\int_{-\infty}^{\infty} F(\Omega)e^{-i\Omega t}d\Omega$, then $f'(t) = \frac{d}{dt}\left(\frac{1}{2\pi}\int_{-\infty}^{\infty} F(\Omega)e^{-i\Omega t}d\Omega\right) = \frac{-1}{2\pi}\int_{-\infty}^{\infty} i\Omega F(\Omega)e^{-i\Omega t}d\Omega$. Hence, the result follows by definition of the transform.

branches mathematically from here, but is shown for clarity in Appendix D.

## 3.2 Dynamic Optomechanics

We continue with the derivation for the dynamic equations of optomechanics, after performing a Fourier transform, that give rise to optomechanical damping, frequency shifts, and backaction:

$$-\Omega^2\delta\hat{x}(\Omega)+\Omega_m^2\delta\hat{x}(\Omega)-i\Omega\Gamma_m\delta\hat{x}(\Omega)=\frac{\hbar G}{m_{\text{eff}}}\bar{a}\left(\delta\hat{a}(\Omega)+\delta\hat{a}^\dagger(\Omega)\right)+\sqrt{\Gamma_m}\delta\hat{\xi}(\Omega), \quad (3.6)$$

$$-i\Omega\delta\hat{a}(\Omega)=\left(i\bar{\Delta}-\frac{\kappa}{2}\right)\delta\hat{a}(\Omega)+iG\bar{a}\delta\hat{x}(\Omega)+\sqrt{\kappa_e}\delta\hat{a}_{\text{in}}(\Omega)+\sqrt{\kappa_0}\delta\hat{a}_{\text{vac}}(\Omega), \quad (3.7)$$

$$-i\Omega\delta\hat{a}^\dagger(\Omega)=\left(-i\bar{\Delta}-\frac{\kappa}{2}\right)\delta\hat{a}^\dagger(\Omega)-iG\bar{a}\delta\hat{x}^\dagger(\Omega)+\sqrt{\kappa_e}\delta\hat{a}_{\text{in}}^\dagger(\Omega)+\sqrt{\kappa_0}\delta\hat{a}_{\text{vac}}^\dagger(\Omega). \quad (3.8)$$

In turning our attention to the mechanical oscillator equation, one can see the dynamical radiation pressure force fluctuations on the RHS has the form

$$\delta\hat{F}_{rp}(\Omega)=\hbar G\bar{a}\left(\delta\hat{a}(\Omega)+\delta\hat{a}^\dagger(\Omega)\right), \quad (3.9)$$

and also identify the thermal driving force (Brownian motion) as:

$$\delta\hat{F}_{th}(\Omega)=m_{\text{eff}}\sqrt{\Gamma_m}\hat{\xi}_{th}(\Omega). \quad (3.10)$$

In order to solve for the radiation forcing terms, we can see from the previous equations in frequency space that

$$\begin{aligned}\left(-i\Omega-i\bar{\Delta}+\frac{\kappa}{2}\right)\delta\hat{a}(\Omega)&=iG\bar{a}\delta\hat{x}(\Omega)+\sqrt{\kappa_e}\delta\hat{a}_{\text{in}}(\Omega)+\sqrt{\kappa_0}\delta\hat{a}_{\text{vac}}(\Omega),\\ \delta\hat{a}(\Omega)&=\frac{iG\bar{a}\delta\hat{x}(\Omega)+\sqrt{\kappa_e}\delta\hat{a}_{\text{in}}(\Omega)+\sqrt{\kappa_0}\delta\hat{a}_{\text{vac}}(\Omega)}{-i\left(\bar{\Delta}+\Omega\right)+\frac{\kappa}{2}},\\ \rightarrow\delta\hat{a}^\dagger(\Omega)&=\frac{-iG\bar{a}\delta\hat{x}(\Omega)+\sqrt{\kappa_e}\delta\hat{a}_{\text{in}}^\dagger(\Omega)+\sqrt{\kappa_0}\delta\hat{a}_{\text{vac}}^\dagger(\Omega)}{i\left(\bar{\Delta}-\Omega\right)+\frac{\kappa}{2}}.\end{aligned}$$

Inserting the previous expressions into Eq. 3.9 yields

$$\begin{aligned}\delta\hat{F}_{rp}(\Omega) &= \hbar G\bar{a}\left[\frac{iG\bar{a}\delta\hat{x}(\Omega)+\sqrt{\kappa_e}\delta\hat{a}_{\rm in}(\Omega)+\sqrt{\kappa_0}\delta\hat{a}_{\rm vac}(\Omega)}{-i\left(\bar{\Delta}+\Omega\right)+\frac{\kappa}{2}}\right.\\ &\qquad\left.+\frac{-iG\bar{a}\delta\hat{x}(\Omega)+\sqrt{\kappa_e}\delta\hat{a}^\dagger_{\rm in}(\Omega)+\sqrt{\kappa_0}\delta\hat{a}^\dagger_{\rm vac}(\Omega)}{i\left(\bar{\Delta}-\Omega\right)+\frac{\kappa}{2}}\right],\\ &= i\hbar G^2\bar{a}^2\frac{\delta\hat{x}(\Omega)}{-i\left(\bar{\Delta}+\Omega\right)+\frac{\kappa}{2}}-i\hbar G^2\bar{a}^2\frac{\delta\hat{x}(\Omega)}{i\left(\bar{\Delta}-\Omega\right)+\frac{\kappa}{2}}\\ &\quad+\hbar G\bar{a}\frac{\sqrt{\kappa_e}\delta\hat{a}_{\rm in}(\Omega)+\sqrt{\kappa_0}\delta\hat{a}_{\rm vac}(\Omega)}{-i\left(\bar{\Delta}+\Omega\right)+\frac{\kappa}{2}}+\hbar G\bar{a}\frac{\sqrt{\kappa_e}\delta\hat{a}^\dagger_{\rm in}(\Omega)+\sqrt{\kappa_0}\delta\hat{a}^\dagger_{\rm vac}(\Omega)}{i\left(\bar{\Delta}-\Omega\right)+\frac{\kappa}{2}}.\end{aligned}$$

We reform the denominator of the two terms containing the mechanical coordinate $\delta\hat{x}$ by multiplying by the complex conjugate and then sorting real and imaginary terms. The result gives the desired radiation pressure force fluctuations:

$$\begin{aligned}\delta\hat{F}_{rp}(\Omega) &= \underbrace{-\hbar G^2\bar{a}^2\left(\frac{\bar{\Delta}+\Omega}{(\bar{\Delta}+\Omega)^2+(\kappa/2)^2}+\frac{\bar{\Delta}-\Omega}{(\bar{\Delta}-\Omega)^2+(\kappa/2)^2}\right)\delta\hat{x}(\Omega)}_{\text{Optical Spring (In Phase)}}\\ &\quad+\underbrace{i\hbar G^2\bar{a}^2\left(\frac{\kappa/2}{(\bar{\Delta}+\Omega)^2+(\kappa/2)^2}-\frac{\kappa/2}{(\bar{\Delta}-\Omega)^2+(\kappa/2)^2}\right)\delta\hat{x}(\Omega)}_{\text{Optical Damping (Out of Phase)}}\\ &\quad+\underbrace{\hbar G\bar{a}\frac{\sqrt{\kappa_e}\delta\hat{a}_{\rm in}(\Omega)+\sqrt{\kappa_0}\delta\hat{a}_{\rm vac}(\Omega)}{-i\left(\bar{\Delta}+\Omega\right)+\kappa/2}+\hbar G\bar{a}\frac{\sqrt{\kappa_e}\delta\hat{a}^\dagger_{\rm in}(\Omega)+\sqrt{\kappa_0}\delta\hat{a}^\dagger_{\rm vac}(\Omega)}{i\left(\bar{\Delta}-\Omega\right)+\kappa/2}}_{\text{Quantum Backaction Terms}}.\end{aligned}$$

A nice picture of the components of radiation pressure force fluctuations is presented above. The dynamical backaction terms are composed of the optical spring and optical damping terms whereas the quantum backaction introduces limitations because it contains the only sources of noise and fluctuations. However, the dynamical backaction terms are rather presented in a mechanical susceptibility, which may make more intuitive sense that the oscillator is responding to the incident electromagnetic field. Intuitively, the mechanical susceptibility describes the response of an mechanically-compliant object to a force. Therefore, the mechanical susceptibility for the oscillator

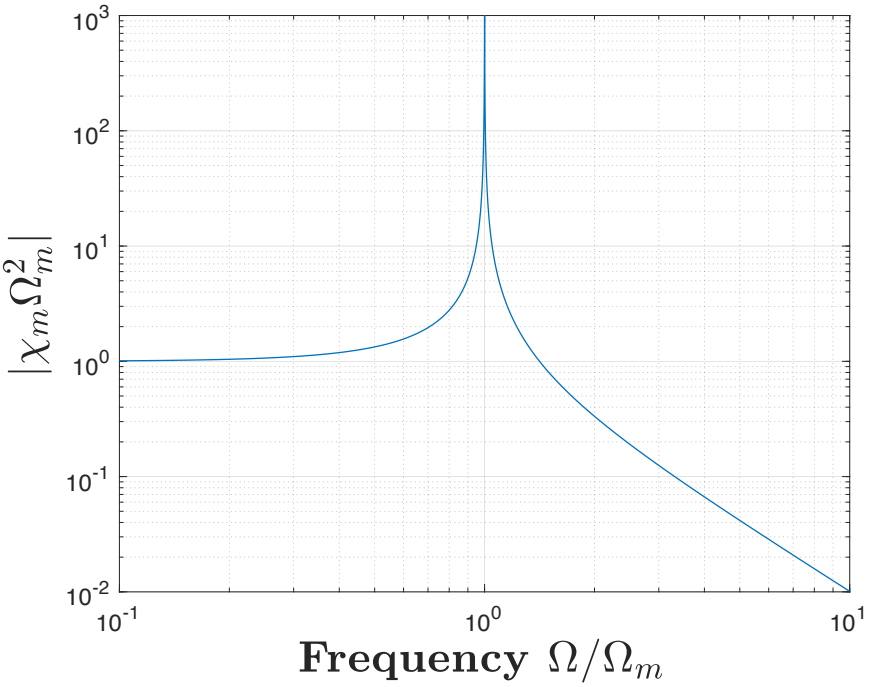


Figure 3.4: The mechanical susceptibility is plotted here with $m_{\text{eff}} = 1$ kg, $\Omega_m/2\pi = 1$ kHz, and $Q_m = 1 \times 10^3$. For frequencies much larger than $\Omega_m$ the response drops off as $|\chi_m(\Omega) \gg \Omega_m| \propto 1/\Omega^2$ (20 dB per decade). For frequencies below $\Omega_m$, the response has a dependence $|\chi_m(\Omega \ll \Omega_m)| = \frac{1}{m_{\text{eff}}\Omega_m^2}$.

is

$$\begin{aligned}\chi_m &= \frac{\delta\hat{x}(\Omega)}{\delta\hat{F}_{rp}(\Omega) + \delta\hat{F}_{th}(\Omega)}, \\ &= m_{\text{eff}}^{-1}(\Omega_m^2 - \Omega^2 - i\Gamma_m\Omega)^{-1}.\end{aligned}$$

In order to group the dynamical terms into the mechanical susceptibility, the radiation pressure force fluctuations only contain the quantum noise (back-action) terms, which are not included in the effective mechanical susceptibility:

$$\delta\hat{F}_{rp}(\Omega) \rightarrow \delta\hat{F}_{rp}(\Omega) = \delta\hat{F}_{rp} + \delta\hat{F}_{rp}^{qba}(\Omega). \tag{3.11}$$

This means the *effective* mechanical susceptibility has the form:

$$\chi_{\text{eff}} = m_{\text{eff}}^{-1}\left[\left(\Omega_m^2 + 2\Omega\delta\Omega_m\right) - \Omega^2 - i\Omega\left(\Gamma_m + \Gamma_{\text{opt}}(\Omega)\right)\right]^{-1}. \tag{3.12}$$

with the following definitions (taken from the previous radiation pressure force fluctuation with a small modification of dividing by $m_{\text{eff}}$ for consistency). Small frequency changes around $\delta(\Omega^2) \approx 2\Omega\delta\Omega_m$ are considered and (for this derivation) the dynamic optomechanical characteristics of mechanical frequency shift and optomechanical damping are:

$$\delta\Omega_m = \frac{1}{2\Omega m_{\text{eff}}}\text{Re}\left[\delta\hat{F}_{rp}(\Omega)\right],$$
$$\Gamma_{\text{opt}} = \frac{1}{\Omega m_{\text{eff}}}\text{Im}\left[\delta\hat{F}_{rp}(\Omega)\right].$$

Using this definition as well as re-arranging the coefficients the final expressions are:

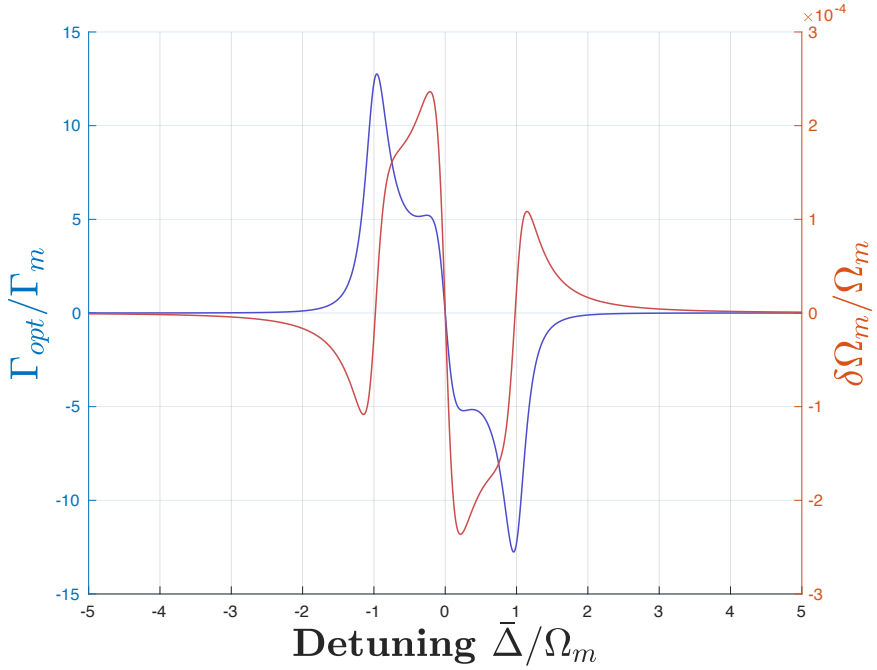


Figure 3.5: The dynamic equations for the optomechanical damping rate (left axis) and mechanical frequency shift (right axis) as a function of detuning. The equations are plotted with parameters: $Q = 1 \times 10^6$, $\Omega_m/2\pi = 25$ kHz, $\kappa_0/2\pi = \kappa_{\text{ex}}/2\pi = 10$ kHz, $m_{\text{eff}} = 1$ mg, $P_{\text{in}} = 0$ dBm, and $G/2\pi = 1$ MHz/$\mu$m. Notice that the optimal detuning may not always be $\bar{\Delta} = \pm\Omega_m$.

$$\delta\Omega_m = \frac{g_0^2 \bar{n}_{\rm cav}\Omega_m}{\Omega}\left(\frac{\bar{\Delta}+\Omega}{(\bar{\Delta}+\Omega)^2+(\kappa/2)^2}+\frac{\bar{\Delta}-\Omega}{(\bar{\Delta}-\Omega)^2+(\kappa/2)^2}\right),$$
$$\Gamma_{\rm opt}(\Omega) = \frac{g_0^2 \bar{n}_{\rm cav}\Omega_m}{\Omega}\left(\frac{\kappa}{(\bar{\Delta}+\Omega)^2+(\kappa/2)^2}-\frac{\kappa}{(\bar{\Delta}-\Omega)^2+(\kappa/2)^2}\right).$$

See Ch. 3.4 below for a detailed and alternative derivation of the modified cavity frequency and damping rates. If we consider frequencies close to the mechanical frequency $\Omega \approx \Omega_m$,

$$\delta\Omega_m = g_0^2 \bar{n}_{\rm cav}\left(\frac{\bar{\Delta}+\Omega_m}{(\bar{\Delta}+\Omega_m)^2+(\kappa/2)^2}+\frac{\bar{\Delta}-\Omega_m}{(\bar{\Delta}-\Omega_m)^2+(\kappa/2)^2}\right), \tag{3.13}$$
$$\Gamma_{\rm opt}(\Omega) = g_0^2 \bar{n}_{\rm cav}\left(\frac{\kappa}{(\bar{\Delta}+\Omega_m)^2+(\kappa/2)^2}-\frac{\kappa}{(\bar{\Delta}-\Omega_m)^2+(\kappa/2)^2}\right) \tag{3.14}$$

and the total effective mechanical frequency and decay rate succinctly stated as:

$$\Omega_{\rm eff} = \Omega_m + \delta\Omega_m, \tag{3.15}$$
$$\Gamma_{\rm eff} = \Gamma_m + \Gamma_{\rm opt}. \tag{3.16}$$

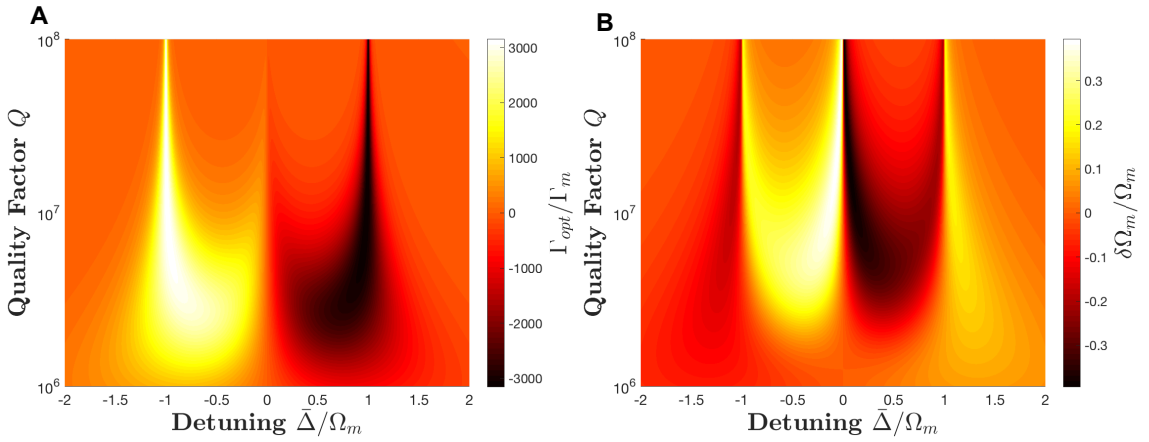


Figure 3.6: (**A**) The optomechanical damping rates as a function of detuning and cavity quality factor. The left-hand side has $\Gamma_{\rm opt} > 0$ (cooling) whereas the right-hand side has $\Gamma_{\rm opt} < 0$ (heating). (**B**) The mechanical frequency shifts due to the optomechanical interaction. This calculation was done for a fairly massive mechanical oscillator at $m_{\rm eff}$ =1 mg with a large amount of power at $P_{\rm in} = 0$ dBm and coupling of $G/2\pi = 1$ MHz/$\mu$m. Notice that a second set of detunings are possible for cooling/heating around $\bar{\Delta} = 0$ for $Q > 5$ million.

See Figs. 3.5, 3.6 for a visual representation how these parameters change depending upon the detuning of the laser (microwave) pump signal. The double-sided force power spectral density can be defined as

$$2\pi\delta(\Omega+\Omega')S_{ff}(\Omega)=\left\langle\delta\hat{f}(\Omega)\delta\hat{f}(\Omega')\right\rangle, \tag{3.17}$$

and the displacement power spectral density includes the mechanical susceptibility for converting the force into a detectable displacement:

$$S_{xx}(\Omega)=\left|\chi_{\text{eff}}\right|^2 S_{FF}(\Omega). \tag{3.18}$$

If we consider the thermal motion as the driving force, namely thermomechanical motion [43], the thermal force in the Heisenberg-Langevin equations is $\delta\hat{F}_{th}(\Omega)=m_{\text{eff}}\sqrt{\Gamma_m}\hat{\xi}(\Omega)$. The corresponding thermal force power spectral density (PSD) would be written as[3]:

$$\begin{aligned}2\pi\delta(\Omega+\Omega')S^{th}_{FF}(\Omega)&=\left\langle\delta\hat{F}_{th}(\Omega)\delta\hat{F}_{th}(\Omega')\right\rangle,\\ \bar{S}^{th}_{FF}(\Omega)&=m_{\text{eff}}\Gamma_m\hbar\Omega\left[\coth\left(\frac{\hbar\Omega}{2k_BT_m}\right)+1\right].\end{aligned}$$

One can evaluate this expression in terms of the thermal force fluctuation PSD to arrive at the classical result of

$$S^{th}_{FF}=2m_{\text{eff}}\Gamma_m\underbrace{\hbar\Omega(\bar{n}+1/2)}_{k_BT}, \tag{3.19}$$

or alternatively, for the single-sided thermal force power spectral density $S^{th}_F=4m_{\text{eff}}\Gamma_m k_BT$. This means the area underneath the Lorentzian curve generated by the signal can be integrated to find the rms displacement of the oscillator:

$$\left\langle\delta\hat{x}^2_{\text{rms}}\right\rangle=\int_{-\infty}^{\infty}S_{xx}(\Omega)\frac{d\Omega}{2\pi}=\int_{-\infty}^{\infty}\left|\chi_{\text{eff}}\right|^2 S_{FF}(\Omega)\frac{d\Omega}{2\pi}. \tag{3.20}$$

[3]The commutation relation for the noise operators is $\left\langle\delta\hat{\xi}_{th}(\Omega)\delta\hat{\xi}^{\dagger}(\Omega')\right\rangle=2\pi\delta(\Omega+\Omega')\hbar m_{\text{eff}}\Omega\left(\coth\left(\frac{\hbar\Omega}{2k_BT}\right)+1\right)$. In addition, we use the notation of the *symmetrised* power spectral density $\bar{S}_{OO}(\Omega)\equiv\frac{S_{OO}(\Omega)+S_{OO}(-\Omega)}{2}$. Also, keep in mind the relationship of the single-sided PSD as well $S_O(\Omega)\equiv 2\bar{S}_{OO}(\Omega)$.

## 3.3 The Mechanical Susceptibility

The mechanical susceptibility can be described as the ability of an arbitrary mechanical resonator to convert a force into a displacement (i.e. transduction of force and displacement). A short section has been devoted to this topic because integrating the mechanical susceptibility requires the use of residue calculus and contour integrals. To start off, the motivation for this topic arrives in obtaining the mean-squared deviation for the mechanical oscillator,

$$\left\langle \delta\hat{x}^2_{\rm rms} \right\rangle = \int_{-\infty}^{\infty} \left|\chi_{\rm eff}(\Omega)\right|^2 \left( S^{\rm th}_{FF}(\Omega) + S^{\rm qba}_{FF}(\Omega) \right) \frac{d\Omega}{2\pi}. \tag{3.21}$$

We recall $\Gamma_{\rm eff} \equiv \Gamma_m + \Gamma_{\rm opt}$ and $\Omega_{\rm eff} = \Omega_m + \delta\Omega_m \approx \Omega_m$. Therefore the mechanical susceptibility can be re-written as

$$\begin{aligned}
\chi_{\rm eff}(\Omega) &= \frac{1}{m_{\rm eff}} \left[ \Omega_m^2 - \Omega^2 - i\Omega\Gamma_{\rm eff} \right]^{-1}, \\
\Rightarrow \left|\chi_{\rm eff}(\Omega)\right|^2 &= \frac{1}{m^2_{\rm eff}} \frac{1}{(\Omega_m^2 - \Omega^2)^2 + \Omega^2\Gamma^2_{\rm eff}}, \\
&= \frac{1}{m^2_{\rm eff}} \frac{1}{(\Omega_m + \Omega)(\Omega_m - \Omega) + i\Omega\Gamma_{\rm eff}} \cdot \frac{1}{(\Omega_m + \Omega)(\Omega_m - \Omega) - i\Omega\Gamma_{\rm eff}}.
\end{aligned}$$

In looking at the denominator, the pole solutions are

$$\Omega = \underbrace{\frac{-i\Gamma_{\rm eff} \pm i\sqrt{\Gamma^2_{\rm eff} - 4\Omega_m^2}}{-2}}_{\text{Solution \#1},\Omega_1}, \qquad \underbrace{\frac{i\Gamma_{\rm eff} \pm i\sqrt{\Gamma^2_{\rm eff} - 4\Omega_m^2}}{-2}}_{\text{Solution \#2},\Omega_2}. \tag{3.22}$$

Notice that only the first solution will play a role due to its positive nature (multiply through the negative in the denominator) in the contour integral because the contour is taken to be in the upper-half plane. Remember that the integral is taken along the real axis (from $-\infty$ to $+\infty$) and has to reconnect because it is a contour, therefore integrating along either the upper or lower imaginary plane. The solutions enclosed within the contour are the residues and the location is the pole. To evaluate the residue at the pole,

$$R(z - z_0) = \lim_{z \to z_0} (z - z_0) f(z). \tag{3.23}$$

So, for the solutions obtained above the residue is:

$$R(\Omega - \Omega_1) = \lim_{\Omega \to \Omega_1} \left( \Omega - \frac{i\Gamma_{\rm eff} \pm i\sqrt{\Gamma^2_{\rm eff} - 4\Omega_m^2}}{2} \right) \left|\chi_{\rm eff}(\Omega)\right|^2.$$

To evaluate this expression it is useful to perform long division. The long division expression cannot be formatted in an elegant manner, so the quotient is written. The solution divides evenly with the factor

$$-\Omega + \frac{i}{2}\Gamma_{\text{eff}} \pm \frac{i}{2}\sqrt{\Gamma_{\text{eff}}^2 - 4\Omega_m^2}.$$

Therefore, in defining $\eta \equiv \sqrt{\Gamma_{\text{eff}}^2 - 4\Omega_m^2}$ for shorthand notation, the residue at the first pole solution can be expressed as (also plugging in the solution #1 for the limit):

$$\begin{aligned}
R(\Omega - \Omega_1) &= \frac{1}{m_{\text{eff}}^2} \cdot \frac{1}{-\Omega + \frac{i\Gamma_{\text{eff}}}{2} \pm \frac{i}{2}\eta} \cdot \frac{1}{\Omega_m^2 - \Omega^2 - i\Omega\Gamma_{\text{eff}}}, \\
&= \frac{1}{m_{\text{eff}}^2} \cdot \frac{1}{\frac{-i\Gamma_{\text{eff}}}{2} \pm \frac{i}{2}\eta + \frac{i\Gamma_{\text{eff}}}{2} \pm \frac{i}{2}\eta} \cdot \frac{1}{\Omega_m^2 - \left(\frac{i\Gamma_{\text{eff}}}{2} \mp \frac{i}{2}\eta\right)^2 - i\Gamma_{\text{eff}}\left(\frac{i\Gamma_{\text{eff}}}{2} \mp \frac{i}{2}\eta\right)}, \\
&= \frac{1}{m_{\text{eff}}^2} \cdot \frac{1}{\pm i\eta} \cdot \frac{1}{\Gamma_{\text{eff}}^2 \mp \Gamma_{\text{eff}}\eta}, \\
&= \frac{1}{m_{\text{eff}}^2} \cdot \left[\frac{1}{i\eta\left(\Gamma_{\text{eff}}^2 - \eta\Gamma_{\text{eff}}\right)} + \frac{1}{-i\eta\left(\Gamma_{\text{eff}}^2 + \eta\Gamma_{\text{eff}}\right)}\right], \\
&= -\frac{i}{m_{\text{eff}}^2} \cdot \left\{\frac{2}{\Gamma_{\text{eff}}^3 - \eta^2\Gamma_{\text{eff}}}\right\}, \\
&= -\frac{i}{m_{\text{eff}}^2} \cdot \left\{\frac{2}{\Gamma_{\text{eff}}^3 - \Gamma_{\text{eff}}^3 + 4\Omega_m^2\Gamma_{\text{eff}}}\right\}, \\
&= -\frac{i}{2m_{\text{eff}}^2\Omega_m^2\Gamma_{\text{eff}}}.
\end{aligned}$$

Now the final step to evaluate the integral is very simple:

$$\int_{-\infty}^{\infty} |\chi_{\text{eff}}|^2 \, d\Omega = 2\pi i \cdot \text{Residue}, \tag{3.24}$$

$$\Rightarrow \int_{-\infty}^{\infty} |\chi_{\text{eff}}|^2 \, \frac{d\Omega}{2\pi} = \frac{1}{2m_{\text{eff}}^2\Omega_m^2\Gamma_{\text{eff}}}. \tag{3.25}$$

Therefore, the effective temperature of the mechanical oscillator mode is [4]:

$$T = \frac{m_{\rm eff}\Omega_m^2 \left\langle \delta\hat{x}_{\rm rms}^2 \right\rangle}{k_B}, \tag{3.26}$$

$$= \frac{m_{\rm eff}\Omega_m^2 S_{FF}^{th}}{k_B} \cdot \frac{1}{2m_{\rm eff}^2\Omega_m^2\Gamma_{\rm eff}}. \tag{3.27}$$

Using this information leads to the expression for the double-sided thermal force fluctuation power spectral density we arrived at earlier,

$$S_{FF}^{th} = 2m_{\rm eff}\Gamma_{\rm eff}k_BT. \tag{3.28}$$

The single-sided PSD for thermal motion would have an additional factor of 2 out front[5]. Keep in mind that this is a very classical result. If one wanted to convert to displacement power spectral density using the thermal force fluctuation PSD, then because of the fact that $x(\omega) = \chi(\omega)F(\omega)$ and thermal motion is the only driving mechanism,

$$S_{xx}(\Omega) = |\chi_m(\Omega)|^2 S_{FF}^{th}(\Omega). \tag{3.29}$$

## 3.4 The Modified Susceptibilities and Rates

We consider an alternative method for deriving the dynamical equations using a common approach with the optomechanical "self-energy" and it is best to begin with the equations of motion. Recall that we assumed the ansatz $\hat{x}(t) = \bar{x} + \delta\hat{x}(t)$ and $\hat{a}(t) = \bar{a} + \delta\hat{a}(t)$ and plugged in (thereby including the radiation force term) for the linearized equations:

$$\delta\ddot{\hat{x}}(t) + \Gamma_m\delta\dot{\hat{x}}(t) + \Omega_m^2\delta\hat{x}(t) = \frac{\hbar G}{m_{\rm eff}}\left(\bar{a}\delta\hat{a}(t) + \bar{a}\delta\hat{a}^\dagger(t) + \delta\hat{a}^\dagger(t)\delta\hat{a}(t)\right) + \frac{F_{\rm therm}}{m_{\rm eff}}, \tag{3.30}$$

$$\delta\dot{\hat{a}}(t) = i\bar{\Delta}\delta\hat{a}(t) + iG\bar{a}\delta\hat{x}(t) - \frac{\kappa}{2}\delta\hat{a}(t) - \hat{F}_{\rm noise}(t). \tag{3.31}$$

[4] Recall that $\langle E\rangle = m_{\rm eff}\Omega_m^2\left\langle \delta\hat{x}_{\rm rms}^2\right\rangle = k_BT$.

[5] Note that $2\int_0^\infty = \int_{-\infty}^\infty$

The term corresponding to $\delta\hat{a}^\dagger\delta\hat{a}$ can be ignored due to smallness. Recalling the definition of the Fourier transform with a few identities,

$$F[f(t)] \equiv f(\Omega) = \int_{-\infty}^{\infty} f(t)e^{i\Omega t}dt, \tag{3.32a}$$

$$F\left[\frac{d}{dt}\hat{a}(t)\right] = -i\Omega\hat{a}(\Omega), \tag{3.32b}$$

$$\delta\hat{a}^\dagger(\Omega) = \left(\delta\hat{a}(-\Omega)\right)^\dagger. \tag{3.32c}$$

Therefore, we take the Fourier transform[6] and arrive at:

$$-\Omega^2\delta\hat{x}[\Omega] - i\Omega\Gamma_m\delta\hat{x}[\Omega] + \Omega_m^2\delta\hat{x}[\Omega] = \frac{\hbar G}{m_{\text{eff}}}\bar{a}\left(\delta\hat{a}^\dagger[-\Omega] + \delta\hat{a}[\Omega]\right) + \frac{F_{\text{therm}}[\Omega]}{m_{\text{eff}}},$$
$$-i\Omega\delta\hat{a}[\Omega] = i\bar{\Delta}\delta\hat{a}[\Omega] + iG\bar{a}\delta\hat{x}[\Omega] - \frac{\kappa}{2}\delta\hat{a}[\Omega] - \hat{F}_{\text{noise}}[\Omega].$$

Simplifying this expression for the field amplitude reduces to:

$$\delta\hat{a}[\Omega]\left(-i\Omega - i\bar{\Delta} + \frac{\kappa}{2}\right) = iG\bar{a}\delta\hat{x}[\Omega] - \hat{F}_{\text{therm}}[\Omega],$$
$$\delta\hat{a}[\Omega] = \chi_c[\Omega]\left(iG\bar{a}\delta\hat{x}[\Omega] - \hat{F}_{\text{noise}}[\Omega]\right),$$

where the cavity susceptibility is introduced and defined here as $\chi_c^{-1} \equiv \kappa/2 - i(\bar{\Delta}+\Omega)$. For simplicity we drop the noise term in the cavity; this can be justified as all the optomechanical interactions will soon be lumped into a single term and dominate the noise terms. Inserting this into the mechanical equation of motion above shows

$$-\Omega^2\delta\hat{x}[\Omega] - i\Omega\Gamma_m\delta\hat{x}[\Omega] + \Omega_m^2\delta\hat{x}[\Omega] = \frac{\hbar G}{m_{\text{eff}}}\bar{a}\Big(\chi_c^*[\Omega]\left(-iG\bar{a}\delta\hat{x}^*[-\Omega]\right) +$$
$$+ \chi_c[\Omega]\left(iG\bar{a}\delta\hat{x}[\Omega]\right)\Big) + \frac{F_{\text{therm}}[\Omega]}{m_{\text{eff}}}.$$

[6]For the derivation of the complex conjugate portion, $\hat{x}[\Omega] = \int \hat{x}[t]e^{i\Omega t}dt \to \hat{x}[t] = \int \hat{x}[\Omega]e^{-i\Omega t}d\Omega$, then taking the complex conjugate $\hat{x}^*[t] = \left[\int \hat{x}[\Omega]e^{-i\Omega t}d\Omega\right]^* = \int \hat{x}^*[\Omega]e^{+i\Omega t}d\Omega$, and letting $\Omega \to -\Omega'$, then $\hat{x}^*[t] = \int \hat{x}^*[-\Omega']e^{-i\Omega' t}d\Omega$. Therefore, $\hat{x}^*[t] = F^{-1}\left[\hat{x}^*(-\Omega)\right]$, which leads to the conclusion $\therefore F\left[\hat{x}^*[t]\right] = \hat{x}^*[-\Omega]$.

Using the definition of a Fourier transform, the real nature of the mechanical fluctuations leads to $\delta\hat{x}[\Omega] = (\delta\hat{x}[-\Omega])^*$:

$$\delta\hat{x}[\Omega]\left[\Omega_m^2 - \Omega^2 - i\Omega\Gamma_m + \frac{i\hbar G^2\bar{a}^2}{m_{\text{eff}}}\Big(\chi_c[\Omega] - \chi_c^*[-\Omega]\Big)\right] = \frac{F_{\text{therm}}}{m_{\text{eff}}},$$
$$\delta\hat{x}[\Omega] = \frac{F_{\text{therm}}}{m_{\text{eff}}\Big(\Omega_m^2 - \Omega^2 - i\Omega\Gamma_m\Big) + \Sigma[\Omega]} \equiv \chi_{xx}F_{\text{therm}},$$

where $\chi_{xx}$ is the modified susceptibility and we are using the definition given by [30] and

$$\Sigma(\Omega) \equiv -i\hbar G^2\bar{a}^2\Big(\chi_c[\Omega] - \chi_c^*[-\Omega]\Big) \tag{3.33}$$

is called the "optomechanical self-energy." This conveniently modifies a conventional susceptibility into one that includes all the optomechanical interactions into a single term. For this reason we can now look at the real and imaginary components of this $\Sigma[\Omega]$ term. Now, using the definition of the cavity susceptibility, let us expand the variable,

$$\Sigma(\Omega) = \hbar G^2\bar{a}^2\left[\frac{-i\kappa/2 + (\bar{\Delta} + \Omega)}{(\kappa/2)^2 + (\bar{\Delta} + \Omega)^2} - \frac{-i\kappa/2 - (\bar{\Delta} - \Omega)}{(\kappa/2)^2 + (\bar{\Delta} - \Omega)^2}\right].$$

The real part of the self-energy term (which is in phase with displacement coordinate from above) is proportional to the mechanical frequency shift (known as the "optical spring") and for $\Omega \approx \Omega_m$[7]:

$$\delta(\Omega^2) = \frac{1}{m_{\text{eff}}}\text{Re}\left[\Sigma(\Omega)\right], \tag{3.34}$$
$$\Rightarrow \delta\Omega_m \approx g_0^2\bar{n}_{\text{cav}}\left[\frac{(\bar{\Delta} + \Omega_m)}{(\kappa/2)^2 + (\bar{\Delta} + \Omega_m)^2} + \frac{(\bar{\Delta} - \Omega_m)}{(\kappa/2)^2 + (\bar{\Delta} - \Omega_m)^2}\right]. \tag{3.35}$$

Similarly, for the imaginary part of the optomechanical self-energy (also changing coefficients and $\Omega \approx \Omega_m$), which is out-of-phase with the displacement coordinate and therefore represents a velocity, or dampening:

$$\Gamma_{\text{opt}} = -\frac{1}{\Omega m_{\text{eff}}}\text{Im}\left[\Sigma(\Omega_m)\right], \tag{3.36}$$
$$\Rightarrow \Gamma_{\text{opt}} = g_0^2\bar{a}^2\left[\frac{\kappa}{(\kappa/2)^2 + (\bar{\Delta} + \Omega_m)^2} - \frac{\kappa}{(\kappa/2)^2 + (\bar{\Delta} - \Omega_m)^2}\right]. \tag{3.37}$$

[7]Remember that we approximate $\delta(\Omega_m^2) \approx 2\Omega\delta\Omega_m$

Therefore, $\Gamma_{\rm opt}$ is the "optomechanical damping rate" and both are identical to the expressions we derived earlier in Eqns. 3.13, 3.14 using the radiation pressure force fluctuations.

## 3.5 Optomechanical Cooling and Amplification

Therefore, in using the equipartition theorem $m_{\rm eff}\Omega_m^2 \langle \delta\hat{x}_{\rm rms}^2 \rangle = k_B T$ we can see that integrating the displacement spectral density leads to a mode temperature of the oscillator,

$$T = \frac{m_{\rm eff}\Omega_m^2 \langle \delta\hat{x}_{\rm rms}^2 \rangle}{k_B}. \tag{3.38}$$

Likewise, knowing the mechanical frequency, the mode temperature of the oscillator can be expressed as an occupation number (phonon quanta) of the oscillator using $\bar{n}_m = \frac{k_B T}{\hbar\Omega_m}$ or Bose-Einstein statistics for small occupation numbers $\bar{n}_m = \left[e^{\frac{\hbar\Omega_m}{k_B T}} - 1\right]^{-1}$. It can be shown from the above equation for the radiation pressure fluctuations (starting with Eq. 3.9) that the quantum backaction force power spectral density is

$$\bar{S}_{FF}^{\rm qba}(\Omega) = \hbar^2 G^2 \bar{n}_{\rm cav}\kappa \left( \frac{1}{(\bar{\Delta}+\Omega)^2 + \left(\frac{\kappa}{2}\right)^2} \right),$$
$$\bar{S}_{FF}^{\rm qba}(\Omega) \approx \bar{S}_{FF}^{\rm qba}(\Omega_m) = \hbar m_{\rm eff}\Omega(A_- + A_+),$$

where

$$A\pm = g_0^2 \bar{n}_{\rm cav}\kappa \left( \frac{1}{(\bar{\Delta} \mp \Omega_m)^2 + \left(\frac{\kappa}{2}\right)^2} \right). \tag{3.39}$$

The convention of $A_\pm$ also allows us to express the optomechanical damping as $\Gamma_{\rm opt} = A_- - A_+$, indicating that the best scattering is achieved for the largest imbalance in the amplitudes proportional to the anti-Stokes ($\propto A_-$) and Stokes ($\propto A_+$) scattering rates (see Fig. 3.7). This is why the aim of a sideband-resolved cavity is important, because the optomechanical damping is maximized. A sideband-resolved cavity implies that sidebands generated on the cavity spectrum by the mechanical element are able to be resolved outside of the cavity linewidth ($\Omega_m \gg \kappa$). Most often the cavities and mechanical oscillators we used were on the border of this criteria ($\Omega_m \approx \kappa$). Using the energy of a harmonic oscillator $E = \hbar\Omega(\bar{n} + 1/2)$ and integrating the full expression

of Eq. 3.20 leads to the phonon occupation of the mechanical resonator:

$$\bar{n} = \frac{\bar{n}_{\rm th}\Gamma_m + A_+}{\Gamma_{\rm eff}}, \tag{3.40}$$

$$= \frac{\bar{n}_{\rm th}\Gamma_m + \frac{x_{\rm zpf}^2}{\hbar^2} S_{FF}^{\rm qba}(-\Omega)}{\Gamma_{\rm eff}}, \tag{3.41}$$

$$= \frac{\bar{n}_{\rm th}\Gamma_m + \bar{n}_{\rm c}\Gamma_{\rm opt}}{\Gamma_{\rm eff}}. \tag{3.42}$$

In other words, the phonon occupation is a weighted balance between the intrinsic mechanical damping and the ability to cool the system using optomechanical damping (see Fig. 3.8). Notice that for any appreciable optomechanical cooling one must have $\Gamma_{\rm opt} \geq \Gamma_m$. The minimal achievable phonon occupation under optimal detuning for both sideband resolved and unresolved cavities is

$$\bar{n}_{\rm min}(\bar{\Delta}_{\rm optimal}) = \frac{\kappa^2}{16\Omega_m^2} \quad \rightarrow \quad \text{Sideband Resolved}, \tag{3.43}$$

$$\bar{n}_{\rm min}(\bar{\Delta}_{\rm optimal}) = \frac{\kappa}{4\Omega_m} \quad \rightarrow \quad \text{Sideband Unresolved}, \tag{3.44}$$

and additional details and alternative derivations (such as Fermi's golden rule and detailed balance equations) can be found in Appendix C. Since the optomechanical damping is positive for a red-detuned pump and negative for a blue-detuned pump, this implies cooling and heating of the mechanical resonator. In order to cool an optomechanical system one needs to red-detune a pump laser and heating occurs for a blue-detuned laser. It may be important to clarify that the sensitivity is not enhanced due to sideband cooling because the mechanical $Q_m$ drops ($\Gamma_{\rm eff} > \Gamma_m$) as the cooling is increased.

## 3.6 Standard Quantum Limit

We have done some calculations assuming an arbitrary power incident on the cavity, however, in all reality there comes a point at which this breaks down. The pump signal under sufficient power will begin to perturb the actual measurement of the oscillator, known as backaction. Under low powers, there is an insufficient signal to accurately measure the oscillator, known as imprecision. The balance of these two processes is known as the standard quantum limit [30, 44, 45].

The analysis for the standard quantum limit picks up with Eqns. 3.6-3.8 and is

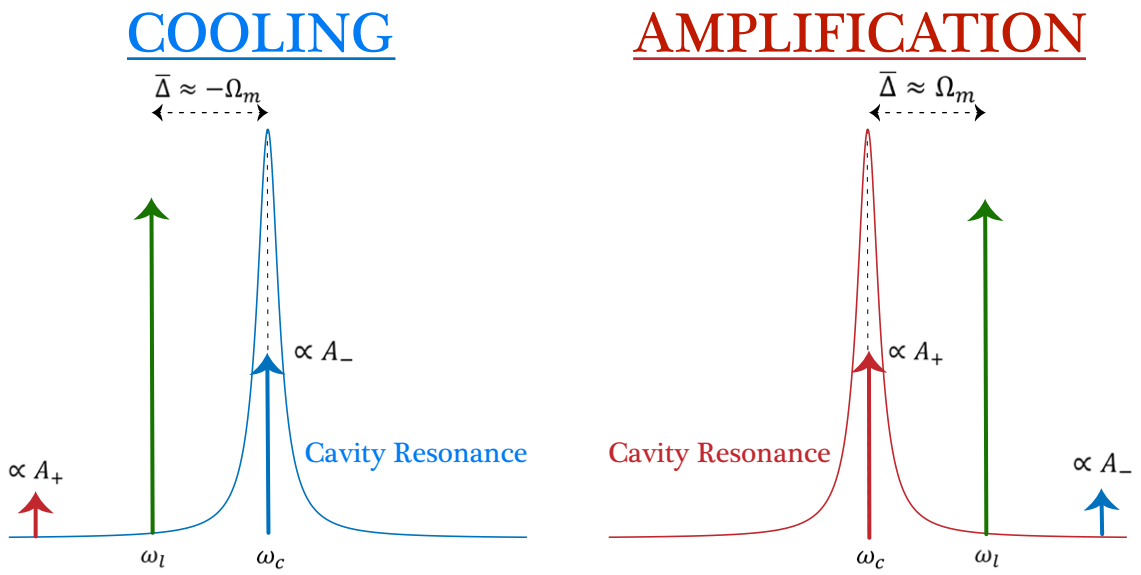


Figure 3.7: The experimental approach for detuning a pump laser (microwave) signal to achieve cooling or amplification (heating). This picture has been drawn for the resolved sideband regime where $\Omega_m \gg \kappa$ and the non-resonant scattered frequencies are far outside the cavity linewidth such that they are considered negligible.

written below for clarification: [8]

$$-\Omega^2\delta\hat{x}(\Omega) + \Omega_m^2\delta\hat{x}(\Omega) - i\Omega\Gamma_m\delta\hat{x}(\Omega) = \frac{\hbar G}{m_{\text{eff}}}\bar{a}\left(\delta\hat{a}(\Omega) + \delta\hat{a}^\dagger(\Omega)\right) + \sqrt{\Gamma_m}\delta\hat{\xi}(\Omega),$$

$$-i\Omega\delta\hat{a}(\Omega) = \left(i\bar{\Delta} - \frac{\kappa}{2}\right)\delta\hat{a}(\Omega) + iG\bar{a}\delta\hat{x}(\Omega) + \sqrt{\kappa_e}\delta\hat{a}_{\text{in}}(\Omega) + \sqrt{\kappa_0}\delta\hat{a}_{\text{vac}}(\Omega),$$

$$-i\Omega\delta\hat{a}^\dagger(\Omega) = \left(-i\bar{\Delta} - \frac{\kappa}{2}\right)\delta\hat{a}^\dagger(\Omega) - iG\bar{a}\delta\hat{x}^\dagger(\Omega) + \sqrt{\kappa_e}\delta\hat{a}_{\text{in}}^\dagger(\Omega) + \sqrt{\kappa_0}\delta\hat{a}_{\text{vac}}^\dagger(\Omega).$$

At this point we can introduce input-output theory $\delta\hat{a}_{\text{out}}(\Omega) = \delta\hat{a}_{\text{in}}(\Omega) - \sqrt{\eta_c\kappa}\delta\hat{a}(\Omega)$ as well as the only non-zero commutation relationship $\left\langle \delta\hat{a}_{\text{in}}(\Omega)\delta\hat{a}_{\text{in}}^\dagger(\Omega')\right\rangle = 2\pi\delta(\Omega + \Omega')$. We also consider resonant-probing of the system (i.e. $\bar{\Delta} = 0$) and introduce a different notation for coupling $\eta_c \equiv \frac{\kappa_e}{\kappa_0+\kappa_e}$ [9], which identifies the waveguide coupling

[8] The Fourier transform is taken here to be $f(\Omega) \equiv \int_{-\infty}^{\infty} f(t)e^{+i\Omega t}dt$. In addition, it is useful to note the property $\delta\hat{a}^\dagger(\Omega) = (\delta\hat{a}(-\Omega))^\dagger$. Using these properties, one can show that $F\left[\frac{d}{dt}f(t)\right] = -i\Omega f(\Omega)$ using the transform in reverse. If $f(t) = \frac{1}{2\pi}\int_{-\infty}^{\infty} F(\Omega)e^{-i\Omega t}d\Omega$, then $f'(t) = \frac{d}{dt}\left(\frac{1}{2\pi}\int_{-\infty}^{\infty} F(\Omega)e^{-i\Omega t}d\Omega\right) = \frac{-1}{2\pi}\int_{-\infty}^{\infty} i\Omega F(\Omega)e^{-i\Omega t}d\Omega$.

[9] $\eta_c$ is a ratio of waveguide loss to total loss, therefore the value cannot exceed 1, whereas $\beta$ is a ratio of waveguide coupling loss to internal cavity loss and can take arbitrarily large values.

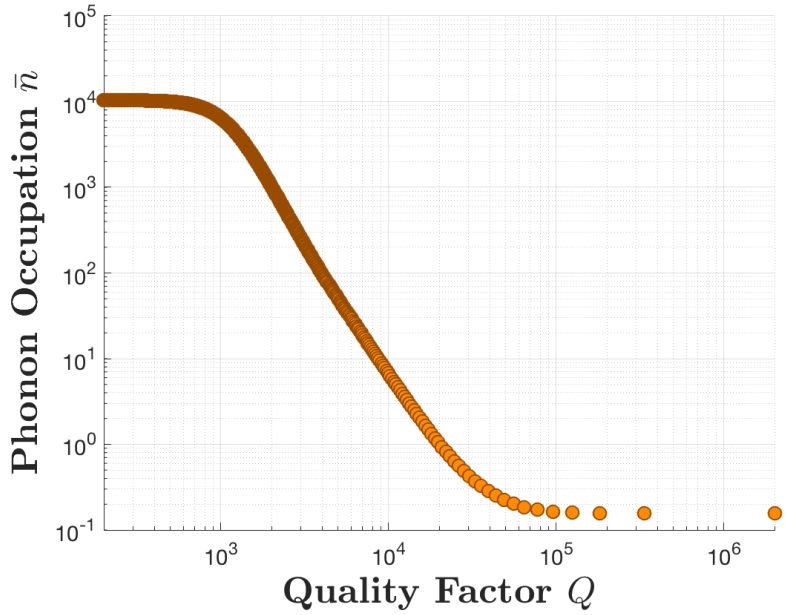


Figure 3.8: Theoretical ground state cooling is shown possible for a mechanical oscillator at $T = 50$ mK with $m_{\text{eff}} = 1$ ng, $\Omega_m/2\pi = 100$ kHz, $P_{\text{in}} = 0$ dBm, and $G/2\pi = 1$ MHz/$\mu$m as a function of the electromagnetic cavity $Q$. The mechanical phononic occupation saturates to the level of the electromagnetic photonic occupation under sufficient cooling parameters. The cooling power is quite large for this calculation, however the coupling can easily be increased to reduce the incident power.

and is frequently seen throughout optomechanics:

$$\hat{a}_{\text{out}}(\Omega) = \delta\hat{a}_{\text{in}}(\Omega) - \frac{\sqrt{\eta_c\kappa}}{-i\Omega + \kappa/2}\left(iG\bar{a}\delta\hat{x}(\Omega) + \sqrt{\kappa_{ex}}a_{\text{in}} + \sqrt{\kappa_0}\hat{a}_{\text{vac}}\right). \tag{3.45}$$

In the same way that a field can be represented as a sum of two quadratures $\alpha = X_1 + iX_2$, we can write the phase quadrature as a sum of the real output field:

$$\delta\hat{p}_{\text{out}}(\Omega) = -i(\hat{a}_{\text{out}}(\Omega) - \hat{a}^\dagger_{\text{out}}(\Omega)). \tag{3.46}$$

Then, by simple definition of the power spectral density:

$$\bar{S}^{\text{out}}_{pp}(\Omega) \equiv \frac{1}{2}\left(S^{\text{out}}_{pp}(\Omega) + S^{\text{out}}_{pp}(-\Omega)\right),$$
$$2\pi\delta(\Omega + \Omega')S^{\text{out}}_{pp}(\Omega) = \left\langle \delta\hat{p}_{\text{out}}(\Omega)\delta\hat{p}^\dagger_{\text{out}}(\Omega')\right\rangle.$$

Therefore, in solving for the phase power spectral density and using the commutators we arrive at:

$$\begin{aligned}\bar{S}_{pp}^{\text{out}}(\Omega) &= 1 + \frac{4\bar{a}^2 G^2 \eta_c \kappa}{\Omega^2 + (\kappa/2)^2}\bar{S}_{xx}(\Omega), \\ &= 1 + \frac{\bar{S}_{xx}(\Omega)}{\bar{S}_{xx}^{\text{im,qn}}(\Omega)},\end{aligned}$$

where we have identified the mechanical displacement spectrum $\bar{S}_{xx}$ and the quantum displacement imprecision power spectral density as

$$\bar{S}_{xx}^{\text{im,qn}}(\Omega) = \frac{\Omega^2 + (\kappa/2)^2}{4\bar{a}^2 G^2 \eta_c \kappa}. \tag{3.47}$$

In order to obtain the backaction power spectral density, we can look at the radiation force as $\hat{F}_{rp} = \hbar G \hat{a}^\dagger \hat{a}$ and then plug in the solution $\hat{a} = \bar{a} + \delta\hat{a}$. We will also ignore terms proportional to $\bar{a}^2$ because they are time-independent (i.e. static shift) and $\delta\hat{a}\delta\hat{a}^\dagger$ because they are negligible:

$$\delta\hat{F}_{rp}(\Omega) = \hbar G \bar{a}\left(\delta\hat{a}(\Omega) + \delta\hat{a}^\dagger(\Omega)\right).$$

In the same manner as before, backaction power spectral density is

$$\begin{aligned}2\pi\delta(\Omega + \Omega')\bar{S}_{FF}^{\text{ba,qn}}(\Omega) &= \left\langle \delta\hat{F}_{rp}(\Omega)\delta\hat{F}_{rp}^\dagger(\Omega')\right\rangle, \\ &= 2\pi\delta(\Omega + \Omega')\bar{a}^2 G^2 \hbar^2 \frac{\kappa}{\Omega^2 + (\kappa/2)^2}.\end{aligned}$$

Just to recall, we have identified the two important spectral densities (at zero temperature):

$$\bar{S}_{xx}^{\text{im,qn}}(\Omega) = \frac{\Omega^2 + (\kappa/2)^2}{4\bar{a}^2 G^2 \eta_c \kappa}, \tag{3.48}$$

$$\bar{S}_{FF}^{\text{ba,qn}}(\Omega) = \bar{a}^2 G^2 \hbar^2 \frac{\kappa}{\Omega^2 + (\kappa/2)^2}. \tag{3.49}$$

As a quick check, we can quickly see that the Heisenberg-Uncertainty principle is satisfied:

$$\bar{S}_{xx}^{\text{im,qn}}(\Omega)\bar{S}_{FF}^{\text{ba,qn}}(\Omega) = \frac{\hbar^2}{4\eta_c} \geq \frac{\hbar^2}{4}.$$

The best approach from here is to identify the intracavity field photon number at the standard quantum limit and plug into the spectral densities. Therefore we can

solve for $\bar{a}^2_{\rm SQL}$ by considering the two mechanisms that contribute to uncertainty are equal $\bar{S}^{\rm im,qn}_{xx}(\Omega) = |\chi_m(\Omega_m)|^2 \bar{S}^{\rm ba,qn}_{FF}(\Omega)$:

$$\bar{a}^2_{\rm SQL} = \frac{\Omega^2 + (\kappa/2)^2}{2G^2\kappa\hbar\sqrt{\eta_c}} m_{\rm eff}\Omega_m\Gamma_m. \tag{3.50}$$

Recall that the photon number (for a single port cavity) is written as

$$\hat{a}^\dagger\hat{a} = |\bar{a}|^2 = \frac{4\eta_c\kappa}{4\Delta^2+\kappa^2}|\bar{s}_{\rm in}|^2,$$

where the incident power is introduced as $P_{\rm in} = \hbar\omega|\bar{s}_{\rm in}|^2$. Another simplification is made when we consider driving on resonance (i.e. $\bar{\Delta} = 0$) $\rightarrow \bar{a}^2_{\rm SQL} = \frac{4\eta_c}{\kappa}|\bar{s}_{\rm in}|^2$, which we can use to identify the power incident on the cavity to reach the standard quantum limit:

$$P_{\rm SQL} = \frac{\hbar\omega_L|\bar{a}_{\rm SQL}|^2\kappa}{4\eta_c}, \tag{3.51}$$

$$= \Gamma_m\hbar\omega_L\frac{\kappa^2}{64g_0^2\eta_c^{3/2}}\left(1+\frac{4\Omega_m^2}{\kappa^2}\right). \tag{3.52}$$

The next steps (for completeness) involve deriving a relationship for the total displacement uncertainty power spectral density. For the general case of the imprecision, let us again solve the following for any frequency $\Omega$ instead of $\Omega_m$ as was done previously:

$$\bar{S}^{\rm im,qn}_{xx}(\Omega) = |\chi_m(\Omega)|^2\bar{S}^{\rm ba,qn}_{FF}(\Omega),$$
$$\Rightarrow \bar{a}^2_{\rm SQL} = \frac{\Omega^2+(\kappa/2)^2}{2G^2\kappa\hbar\sqrt{\eta_c}}\cdot m_{\rm eff}\left((\Omega_m^2-\Omega^2)^2+\Omega^2\Gamma_m^2\right)^{1/2}.$$

In plugging back in to Eq. 3.48 we have

$$\bar{S}^{\rm im,qn}_{xx}(\Omega) = \frac{\hbar}{2\sqrt{\eta_c}}\frac{1}{m_{\rm eff}\left((\Omega_m^2-\Omega^2)^2+\Omega^2\Gamma_m^2\right)^{1/2}},$$
$$= \frac{\hbar}{2\sqrt{\eta_c}}|\chi_m(\Omega)|.$$

Note that on resonance $\Omega = \Omega_m$ the displacement imprecision power spectral density

at the standard quantum limit is:

$$\bar{S}_{xx}^{\mathrm{im,SQL}}(\Omega_m) = \frac{\hbar}{2\sqrt{\eta_c} m_{\mathrm{eff}} \Omega_m \Gamma_m},$$
$$\bar{S}_{FF}^{\mathrm{ba,SQL}}(\Omega_m) = \frac{\hbar m_{\mathrm{eff}} \Omega_m \Gamma_m}{2\sqrt{\eta_c}}.$$

The final step is to solve for the total added noise at zero temperature (sometimes denoted $\bar{S}_{xx}^{\mathrm{add}}$) by identifying that the minimum is a sum of the two uncertainties:

$$\bar{S}_{xx}^{\mathrm{add}}(\Omega) = \bar{S}_{xx}^{\mathrm{im,qn}}(\Omega) + |\chi_m(\Omega)|^2 \bar{S}_{FF}^{\mathrm{ba,qn}}. \tag{3.53}$$

The total added uncertainty for the displacement spectral density (illustrated in Fig. 3.9) in the presence of a non-zero temperature is:

$$\bar{S}_{xx}^{\mathrm{tot}}(\Omega) = \bar{S}_{xx}^{\mathrm{im,qn}}(\Omega) + |\chi_m(\Omega)|^2 \bar{S}_{FF}^{\mathrm{ba,qn}} + |\chi_m(\Omega)|^2 \bar{S}_{FF}^{\mathrm{th}}. \tag{3.54}$$

Note that the added displacement imprecision due to thermal noise is $\bar{S}_{xx}^{\mathrm{th}}(\Omega) = |\chi_m(\Omega)|^2 \bar{S}_{FF}^{\mathrm{th}}$.The minimum added noise in measuring the optomechanical device is $S_{xx}^{\mathrm{add}}(\Omega) \geq S_{xx}^{\mathrm{SQL}}(\Omega) = \hbar|\mathrm{Im}[\chi_m(\Omega)]|$, in which both noise sources contribute equally at the standard quantum limit. This can be easily seen by evaluating Eq. 3.53. A simple ratio can be seen by considering the thermal noise peak with respect to the displacement spectral density of the standard quantum limit:

$$\frac{S_{xx}^{\mathrm{th}}(\Omega_m)}{S_{xx}^{\mathrm{SQL}}(\Omega_m)} = 2n_{\mathrm{th}}. \tag{3.55}$$

In other words, the relationship between the thermal mechanical peak and the standard quantum limit is only 2 times the mechanical occupancy. Another useful relationship to consider is the amount of backaction in comparison to the thermal force fluctuations:

$$\frac{S_{FF}^{\mathrm{ba,qn}}(\Omega_m)}{S_{FF}^{\mathrm{th}}} = \frac{1}{1 + \frac{4\Omega_m^2}{\kappa^2}} \frac{4g_0^2 \bar{a}^2}{\kappa \Gamma_m n_{\mathrm{th}}} \approx \mathcal{C}_0 \frac{n_{\mathrm{cav}}}{n_{\mathrm{th}}}, \tag{3.56}$$

where the approximation is valid for the bad-cavity limit $\Omega_m \ll \kappa$ and the optomechanical bare cooperativity $\mathcal{C}_0 \equiv \frac{4g_0^2}{\kappa\Gamma_m}$ has been introduced.

## 3.7 Effective Mass and Thermomechanical Noise

A quick discussion of the effective mass is needed to better understand the concepts of thermomechanical noise and cooling. The effective mass of an oscillator is best

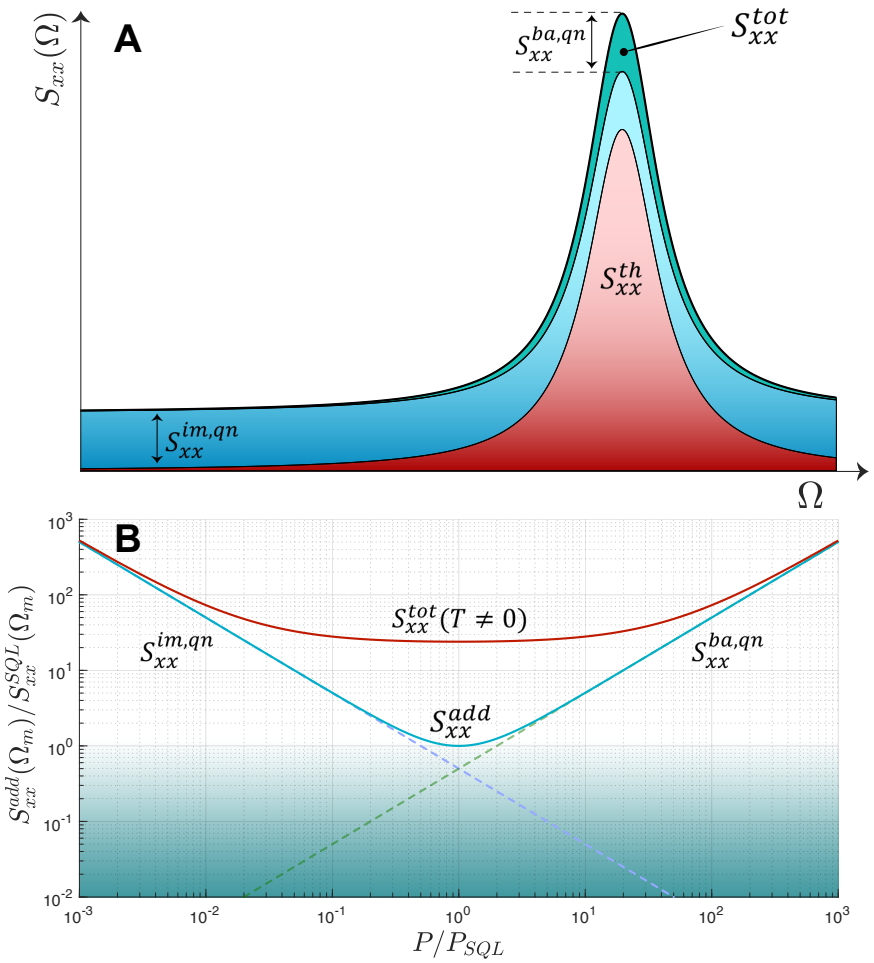


Figure 3.9: (**A**) The frequency domain representation of the total imprecision and contributions as it relates to the observed mechanical spectrum. (**B**) The standard quantum limit illustrated as a trade-off between imprecision and backaction. The highlighted blue region corresponds to squeezing where the imprecision drops below the SQL at the expense of increased noise in the opposite quadrature being measured. The total uncertainty also includes the thermal noise of the mechanical resonator and is thus raises the imprecision level.

understood as the fraction of total mass that is mechanically compliant. For example, the mass near the frame of a tensioned circular membrane does not contribute much to the overall motion of the resonator. Additionally, the thermomechanical noise does not need to be obtained from the fundamental mode of a mechanical resonator [43]. If one knows the effective mass of the higher-order modes, the thermomechanical temperatures can be extracted from those higher frequencies. While the effective

masses for a circular membrane vary depending upon the mode of interest, the square, or rectangular, membrane has equal effective mass for all modes and evaluates to a simple fraction $m_{\text{eff}} = m/4$.

In the absence of driving the mechanical resonator experiences Brownian motion at temperature $T$, a white noise force with a single-sided force power spectral density:

$$S_F^{\text{th}} = \frac{4k_B T m_{\text{eff}} \Omega_m}{Q_m}.$$

The introduction of $m_{\text{eff}}$ is important because we are not limited to the calibrating the thermal motion of the fundamental mode [43]. For our system, this proves to be valuable because the spectrum is much more quiet around the higher radially-symmetric (0,2) and (0,3) modes. We can relate this force to the displacement $S_x^{th}(\Omega) = |\chi_m(\Omega)|^2 S_F^{th}$ through the mechanical susceptibility:

$$S_x^{\text{th}}(\Omega) = \frac{4k_B T \Omega_m}{m_{\text{eff}} Q_m \left( (\Omega_m^2 - \Omega^2)^2 + \left( \frac{\Omega \Omega_m}{Q_m} \right)^2 \right)}.$$

Especially for the re-entrant cavity, the sensitivity is highly dependent upon the gap size and decreases as the gap is increased. We use a phase-bridge microwave circuit to detect the frequency shift ($\frac{dV}{df}$) of the mechanical motion ($\frac{df}{dx}$) imprinted onto the microwave signal to generate a conversion of volts to meters,

$$\frac{dV}{dx} = \frac{dV}{df}\frac{df}{dx}. \tag{3.57}$$

In the context of a phase-bridge discriminator circuit $S_{FD} \equiv \frac{dV}{df}$ is referred to as the "discriminator sensitivity" (discussed further below in Sec. 3.8) while $G/2\pi \equiv \frac{df}{dx}$ is the "frequency-pull parameter" using the language of optomechanics. The discriminator sensitivity is found by adjusting the local oscillator phase to be phase-sensitive and modulating the microwave frequency. Conveniently, this also accounts for changes in cavity $Q$ and coupling as the gap size changes. For each point measurement of thermomechanical noise, a modulated microwave tone was applied to determine $\frac{dV}{df}$. The frequency-pull parameter is determined analytically for the re-entrant cavities. Since frequency and cavity quality factors change depending on the gap spacing, we require coefficients for both domains. Therefore, the expression we fit as detected on the FFT machine (in angular frequency units) is

$$S_{\text{v}}^{th}(\Omega, \omega) = \frac{4k_B T \Omega_m}{m_{\text{eff}} Q_m \left( (\Omega_m^2 - \Omega^2)^2 + \left( \frac{\Omega \Omega_m}{Q_m} \right)^2 \right)} \left( S_{FD}(\omega) G(\omega) \right)^2. \tag{3.58}$$

## 3.8 Phase-Bridge Configuration

After attending Dr. Tobar's lab in Australia, I was introduced to the simplistic, yet powerful, concept of the phase-bridge setup to detect mechanical motion from the microwave signal. Intuitively, an interference is made between a microwave tone that has undergone modulation via the membrane motion and the microwave tone with no modulation. Therefore, when the two signals recombine at a mixer, the IF output reveals the mechanical oscillator spectrum. The phase bridge essentially detects phase modulations of the cavity resonance arising from the mechanical resonator.

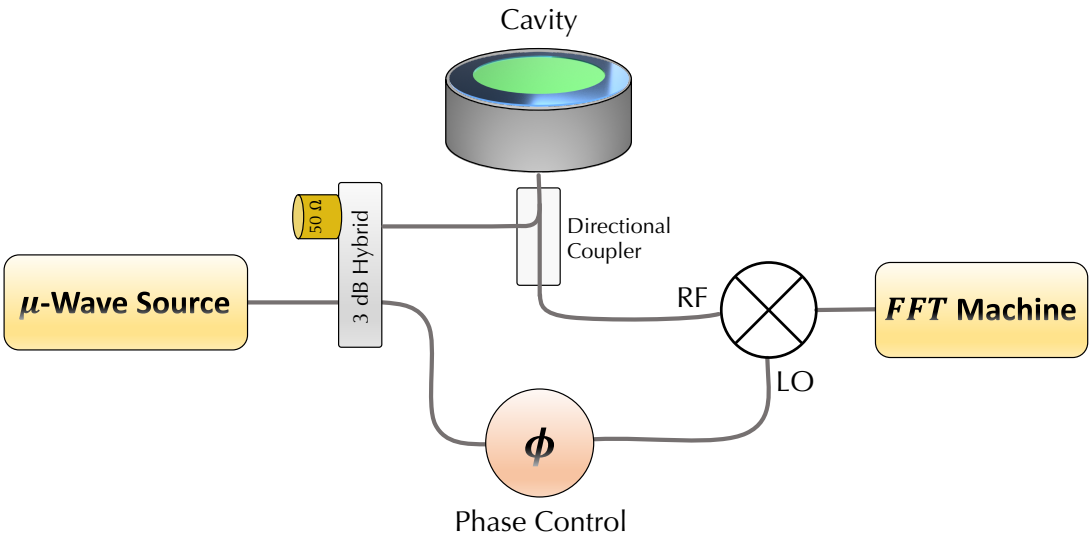


Figure 3.10: The microwave phase bridge circuit used to detect phase modulations of the cavity resonance.

We consider a phase-bridge system in which the signal is reflected off of the cavity rather than used in transmission. The two signals acting on the mixer are represented here:

$$u_{\mathrm{RF}}(t) = u_{\mathrm{inc}}|\Gamma|\cos(\omega_{\mathrm{synth}}t + \phi_r), \tag{3.59}$$

$$u_{\mathrm{LO}}(t) = u_{\mathrm{LO}}\cos(\omega_{\mathrm{synth}}t + \theta). \tag{3.60}$$

The output voltage of the mixer is an ideal multiplier of the two incident signals with a coefficient of proportionality (i.e. includes conversion loss, etc.). Here the

voltage is DC because the two paths share the same frequency up to a phase-shift,

$$\begin{aligned} u_{\text{mix}}(t) &= 4ku_{\text{RF}}(t)u_{\text{LO}}(t), \\ &= 2ku_{\text{inc}}|\Gamma|u_{\text{LO}}\cos(\phi_r - \theta), \\ &= 2ku_{\text{inc}}u_{\text{LO}}\ \text{Im}\left[\Gamma\right]\Big|_{\theta=\pi/2}, \end{aligned}$$

where the last line makes use of the expression $\Gamma = |\Gamma|\, e^{i\theta}$. The reflection coefficient takes the form:

$$\Gamma = \frac{\beta - 1 - j\xi}{\beta + 1 + j\xi}, \tag{3.61}$$

where the variable $\xi$ is defined by

$$\xi \equiv \frac{\omega - \omega_c}{\Delta\omega_{0.5}}, \tag{3.62}$$

and $\Delta\omega_{0.5}$ is the loaded half-maximum at half-bandwidth $\Delta\omega_{0.5} = \frac{\omega_c}{2Q}$. The reflection coefficient is rewritten in polar form in the complex plane as:

$$\begin{aligned} \Gamma &= \frac{|z_1|e^{i\phi_1}}{|z_2|e^{i\phi_2}}, \\ &= \sqrt{\frac{(\beta-1)^2+\xi^2}{(\beta+1)^2+\xi^2}}\exp\left\{j\left[\arctan\left(\frac{\xi}{1-\beta}\right) - \arctan\left(\frac{\xi}{1+\beta}\right)\right]\right\}, \end{aligned}$$

where we have made use of $\arctan(-x) = -\arctan(x)$. The phase of the reflected signal is the argument of the exponential

$$\phi_r = \arctan\left(\frac{\xi}{1-\beta}\right) - \arctan\left(\frac{\xi}{1+\beta}\right). \tag{3.63}$$

Now, to continue with evaluating the expression for the voltage signal at the output of the mixer we need to evaluate $\text{Im}[\Gamma] = \Gamma\sin\phi_r$[10]:

$$\begin{aligned} \Gamma\sin\phi_r &= \sqrt{\frac{(\beta-1)^2+\xi^2}{(\beta+1)^2+\xi^2}}\frac{\frac{2\beta\xi}{(1-\beta)(1+\beta)}}{\sqrt{1+\left(\frac{\xi}{1-\beta}\right)^2}\sqrt{1+\left(\frac{\xi}{1+\beta}\right)^2}}, \\ \Gamma\sin\phi_r &= \frac{2\beta\xi}{(1+\beta)^2+\xi^2}. \end{aligned}$$

[10]The following trigonometric identities are useful: $\sin(\arctan(x)) = \frac{x}{\sqrt{1+x^2}}$ and $\sin(u \pm v) = \sin u\cos v \pm \cos u\sin v$.

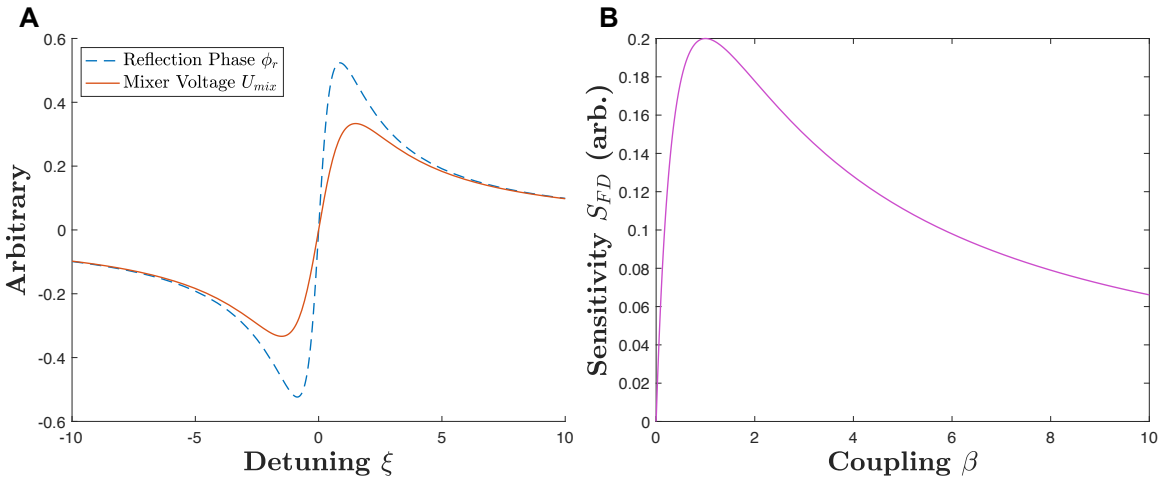


Figure 3.11: (**A**) The phase bridge response as a function of pump detuning and (**B**) the sensitivity of the phase bridge is optimized for a coupling coefficient of $\beta = 1$ (critically-coupled).

Furthermore, the incident power acting on the resonator is

$$P_{\text{inc}} = \frac{u_{\text{inc}}^2}{2R},$$
$$\rightarrow u_{\text{inc}} = \sqrt{2P_{\text{inc}}R}.$$

Here $R$ is the characteristic impedance of the line and is typically $50\Omega$. Therefore, the output mixer voltage signal of the microwave phase-bridge is written as

$$u_{\text{mix}} = \mathcal{H}\sqrt{P_{\text{inc}}}\frac{2\beta\xi}{(1+\beta)^2+\xi^2}, \tag{3.64}$$

where $\mathcal{H} = 2ku_{\text{LO}}\sqrt{2R}$ accounts for coefficients. We can now take a look at the sensitivity of the phase-bridge circuit. In other words, the sensitivity defines the amount of voltage output per frequency shift, often denoted the sensitivity of the frequency discriminator:

$$S_{FD} = \frac{du_{\text{mix}}}{d\xi}\frac{d\xi}{d\omega}, \tag{3.65}$$

$$S_{FD}\Big|_{\omega\approx\omega_c} = \mathcal{H}\sqrt{P_{\text{inc}}}\frac{2\beta}{(1+\beta)^2}\frac{1}{\Delta\omega_{0.5}}. \tag{3.66}$$

The analytical behavior of the phase-bridge microwave circuit is shown in Fig. 3.11. For better performance and sensitivity a microwave interferometer needs to be built in which carrier suppression takes place. The "dark port" is amplified by a low-noise

amplifier, which sets the noise floor for the detection system and is much lower than the noise floor of the mixer.

# Chapter 4

# Electrostatic Tunability of Resonances

*"You want to set a goal that is big enough that in the process of achieving it you become someone worth becoming."* – *Jim Rohn*

The material contained in this chapter is comprised mainly of the paper submitted to AIP Advances [46] and constitutes the majority of the research because this technique was used for subsequent experiments after the results were published. The chapter covers three main segments of this development: 1) the physical device in concept and creation, 2) the electronics developed for detection, and 3) the performance of the tunable system in its entirety.

## 4.1 Physical Device

The concept of the external electrode came about in speaking with Dr. Keith Schwab. We decided to build a bracket that adapts to the membrane to form a capacitor since there was a metallic coating on the silicon nitride (usually 500 nm Nb or 500 nm Au). The inspiration for this came from Keith's old work that involved flexible diaphragms and superfluid helium [20,47,48]. In the discussion of the created device we often used Imperial units as was required in the machine shop and discussion with the machine shop supervisor. Nearly all (95%) of the machine shop work was performed by the author from vacuum flanges, to cavities, to cryogenic translation stage adapters.

An aluminum adapter plate was machined for the cavity as well as a copper electrode (0.488" in diameter). The copper electrode was polished by hand on a polishing

lap wheel and then sent to Caltech to coat the tip in gold. In order to electrically isolate the copper from the aluminum bracket, some epoxy was used that was compatible with cryogenic use. Stycast 2850FT Black was chosen for its thermally conductive and electrically isolating properties. A separate aluminum piece, designated the epoxy bracket, was machined to mimic the cavity design and bond the copper electrode to the aluminum bracket. In hindsight, there were issues once in a while with the electrode shorting to the bracket; to correct this the electrode should have been wrapped in Teflon tape before bonding the two pieces together as a better design.

Figure 4.1: Left: The original design of the external sensing electrode adapter with aluminum bracket before bonded together. Grooves were machined into the aluminum bracket inner slot and copper electrode to have the epoxy maintain a firm grip on both surfaces. Right: The assembled design with cavity that was placed into the dilution refrigerator.

Not long after this was put into place did we decide to put in a second, smaller electrode to drive the membrane into resonance rather than simply sensing motion (seen in Fig. 4.2). The second electrode was smaller (0.393") and placed off-center at a distance roughly half of the membrane radius. Another fact was that the drive electrode had a less stringent requirement to be close to the membrane, therefore it was placed roughly 300 $\mu$m away from the membrane. The electrodes were arranged to ensure that the distance to the membrane was much closer than the separation between the two electrodes. In this manner, the stray capacitance and pickup noise are drastically reduced.

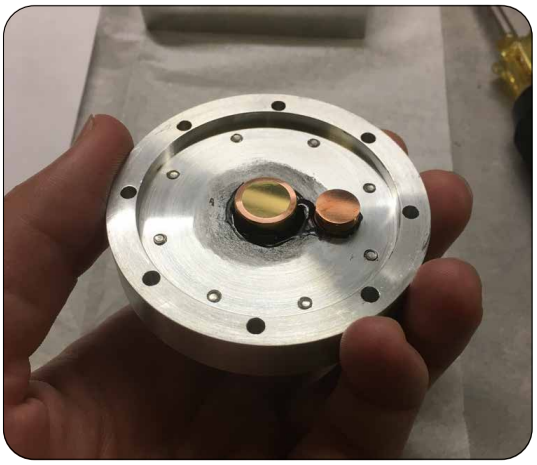

Figure 4.2: The aluminum adapter for the cavities with two electrodes. The center electrode is closer to the membrane and is typically used for the electrostatic actuation and sensing whereas the off-center electrode can be used for driving.

## 4.2 Membrane and Capacitor - Electromechanical Model

Consider the following setup in Fig. 4.3 where a charged electrode is brought near to the surface of the membrane. We begin by analyzing a small displacement, $x$, in one plate of a capacitor where the capacitance is written

$$C = \frac{\epsilon A}{d+x} \approx \frac{\epsilon A}{d}\left(1 - \frac{x}{d}\right) \equiv C_0\left(1 - \frac{x}{d}\right). \tag{4.1}$$

Then, by looking at the potential energy of the capacitor and assuming there is a DC bias voltage with an AC (oscillating) component such that $V = V_{\mathrm{DC}} + V_{\mathrm{AC}}$:

$$U(x) = \frac{1}{2}C(x)V^2, \tag{4.2}$$

$$= \frac{1}{2}C_0\left(1 - \frac{x}{d}\right)\left(V_b + V_s\cos\omega t\right)^2. \tag{4.3}$$

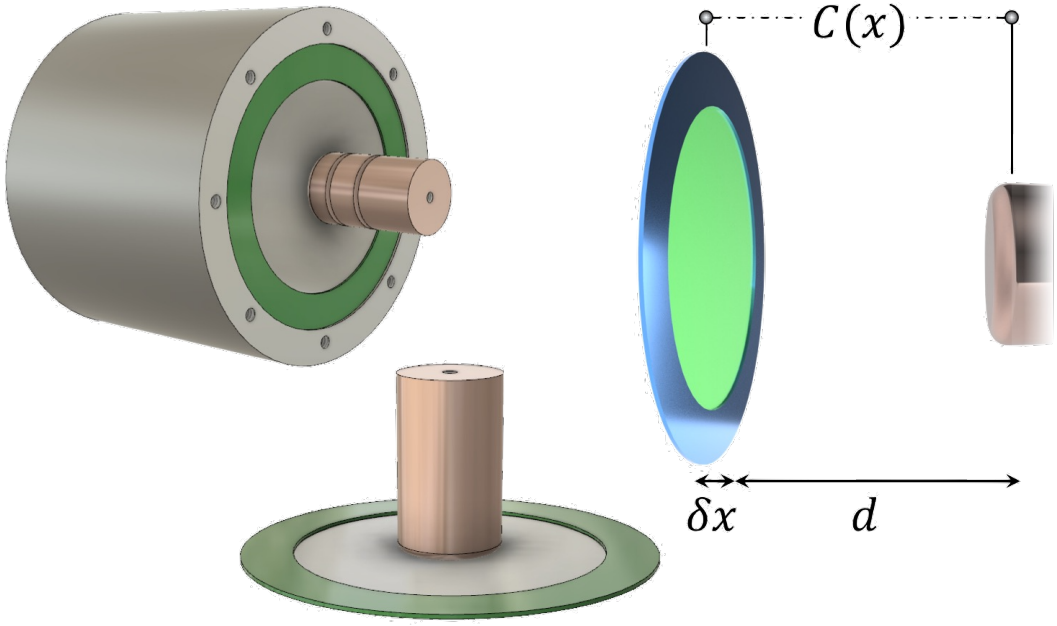


Figure 4.3: The external capacitor that is made on the outside of the cylindrical microwave cavity.

The force is then calculated to be,

$$F = -\frac{dU}{dx} = \frac{1}{2}\frac{C_0}{d}\left(V_b + V_s\cos\omega t\right)^2, \tag{4.4}$$

$$= \frac{1}{2}\frac{C_0}{d}\left(\underbrace{{V_s}^2\cos^2\omega t}_{\text{Force at } 2\omega} + \underbrace{2V_sV_b\cos\omega t}_{\text{Driving term}} + \underbrace{{V_b}^2}_{\text{Static}}\right). \tag{4.5}$$

We will only focus on the driving terms and neglect the oscillating force at $2\omega$ and the static forcing term. Meanwhile, for a damped simple harmonic oscillator the equation of motion with the external force arising from the capacitor is

$$m_{\text{eff}}\ddot{x} + m_{\text{eff}}\Gamma_m\dot{x} + kx = \frac{C_0}{d}V_sV_b\cos\omega t \tag{4.6}$$

and we assume a solution of the form $x(t) = x_0e^{i\omega t}$. In addition, the forcing term will be written as an exponential with a reminder that only the real portion contributes ($\cos\omega t \rightarrow e^{i\omega t}$). The displacement amplitude can be obtained by plugging in the assumed solution:

$$x_0(\omega) = \frac{V_sV_bC_0}{m_{\text{eff}}d}\frac{1}{({\omega_0}^2 - \omega^2) + i\omega\Gamma_m}. \tag{4.7}$$

Now, we can look at the current flow through the capacitor[1]:

$$q(t) = C \cdot V, \tag{4.8}$$

$$= C_0 \left(1 - \frac{x(t)}{d}\right) \left(V_b + V_s e^{i\omega t}\right), \tag{4.9}$$

$$= C_0 \left(V_b + V_s e^{i\omega t}\right) - \frac{C_0}{d} V_b x_0(\omega) e^{i\omega t}. \tag{4.10}$$

The product of $V_s e^{i\omega t} \cdot x_0(\omega) e^{i\omega t}$ oscillates at $2\omega$ and was therefore ignored. The current is obtained via derivative of the charge:

$$I = \dot{q} = \left[ i\omega C_0 - \frac{i\omega C_0 V_b}{d} \cdot \frac{C_0 V_b}{m_{\text{eff}} d} \frac{1}{(\omega_0{}^2 - \omega^2) + i\omega\Gamma_m} \right] V_s e^{i\omega t}, \tag{4.11}$$

where we have inserted the expression for $x_0(\omega)$ from Eq. 4.7. This equation can be considered with the perspective of an electric circuit with $I = V/|Z|$. Using this frame of thought, the impedance appears to be a parallel combination of a capacitor (first term) and LCR circuit. To illustrate this point we will take a quick detour to examine an LCR circuit in series. Let us write the equation for the voltage drop around a loop:

$$\varepsilon - IR - \frac{q}{C} - L\frac{dI}{dt} = 0, \tag{4.12}$$

$$L\frac{d^2 q}{dt^2} + R\frac{dq}{dt} + \frac{q}{C} = \varepsilon. \tag{4.13}$$

Again, assuming an oscillatory forcing and response at frequency $\omega$ ($q(t) = q_0 e^{i\omega t}$) we can write the following

$$q_0(\omega) = \frac{1}{L} \frac{\varepsilon}{(\omega_0{}^2 - \omega^2) + i\omega\frac{R}{L}}. \tag{4.14}$$

The current running through the LCR circuit is,

$$I = \dot{q} = \frac{i\omega}{L} \frac{1}{(\omega_0{}^2 - \omega^2) + i\omega\frac{R}{L}} \varepsilon e^{i\omega t}. \tag{4.15}$$

Remarkably, we can now begin to identify the mechanical oscillator as an electric circuit. Let us closely compare the forms of Eq. 4.11 and Eq. 4.15 using the immediate

[1] Note that the dielectric layer of SiN can be ignored in the capacitance and we only look at the conductive, metallic layer $C = \frac{1}{\frac{1}{C_0} + \frac{1}{C_1}} \approx C_0$. This is completely valid even though the relative permittivity of SiN is seven times larger than air.

useful conversions $\Gamma_m \to R/L$ and ${\omega_0}^2 \to 1/(LC)$, we will also let $\varepsilon \to V_s$:

$$L_m = \frac{m_{\text{eff}} d^2}{{C_0}^2 {V_b}^2} \qquad \text{Mechanical Inductance,} \tag{4.16}$$

$$C_m = \frac{{C_0}^2 {V_b}^2}{{\omega_0}^2 m_{\text{eff}} d^2} \qquad \text{Mechanical Capacitance,} \tag{4.17}$$

$$R_m = \frac{m_{\text{eff}} d^2}{{C_0}^2 {V_b}^2} \frac{\omega_0}{Q} \qquad \text{Mechanical Resistance.} \tag{4.18}$$

As a reminder the parameters are $d \equiv$ distance between capacitor plates (oscillator to electrode), $C_0 \equiv$ bare capacitance of stationary membrane and electrode, $V_b \equiv$ bias voltage, $\omega_0 \equiv$ resonant frequency, $Q \equiv$ quality factor of the oscillator. Therefore, the electromechanical model of a mechanical oscillator and capacitor placed closely together can be modeled as a series LCR circuit in parallel with a capacitor (see Fig. 4.4 (c)).

## 4.3 Condenser Microphone Circuit

In order to detect the vibrations of the circular membrane, a common technique was adopted from the microphone community known as the condenser microphone circuit [49]. The method of approach is to charge up the capacitor and observe the voltage fluctuations arising from the motion of the membrane. Therefore, a pull-up resistor is used with resistance typically on the order of 100 MΩ to 1 GΩ. Following the resistor is a capacitor large enough to block the voltage bias on the pull-up resistor before entering the pre-amplifier stage.

One of the difficulties we had was impedance matching the op-amp to the external capacitor. Apparently, for the op-amp we were using, this became an important issue for input impedances less than 300 pF. One of the important sources of stray capacitance is the SMA cable capacitance for UT-85 cables, which is approximately 30 pF per foot. Since the device was at the lower stage of the dilution refrigerator and including cable windings we estimated the length of SMA cable before the pre-amplifier. The total source capacitance ended up being around 250 pF, of which only about 7 pF is due to the external capacitor. This results in an effective signal loss of approximately 35 by $\frac{C_{\text{cap}}}{C_{\text{cable}}}$.

Later, Dr. Keith Schwab helped us develop a better pre-amplifier stage with a voltage noise floor of 1.5 nV/Hz$^{1/2}$ at $\Omega/2\pi = 10$ kHz. The new circuit was comprised of junction field effect transistor (JFET) amplifiers instead of an op-amp stage and this reduced the complexity of balancing the op-amp arms for input impedance. The specifics of this amplifier are not discussed any further due to the intellectual property of this circuit that Dr. Schwab's company, Sierra Op Amps, now sells to consumers.

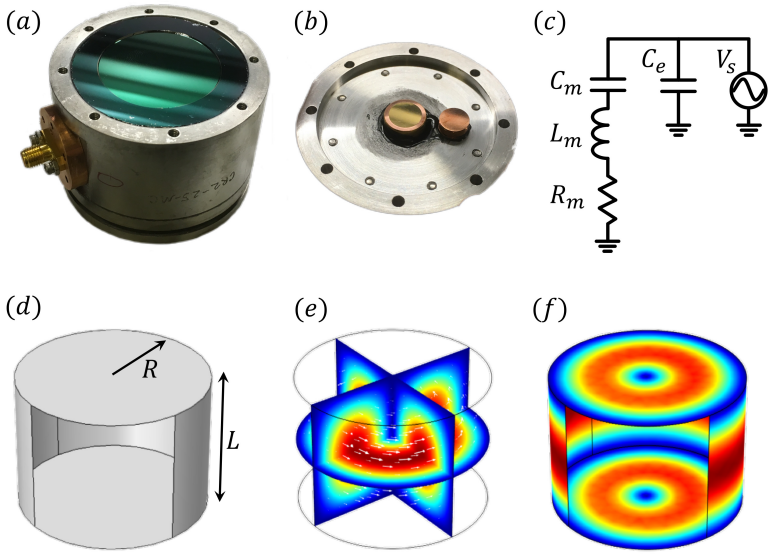


Figure 4.4: (a) Image of the SRF cavity with the silicon nitride membrane. The antennae are anchored to the niobium body with copper adapters. (b) Image of the electrodes epoxied to the aluminum bracket. The sensing electrode is 8.7 mm in diameter while the driving electrode is 12.5 mm in diameter. The bracket flips over and attaches to the body of cavity with corresponding threaded holes. (c) The electrical model [20] of the mechanical resonator ($C_m$, $L_m$, and $R_m$) and capacitance $C_e$ formed between the copper electrode and the membrane with source voltage $V_s$. (d) Geometric model of the cylindrical cavity. (e) Electric field multislice of the $TE_{011}$ mode. (f) Magnetic field surface plot of the $TE_{011}$ mode.

## 4.4 Mechanical Detection

The initial measurements of the mechanical oscillator and detecting the modes of a circular drum using an electrostatic approach are presented in Fig. 4.7. The membrane is charged up by some bias voltage $V_{\mathrm{DC}}$ on a pull-up resistor while a lock-in amplifier sweeps a smaller, probe voltage $V_{\mathrm{AC}}(\Omega)$, in frequency. As the membrane oscillates the external capacitor generates a voltage proportional to the displacement of the oscillator, thereby observing resonance as $\Omega = \Omega_m$. The resonance appears to be a Fano-lineshape and has excellent agreement with the fit to the equation:

$$V_{\mathrm{meas}} = \frac{V_0}{1 - 2iQ_m \frac{\Omega - \Omega_m}{\Omega_m}} + \alpha e^{i\phi}. \tag{4.19}$$

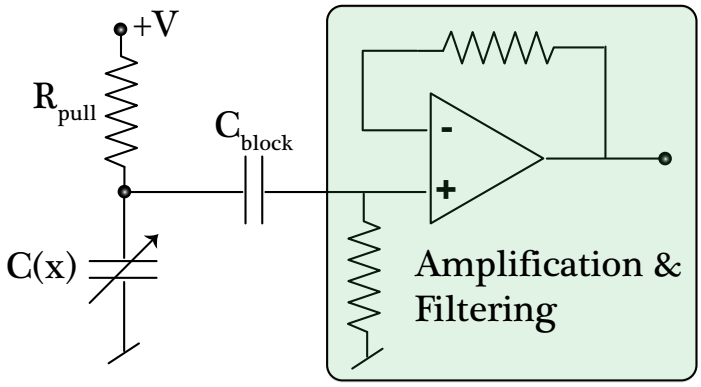


Figure 4.5: The electrical circuit model for the condenser microphone. The microphone is charged up with a resistor while the front-end capacitor blocks the large DC voltage to avoid damaging the amplifier. After the blocking capacitor, the signal is amplified and filtered in subsequent stages (not shown).

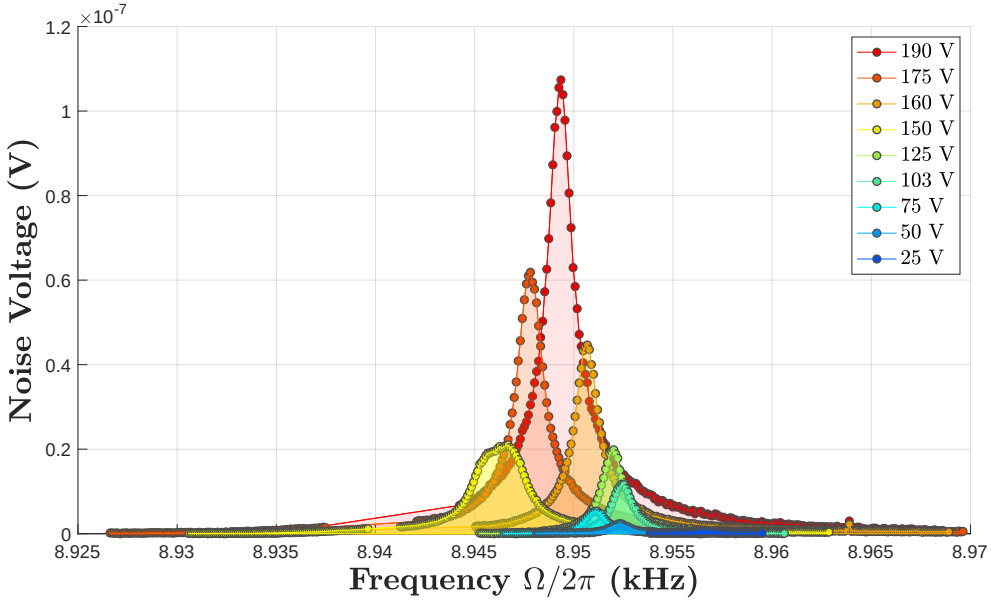


Figure 4.6: The sensitivity to detect the mechanical signal is shown to rise for the (0,2) niobium membrane mode with an increased DC bias on the pull-up resistor.

We have used the notation that $V_0$ is a scaling factor, $\Omega_m/2\pi$ is the mechanical resonance frequency, $Q_m$ is the mechanical quality factor, and $\alpha e^{i\phi}$ is an offset that leads to the Fano-lineshape.

The membrane quality factor was measured as a function of air pressure (mbar)

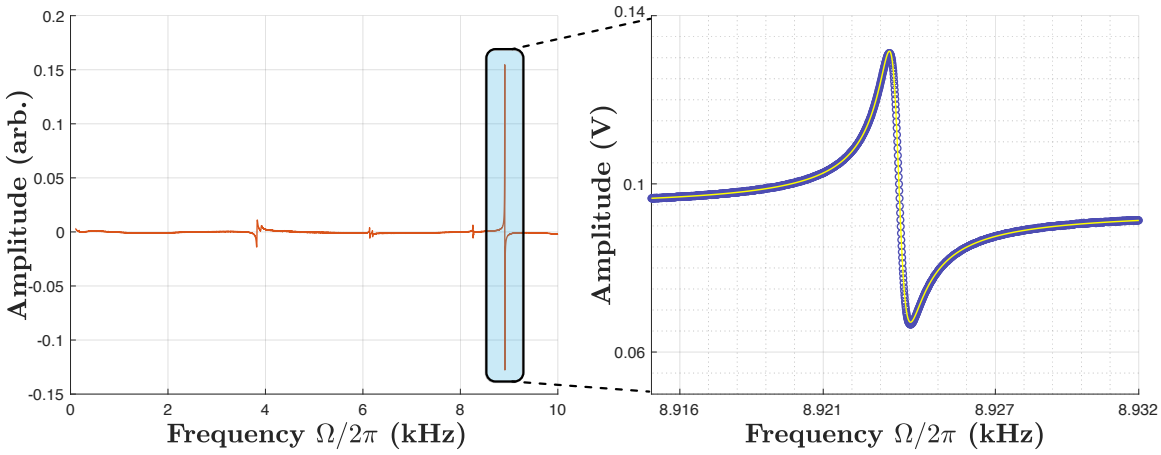


Figure 4.7: The initial measurements as seen on a lock-in amplifier with a polynomial fit to the background subtracted. The resonances take on a Fano-like lineshape as seen on the right-hand side for the (0,2) mode.

and can be seen in Fig. 4.8. We noticed the quality factor of the membrane saturated to a pressure of about $1.2 \times 10^{-3}$ mbar. The quality factor of the (0,1) mode was typically around $Q_m = 1 \times 10^3$ whereas the (0,2) mode was $Q_m = 12.5 \times 10^4$, nearly an order of magnitude higher. Cooling the membrane resulted in a further increase of about five. The (0,2) mode was measured several times to possess a quality factor between $Q_m = 6.5 - 7 \times 10^4$ at cryogenic temperatures.

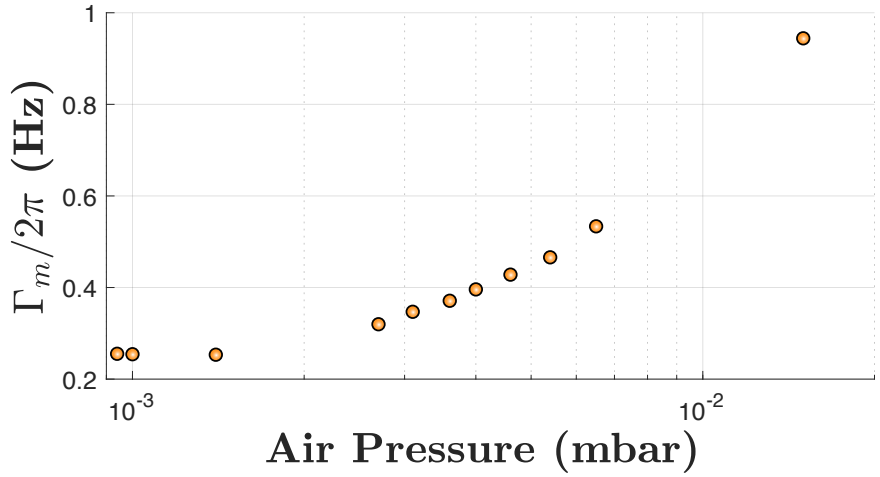


Figure 4.8: The decay rates are shown for the (0,3) mode of the niobium membrane. We can see the $Q = \Omega_m/\Gamma_m$ saturates at a pressure around $1 \times 10^{-3}$ mbar.

### 4.4.1 Displacement Estimates

We can get a rough approximation of the rms displacement of the membrane by considering the voltage generated at the input of the pre-amplifier:

$$\begin{aligned} & V(x) = \frac{Q}{C(x)}, \\ & V(x) = \frac{Q}{C_0 + C_s(x)}, \qquad C_s(x) = \frac{\epsilon A}{(d+x)}, \\ & \delta V = \frac{Q}{(C_0 + C_s)^2} \frac{C_s}{d} \delta x, \\ \rightarrow \quad & \frac{\delta V}{V_{\mathrm{DC}}} = \left( \frac{C_s}{C_0 + C_s} \right) \frac{\delta x}{d}. \end{aligned}$$

We made the approximation that $\frac{\epsilon A}{(d+x)^2}\delta x \approx \frac{C_s}{d}\delta x$. The signal loss due to stray capacitance can be identified as the factor of $\frac{C_s}{C_0+C_s}$, which happens to be about 35. Secondly, we can see that the sensitivity to observe a smaller displacement can be done in two ways (assuming the cable length remains unchanged): 1) increase the DC bias voltage, or 2) reduce the gap between the electrode and the membrane. However, these displacement estimations are rough approximations simply because the effective mass of the oscillator is an estimation.

## 4.5 Calibrating the Electrostatic Force

This section investigates the capacitance between the electrode and the flexible membrane. We first start with the potential energy of a capacitor:

$$U = \frac{1}{2} C(x) V^2.$$

Here $V^2$ represents the AC-voltage within the cavity. We approximate the capacitor as a parallel plate capacitor and that the total actuation is much less than the distance between electrode and membrane, $x \ll d$:

$$C(x) = \frac{\epsilon_0 A}{d - x} = \frac{\epsilon A}{d\left(1 - \frac{x}{d}\right)} = C_0 \left(1 + \frac{x}{d}\right)^{2}.$$

[2]Use a Taylor expansion $\frac{1}{1-x} \approx 1 + x$ for $x \ll d$

We let $A = \pi r_c^2$ be the overlapping area between the electrode and the membrane. Now the force can be written down:

$$\begin{aligned} F_{cap} &= -\frac{\partial U}{\partial d}, \\ &= -\frac{1}{2}V^2\frac{\partial C(x)}{\partial d}, \\ &= \frac{C_0 V^2}{2}\left(\frac{1}{d} + \frac{2x}{d^2}\right). \end{aligned}$$

Experimentally, this is observed by looking at the shift in the mechanical resonance frequency known as "spring softening" (aka "pull-in") since the membrane wants to be pulled into the electrode. The real data is shown in Fig. 4.9. Mathematically, this can be derived by looking at the Taylor expansion of the fundamental resonance.

$$\Omega_m = \sqrt{\frac{k_m + k_e}{m}}, \tag{4.20}$$

$$\approx \sqrt{\frac{k_m}{m}}\left(1 + \frac{k_e}{2k_m} + \cdots\right). \tag{4.21}$$

We can also identify the electrical spring constant $k_e$ by considering the forces above. Re-written slightly differently, the total force acting on the membrane (only considering electrostatic and restoring spring forces) is

$$F_{\text{total}} = V^2\frac{C_0}{2d}\left(1 + \frac{2x}{d}\right) - k_m x, \tag{4.22}$$

$$= V^2\frac{C_0}{2d} + \left(V^2\frac{C_0 x}{d^2} - k_m\right)x. \tag{4.23}$$

If we define the effective spring constant be the sum of two terms, electrical and mechanical: $k = k_e + k_m$. We let the electrical spring constant be denoted as

$$k_e = -\frac{\epsilon V^2 \pi r_c^2}{d^3}. \tag{4.24}$$

Therefore[3], the first order shift in the resonance frequency is expressed as

$$\frac{\delta\Omega_m}{\Omega_m} \approx \frac{1}{2}\frac{k_e}{k_m} = -\frac{\epsilon\pi r_c^2 V^2}{2d^3\Omega_m^2 m_{\text{eff}}}. \tag{4.25}$$

[3]I used the approximation $\sqrt{1+x} \approx 1 + \frac{1}{2}x + \cdots$

The frequency shift has a cubic dependence upon the distance. The room temperature mechanical quality factor for the (0,2) membrane mode was $Q_m \approx 1.1 \times 10^4$ at a low DC driving voltage and drops linearly to $Q_m \approx 8.9 \times 10^3$ at the largest applied DC voltage.

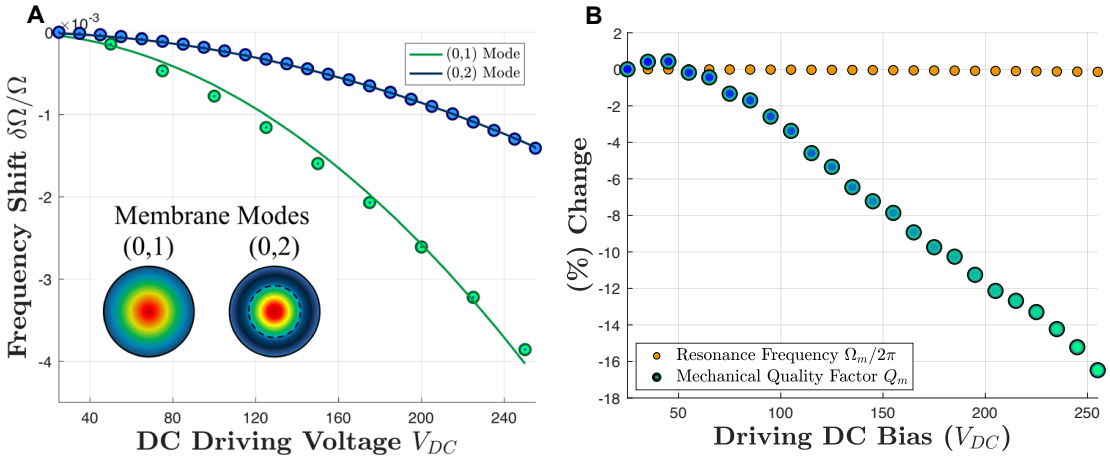


Figure 4.9: (**A**) The mechanical frequency shifts seen as a function of DC voltage bias. (**B**) The percentage shift of the quality factor and mechanical frequency as the DC voltage is increased. These effects are analogous to "spring-softening" typically seen in MEMs devices.

## 4.6 Superconducting Cavity Experiments

### 4.6.1 Superconducting Frequency Tunability

The room temperature electrostatic frequency shifts were a success for the membrane, however, we needed to test the cavities at cryogenic temperatures to see how the electromagnetic frequencies behaved. At room temperatures, the niobium cavities have $Q \sim 3 \times 10^3$ for a $\omega_c/2\pi = 10.3$ GHz, which means the bandwidth is fairly large ($\approx 3.4$ MHz) and any small frequency translation was not able to be observed, especially in combination with the limiting resolution of the network analyzer (100 kHz per point). This highlights the importance of the superconducting cavities with increased $Q$ because smaller frequency adjustments can be observed (using a Schottky-diode for microwave detection). The transmission of the cavity is sent to a high-electron-mobility transistor (HEMT) amplifier at the 4K plate and further amplified at room temperature by two, smaller, post amplifiers.

We performed measurements on two different cavities [46] denoted CR2 and CR5 with respective loaded quality factors of $Q_L = 1.1 \times 10^6$ and $Q_L = 2.5 \times 10^6$. Referring

the reader to Fig. 4.10, we observed an SRF resonance shift of almost 35 kHz for cavity CR2, slightly over three linewidths while cavity CR5 displayed about 25 kHz, or six linewidths, of frequency translation. In addition, the measured frequency-pull parameter of our cavities is $G \equiv (d\omega/dL) = 2\pi \cdot 3.2 \times 10^{10}$ Hz/m. The color bar depicts 250 V as the maximum DC driving voltage, but it should be noted that the furthest resonance shift for cavity CR2 was performed at 255 V. The full range of tunable bandwidth is slightly different between the two cavities due to small cavity geometric variations, machining imprecision, and the use of different membranes. Upon cooling down the fridge, there is a negligible frequency shift of the cavities' resonance, aside from the superconducting transition, over the course of a week. There is also no observable heat generated in the tuning process when we monitored the base fridge temperature.

This work has demonstrated non-contacting tunable superconducting cavities without sacrificing $Q$ or generating heat through compression or strain induced by the more common method of tuning bulk cavities with piezoelectric transducers [50–52].

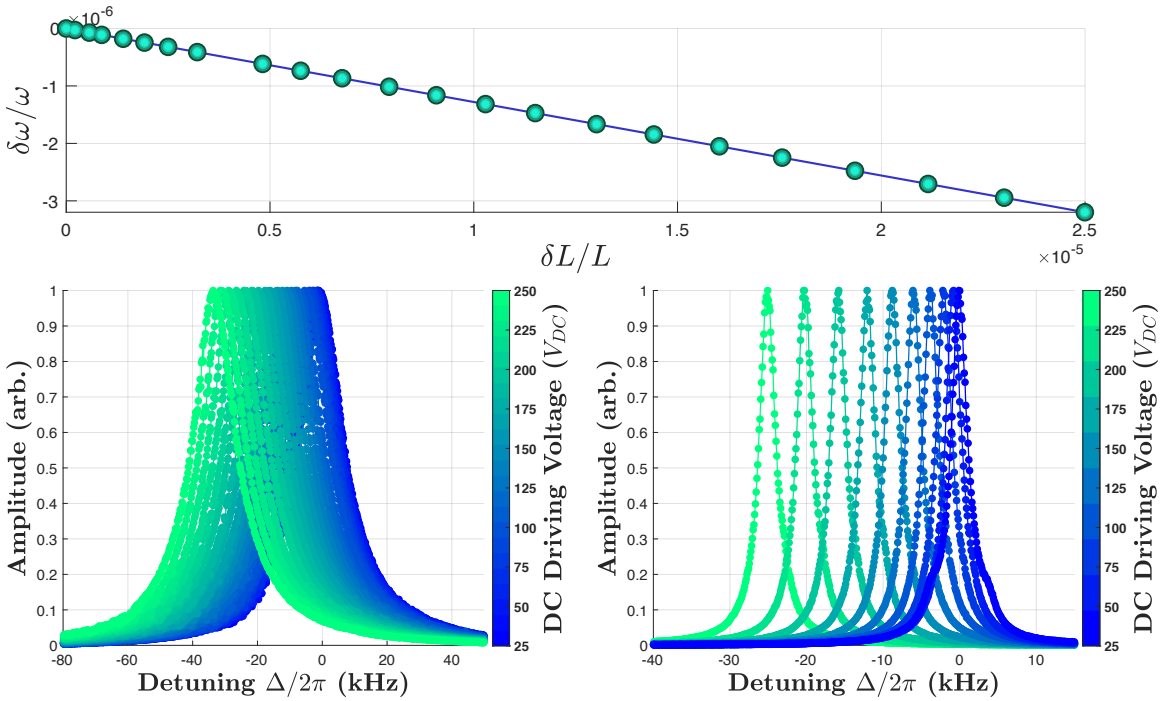


Figure 4.10: The superconducting cavities of CR2 (left) and CR5 (right) showing electrostatic tunability of the superconducting resonances.

### 4.6.2 Driven Superconducting Experiments

The static measurements led to interesting superconducting observations in the context of dynamic measurements, or the microwave response with a driven membrane. The work was never published but certainly deserves future effort and investigation. In keeping a small AC voltage $V_{\mathrm{AC}}(\Omega \approx \Omega_m)$ we can see some interesting dynamical effects manifest on the microwave resonance the electrostatic response along with a small $V_{\mathrm{AC}}$ is shown in Fig. 4.11.

The disappearance of the central peak in Fig. 4.11 can be described by the mechanical oscillator shifting the cavity frequency by an amount $\delta\omega \gg \kappa$. The reason this only occurred for a particular DC voltage range is that the electrostatic shift also affects the membrane. Therefore the AC voltage is only resonant for $V_{\mathrm{AC}}(\Omega_m)$ before the membrane is pulled out of resonance for $\Omega < \Omega_m$ and $\Omega > \Omega_m$.

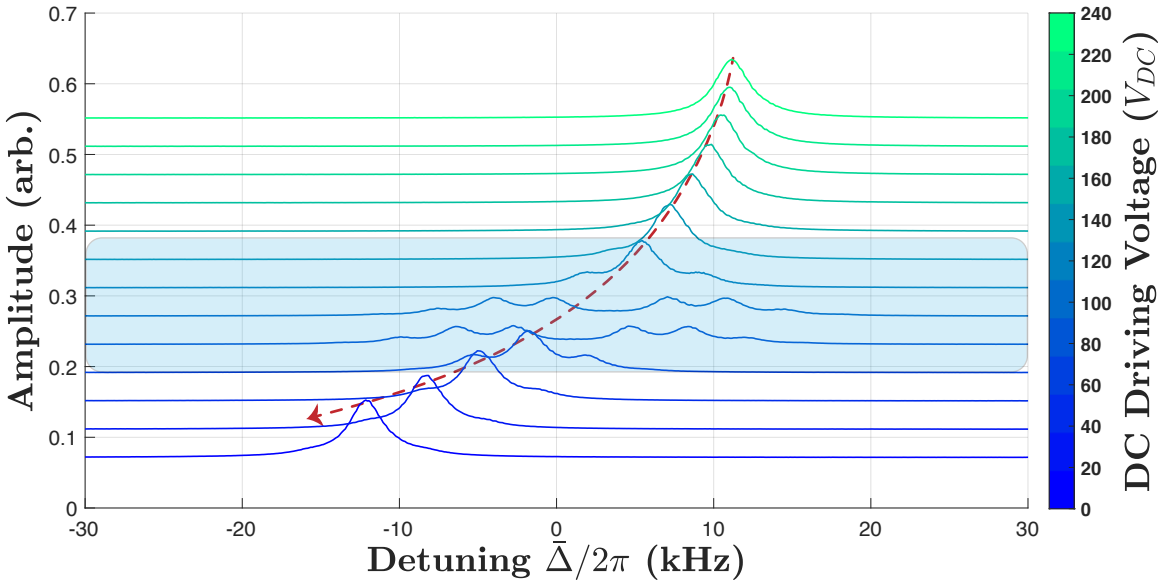


Figure 4.11: The divergence from the normal microwave transmission response becomes apparent in the highlighted blue box. The red dashed line shows the electrostatic shift of the cavity frequency.

Eventually, the system reaches a maximum splitting of $\sim 70\Omega_m/2\pi$ for a given DC bias and probe voltage which is shown in Fig. 4.13. The maximum splitting can be extended to a larger span under the influence of a stronger probe voltage or stronger coupling (see Sec. 5.2 below). We will see similar behavior like this, but on a much larger scale in Sec. 5.2 where we used re-entrant microwave cavities and increased the coupling by a factor of $G_{\mathrm{new}}/G_{\mathrm{old}} \sim 5 \times 10^4$ and the frequency separation reached a peak value of 1.88 GHz, or $7.5 \times 10^5 \cdot (\Omega_m/2\pi)$.

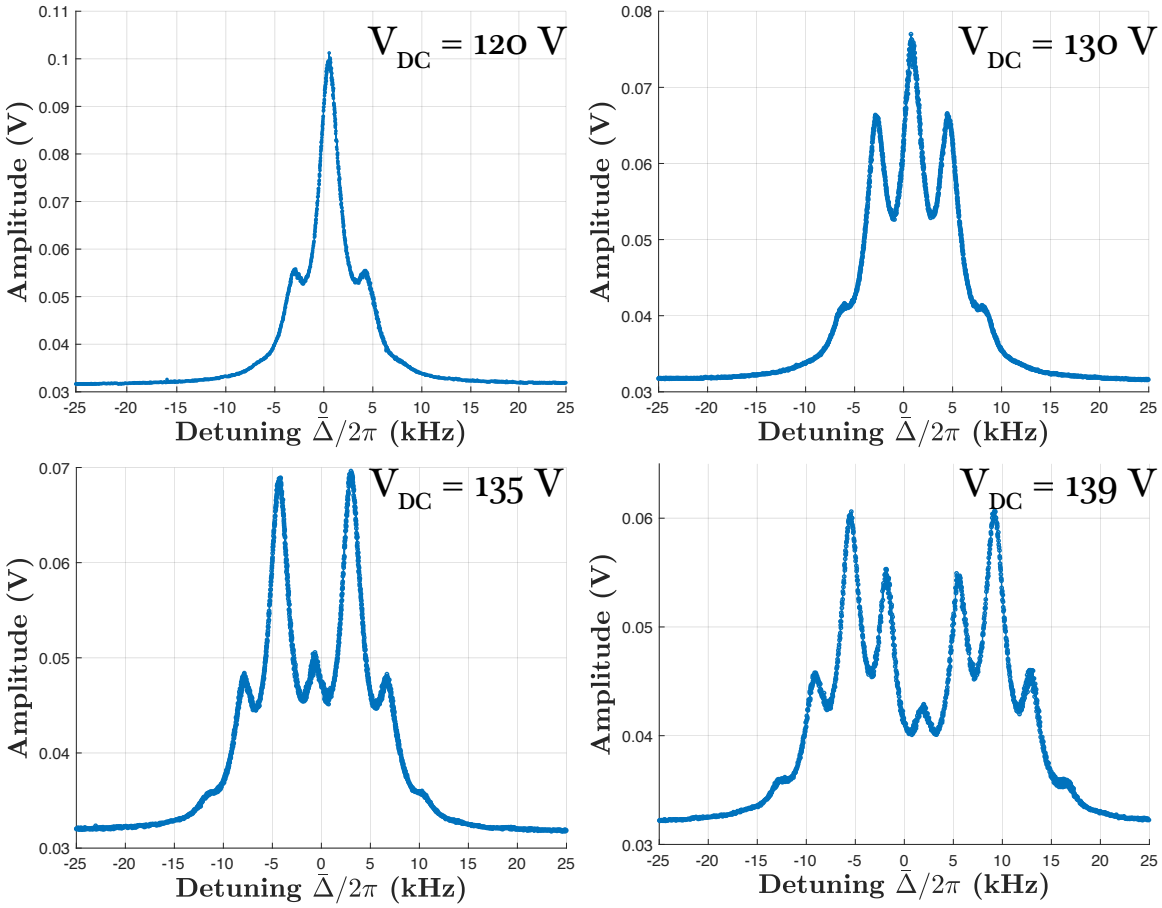


Figure 4.12: As the DC bias is increased, the electrostatic shift of the membrane brings the small probe voltage into resonance with the membrane $V_{\mathrm{DC}}(\Omega = \Omega_m)$, thereby increasing the "splitting."

Notice that this effect would not have been observable for the room temperature cylindrical cavities because of the low coupling rates. The splitting, or microwave mode hopping as described later, are two in the same effects wherein the cavity frequency is modulated by the membrane. The difference is that the low coupling to the membrane with the cylindrical cavities prevents any modulation beyond the cavity bandwidth, which is why this effect was only observed when the bandwidth is significantly decreased (high-$Q$) under the effect of superconductivity. In the end, the observed effect is commonly referred to as frequency modulation (FM), but is rarely mentioned in the community of optomechanics because of the extremely small mechanical displacements. The different responses can be explained by various modulation indexes for a given carrier frequency.

An alternative design for tunable cavities was developed for the coaxial $\lambda/4$ stub

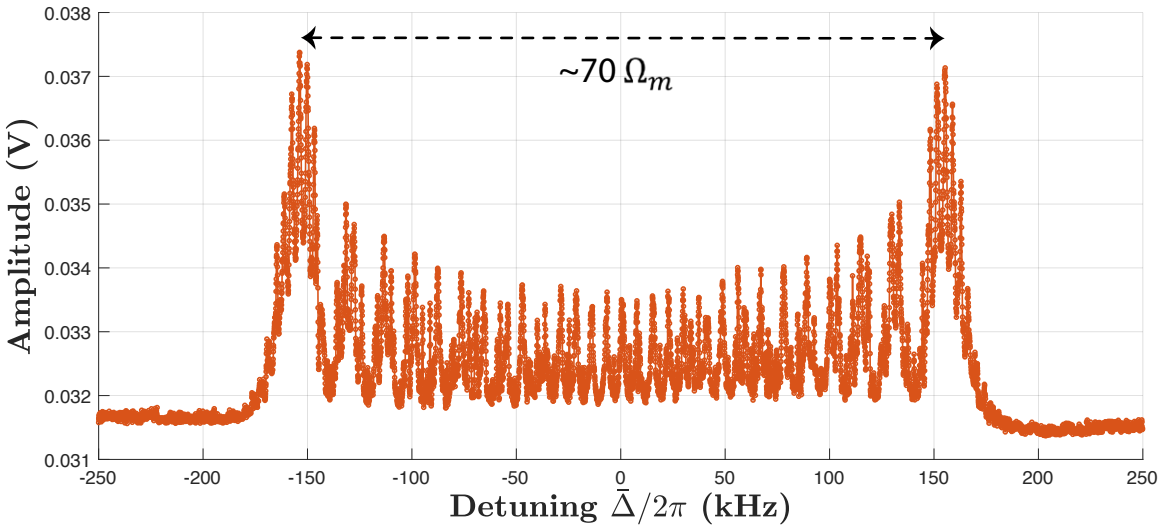


Figure 4.13: The maximal splitting shown for $V_{\mathrm{DC}} = 150$ V bias and small probe voltage ($\sim 50$ $\mathrm{mV_{rms}}$).

cavities in which a dielectric material (sapphire) was inserted to adjust the resonance frequency. We purchased a device from Janssen Precision Engineering for a cryogenic linear translation stage, however, the minimum movement was a few microns, which correlated to a resonance shift of around $\delta f = 150$ kHz near the stub. An adapter stage was designed and machined to house a smaller piezoelectric transducer for better control. The completed stage was never fully used because the research goals were redirected to focus on stronger coupling, however, the room temperature proof-of-concept was completed and is shown in Fig. 4.15. Coarse tuning was provided by the main translation stage with the fine-tuning provided by the PZT. One drawback to this tuning capability is the current draw from the translation stage that heats the fridge and requires some time before settling back to base temperature.

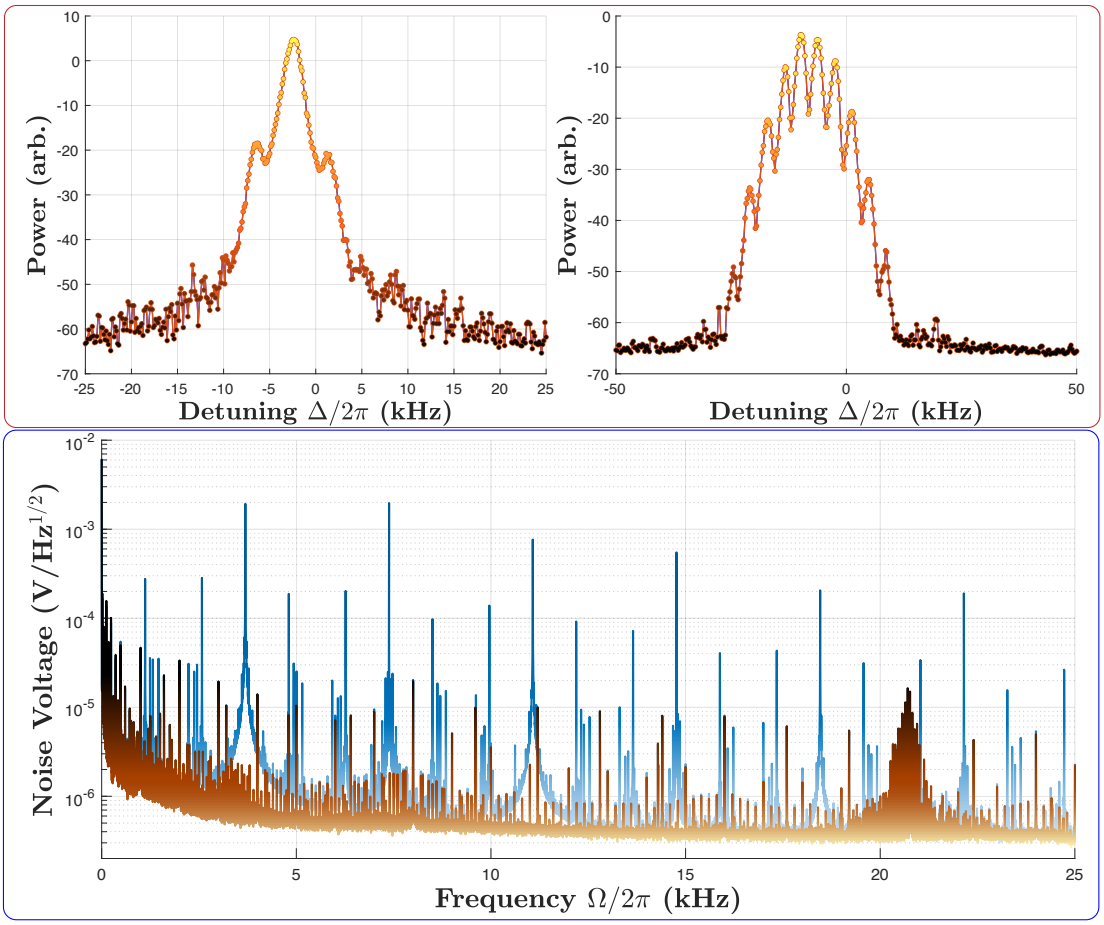


Figure 4.14: The upper panel shows the RF spectrum in the undriven (left) and driven (right) mode under the influence of an acoustic voltage at the membrane frequency. The lower panel shows the acoustic spectrum and the effect of optomechanical amplification using a blue-detuned microwave (GHz) pump source at -20 dBm (orange/brown) and 0 dBm (blue) with a clear difference between the two. Here we have shown two distinct methods of inducing mechanical motion.

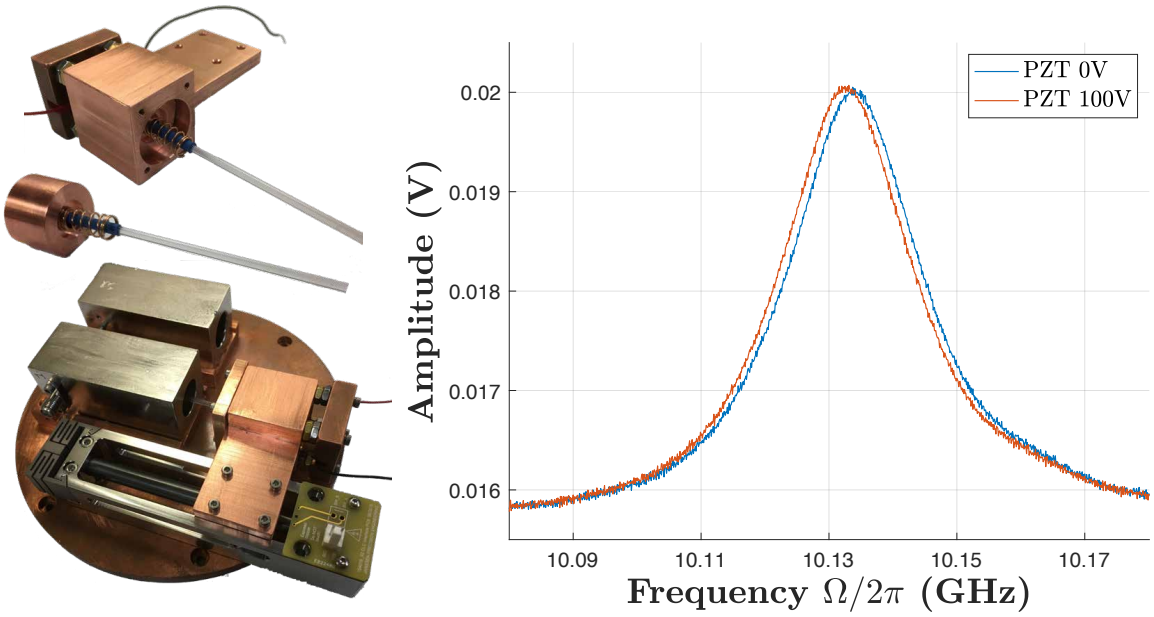


Figure 4.15: The device and its mounting configuration is pictured on the left hand side with the room-temperature data displayed on the right hand side.

# Chapter 5

# Narrow Gap Re-entrant Cavities

*"Only those who dare to fail greatly can ever achieve greatly."* – *John F. Kennedy*

The majority of this chapter has been adapted from the submitted paper titled, "*Casimir spring and dilution in macroscopic cavity optomechanics.*"

## 5.1 Room Temperature Experiments

The primary importance of optomechanical coupling is focused on optimizing the cavity $Q$ and coupling $G$ to the membrane. Since we did not see any major improvements with the cavity $Q$ in the last couple of years, we focused our attention towards the coupling parameter. The optomechanical coupling does not require a superconducting cavity and this allowed us to make quick changes to design configurations and rapid progress. Furthermore, if we could simply conduct room temperature measurements this would drastically reduce the experimental time. A vacuum chamber and pressure goal of $1 \times 10^{-3}$ mbar were required to observe the mechanical resonances. This pressure was chosen as a good saturation level where air pressure is no longer the limiting $Q$ factor in the big membranes according to Fig. 4.8.

Never having experience in machining a vacuum testbed before the author took a bell jar in the lab and machined an aluminum faceplate for the bottom with a double O-ring seal, a threaded valve, and six SMA ports. As we should have expected, this did not work very well because the threaded valve (with Teflon tape) does not provide a great seal. We went back and copied the designs of the vacuum flanges on the dilution refrigerators and made a custom aluminum flange to house a rubber O-ring. The system achieved $5 \times 10^{-4}$ mbar on the first try. Now, rapid progress with

room temperature measurements was possible because the bell jar reached pressures of $1 \times 10^{-3}$ mbar within 10 minutes. To compare the speed up time, a room temperature measurement within the dilution refrigerator (pumped out, no cooling) would take roughly 8 hours to reach the same vacuum level — nearly 50 times longer for the same experiment. Lastly, a miniature mounting system for the cavities was made on the aluminum faceplate and any potential optical equipment by drilling sixteen 1/4"-20 holes.

Figure 5.1: The custom vacuum chamber made to perform room temperature experiments and reduce time needed to pump down.

Over half a dozen different prototype re-entrant cavities were made by trial and error to achieve the strongest coupling possible. The best device is pictured in Fig. 5.2 with the three pieces that comprise the re-entrant cavity: the cavity body, the membrane, and the electrode adapter. The cavity was constructed using traditional machining methods on a lathe, CNC, and milling machine. The tolerance of the machines did not allow for the manufacturing of gap sizes of less than 10 $\mu$m. Instead, a cylinder of 6061 aluminium was cut on a horizontal band saw, faced-off with a lathe, and polished on a polishing lap wheel with water for several hours starting from fine sandpaper and ending with felt. Afterward, the aluminium cylinder was bored out

on a lathe taking care never to touch the center of the polished aluminium with a tool. The final reduction of the gap to $\sim 1$ $\mu$m was achieved by iteratively measuring the cavity resonance frequency with a network analyzer and performing light surface removal of the outer ledge using Scotch-Brite on a lathe.

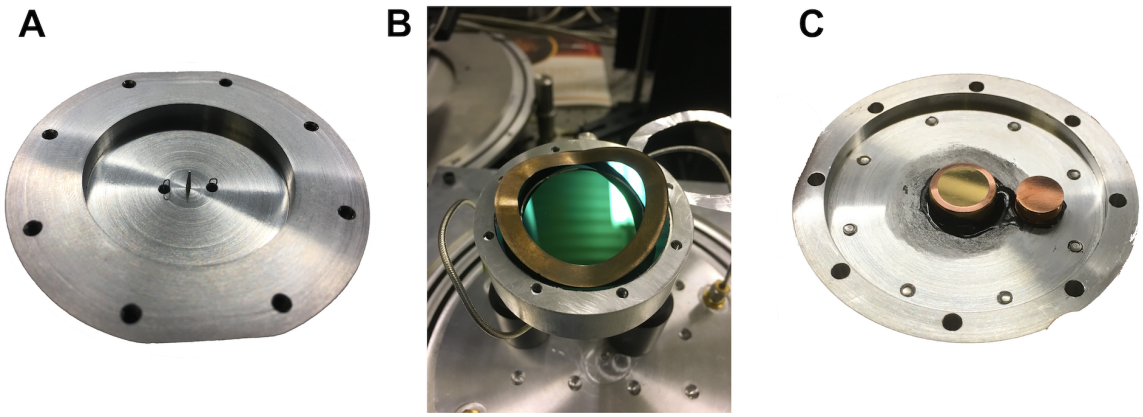


Figure 5.2: (**A**) The bare re-entrant cavity shown with cone and loop antennas. (**B**) The SiN membrane (gold underneath) acted as the cavity boundary and determines the resonance frequency. The bronze spring washer was pressed against the membrane and held it securely in place. A thin (1 mm) aluminum washer created the space needed to bring the electrodes close to the uncoated membrane surface. The cavity was mounted in a vacuum chamber on an optical table. (**C**) The center gold-plated electrode for actuating the membrane. The electrodes and mounting bracket were flipped over and placed above the bronze spring washer. The smaller, off-center electrode was traditionally designed to "drive" the membrane with the center electrode originally created to "sense" the vibrations, however for these experiments the second electrode was not used and the center electrode was purely used as an active device.

The gap size was numerically obtained as a function of the applied electrostatic force using the measurement of the re-entrant cavity frequency and the well known LC model (see Fig. 5.4). Based upon the starting resonance frequency we estimated the smallest gap achieved for the gold membrane to be $x = 585 \pm 61$ nm. Numerical estimates yielded a frequency-pull parameter of $G/2\pi \equiv \frac{df}{dx} = 1.66 - 0.57$ GHz/$\mu$m for the range of resonances presented in this paper. The intrinsic microwave cavity quality factors ranged between $20 < Q_0 < 300$ at room temperature, which is expected due to a small geometry factor of the re-entrant mode.

For the mechanical oscillator we used Silicon-Nitride (SiN) membranes (Norcada) of diameter of 38.1 mm and total thickness of 800 nm (500 nm SiN and 300 nm of

metal deposited on the underside). Two different membranes were used, one with a gold and the other with a niobium coating. The fundamental frequency of the gold and niobium membranes were $\Omega_m/2\pi = 2.51$ kHz and $\Omega_m/2\pi = 4.3$ kHz, respectively, with effective masses of $m_{\text{eff}} = 2.3$ mg and $m_{\text{eff}} = 1.3$ mg, respectively. An external gold-coated copper electrode was placed near the uncoated surface of the membrane forming a capacitor. This electrode actuated the static mechanical motion of the membrane through a DC bias [46]. The whole re-entrant cavity-membrane system was held in a vacuum chamber with microwave and DC voltage feedthroughs attached to allow control, measurement and characterization at a pressure of about $1 \times 10^{-3}$ mbar.

Outside the microwave cavity, there was an aluminum bracket that housed both of the copper electrodes. An additional adapter (not shown) was created to set the distance between the electrodes and the membrane. The copper electrodes were epoxied to the aluminum bracket using Stycast 2850, which is electrically insulating and thermally conducting. We used a 1 mm thick aluminum washer to raise the entire electrode adapter and position the electrodes below the plane of the membrane frame. The distance of the electrode to the membrane was calibrated by fitting a quadratic function to the electrostatic frequency shift (outside the thermal Casimir region) of the fundamental mode, as shown in Fig. 5.3. The fit has a parabolic shape, and from a Taylor-expansion of the resonance frequency under the influence of an electrostatic force is given by [46, 53]:

$$\frac{\delta\Omega_m}{\Omega_m} \approx \frac{1}{2}\frac{k_{\text{elec}}}{k_{\text{mech}}} = -\frac{\epsilon A}{2d^3 k_{\text{mech}}} V_{\text{DC}}^2. \tag{5.1}$$

The uncertainty in the model (from Eq. 2.30) for the microwave resonance frequency according to the post top radius is shown in Fig. 5.4. The points in the figure are the initial (unperturbed) resonances for varying gap sizes and $V_{\text{DC}} = 0$.

After moving the experiment to Australia and setting up the voltage power supply it became clear that the high-voltage supply was noisy and driving the membrane, which was observed as fringes around all mechanical modes. As such, Dr. Eugene Ivanov helped create a passive, two-pole, low-pass filter (see Fig. 5.5) that attenuated the voltage noise by at least 60 dB and gave a clear mechanical, undriven spectrum. The resulting transfer function for the passive, two-pole, low-pass filter, assuming $R_1 = R_2$ and $C_1 = C_2$ is written as:

$$|H| \equiv \left|\frac{V_{\text{out}}}{V_{\text{in}}}\right| = \left|\frac{1}{1 + 3j\omega CR + (j\omega CR)^2}\right|.$$

The room temperature measurements in the vacuum are solely devoted to the re-entrant cavities because of the strong coupling to the mechanical resonator $G/2\pi$.

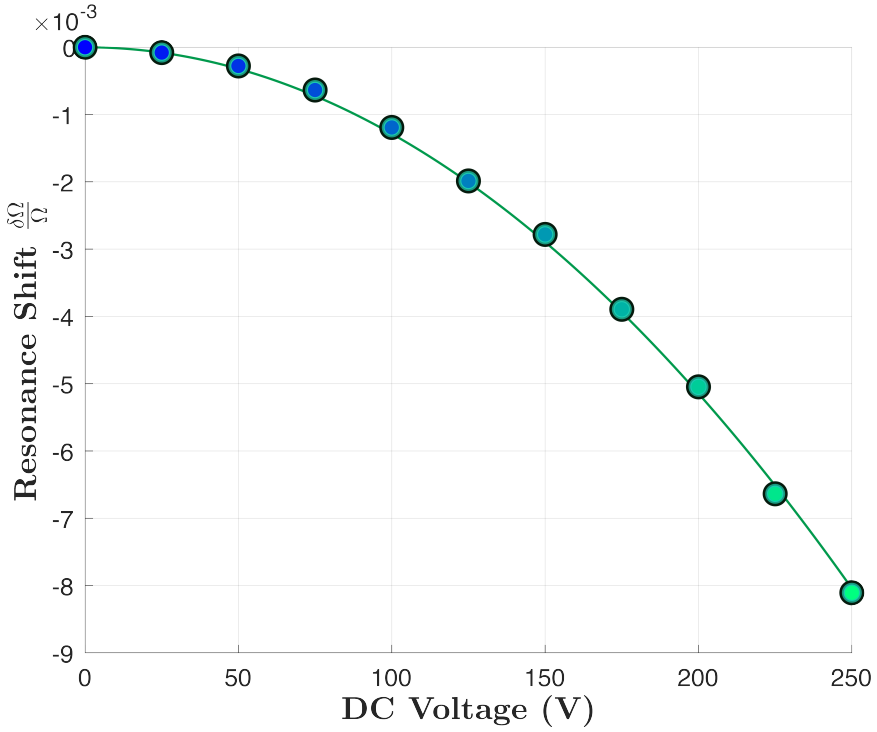


Figure 5.3: The gold membrane frequency shift of the (0,1) mode due to the electrostatic force, which allowed the calculation of the approximate distance of the electrode to membrane, to be 195 $\mu$m using Eq. 5.1.

Alternative experiments that make use of high-$Q$ require cryogenic temperatures for the superconductivity. However, the quality factor doesn't increase several orders of magnitude for the re-entrant cavity as it does for the cylindrical cavities, therefore, the vacuum chamber and room temperature setup are ideal for the re-entrant cavity.

## 5.2 Casimir Spring and Dilution

The Casimir force was predicted in 1948 [54] as a force arising between macroscopic bodies from the zero-point energy. The force arises from the unequal pressures exerted by quantum vacuum fluctuations on the inside and outside boundaries of a cavity. This occurs because there is a discrete energy spectrum within a cavity, while outside the electromagnetic energy spectrum is continuous. Thus, an inward pressure exists on the cavity because the vacuum energy density is larger outside than inside. At finite temperatures, it has been shown that a thermal Casimir force exists due to thermal fluctuations of the electromagnetic field rather than zero-point fluctuations

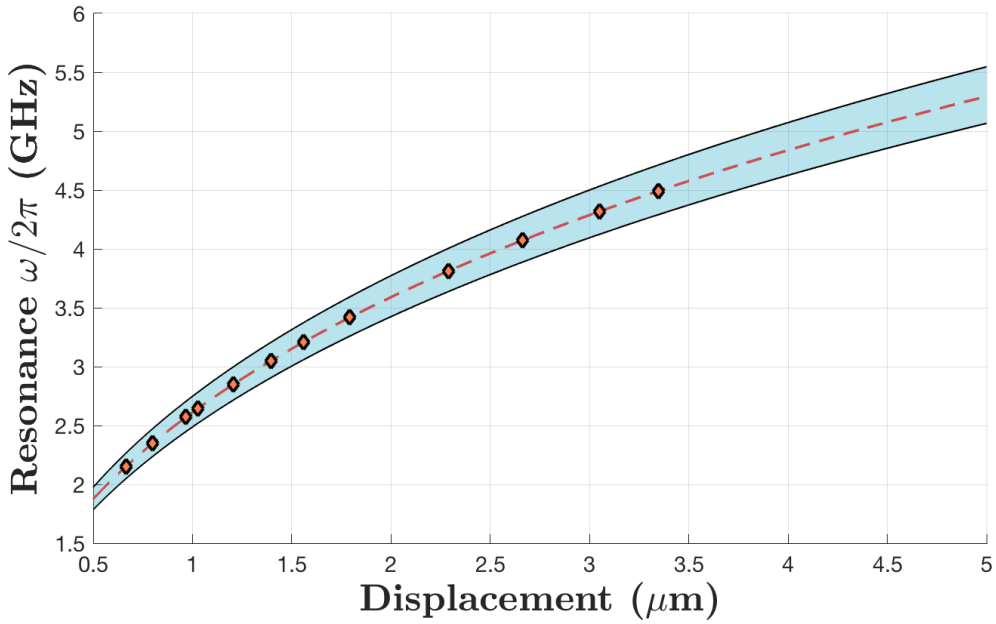


Figure 5.4: This graph was generated for a geometric uncertainty of $\pm 10$ $\mu$m in the top cone radius. This uncertainty translates to the displacement uncertainty in subsequent graphs. The solid diamonds are data at which we used the resonance frequencies with $V_{\mathrm{DC}} = 0$ to generate displacements according to the geometric model.

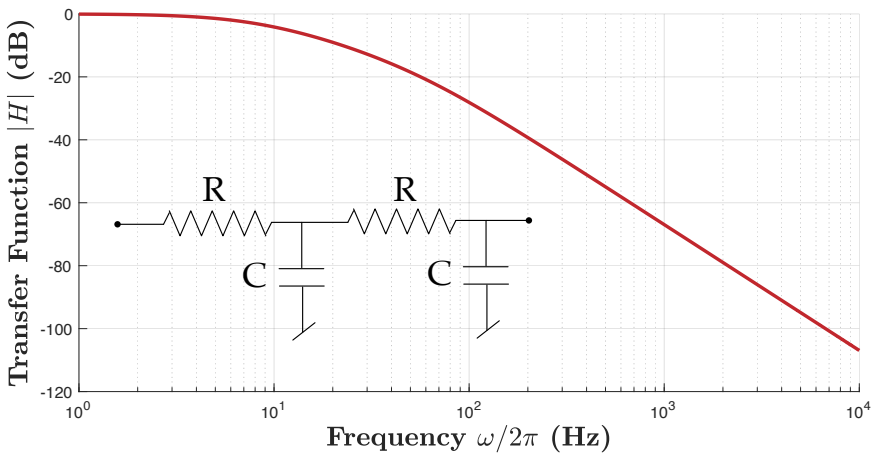


Figure 5.5: Two-pole low pass filter ($R = 750\Omega$ and $C = 10\mu$F) made to reduce voltage noise at least 60 dB near the fundamental frequency around 4 kHz.

and there are a growing number of experiments that characterise the effect at a range of temperatures and distances [55–60]. This thermal modification increases with

temperature and thus increases the range of separations between two objects where Casimir forces are observable [55, 61, 62]. The Casimir force is now not just solely of academic importance, but has been recently drawing more interest in the arena of sensors, switches, amplifiers, and photonic sources [63–67]. This work significantly adds to the tool kit available for such applications and opens new avenues for device manipulation as well as a new way to investigate the Casimir force.

In this work, the ability to sense the Casimir force was achieved by realising a small gap ($\sim \mu$m) between a cm-scale microwave re-entrant cavity post and 38 mm diameter SiN metal-plated membranes. A calibrated force varied the re-entrant gap to tune the microwave resonator and transition in and out of the Casimir regime, which revealed extra stiffening of the membrane (Casimir spring). Importantly, we have determined that a spatially-localised Casimir spring may act as a lossless non-contacting boundary (pinning effect), which was verified with finite element simulations of acoustic mode frequencies. Our results have shown that this "Casimir boundary" created "Casimir dilution" and significantly increased the acoustic $Q$-factor of the acoustic mode. Dilution has been used as an engineering technique to reduce phononic losses through the addition of strain [27, 28, 68]. Thus, this technique has allowed us to create a new way to engineer non-contacting boundary conditions in a lossless way using only thermal photons, where decreasing the gap increased both the strain and $Q$-factor in the membrane. These new techniques presented in this work have high potential to create new "*in situ*" agile programmable devices, engineered to manipulate mode structures and improve resonator losses as needed at room temperature, which could have far-reaching consequences. Furthermore, we also observed a new form of acoustic non-linearity near the gap spacing where the Casimir and spring constant force were equal, allowing the measurement of bistability and other enhanced non-linear effects.

A microwave re-entrant cavity is a type of 3D lumped microwave resonator, which consists of a post enclosed in a cavity, with a gap, $x$, between the end post and end-wall boundary as shown in Fig. 5.6, and discussed in more detail below [38, 40]. The cavity resonance frequency, $\omega/2\pi$, is primarily determined by the gap and, classically, the sensitivity of the frequency shift with respect to displacement, $d\omega/dx$, is inversely proportional to the gap. The structure acts as a reliable transducer between frequency and gap size with the microwave resonance governed by a lumped $LC$ circuit model $\omega = \left[\sqrt{LC}\right]^{-1}$ [40,69] where the re-entrant cone acts as an inductor, $L$, and the gap behaves as a capacitor, $C$. Thus, if the end wall is constructed as a mechanical oscillator, the system may be configured as a sensitive optomechanical device [30], increasing in sensitivity as the gap becomes smaller. For example, if the end wall vibrates or is displaced, a frequency shift of the microwave mode is produced. From this effect very sensitive devices have been realised previously for a range of applications, such as the readout for a resonant-mass gravitational wave detector

[69,70], transducers to read out induced displacement at high sensitivity [71–73], and the realisation of tuneable microwave cavities for a variety of applications [46,74,75].

Our system was constructed with a membrane as the end wall and by applying an electrostatic force we achieved exquisite positioning of the re-entrant gap [46]. The gap size was numerically obtained as a function of the applied electrostatic force using the LC model. When the re-entrant gap was sufficiently large so it did not experience the Casimir force, we observed normal behavior as expected for a macroscopic cavity optomechanical system (denoted as the "free" state) and the acoustic membrane had an unperturbed static spring constant of $k_S$. For small gaps, inside the Casimir region, the Casimir force became large compared to the membrane restoring force, causing reduced motion directly under the re-entrant post with an effective spring constant of $k_C(x)$ (Casimir spring), which effectively "pinned" the membrane at this point due to the attractive nature of the force. This "pinning" changed the acoustic mode shape of the membrane and hence state of the membrane (denoted as the "pinned" state). This change in mobility is similar to the "buckled up" and "buckled down" states seen in micromechanical oscillators [76]. Interesting features were also demonstrated when the gap was spaced such that the Casimir and the spring force were of equal magnitude. Here we observed the existence of a region of increased force sensitivity for the re-entrant microwave cavity readout of the mechanical motion. These results show the most sensitive re-entrant cavities may not require the smallest gap sizes, but rather a careful balance of forces to gain the best sensitivity at room temperature. Other non-linear effects also occurred around this region, such as modifications to the driven microwave mode and optomechanical bistability indicated by the effect of mode hopping (see below for more experimental and device details).

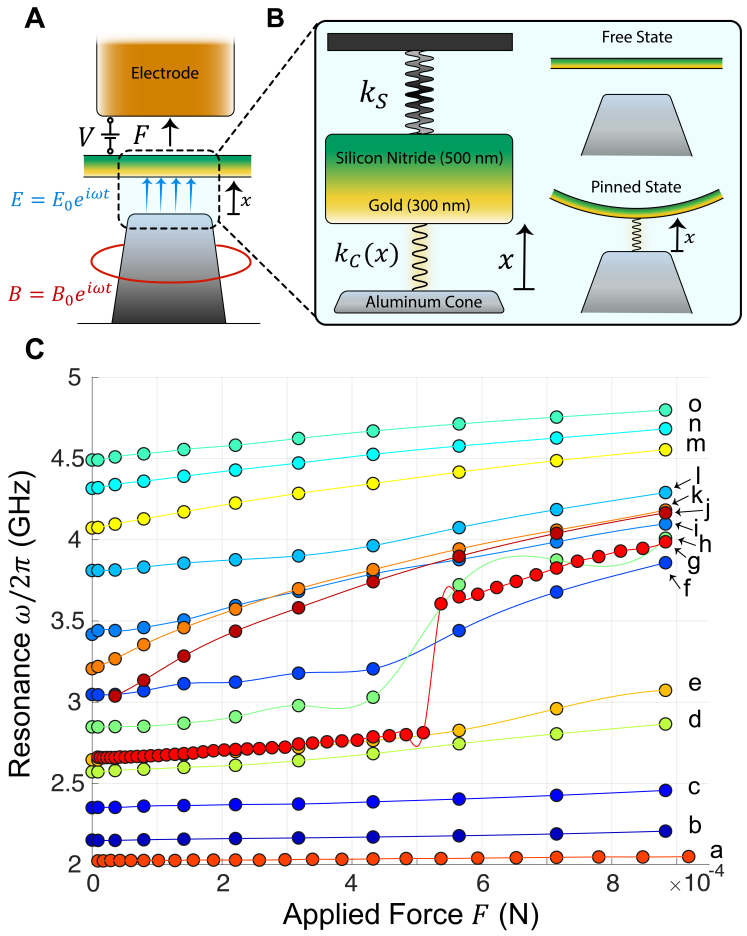


Figure 5.6: (**A**) Diagram (not to scale) of the cross-section of the electromechanical elements of the re-entrant cavity and associated electric, $E$ and magnetic, $B$ field of the re-entrant mode. A bias voltage, $V$, on the electrode produced an attractive electrostatic force, $F$, that pulled the membrane, increasing the gap size $x$ and shifting the microwave resonance frequency, $\omega/2\pi$. (**B**) The left-hand image is a simplified model of the setup illustrating the Casimir spring, $k_C(x)$, and the normal restoring spring, $k_S$, intrinsic to the membrane. The right-hand image shows the influence of the Casimir spring acting on the membrane in the vicinity of the re-entrant cone. (**C**) Microwave cavity resonance frequency, $\omega/2\pi$, versus applied electrostatic force, $F$, for a range of initial gap spacings labeled *a*-*o* (smallest gap of 0.59 $\mu m$ to largest gap of 3.9 $\mu m$). For the smallest values of initial gap spacing (*a*-*c*), the membrane experienced the thermal Casimir force significantly reducing the actuation and producing a pinned state. As the gap spacing increased (*d*-*l*) a transition to non-linear behaviour was observed. For the largest initial gap spacings (*m*-*o*) the membrane was in the free state where the Casimir response is negligible. The labels *a*-*o* correlate with the same labels in Fig. 5.7.

An advantage of this macroscopic system over many other micromechanical systems used for Casimir force sensing is the capability to achieve a large dynamic range of membrane gap sizes. To understand the response of the membrane as a function of its distance from the tip of the re-entrant cone, or gap size ($x$), a thin metallic spacer was inserted on the outer edge of the cavity and a static DC voltage ranging from 0 to 250 V was applied between the external electrode and membrane. Labeled as "*a-o*" in Fig. 5.6C, the measurements were repeated for various spacer sizes in order to build a map of the cavity response. The frequency shift as a function of the electrostatic force applied by the external electrode is shown for each experimental run of voltage sweeps with splines shown for clarity. The applied force of the electrode to the membrane was calibrated by measuring the electrostatic mechanical frequency shift outside of the Casimir regime [46, 53, 77].

The calculation of the thermal Casimir force for the given geometry is challenging due to several factors [61, 64]. The 3D re-entrant cavity deviates from the typical geometric configurations of sphere-plate, sphere-sphere, or plate-plate as the re-entrant microwave mode occurs in a sub-wavelength gap size between the membrane and cone. Additionally, we note that the skin depth ($1.76 - 1.17$ $\mu$m for $\omega/2\pi = 2 - 5$ GHz) of the electromagnetic field exceeds the layer of gold roughly by a factor of five and interacts with the SiN dielectric layer. These considerations change the magnitude of the thermal Casimir force and should be considered in future investigations, but the scaling of the force as a function of gap size is preserved, and we use this scaling to unequivocally identify its nature.

Figure 5.7 shows the observation of the inverse-cubic power law dependence ($x^{-3}$) of the force with respect to the cavity gap size, demonstrated in the form of the effective Casimir spring. The effective static spring constant, $k_{\text{eff}}$, was obtained by considering small displacements $\delta x$ around the static value of the gap spacing, $x_0$, caused by the application of a small applied electrostatic force, $\delta F$, with the setup illustrated in Fig. 5.6 (see below for the niobium membrane data). From this measurement the effective spring constant was calculated by,

$$k_{\text{eff}} = \frac{\delta F}{\delta x} = \frac{\partial F}{\partial \omega}\frac{\partial \omega}{\partial x}\Big|_{x \approx x_0}. \tag{5.2}$$

Here, we used the well-determined microwave cavity frequency shift, $\delta\omega$, to calibrate the position shift of $\delta x$. Only the initial linear regime corresponding to smaller applied electrostatic forces around $x = x_0$ were considered for the calculation of $k_{\text{eff}}$. This was to prevent possible distortions of the membrane, which could occur on the application of a large force under the influence of the Casimir pinning mechanism. Any such distortions would be very minimal under a small applied force of $\delta F$.

In Fig. 5.7, the highlighted portions of the graph designate areas of non-linear behaviour and defines the gap region where the spring constant of the membrane was

the same order as the Casimir spring constant. Outside this regime, for smaller gaps, spring hardening takes place ($x < 1.5$ $\mu$m for the gold membrane and $x < 1.2$ $\mu$m for the niobium membrane) due to the dominance of the Casimir force where the effective spring constant increases sharply as $x^{-4}$ as the gap decreases. For larger gap spacings outside the non-linear and Casimir regimes the value of the measured static spring constant was the same order as the dynamic spring constant of the fundamental frequency of the membrane. Because the niobium membrane was stiffer than the gold one, it required a larger Casimir force to enter the non-linear regime, and thus occurs at a smaller gap compared to the gold membrane.

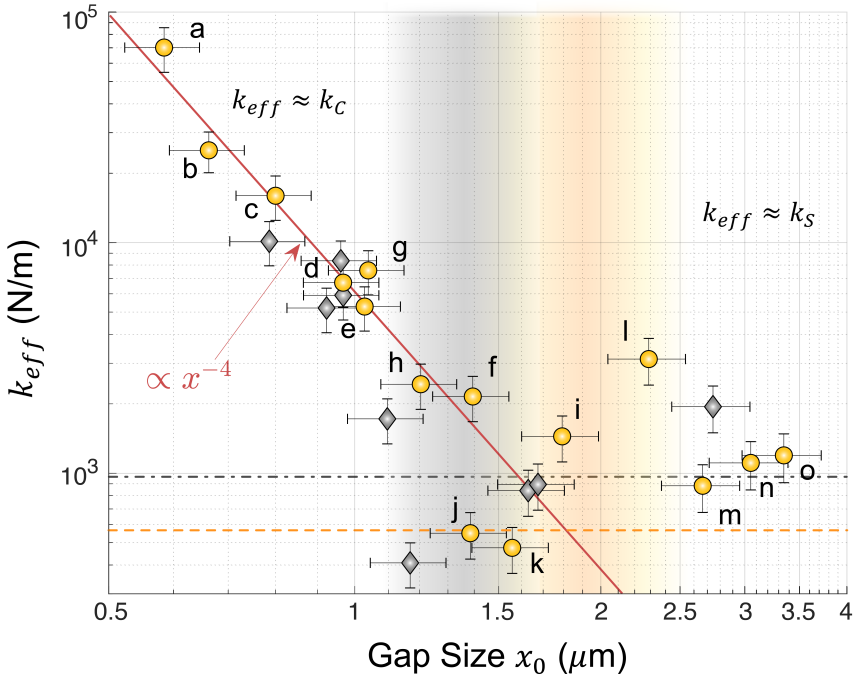


Figure 5.7: Thermal Casimir force graph showing effective static spring constant with inverse distance power law showing $x^{-4}$ for the gold membrane cavity (gold points) and niobium membrane cavity (gray points), corresponding to $x^{-3}$ in force. The dashed (orange) and dash-dotted (gray) flat lines represent the fundamental dynamical spring constant for the gold and niobium membranes respectively, as determined by the fundamental mode of the mechanical oscillator. The letters coincide with the lines in Fig. 5.6C. The gold and gray shaded regions embody the non-linear zones of the mechanical resonator for the gold and niobium membranes, respectively.

The dynamical response of the acoustic modes was also strongly modified due to the Casimir force. This is illustrated from measurements of the mechanical modes of

the membranes using two techniques. The first was by strongly driving the acoustic modes and observing the microwave mode hopping, and the second was through the measurements of the non-driven acoustic spectrum due to Nyquist thermal fluctuations.

Mode hopping effects were observed by measuring the response of the microwave resonance while applying to the external electrode a DC bias voltage, $V_{\mathrm{DC}}$, combined with an oscillating drive voltage, $V_{\mathrm{AC}}(\Omega)$, of frequency $\Omega/2\pi$. The membranes were electrically driven into motion at its acoustic mode frequency, $\Omega_m$, when $\Omega = \Omega_m$. Measurements were taken for a range of gap sizes and the maximum product of the two signals $F(\Omega) \propto V_{\mathrm{DC}}V_{\mathrm{AC}}(\Omega)$ was held constant to preserve a steady oscillating applied force. This was a very good approximation because the external electrode gap spacing was of the order 200 $\mu$m, so there was minimal change in the electrode gap over the dynamic range of the measurements.

Fig. 5.8 shows the behaviour of the microwave resonance as the gold membrane was electrically driven into motion at frequencies close to $\Omega_m/2\pi$. As shown in the insets (a)-(c), the resonance separates in two as the applied force increases. This is because the membrane oscillates much faster than the acquisition rate of the network analyzer and appears as a separation. We describe this separation as "mode hopping", which is distinct from normal-mode splitting. There are three distinct regions characterized by the position of the membrane as it is electrically driven [76]. In our configuration, the region at which the cavity displays the largest mode separation does not occur for the smallest gap size due to the presence of the Casimir force. The maximum separation reaches 1.88 GHz, which is 43% of the unperturbed cavity frequency at a gap size of $x_0 = 3.3 \pm 0.4$ $\mu$m. This data and the observation of mechanical bistability (see Fig. 5.10 below) are analogous to previous results of a micromechanical oscillator [78] by considering the gap size and the maximum frequency separation as a measure of oscillator amplitude.

The Casimir force tensioned the mechanical oscillator, making it stiffer so diminished microwave mode hopping was observed as shown in Fig. 5.8 inset A. This is because the gold membrane is in the pinned state. Conversely, we observed the lowest threshold of mode splitting due to $F(\Omega)$ around 3.5 GHz, shown in inset B, which is in the middle of the non-linear regime (even though the splitting is not maximum). This low threshold is a key sign that the mechanical oscillator is more susceptible to a small applied force and thus exhibits increased force sensitivity. An asymmetry is observed, shown in inset C, which is explained by considering the region of the Casimir force. The lower frequency branch represents a smaller value of $x$ and is thus perturbed more by the influence of the Casimir force compared to the higher frequency branch.

For the niobium membrane, we acquired the acoustic mode spectrum through the use of a microwave phase-bridge read-out circuit. In the demodulated microwave

spectrum, we distinguished the mechanical resonances from residual noise peaks by sweeping the frequency of $V_{\mathrm{AC}}(\Omega)$ on the external electrode and observing the modes which exhibited microwave mode hopping. The multitude of mechanical resonances were not as easily characterised or observed in the company of the Casimir force due to the pinned response. However, we observe driven microwave mode hopping for acoustic frequencies of 4.85 kHz, 10.44 kHz, 16.06 kHz, 21.66 kHz, and 27.29 kHz confirming they were membrane modes. Interestingly, these modes were not defined by the traditional modes of a clamped circular membrane. Under further investigation, we verified through finite element analysis that these resonances were radially-symmetric modes, pinned in the middle of the membrane, and justified by the frequency shifts in the acoustic spectrum as they transitioned into the Casimir force region. In contrast, as the gap size moved beyond the Casimir region ($\omega/2\pi > 2.8$ GHz), into the free state, the mechanical modes were confirmed to be well-defined by the expected frequencies of a clamped, circular membrane and identified in both the microwave and acoustic spectrum (see Fig. 5.12 below for data regarding the acoustic spectrum).

The discovery of the aforementioned effect has allowed us to utilise the Casimir force to strain engineer an acoustic membrane via dissipation dilution, enhancing the mechanical resonator $Q$-factor [27, 28]. This is illustrated in Fig. 5.9 by the niobium membrane shifting upwards in frequency while the acoustic $Q$-factor, $Q_m$, increases as the gap size becomes smaller for both (0,2) and (0,3) modes. The increased tension is non-contacting, which reduces clamping losses commonly seen in mechanical resonators. Initially, as the gap size became smaller and transitioned into the non-linear and Casimir regimes, the mechanical spring first softened and then hardened as the Casimir force increased, consistent with the microwave data taken for the static gap spacings. The mechanical modes also varied in quality factor between the pinned and free states. We have identified that $Q_m$ undergoes large swings in the non-linear shaded area. Outside of the non-linear region, $Q_m$ saturates to a single value for large gaps, but continues to increase under the influence of the Casimir force for small gaps. Considering the point of least stiffness there is an improvement in $Q_m$ by factors of 14.5 and 13.1 for the (0,2) and (0,3) modes, respectively. Moreover, the quality factor was improved by an order of magnitude beyond the bare membrane $Q_m$ for the (0,2) mode, and continues to rise for smaller displacements. Thus, $Q_m$ is expected to improve as a result of increased dilution if the gap size was further reduced. We were limited in our capability to measure smaller gaps, as in the pinned state our readout cavity is in proximity to a node of the acoustic mode shape. The addition of a second resonator sensing at the acoustic anti-node, but with a gap large enough to avoid pinning, would allow improved measurements at smaller gaps, and the possibility of measuring a higher $Q_m$.

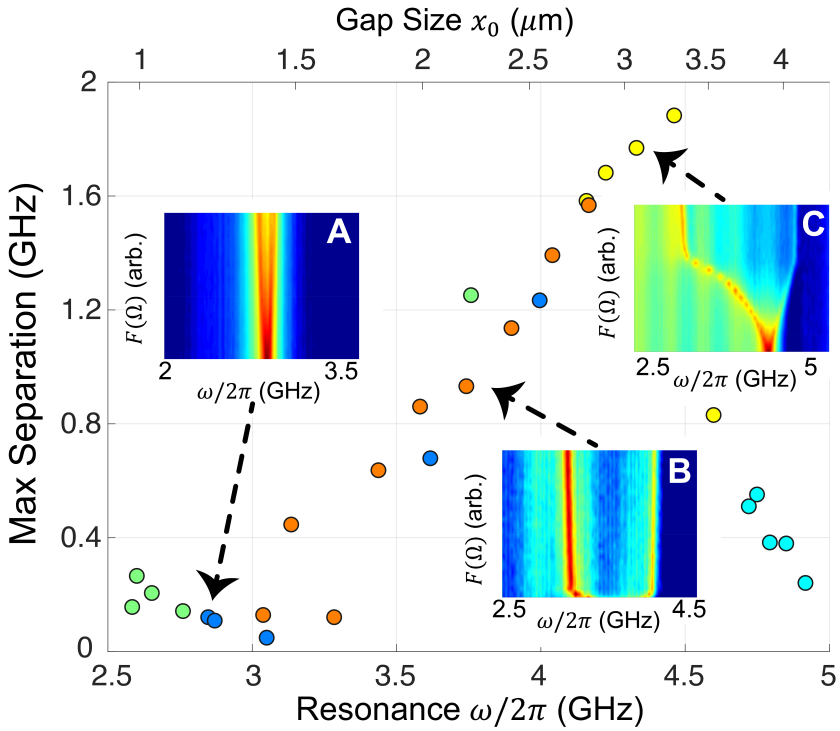


Figure 5.8: Five separate experimental runs of the gold membrane, showing the value of the maximum mode hopping separation of the driven microwave mode as a function of unperturbed microwave cavity frequency (lower $x$-axis label) or equivalent initial gap spacing (upper $x$-axis label). For every point the membrane experienced the same, maximum applied electrostatic force, $F(\Omega)$, and represents the maximum frequency separation between the two resonance peaks illustrated in the insets **A-C**. The insets display the microwave transmission (dB) of the cavity as the electrostatic force was increased, leading to mode separation in three distinct regions, **A** the Casimir dominated region, **B** the non-linear region and **C** outside the Casimir region.

Fig. 5.9 also shows good agreement of experimental data with the frequency shifts calculated from a COMSOL model of the membrane under the influence of the Casimir force, which is approximated as a variable-spring at the point below the re-entrant post. We chose a point spring to approximate the presence of the Casimir force because the ratio of re-entrant cone radius to cavity radius is only 1%. The lower arrows in both panels show the points of the (0,2) and (0,3) bare mode frequencies without a spring and the upper arrows are locations at which the mode frequency appeared to saturate for an arbitrarily-large spring (see Fig. 5.13). The inset images display the mode shapes for both pinned (Casimir) and free (non-Casimir) states.

In summary, we have tested the narrowest gap re-entrant microwave cavities coupled to a mechanical resonator to date and observed that the Casimir force gives rise to a plethora of interesting phenomena. For example, we have made the first observation of the Casimir spring and dilution effect in a macroscopic optomechanical system. The Casimir spring was observed by examination of the power law of the Casimir force as a function of gap size between the SiN metallic-coated membranes and a re-entrant post. This was possible because the re-entrant post formed a microwave cavity, which allowed self-calibration of the gap from the readout of the microwave frequency. Casimir dilution was also witnessed from the creation of an effective non-contacting boundary condition due to the localisation of the Casimir force under the re-entrant post, pinning the movement of the membrane at that point. This caused the acoustic mode of the membrane to change from a "free" state to a "pinned" state as it transitioned into the Casimir region for small gaps. Mechanical frequency shifts occurred for all radially-symmetric modes during this transition, which also increased the mechanical quality factor by over an order of magnitude as the Casimir force was increased. The transition of the mechanical modes from the traditional circular drum model, to a mode with a pinned boundary in the middle of the drum is in excellent agreement with finite-element simulations.

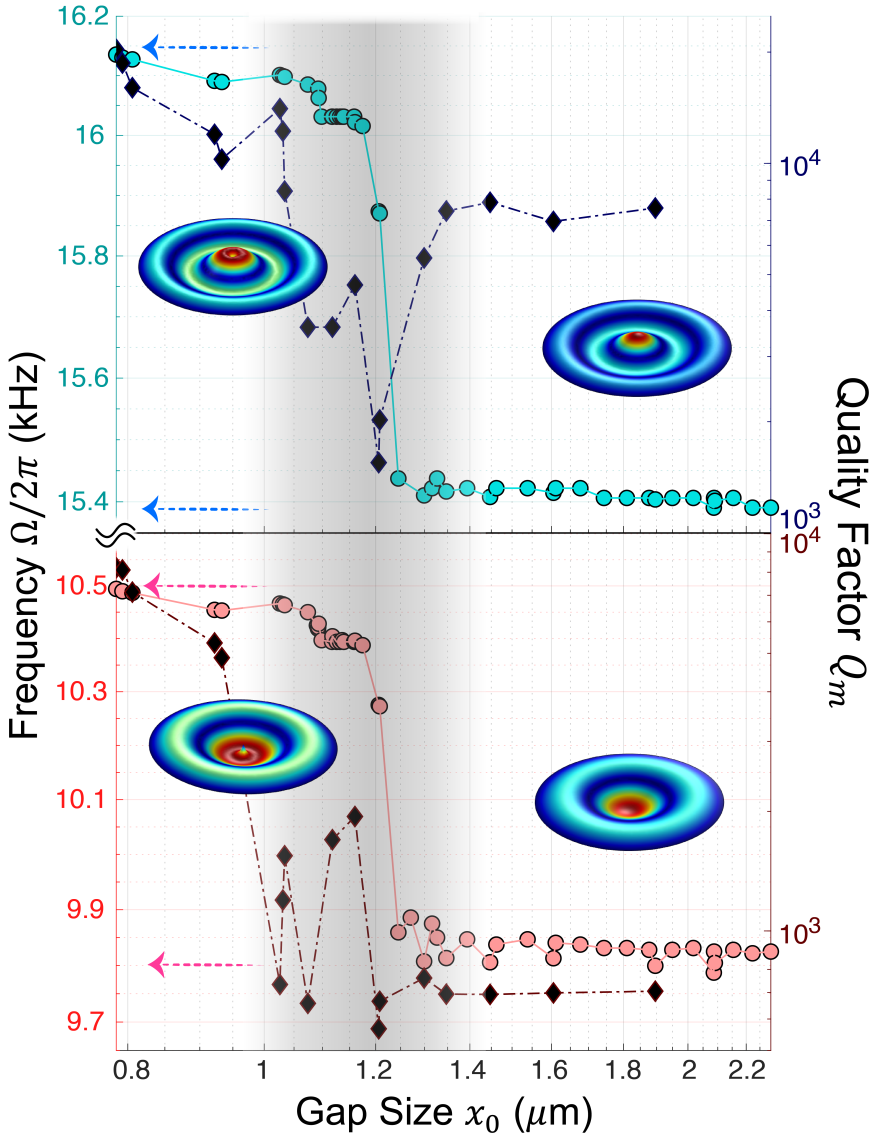


Figure 5.9: The effect of Casimir pinning and dilution on the (0,2) and (0,3) niobium membrane modes. The filled circles are the membrane frequencies and the filled diamonds are the corresponding mechanical quality factors. The inset images on the left show the pinning in the center of the modal structure which gives rise to the frequency shift. The inset images on the right show the mode in the free state, where the center is allowed to move. The lower arrows on both panels are the starting resonances from simulations for the (0,2) and (0,3) modes. The upper arrows for both graphs correspond to the frequency at which the simulated mode frequency saturate due to increased pinning force, in good agreement with the data. The shaded regions are areas of mechanical non-linearity, which divides the pinned state (on the left) and the free state (on the right).

The observation of a new way to engineer non-contacting dissipation dilution and boundary conditions creates a path forward to realise unique, topological mechanical oscillators while also increasing the acoustic $Q$-factor. We anticipate this effect will have a large impact on the field of cavity optomechanics and the hybrid integration of optical, electrical, and mechanical systems [9, 10, 28, 79]. For example, recently invented multiple post re-entrant cavities utilising posts and rings [39,73,80] could be coupled to an acoustic membrane in a similar way as described here. This would allow the manipulation of many degrees-of-freedom and the coupling of multiple photon resonances for membrane manipulation and readout. These systems could also in principle be configured to strongly couple the acoustic membrane to spin systems such as magnons [81,82] and defects in diamonds [83], as the multiple post re-entrant cavity has produced the strongest such couplings to date.

Furthermore, we established the existence of a very interesting non-linearity when the Casimir and membrane spring constant are of similar magnitude. Future work will further seek to explore this non-linear phenomena of the mechanical resonator and its relation to the thermal Casimir force [84, 85]. Moreover, this work could be developed for a system, which utilises the non-linearity generated by the thermal Casimir force to enhance force sensing [66,84]. Additional avenues for this particular research intersect with the active field of searching for the axion particle as well as a candidate for a possible fifth fundamental force [86, 87] because of our ability to transition in and out of the thermal Casimir regime.

## 5.3 Supplementary Methods

### 5.3.1 Mechanical Bistability

In conjunction with the microwave mode hopping presented in Fig. 3 of the main text, the bi-stability of the membrane was recorded in Fig. 5.10 through the observation of the microwave mode hopping. The bias voltage was kept fixed and the frequency of the acoustic drive $V_{\mathrm{AC}}$ was swept through the fundamental mechanical resonance of the gold membrane. The maximum frequency separation of the two modes was tracked as $V_{\mathrm{AC}}$ passed over the resonance and "traced" out the non-linear mechanical response.

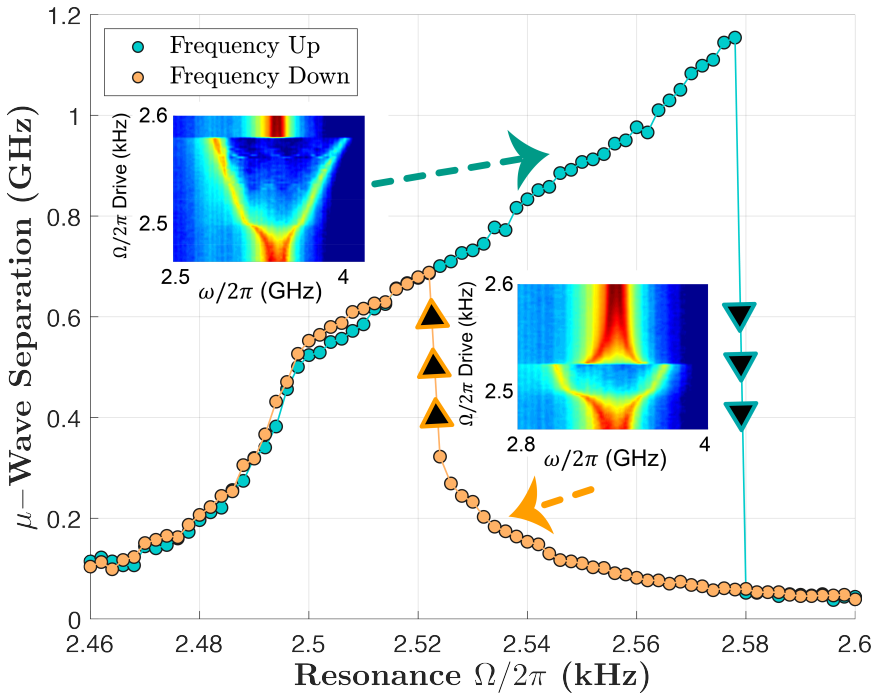


Figure 5.10: Mechanical bistability of the gold membrane observed using the strength of microwave mode hopping as $V_{\mathrm{AC}}$ was swept through the acoustic resonance. Both of the lines were acquired from the maximum separation distance of the two microwave resonances.

### 5.3.2 Niobium Membranes and Acoustic Response

Figure 5.11 shows the similar static Casimir spring experiments for the niobium membrane as was shown for the gold membrane in the main text. The cavity experienced a smaller transition between the pinned and free state when compared to the gold membrane, but occurred at a lower frequency of $\omega_c/2\pi \approx 2.8$ GHz. The reduced nonlinear transition at a lower microwave frequency can be explained by the fact that the niobium membrane was stiffer than the gold membrane, so the balance between the Casimir spring constant and the membrane spring constant occurred at a larger value and hence at a smaller value of the gap spacing.

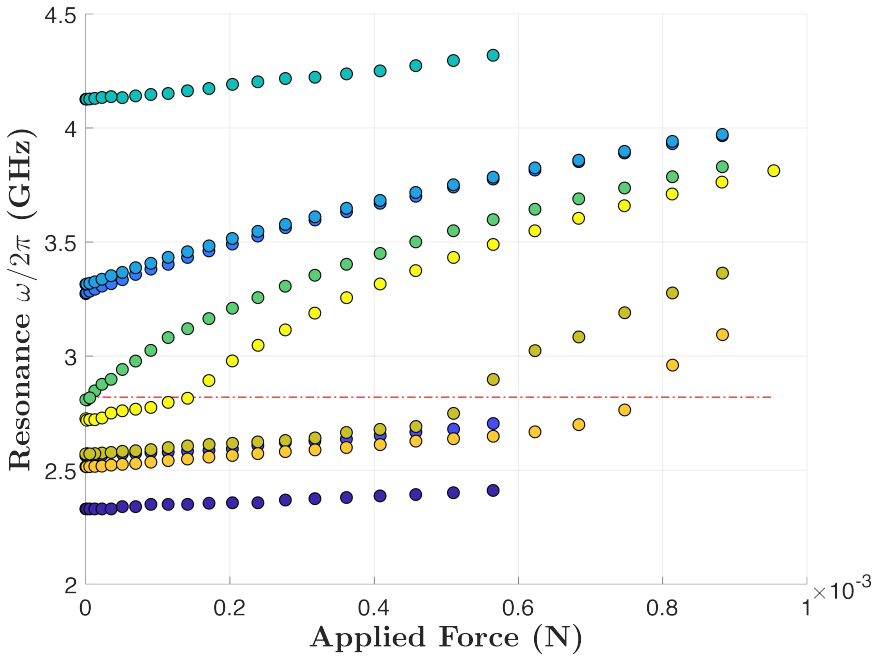


Figure 5.11: Similar Casimir spring behavior was observed with the niobium membrane cavities as was the case with the gold membrane cavities. Some of the curves do not extend to 250 V because the same voltage power supply was not available as the other curves that extend further. The red line represents a gap size of $x = 1.2$ $\mu$m and the point at which the frequency experiences a large shift.

The microwave phase-bridge circuit pictured in Fig. 3.10 allowed us to detect the phase modulation of the cavity resonance. The sensitivity of the phase-bridge circuit, $\frac{dV}{df}$, was measured using a known modulation when the phase bridge was tuned to the resonance frequency of the cavity. This was repeated at each point of the tuning that the acoustic quality factor and frequency were measured. The direct measurement of the sensitivity naturally accounted for changes in coupling and electromagnetic $Q$-factor of the microwave cavity, and any other variations in frequency response as the gap spacing was tuned.

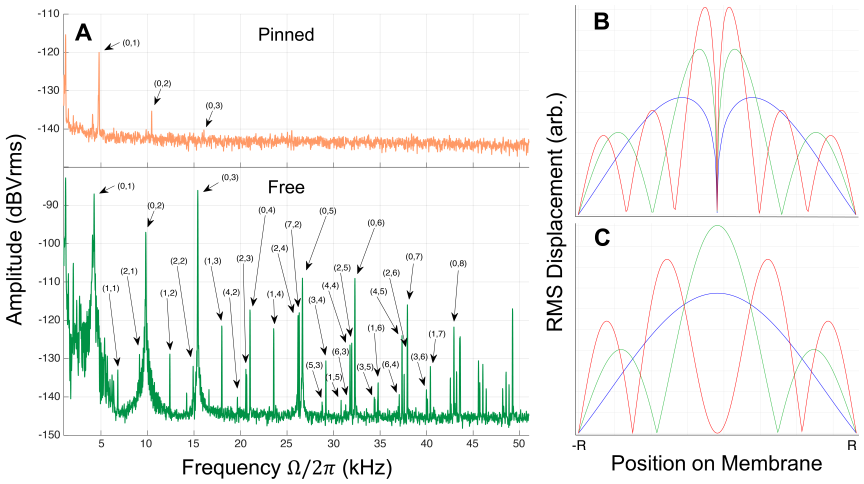


Figure 5.12: (**A**) Experimental results of the spectrum at the output of the microwave phase bridge in Fig. 3.10 for the niobium membrane for two different re-entrant cavity gap sizes, where the top orange curve is in the pinned state while the bottom green curve is in the free state. Here, the re-entrant cavity frequencies were measured to be $\omega_c/2\pi$=2.51 GHz ($x_0$ = 0.92 $\mu$m, orange) and $\omega_c/2\pi$=3.15 GHz ($x_0$ = 1.50 $\mu$m, green) respectively. (**B**) The mode displacement profile as modeled by COMSOL in the strongly-pinned state as a function of radial position for the (0,1), (0,2), and (0,3) modes of the membrane in blue, green, and red, respectively. (**C**) The same modes as modeled by COMSOL in the free state. Here, the re-entrant post was modeled to exist at the radial position equal to zero, equivalent to the real cavity implemented in experiments. Because the pinned state measurements were made at a displacement node, while in the free state measurements were made at a displacement anti-node, there is a large discrepancy in signal to noise ratio between the two measurements. For example, in the free state, some modes are 50 dB above the noise floor wherein for the pinned state only a few modes were detectible with significantly reduced sensitivity.

Fig. 5.12A shows the acoustic spectrum as measured by the phase bridge technique in the "free" state and "pinned" state. There was an increased signal amplitude (up to 50 dB for some modes), frequency shift, and appearance of additional circular drum modes as the membrane transitioned from the pinned into the free state. This was because in the pinned state, the microwave re-entrant cavity measured the acoustic mode near a node, while the free state was near an anti-node, as indicated in Fig. 5.12 B,C.

The modes of the niobium membrane were identified from the driven response of the membrane, that is, from the observation of microwave mode hopping. This

Table 5.1: Tabulated list of the experimental measured acoustic resonance modes of the niobium membrane in the pinned and free state, identified as acoustic modes using the microwave mode hopping technique. We only show measured modes of up to 27 kHz for the comparison, even though additional modes of up to 50 kHz were found when $\omega_c/2\pi \approx 3.15$ GHz. The resonances in parentheses were obtained with the COMSOL simulation for comparison with experimental results.

| $\omega_c/2\pi \approx 2.50$ GHz (Pinned), Measured Resonances $\Omega_m/2\pi$ (kHz) | $\omega_c/2\pi \approx 3.15$ GHz (Free), Measured Resonances $\Omega_m/2\pi$ (kHz) |
|---|---|
| 4.880 (4.851) | 4.141 |
| 10.442 (10.501) | 4.187 |
| 16.064 (16.150) | 4.258 |
| 21.661 (21.728) | 4.348 |
| 27.291 (27.478) | 4.480 |
| | 9.806 |
| | 9.890 |
| | 12.393 |
| | 12.550 |
| | 13.525 |
| | 14.921 |
| | 14.969 |
| | 15.421 |
| | 17.981 |
| | 18.207 |
| | 20.655 |
| | 21.043 |
| | 23.560 |
| | 23.871 |
| | 26.185 |
| | 26.300 |
| | 26.690 |

allowed us to distinguish between the real mechanical modes and other forms of narrowband interference. The identified mode frequencies are documented in Table 5.1. There was a big difference in the acoustic spectrum for the two gap sizes with microwave resonance frequencies of 2.50 GHz (pinned state) and 3.15 GHz (free state). Only five modes of up to 27 kHz were observed due to the reduced sensitivity for

our configuration when in the pinned state. By modeling the membrane with COMSOL, we verified these to be radially-symmetric (0,1) to (0,5) modes. The COMSOL modeling revealed that under the influence of a strong Casimir force, each mode was shifted by an asymptotic amount in the limit of a large Casimir spring (see Fig. 5.13) $\Omega_{(0,n),\mathrm{cas}}/2\pi \rightarrow \Omega_{(0,n)}/2\pi + \delta_{(0,n)}$. This asymptotic approach is only a manifestation of the fact that the pinning site does not exceed the area of the re-entrant cone. The notation of $\Omega_{0,n}$ signifies that only the radially symmetric ($m = 0$) modes in the Casimir region were able to be observed.

A finite-element model in COMSOL was created to see if the Casimir modification to the membrane agrees with the observed mechanical frequency shifts during the transition from the free state to the pinned state for the (0,2) and (0,3) modes as shown in Fig. 5.13. The simplest approach was to model the Casimir pinning effect as a variable spring at the center point of the membrane. The power law curve of $x^{-4}$ from Fig. 2 of the main text was used to generate a conversion for $k_{eff} \Leftrightarrow x$ in the Casimir region to compare with the COMSOL simulations. The modeled COMSOL data was statically shifted up in effective spring value by identical amounts ($k_{\mathrm{COMSOL,eff}} = k_{\mathrm{COMSOL}} + 2350$) for both modes to see the same relative increase in effective spring constant due to the Casimir force. From here, the point at which the membrane frequencies deviated in the Casimir regime for both simulation and real data becomes easier to observe. Good agreement was found with the simulation and measurement for the transitional frequency shifts of the two modes. There appeared to be additional modes near the (0,1) mode fundamental frequency, perhaps global or coupled modes, that made the measurement of the frequency shift and determination of $Q_m$ more difficult, which was why the higher-order modes were chosen.

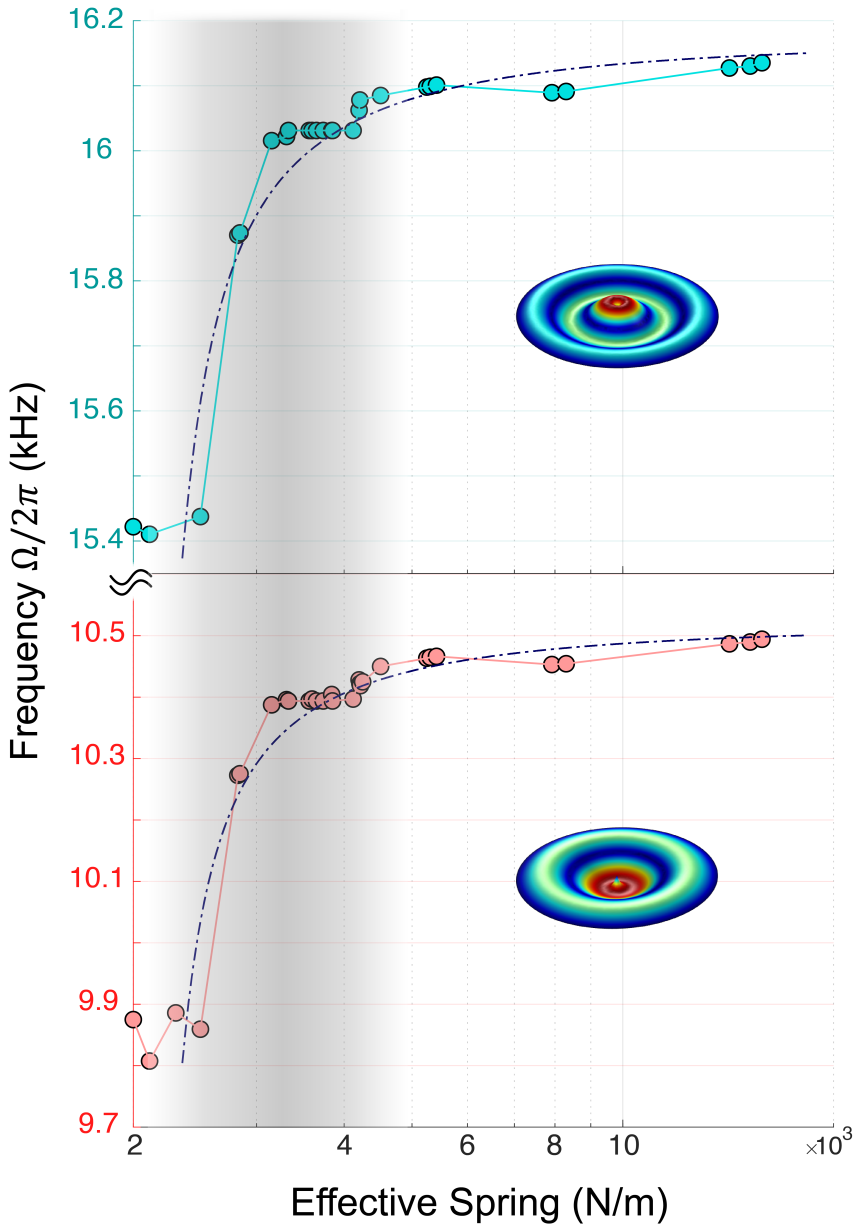


Figure 5.13: The mechanical resonance frequency shift for the niobium membrane as a function of effective spring. The black line represents the COMSOL model for a variable spring attached to the center of the membrane. The calculated resonance frequency shifts for both (0,3) (upper panel) and (0,2) (lower panel) modes agreed well with increased pinned tension. The shown inset images illustrate the pinned states of the membrane. The shaded region represent regions of non-linear behavior of the membrane.

# Chapter 6

# Outlook

*"If we did all the things we are capable of doing, we would literally astound ourselves."* – *Thomas Edison*

Cavity optomechanics remains an incredible platform for studying metrology, information technology, and quantum science with promising future applications in frequency conversion [8], photonic sources [16, 67], non-reciprocal devices [10], and much more. Optomechanics entails the interaction between radiation, photons, and vibrations, phonons, within a confined space. Future platforms are emerging known as hybrid systems in which multiple methods of coupling are assembled, such as an opto-electro-mechanical [9] system and can be used as an efficient mechanism for frequency conversion. As mechanical resonators continually evolve [13, 27, 28, 88] and electromagnetic cavities are enhanced [15, 44, 89, 90], an exciting new frontier of applied technology is about to unfold!

## 6.1 Summary

This work is best summarized as cavity prototyping and optimization in an attempt to see macroscopic cavity optomechanics, but has resulted in great experimental outcomes. The first of which was the complete ground-up development of a tunable superconducting system with a custom microphone circuit to detect mechanical oscillations in a SiN membrane. This gave rise to the implementation of lossless, non-contacting tunable superconducting cavities as well as a dynamic approach to manipulate the electromagnetic modes inside the cavity. Quality factors as high as $Q = 17$ million were reached with the large-scale membrane in the cylindrical geometry. Additionally, proper treatment (chemical etching, annealing, etc.) of the cavity in addition to a

good galvanic connection [91] (perhaps wire bonding) could result in drastic increases in $Q$. Calculations for our cylindrical geometry cavities put theoretical upper limits on $Q$ well above 1 billion. Therefore, there is great potential for increasing the cavity $Q$ with a cm-scale mechanical resonator.

The second important development originated in the attempt to create strongly-coupled (large $G$) microwave cavities and resulted in the creation of re-entrant microwave cavities. Eventually, we stumbled upon experimental evidence of the Casimir spring and dilution using the thermal (blackbody) Casimir force in the pursuit of extremely narrow-gap cavities. The aid of Dr. Tobar and Dr. Gorychev helped realize the theoretical understanding of the cavity response as a manifestation of the Casimir force at room temperature. This work demonstrated the capability to create artificial boundaries using increased (non-contacting) tension. The outcome of this work will evolve into creating arbitrary, re-configurable mechanical oscillators with increased mechanical quality factors $Q_m$ using the Casimir force as a non-contacting boundary.

## 6.2 Next Steps

Future graduate students would benefit from the investigation of two main experimental observations in this work that were not pursued in-depth either due to time restriction or a refocusing of efforts: 1) driven high-$Q$, coupled, superconducting cavities and undriven coupled microwave cavities in which the optomechanical effects are enhanced in comparison to single, non-resolved sideband cavities and 2) using the thermal Casimir force as a demonstration of the ability to create artificial resonators.

### 6.2.1 Coupled Cavities

In regards to the driven membrane-cavity system, it would be interesting to consider a double-cavity configuration. One of the initial goals was to construct a double-cavity system in which two cavities are electromagnetically separated by a membrane. If one cavity is capable of performing work on the membrane, it would be fascinating to observe the resulting physics on the second, unperturbed cavity. Experimental endeavors of this setup include: squeezing, microwave amplification by stimulated emission of radiation (MASER), and attempting to reach the standard quantum limit.

While the natural motion of a mechanical resonator and it's interaction with the electromagnetic field is a worthy pursuit, the driven membrane also provides a different experimental outcome such as active devices. For example, positioning two microwave resonances nearby in such a way that the scattered signal drives the mechanical resonator into motion could create phononic MASER-like action. Another such implementation could be stimulating the membrane itself and allowing the scattered microwave mode to be resonantly enhanced within a secondary, coupled cavity.

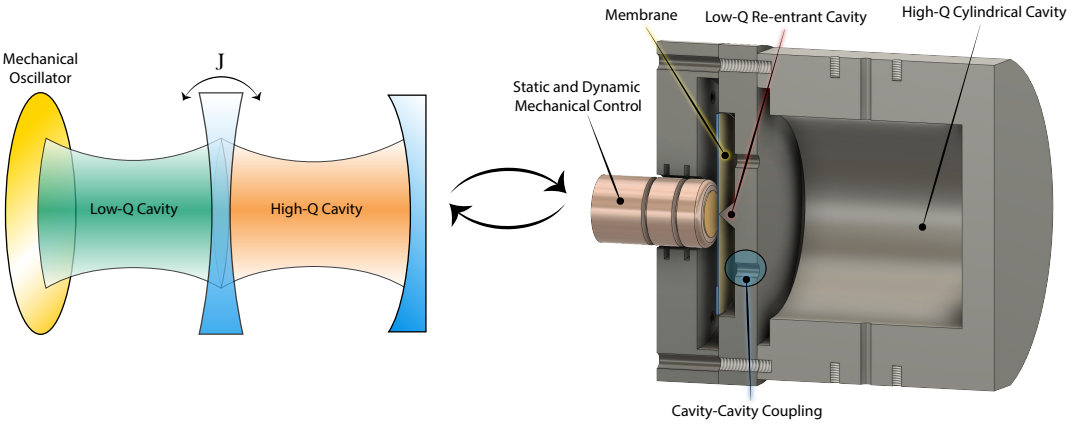


Figure 6.1: A coupled cavity example in which one cavity is coupled to the membrane and the second cavity couples subsequently to the first cavity. An example implementation of such a system is shown on the right-hand side involving a re-entrant and cylindrical cavity.

One such possibility for a room-temperature setup involving a strongly-coupled cavity and a high-$Q$ cavity is shown in Fig. 6.1. A re-entrant microwave cavity is coupled to a cylindrical cavity or even a sapphire whispering gallery mode (WGM) resonator cavity [92–94] for room temperature experiments, which can exhibit $Q$ on the order of several hundred thousand at room temperature and exceed 1 billion at cryogenic temperatures.

One of the challenges with the large mechanical resonators is the low resonance frequency. Often it is the amount of detuning from the cavity resonance or the regime in which the mechanical frequency is larger than the cavity bandwidth that cavity optomechanics starts to become noticeable (i.e. the resolved-sideband regime). Therefore, for the ease of incorporating macroscopic mechanical resonators within the electromagnetic cavity, a good choice of investigation would be to test bulk acoustic wave (BAW) resonators. Such resonators have a low effective mass for the modes in addition to their high frequency (MHz to GHz) and robust nature, which makes them suitable for integration within microwave cavities. Furthermore, many of the BAW devices are made of quartz, which is a piezoelectric material and makes them much easier to couple to the mechanical modes by applying a high-frequency AC voltage. One of the foreseeable challenges with integrating a re-entrant microwave cavity and a cylindrical cavity or WGM resonator is aligning the electromagnetic frequencies close together. Perhaps the higher-order re-entrant modes would be preferred in this situation with only slightly reduced coupling.

Additionally, coupled cavities with a mechanical resonator have been proposed

as a means to avoid the problem of requiring a sideband-resolved single cavity to observe optomechanical effects such as squeezing and cooling [95–97]. The general principle is that the interference of the two electromagnetic resonances creates a Fano-like lineshape in the spectrum, which is used as an artificial means to create a sideband-resolved system. In other words, with the interference dip there can be a large asymmetry between the two scattering rates $\Gamma_{\rm opt} = A_- - A_+ > 0$, which would not occur for a "bad" cavity. One such experiment that would benefit from this is sideband cooling a strongly-coupled mechanical resonator within a microwave re-entrant cavity.

### 6.2.2 Thermal Casimir Investigations

The next steps with the observation of the thermal Casimir force include a few new experiments: 1) create a second readout microwave post, 2) manipulate the mechanical resonator to create a new, artificial resonator, 3) create multiple-coupled resonators (resonator array) on a single membrane, and 4) inject microwave noise at cryogenic temperatures to stimulate the thermal (blackbody) Casimir effect.

The implementation of a second readout post (off-center) and out of the Casimir-regime is made to enhance the sensitivity of the microwave mode because of the main cavity post that acts to "pin" the membrane at the center. Therefore, this might allow the off-center structure of the membrane to oscillate more — much like the (0,2) mode of a circular drum. Under the influence of the central pin the thermal Casimir effect would act to reduce the sensitivity of the re-entrant cavity, which is observed as a reduction of the membrane thermal peak, whereas the off-center pin would simultaneously see an increase in the membrane thermal response.

The observation of an intentionally designed topological mechanical resonator using the thermal Casimir force would be an ambitious, yet rewarding project! In particular, the individual would have successfully manipulated the phonons using thermal blackbody photons to create a new mechanical structure for higher $Q$ and desired mode profile. The success of this experiment leads to the development of coupled mechanical resonators using the Casimir force. For example, creating two ring structures underneath the gold (niobium) membrane would allow the existence of two, higher frequency circular drums. Such configurations can lead to phonon-phonon coupling and mechanical bright/dark states.

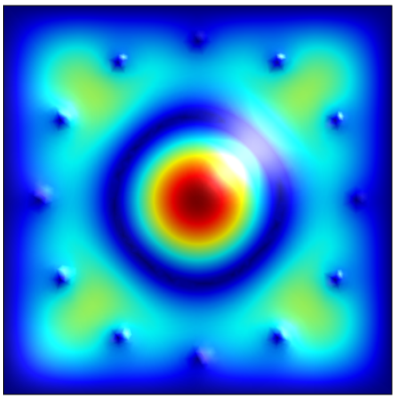

Figure 6.2: The square membrane is partially transformed into a circular membrane under the influence of twelve simulated posts in COMSOL. The mode shows signs of confinement within the post structure.

As an example, Fig. 6.2 shows a square membrane as modeled in COMSOL with twelve nearby posts that begin to show signs of a changing mode profile. If the posts were made to be a continuous structure (i.e. ring), the new mechanical resonator would be a circular drum — trapped within a square membrane! The mechanical resonance frequencies would increase as well as the quality factors with the strong pull of the thermal Casimir force (e.g. dilution).

The last example experiment would be the demonstration of the appearance of the thermal Casimir effect at cryogenic temperatures. Since the zero-temperature Casimir effect scales as $1/d^4$, it would be an incredible observation to develop a system that has sufficient gap size as not to see the Casimir effect at cryogenic temperatures, then inject microwave noise to witness the $1/d^3$ scaling of the thermal Casimir force appear. In this case, a force would appear that would (ideally) cause sufficient frequency shift and $Q$ increase to clearly demonstrate the appearance/disappearance of the thermal Casimir effect.

# Appendix A

# Rotating Wave Approximation

## A.1 Rotating Frame

In this section we explicitly solve the frequently-stated, but seldom demonstrated problem of the rotating wave approximation. The rotating-wave approximation can be viewed as moving in a frame at the same frequency of the dynamics of interest (which is near the cavity resonance) and assuming other higher order terms ($\omega \geq 2\omega_0$ or $\omega \ll \omega_0$) are so far off resonance that they do not contribute to the dynamics ($\omega_0 \equiv \omega_c$). For the reader, perhaps the best way to solve this problem algebraically is to consider the **Baker-Campbell Hausdorff theorem**. We would like to transform to a rotating frame that captures the physics around the resonance of interest:

$$H' \rightarrow U^\dagger H_{\text{old}} U - A \tag{A.1}$$

with

$$H = \hbar\omega_0 \hat{a}^\dagger \hat{a} + \hbar\Omega_m \hat{b}^\dagger \hat{b} + \hbar g_0 \hat{a}^\dagger \hat{a}(\hat{b}^\dagger + \hat{b}), \tag{A.2}$$

and

$$U = e^{-iAt/\hbar}, \quad A = \hbar\omega_\ell \hat{a}^\dagger \hat{a}. \tag{A.3}$$

This setup for the equation presents itself as $f(s) = e^{sA} B e^{-sA}$. The simplest approach to solving this problem is to just take a Taylor expansion,

$$f(s) = f(0) + f'(0)s + \frac{1}{2!} f''(0)s^2 + \cdots .$$

Using this information, the series expansion is represented as

$$\begin{aligned} f(0) &= H, \\ f' &= e^{iAt/\hbar}AHe^{-iAt/\hbar} - e^{iAt/\hbar}AHe^{-iAt/\hbar} = e^{iAt/\hbar}[A,H]e^{-iAt/\hbar}, \\ f'' &= e^{iAt/\hbar}A[A,H]e^{-iAt/\hbar} - e^{iAt/\hbar}[A,H]Ae^{-iAt/\hbar} = e^{iAt/\hbar}[A,[A,H]]e^{-iAt/\hbar}, \\ &\vdots \end{aligned}$$

From this point it's easy to show that $[A,H]=0$, therefore the equation simplifies to $H' = H - A$:

$$H' = -\hbar\Delta\hat{a}^\dagger\hat{a} + \hbar\Omega_m\hat{b}^\dagger\hat{b} + \hbar g_0\hat{a}^\dagger\hat{a}(\hat{b}^\dagger + \hat{b}), \tag{A.4}$$

where we have introduced the detuning parameter $\Delta \equiv \omega_\ell - \omega_0$. This is essentially very similar to the Baker-Campbell Hausdorff theorem:

$$e^A B e^{-A} = B + [A,B] + \frac{1}{2!}[A,[A,B]] + \cdots . \tag{A.5}$$

It may be too simplistic at first in looking at the Hamiltonian and the $\Delta$ term, but the exponential dependence of the rotating frame shows itself when one expands out the interaction Hamiltonian and throws away non-resonant terms such as $\hat{a}\hat{b}$ and $\hat{a}^\dagger\hat{b}^\dagger$. This is the **rotating-wave approximation**. Then, the leftover terms $\hat{a}\hat{b}^\dagger$ and $\hat{a}^\dagger\hat{b}$ will have the rotating frame dependence of $e^{-i(\omega_\ell \pm \Delta)t}$. An explicit example is given below regarding the intracavity field amplitudes.

Let us introduce the unitary operator $U(t) = e^{i\omega_\ell\hat{a}^\dagger\hat{a}t}$ that represents the frame we want to rotate into, in this case the laser frame at frequency $\omega_\ell$,

$$\begin{aligned} \hat{a}(t) &\to \hat{U}^\dagger\hat{a}\hat{U}, \\ &= \hat{a} + [i\omega_\ell\hat{a}^\dagger\hat{a}t, \hat{a}] + \frac{1}{2}[i\omega_\ell\hat{a}^\dagger\hat{a}t, [i\omega_\ell\hat{a}^\dagger\hat{a}t, \hat{a}]] + \cdots , \\ &= \hat{a} + (-i\omega_\ell t)\hat{a} + \frac{1}{2}(-1)^2(i^2)(\omega_\ell t)^2\hat{a} + \cdots , \\ &= ae^{-i\omega_\ell t}. \end{aligned}$$

### A.1.1 Alternative Method:

In a different approach, one can identify that if

$$B(\lambda) = e^{\lambda A}Be^{-\lambda A}, \tag{A.6}$$

then, under the condition that $B(\lambda)$ is central (i.e. commuting with both $B$ and $A$), one can write:

$$\dot{B}(\lambda) = [A, B].$$

Therefore, if $\hat{a}(t) = \hat{U}^\dagger \hat{a} \hat{U}$, then we can solve and integrate for the general solution:

$$\begin{aligned} \dot{a}(t) &= i\omega_\ell [\hat{a}^\dagger \hat{a}, \hat{a}] = -i\omega_\ell \hat{a}, \\ \Rightarrow \qquad \hat{a}(t) &= a e^{-i\omega_\ell t}. \end{aligned}$$

### A.1.2 Additional Methods:

One can look at the quantum mechanical state approach. Applying time-evolution via a unitary operator to a state, the transformed state can be derived as:

$$\begin{aligned} |\psi_R(t)\rangle &= e^{iH't/\hbar} |\psi(t)\rangle , \\ \Rightarrow i\hbar \frac{\partial}{\partial t} |\psi_R(t)\rangle &= i\hbar \frac{\partial}{\partial t} \left( e^{iH't/\hbar} |\psi(t)\rangle \right), \\ &= i\hbar \left( \frac{iH'}{\hbar} e^{iH't/\hbar} |\psi(t)\rangle + e^{iH't/\hbar} \frac{\partial}{\partial t} |\psi(t)\rangle \right), \\ &= -H' e^{iH't/\hbar} \underbrace{e^{-iH't/\hbar} |\psi_R(t)\rangle}_{|\psi(t)\rangle = e^{-iH't/\hbar}|\psi_R(t)\rangle} + e^{iH't/\hbar} \underbrace{H |\psi(t)\rangle}_{i\hbar\frac{\partial}{\partial t}|\psi\rangle = H|\psi\rangle} , \\ &= -H' |\psi_R(t)\rangle + e^{iH't/\hbar} H \underbrace{e^{-iH't/\hbar} |\psi_R(t)\rangle}_{\text{Again: } |\psi(t)\rangle = e^{-iH't/\hbar}|\psi_R(t)\rangle} , \\ &= \left[ e^{iH't/\hbar} H e^{-iH't/\hbar} - H' \right] |\psi_R(t)\rangle , \\ &= H_R |\psi_R(t)\rangle , \end{aligned}$$

where, $H_R$ has been identified as the new Hamiltonian in the rotating frame.

# Appendix B

# Intracavity Field Expressions

In this section we identify the expressions for the intracavity field to first order in a couple of various manners. The first is a simple perturbation approach while the second uses the Jacobi-Anger expansion. The goal behind this is to develop an expression that yields the familiar resonance-with-sidebands picture.

### B.0.3 Simple Perturbative Approach

For the simple, straightforward approach we shall start with the Heisenberg-Langevin equation of motion for the intracavity field,

$$\dot{\hat{a}}(t) = i(\Delta + G\hat{x})\hat{a}(t) - \frac{\kappa}{2}\hat{a}(t) + \sqrt{\kappa_{\rm ex}}\hat{a}_{\rm in} + \sqrt{\kappa_0}\hat{a}_{\rm vac}. \tag{B.1}$$

From here we will begin the perturbation analysis such that $a(t) = \sum_n \epsilon^n a_n(t)$ with $x(t) = \sum_n \epsilon^n x_n(t)$. This expansion yields $x(t) = x_0 + \epsilon x_1(t) + \ldots$ and we shall assume sinusoidal motion such that $x_1(t) = \cos(\Omega_m t)$. In addition, I will neglect the small vacuum fluctuation term:

$$\dot{a}_0(t) + \epsilon\dot{a}_1(t) = i\left(\Delta + G(x_0 + \epsilon x_1(t))\right)\left(a_0(t) + \epsilon a_1(t)\right) - \frac{\kappa}{2}(a_0(t) + \epsilon a_1(t)) + \sqrt{\kappa_{\rm ex}}a_{\rm in}.$$

We now equate similar powers of $\epsilon$ (to only first order),

$$\begin{aligned}
\dot{a}_0(t) &= \left(i\Delta - \frac{\kappa}{2}\right) a_0(t) + iGx_0 a_0(t) + \sqrt{\kappa_{\mathrm{ex}}} a_{\mathrm{in}}, \\
&= \left(i\Delta' - \frac{\kappa}{2}\right) a_0(t) + \sqrt{\kappa_{\mathrm{ex}}} a_{\mathrm{in}}(t), \\
\dot{a}_1(t) &= \left(i\Delta - \frac{\kappa}{2}\right) a_1(t) + iGx_0 a_1(t) + iGx_1(t) a_0(t), \\
&= \left(i\Delta' - \frac{\kappa}{2}\right) a_1(t) + iGx_1(t) a_0.
\end{aligned}$$

A new detuning term is defined $\Delta' \equiv \Delta + Gx_0$. Since there are no time-varying components for $a_0$ and $x_0$ is a constant, we know that $\dot{a}_0 = 0$, which leads to the familiar steady-state expression for the optical field:

$$a_0 = \frac{\sqrt{\kappa_{\mathrm{ex}}} a_{\mathrm{in}}}{-i\Delta' + \kappa/2}.$$

If we consider the modulus-square of the last term $n_c \approx |a_0|^2$, this gives the approximate intracavity photon number, neglecting the sidebands. Following along with the derivation, we take the Fourier transform of the equation of motion for the first-order perturbation,

$$-i\omega a_1(\omega) = \left(i\Delta' - \frac{\kappa}{2}\right) a_1(\omega) - iGx_1(\omega) a_0, \tag{B.2}$$

$$\Rightarrow a_1(\omega) = -\frac{iGx_1(\omega) a_0}{-i(\omega + \Delta') + \kappa/2}\ , \quad a_1^\dagger(\omega) = \frac{iGx_1(\omega) a_0^\dagger}{-i(\omega - \Delta') + \kappa/2}. \tag{B.3}$$

If one now looks at the intracavity field photon number to first order (recall $a(t) = a_0 + \epsilon a_1 + \cdots$), one has

$$n_c = |a(t)|^2, \tag{B.4}$$

$$= |a_0|^2 + a_0^\dagger a_1 + a_0 a_1^\dagger, \tag{B.5}$$

$$= |a_0|^2 + iGx_1(\omega)|a_0|^2 \left(\frac{1}{-i(\omega - \Delta') + \kappa/2} - \frac{1}{-i(\omega + \Delta') + \kappa/2}\right), \tag{B.6}$$

$$= |a_0|^2 \Bigg[1 + Gx_1(\omega) \left(\frac{\Delta' - \omega}{(\omega - \Delta')^2 + (\kappa/2)^2} + \frac{\Delta' + \omega}{(\omega + \Delta')^2 + (\kappa/2)^2}\right) \tag{B.7}$$

$$+ \frac{i\omega x_1(\omega) G}{\omega} \left(\frac{\kappa/2}{(\omega - \Delta')^2 + (\kappa/2)^2} - \frac{\kappa/2}{(\omega + \Delta')^2 + (\kappa/2)^2}\right)\Bigg]. \tag{B.8}$$

### B.0.4 Jacobi-Anger Expansion

A second, perhaps more elegant approach, is to consider Jacobi-Anger expansions [42, 44, 98, 99]. To start, we shall consider the equation of motion for the field inside the resonator without the rotating wave approximation (dropping hats for simplicity):

$$\dot{a}(t) = \left[i(-\omega_c + Gx(t)) - \frac{\kappa}{2}\right] a(t) + \sqrt{\kappa_{\text{ex}}} a_{\text{in}}(t), \tag{B.9}$$

$$= \left[i(-\omega_c + Gx_0 \sin(\Omega_m t)) - \frac{\kappa}{2}\right] a(t) + \sqrt{\kappa_{\text{ex}}} a_{\text{in}}(t). \tag{B.10}$$

The same expression was used before for sinusoidal motion of the membrane, $x(t) = x_0 \sin(\Omega_m t)$. The solution to this equation is $a(t) = a_p(t) + a_h(t)$. The homogenous solution can be solved by taking out the driving term and integrating the equation with the simple exponential form,

$$\dot{a}_h(t) = \left[i(-\omega_c + Gx_0 \sin(\Omega_m t)) - \frac{\kappa}{2}\right] a_h(t), \tag{B.11}$$

$$\Rightarrow \qquad a_h(t) \propto e^{\left(-i\omega_c - \frac{\kappa}{2}\right)t - \frac{iGx_0}{\Omega_m}\cos(\Omega_m t)}. \tag{B.12}$$

The mechanical component of the motion has also been integrated. Now to solve for the particular solution, we recognize that because $a_h$ is exponentially damped due to $\kappa/2$, as time goes to infinity the solution converges to $a(t) \to a_p(t)$. We assume an ansatz of the form $a(t) = a_p(t) = C(t)a_h(t)$. Therefore, $C(t) = a(t)/a_h(t)$ and the time derivative is now taken:

$$\begin{aligned}
\dot{C}(t) &= \frac{\dot{a}(t)a_h(t) - a(t)\dot{a}_h(t)}{a_h^2(t)}, \\
&= \frac{1}{a_h^2(t)} \Bigg\{ \left[i(-\omega_c + Gx_0 \sin(\Omega_m t)) - \frac{\kappa}{2}\right] a(t)a_h(t) + \sqrt{\kappa_{\text{ex}}} a_{\text{in}}(t) a_h(t) \\
&\quad - \left[i(-\omega_c + Gx_0 \sin(\Omega_m t)) - \frac{\kappa}{2}\right] a(t)a_h(t) \Bigg\}, \\
&= \frac{\sqrt{\kappa_{\text{ex}}} a_{\text{in}}(t)}{a_h(t)}, \\
&= \sqrt{\kappa_{\text{ex}}} \bar{a}_{\text{in}} e^{\left(-i\Delta + \frac{\kappa}{2}\right)t + \frac{iGx_0}{\Omega_m}\cos(\Omega_m t)}.
\end{aligned}$$

The detuning from cavity resonance was applied here with the driving term $a_{\text{in}}(t) = \bar{a}_{\text{in}} e^{-i\omega_\ell t}$ where $\Delta \equiv \omega_\ell - \omega_c$ as usual notation. If we make this equation look like a

Jacobi-Anger expression, we can immediately expand the solution:

$$e^{i\beta\cos\theta} = \sum_{\mathrm{n}=-\infty}^{\infty} i^{\mathrm{n}} J_{\mathrm{n}}(\beta) e^{i\mathrm{n}\theta}. \tag{B.13}$$

Then, by observation we have $\beta_m = \frac{x_0 G}{\Omega_m}$ and $\theta = \Omega_m t$,

$$\begin{aligned} \dot{C}(t) &= \sqrt{\kappa_{\mathrm{ex}}}\bar{a}_{\mathrm{in}} e^{\left(-i\Delta+\frac{\kappa}{2}\right)t} e^{\frac{iGx_0}{\Omega_m}\cos(\Omega_m t)}, \\ \Rightarrow \qquad C(t) &= \sqrt{\kappa_{\mathrm{ex}}}\bar{a}_{\mathrm{in}} e^{(-i\Delta+\kappa/2)t} \sum_{\mathrm{n}=-\infty}^{\infty} \frac{i^{\mathrm{n}} J_{\mathrm{n}}(\beta_m)}{-i(\Delta-\mathrm{n}\Omega_m)+\frac{\kappa}{2}} e^{i\mathrm{n}\Omega_m t}. \end{aligned}$$

The final solution is expressed as

$$a(t) = C(t)a_h(t) = \sqrt{\kappa_{\mathrm{ex}}}\bar{a}_{\mathrm{in}} \sum_{\mathrm{n}=-\infty}^{\infty} \frac{i^{\mathrm{n}} J_{\mathrm{n}}(\beta_m)}{-i(\Delta-\mathrm{n}\Omega_m)+\kappa/2} e^{-i(w_\ell-\mathrm{n}\Omega_m)t - i\beta_m\cos(\Omega_m t)}, \tag{B.14}$$

$$= \sqrt{\kappa_{\mathrm{ex}}}\bar{a}_{\mathrm{in}} \sum_{\mathrm{n,m}=-\infty}^{\infty} \frac{i^{\mathrm{n\text{-}m}} J_{\mathrm{m}}(\beta_m) J_{\mathrm{n}}(\beta_m)}{-i(\Delta-\mathrm{n}\Omega_m)+\kappa/2} e^{-iw_\ell t} e^{i(\mathrm{n}+\mathrm{m})\Omega_m t}. \tag{B.15}$$

Each term represents a mechanical sideband of the optical field at $\pm n\Omega_m$. This can be linearized for small modulation values of $\beta_m \ll 1$. For a simple back of the hand observation, let us assume the modulation in the cavity's frequency is much less than the mechanical resonance. To obtain an approximate expression of the solution[1] let's expand to first order (in frequency modulation $\pm\Omega_m$). As such, we will use $n = m = 0$

[1]The solution to the Bessel function is $J_\alpha(x) = \sum_{m=0}^{\infty} \frac{(-1)^m}{m!\Gamma(m+\alpha+1)}\left(\frac{x}{2}\right)^{2m+\alpha}$ where the gamma function is $\Gamma(n) = (n-1)!$. Another useful expression is $J_{-n}(x) = (-1)^n J(x)$. Also note the following was used $e^{-i\beta\cos\theta} = \sum_{\mathrm{n}=-\infty}^{\infty} i^{-\mathrm{n}} J_{\mathrm{n}}(\beta) e^{i\mathrm{n}\theta}$.

and $n, m = \pm 1$ for the series:

$$\begin{aligned}
J_0(\beta_m) &= \underbrace{\frac{1}{1}\Big(\frac{\beta_m}{2}\Big)^0}_{m=0} + \underbrace{\frac{-1}{1}\Big(\frac{\beta_m}{2}\Big)^2}_{m=1} + \underbrace{\frac{1}{4}\Big(\frac{\beta_m}{2}\Big)^4}_{m=2} + \cdots, \\
&= 1 - \frac{\beta_m^2}{4} + \frac{\beta_m^4}{64} + \cdots, \\
J_1(\beta_m) &= \underbrace{\frac{1}{1}\Big(\frac{\beta_m}{2}\Big)^1}_{m=0} + \underbrace{\frac{-1}{2}\Big(\frac{\beta_m}{2}\Big)^3}_{m=1} + \underbrace{\frac{1}{12}\Big(\frac{\beta_m}{2}\Big)^5}_{m=2} + \cdots, \\
&= \frac{\beta_m}{2} - \frac{\beta_m^3}{16} + \frac{\beta_m^5}{384} + \cdots.
\end{aligned}$$

Realistically, we are only considering the expansion for $J_0(\beta_m) \approx 1$ and $J_{\pm 1}(\beta_m) = \pm\beta_m/2$. Therefore, the expression now reads (for notation $a_{m,n}$)[2],

$$\begin{aligned}
a(t) = \sqrt{\kappa_{\text{ex}}}\bar{a}_{\text{in}}\Bigg\{ & \underbrace{\frac{J_0^2(\beta_m)e^{-i\omega_\ell t}}{-i\Delta + \kappa/2}}_{a_{0,0}} + \underbrace{\frac{iJ_1(\beta_m)J_0(\beta_m)e^{-i(\omega_\ell - \Omega_m)t}}{-i\Delta + \kappa/2}}_{a_{1,0}} \\
& - \underbrace{\frac{iJ_{-1}(\beta_m)J_0(\beta_m)e^{-i(\omega_\ell + \Omega_m)t}}{-i\Delta + \kappa/2}}_{a_{-1,0}} - \underbrace{\frac{iJ_0(\beta_m)J_1(\beta_m)e^{-i(\omega_\ell - \Omega_m)t}}{-i(\Delta - \Omega_m) + \kappa/2}}_{a_{0,1}} \\
& + \underbrace{\frac{i^{+1}J_0(\beta_m)J_{-1}(\beta_m)e^{-i(\omega_\ell + \Omega_m)t}}{-i(\Delta + \Omega_m) + \kappa/2}}_{a_{0,-1}}\Bigg\}, \\
= \sqrt{\kappa_{\text{ex}}}\bar{a}_{\text{in}}\Bigg\{ & \frac{J_0^2(\beta_m)e^{-i\omega_\ell t}}{-i\Delta + \kappa/2} + \left[\frac{iJ_1(\beta_m)J_0(\beta_m)}{-i\Delta + \kappa/2} - \frac{iJ_0(\beta_m)J_1(\beta_m)}{-i(\Delta - \Omega_m) + \kappa/2}\right]e^{-i(\omega_\ell - \Omega_m)t} \\
& + \left[-\frac{iJ_{-1}(\beta_m)J_0(\beta_m)}{-i\Delta + \kappa/2} + \frac{iJ_0(\beta_m)J_{-1}(\beta_m)}{-i(\Delta + \Omega_m) + \kappa/2}\right]e^{-i(\omega_\ell + \Omega_m)t}\Bigg\}.
\end{aligned}$$

As an aside, we can factor out a common factor to simplify things a bit:

$$\begin{aligned}
\frac{1}{-i\Delta + \kappa/2} - \frac{1}{-i(\Delta - \Omega_m) + \kappa/2} &= \frac{i\Delta - \kappa/2 - i(\Delta - \Omega_m) + \kappa/2}{(-i\Delta + \kappa/2)(-i(\Delta - \Omega_m) + \kappa/2)}, \\
&= \frac{i\Omega_m}{(-i\Delta + \kappa/2)(-i(\Delta - \Omega_m) + \kappa/2)}.
\end{aligned}$$

[2]Recall that $i^{-1} = -i$.

Now, re-writing and combining terms we arrive at the following equation:

$$a(t) = \sqrt{\kappa_{\rm ex}}\bar{a}_{\rm in}\Bigg\{\frac{e^{-i\omega_\ell t}}{-i\Delta+\kappa/2} + \frac{\Omega_m\beta_m/2}{-i\Delta+\kappa/2}\Bigg[\frac{e^{-i(\omega_\ell+\Omega_m)t}}{-i(\Delta+\Omega_m)+\kappa/2} \tag{B.16}$$

$$- \frac{e^{-i(\omega_\ell-\Omega_m)t}}{-i(\Delta-\Omega_m)+\kappa/2}\Bigg]\Bigg\}, \tag{B.17}$$

$$= \sqrt{\kappa_{\rm ex}}\bar{a}_{\rm in}\Bigg\{\frac{e^{-i\omega_\ell t}}{-i\Delta+\kappa/2} + \frac{x_0G}{2}\frac{1}{-i\Delta+\kappa/2}\Bigg[\frac{e^{-i(\omega_\ell+\Omega_m)t}}{-i(\Delta+\Omega_m)+\kappa/2} \tag{B.18}$$

$$- \frac{e^{-i(\omega_\ell-\Omega_m)t}}{-i(\Delta-\Omega_m)+\kappa/2}\Bigg]\Bigg\}. \tag{B.19}$$

Finally, the output field coming from the cavity is (recalling some input-output theory),

$$a_{\rm out}(t) = a_{\rm in}(t) - \sqrt{\kappa_{\rm ex}}a(t), \tag{B.20}$$

$$= \frac{-i\Delta+\kappa/2-\kappa_{\rm ex}}{-i\Delta+\kappa/2}\bar{a}_{\rm in}e^{-i\omega_\ell t} \tag{B.21}$$

$$\times\Bigg\{1+\frac{x_0G}{2}\Bigg[\underbrace{\frac{e^{-i\Omega_m t}}{-i(\Delta+\Omega_m)+\kappa/2}}_{a_{USB}} - \underbrace{\frac{e^{i\Omega_m t}}{-i(\Delta-\Omega_m)+\kappa/2}}_{a_{LSB}}\Bigg]\Bigg\}. \tag{B.22}$$

Note that this derivation can account for higher modulation values and it is likely the case that this method would need to be adopted to consider the large modulation that we saw during the cryogenic experiments in Chapter 4. The power (in photons per second) for upper and lower sidebands is easily identified from the expression as proportional to $|a_{USB}|^2$ and $|a_{LSB}|^2$ respectively.

# Appendix C

# Optomechanical Cooling Extended

The following will be a detailed derivation of the useful concepts related to cooling in the context of optomechanics [100]. In order to begin understanding the cooling rate for an oscillator, the expressions for the transitions must be derived from Fermi's Golden Rule (perturbation theory in quantum mechanics). To begin, we consider only the dynamics of the interaction picture, specifically the energy exchange between the bath and the system. The Schrödinger equation in the interaction picture can be represented as

$$i\hbar\frac{\partial}{\partial t}|\psi(t)\rangle_I = V_I(t)|\psi(t)\rangle_I. \tag{C.1}$$

We can relate the time evolution of the interaction state with $|\psi(t)\rangle_I = \hat{U}_I(t,t_0)|\psi(t_0)\rangle_I$ and plug into the Schrödinger above,

$$i\hbar\frac{\partial}{\partial t}\hat{U}_I(t,t_0)|\psi(t_0)\rangle_I = V_I(t)\hat{U}_I(t,t_0)|\psi(t_0)\rangle_I.$$

Since this equation must hold true for any state $|\psi(t_0)\rangle_I$:

$$i\hbar\frac{\partial}{\partial t}\hat{U}_I(t,t_0) = V_I(t)\hat{U}_I(t,t_0). \tag{C.2}$$

Now we integrate the LHS from $t_0$ to $t$ in order to arrive at,

$$i\hbar\int_{t_0}^{t} dt'\frac{\partial}{\partial t'}\hat{U}_I(t',t_0) = i\hbar(\hat{U}_I(t,t_0) - \mathbb{1}). \tag{C.3}$$

In this expression we used the boundary condition $\hat{U}_I(t_0,t_0) = \exp(-iH(t_0-t_0)/\hbar) = \mathbb{1}$. Insert this expression back into Eq. (C.2),

$$i\hbar(\hat{U}_I(t,t_0) - \mathbb{1}) = \int_{t_0}^{t} dt' V_I(t')\hat{U}_I(t',t_0), \tag{C.4}$$

$$\hat{U}_I(t,t_0) = \mathbb{1} - \frac{i}{\hbar}\int_{t_0}^{t} dt' V_I(t')\hat{U}_I(t',t_0). \tag{C.5}$$

Now is time for the iteration process to introduce the perturbation. Equation (C.5) is inserted back into itself:

$$\begin{aligned}\hat{U}_I(t,t_0) &= \mathbb{1} - \frac{i}{\hbar}\int_{t_0}^{t} dt' V_I(t')\Big[\mathbb{1} - \frac{i}{\hbar}\int_{t_0}^{t'} dt'' V_I(t'')\hat{U}_I(t'',t_0)\Big] + \cdots, \\ &= \mathbb{1} - \frac{i}{\hbar}\int_{t_0}^{t} dt' V_I(t') + \left(-\frac{i}{\hbar}\right)^2 \int_{t_0}^{t} dt' V_I(t') \int_{t_0}^{t'} dt'' V_I(t'')\hat{U}_I(t'',t_0) + \cdots.\end{aligned}$$

Hence, the iteration process can be summarized as

$$\hat{U}_I(t,t_0) = \sum_{n=0}^{\infty}\left(-\frac{i}{\hbar}\right)^n \int_{t_0}^{t} dt_1 \cdots \int_{t_0}^{t_{n-1}} dt_n V_I(t_1)\cdots V_I(t_n). \tag{C.6}$$

If the system is prepared in an initial state $|i\rangle$, then after some time $t$ the system will have evolved according to $\hat{U}_I(t,t_0)|i\rangle$. Then, insert a fancy factor of $\mathbb{1}$,

$$\hat{U}_I(t,t_0)|i\rangle = \sum_n |n\rangle \underbrace{\langle n|\hat{U}_I(t,t_0)|i\rangle}_{c_n(t)}. \tag{C.7}$$

In other words, $c_n(t)$ are the coefficients of the perturbation process ($c_n(t) = c_n^{(1)}(t) + c_n^{(2)}(t) + \cdots$),

$$c_n(t) = \delta_{ni} - \frac{i}{\hbar}\int_{t_0}^{t} dt' \langle n|V_I(t')|i\rangle - \frac{1}{\hbar^2}\int_{t_0}^{t} dt' \int_{t_0}^{t'} dt'' \langle n|V_I(t')V_I(t'')|i\rangle \hat{U}_I(t'',t_0) + \cdots, \tag{C.8}$$

$$= \delta_{ni} - \frac{i}{\hbar}\int_{t_0}^{t} dt' \langle n|V_I(t')|i\rangle - \frac{1}{\hbar^2}\int_{t_0}^{t} dt' \int_{t_0}^{t'} dt'' \sum_m \langle n|V_I(t')|m\rangle\langle m|V_I(t'')|i\rangle \hat{U}_I(t'',t_0) + \cdots. \tag{C.9}$$

Before this gets any uglier, recall that the interaction picture is defined as $V_I(t) =$

$e^{iHt/\hbar}V(t)e^{-iHt/\hbar}$ and therefore,

$$\begin{aligned}\langle n|V_I(t)|m\rangle &= \langle n|e^{iHt/\hbar}V(t)e^{-iHt/\hbar}|m\rangle,\\ &= \langle n|V(t)|m\rangle e^{i(E_n-E_m)/\hbar},\\ &= \langle n|V(t)|m\rangle e^{i\omega_{mn}t}.\end{aligned}$$

The term in the last line is defined $\omega_{mn} \equiv \frac{(E_n-E_m)}{\hbar}$. If the second-order perturbation is considered to be too small to include, then to first order correction

$$c_n^{(1)}(t) = -\frac{i}{\hbar}\int_{t_0}^{t} dt' e^{i\omega_{mn}t} V_{ni}(t'). \tag{C.10}$$

The state of the interaction picture will now be introduced as $|n,k\rangle$ denoting the oscillator state as $|n\rangle$ and the bath state as $|k\rangle$. The coefficient for a transition occurring from an initial state to a final state $P_{i\to n}(t) = |c_n^{(1)} + c_n^{(2)} + \cdots|^2$ assuming the oscillator begins in $|n\rangle$ and transitions to $|n+1\rangle$ as well as the bath going from $|j\rangle$ to $|k\rangle$ is

$$c_{i\to f}(t) = -\frac{i}{\hbar}\int_{t_0}^{t} dt' \langle n+1,k|\hat{V}_I(t')|n,j\rangle, \tag{C.11}$$

$$= -\frac{i}{\hbar}\int_{t_0}^{t} dt' e^{i\Omega t'} \langle n+1|\hat{q}_I|n\rangle\langle k|\hat{F}_I(t')|j\rangle, \tag{C.12}$$

$$= -\frac{ix_{\text{zpf}}}{\hbar}\int_{t_0}^{t} dt' e^{i\Omega t'} \langle n+1|a^\dagger + a|n\rangle\langle k|\hat{F}_I(t')|j\rangle, \tag{C.13}$$

$$= -\frac{ix_{\text{zpf}}\sqrt{n+1}}{\hbar}\int_{t_0}^{t} dt' e^{i\Omega t'} \langle k|\hat{F}_I(t')|j\rangle. \tag{C.14}$$

Since we are only interested in the state of the oscillator and unable to determine the state of the bath, we sum over all bath states for a given oscillator state. The

probability for the oscillator to transition from $|n\rangle$ to $|n+1\rangle$ is:

$$\begin{aligned}
P_{n\to n+1} &= \sum_k |A_{i\to f}(t)|^2, \\
&= \frac{x_{\text{zpf}}^2(n+1)}{\hbar^2}\int_{t_0}^{t}\int_{t_0}^{t'} dt'dt'' e^{i\Omega(t''-t')}\sum_k \underbrace{\langle j|\hat{F}_I(t')|k\rangle}_{F_I^\dagger(t')}\langle k|\hat{F}_I(t'')|j\rangle, \\
&= \frac{x_{\text{zpf}}^2(n+1)}{\hbar^2}\int_{t_0}^{t}\int_{t_0}^{t'} dt'dt'' e^{i\Omega(t''-t')}\langle \hat{F}_I(t')\hat{F}_I(t'')\rangle, \\
&= \frac{x_{\text{zpf}}^2(n+1)}{\hbar^2}\int_{t_0}^{t}\int_{t_0}^{t'} d\tau_1 d\tau_2 e^{i\Omega(\tau_2-\tau_1)}\langle \hat{F}_I(\tau_1)\hat{F}_I(\tau_2)\rangle.
\end{aligned}$$

For ease of readability and without loss of generality, the last line switched variables $t' \to \tau_1$ and $t'' \to \tau_2$. This probability expression assumes the force is Hermitian ($F^\dagger = F$). The expression is only valid for short time scales $P_{n\to n+1} \ll 1$ because it only considers the first order perturbation. The substitutions $\tau_1 = t' + \tau$ and $\tau_2 = t'$ are introduced here,

$$P_{n\to n+1} = \frac{x_{\text{zpf}}^2(n+1)}{\hbar^2}\int_0^t dt' \int_{-t'}^{t-t'} d\tau e^{-i\Omega\tau}\langle \hat{F}_I(t'+\tau)\hat{F}_I(\tau)\rangle, \tag{C.15}$$

$$= \frac{x_{\text{zpf}}^2(n+1)}{\hbar^2}\int_0^t dt' S_{FF}(-\Omega), \tag{C.16}$$

$$= \frac{x_{\text{zpf}}^2(n+1)}{\hbar^2} t S_{FF}(-\Omega). \tag{C.17}$$

The expression in the second line above results from the definition of the power spectral density for an arbitrary operator

$$S_{OO}(\omega) = \int_{-\infty}^{\infty} d\tau e^{i\omega\tau}\langle \hat{O}^\dagger(t+\tau)\hat{O}(t).$$

The time derivative of Eq. (C.17) yields the upwards transition rate:

$$\gamma_{n\to n+1} = \frac{x_{\text{zpf}}^2}{\hbar^2}(n+1)S_{FF}(-\Omega). \tag{C.18}$$

Similarly, for the downwards transition rate we arrive at,

$$\gamma_{n\to n+1} = \frac{x_{\text{zpf}}^2}{\hbar^2} n S_{FF}(\Omega). \tag{C.19}$$

Using Bose-Einstein statistics, the probability can be expressed as

$$p(n) = \exp\left(\frac{-\hbar\Omega n}{k_B T}\right)\left[1 - \exp\left(\frac{-\hbar\Omega}{k_B T}\right)\right], \tag{C.20}$$

whereas the average is shown to be

$$\bar{n} = \langle n \rangle = \sum n p_n = \left[\exp\left(\frac{\hbar\Omega}{k_B T}\right) - 1\right]^{-1}. \tag{C.21}$$

Therefore, the ratio of probabilities between $n+1$ and $n$ is:

$$\frac{p(n+1)}{p(n)} = \frac{\exp\left(-\frac{\hbar\Omega(n+1)}{k_B T}\right)}{\exp\left(-\frac{\hbar\Omega n}{k_B T}\right)} = \exp\left(-\frac{\hbar\Omega}{k_B T}\right). \tag{C.22}$$

Now, consider the transition probabilities in thermal equilibrium (known as a *detailed balance equation*):

$$\frac{p(n+1)}{p(n)} = \frac{\gamma_{n\to n+1}}{\gamma_{n+1\to n}} = \frac{S_{FF}(-\Omega)}{S_{FF}(\Omega)} = \exp\left(\frac{-\hbar\Omega}{k_B T}\right). \tag{C.23}$$

We have now arrived at an expression relating the power spectral densities and the mean phonon number:

$$\frac{S_{FF}(-\Omega)}{S_{FF}(\Omega)} = 1 + \frac{1}{\bar{n}}, \tag{C.24}$$

or perhaps solving for the mean phonon number,

$$\bar{n} = \frac{S_{FF}(-\Omega)}{S_{FF}(\Omega) - S_{FF}(-\Omega)}. \tag{C.25}$$

In addition, instead of substituting the exponential factor, but expanding it there is a nice relation involving the temperature of the mechanical oscillator;

$$T = \frac{\hbar\Omega}{k_B}\left[\ln\left(\frac{S_{FF}(\Omega)}{S_{FF}(-\Omega)}\right)\right]^{-1}. \tag{C.26}$$

Going back to the transition rates, define $\gamma_{n\to n+1} \equiv (n+1)\gamma_\uparrow$ and $\gamma_{n\to n-1} \equiv n\gamma_\downarrow$ so as to introduce the familiar optomechanical damping as

$$\Gamma_{\text{opt}} \equiv \gamma_\downarrow - \gamma_\uparrow = \frac{x_{\text{zpf}}^2}{\hbar^2}\left[S_{FF}(\Omega) - S_{FF}(-\Omega)\right]. \tag{C.27}$$

In order to get a better expression of the optomechanical damping, let us go back to the power spectral density. Consider the quantity

$$\begin{aligned}\frac{S_{FF}(\Omega)+S_{FF}(-\Omega)}{S_{FF}(\Omega)-S_{FF}(-\Omega)} &= \frac{\frac{S_{FF}(\Omega)}{S_{FF}(-\Omega)}+1}{\frac{S_{FF}(\Omega)}{S_{FF}(-\Omega)}-1},\\ &= \frac{1+\frac{1}{\bar{n}}+1}{1+\frac{1}{\bar{n}}-1},\\ &= \frac{2+\frac{1}{\bar{n}}}{\frac{1}{\bar{n}}},\\ &\equiv 2\bar{n}+1.\end{aligned}$$

In fact, the two quantities are generally taken to be a definition as displayed in the last step. Expanding the LHS and equating to the previous RHS yields [1]:

$$\begin{aligned}\frac{S_{FF}(\Omega)+S_{FF}(-\Omega)}{S_{FF}(\Omega)-S_{FF}(-\Omega)} &= \frac{2\bar{S}_{FF}(\Omega)}{\hbar^2\Gamma_m/x_{\text{zpf}}^2},\\ \frac{2\bar{S}_{FF}(\Omega)}{\hbar^2\Gamma_m/x_{\text{zpf}}^2} &= 2\bar{n}+1,\\ \bar{S}_{FF}(\Omega) &= \frac{\hbar^2\Gamma_m}{2x_{\text{zpf}}^2}(2\bar{n}+1),\\ \Rightarrow \bar{S}_{FF}^{\text{th}}(\Omega) &= m_{\text{eff}}\hbar\Omega\Gamma_m(2\bar{n}+1).\end{aligned}$$

Notice that in the limit of $k_BT \gg \hbar\Omega$, this result collapses to the classical thermal force power spectral density $\bar{S}_{FF}(\Omega) = 2\Gamma_m m k_B T$. In order to determine the minimum phonon occupancy for optomechanical cooling, we use the quantum backaction spectral density derived earlier in Eq. (C.27) and express the effective damping rate

[1] This expression is usually derived in considering the quantum thermal Langevin force $\delta F_{th} = m_{\text{eff}}\sqrt{\Gamma_m}\hat{\xi}_{th}(t)$ and then using the relationship for thermal noise operators $\left\langle \delta\hat{\xi}_{th}(\Omega)\delta\hat{\xi}^{\dagger}(\Omega')\right\rangle = 2\pi\delta(\Omega+\Omega')\hbar m_{\text{eff}}\Omega\left(\coth\left(\frac{\hbar\Omega}{2k_BT}\right)+1\right)$ to obtain the thermal power spectral density $S_{FF}^{th}(\Omega) = \int_{-\infty}^{\infty} e^{i\Omega t}\left\langle \delta\hat{\xi}(t+t')\delta\hat{\xi}(t)\right\rangle dt' = \left\langle \delta\hat{\xi}_{th}(\Omega)\delta\hat{\xi}^{\dagger}(\Omega')\right\rangle$. From here the symmetrised power spectral density is then computed. The symmetrised power spectral density is defined $\bar{S}_{OO}(\Omega) \equiv \frac{S_{OO}(\Omega)+S_{OO}(-\Omega)}{2}$.

as the following

$$\Gamma_{\text{eff}} = \Gamma_m + \Gamma_{\text{opt}}, \tag{C.28}$$

$$= \Gamma_m + \frac{x_{\text{zpf}}^2}{\hbar^2}\left[S_{FF}^{\text{qba}}(\Omega) - S_{FF}^{\text{qba}}(-\Omega)\right], \tag{C.29}$$

$$= \Gamma_m + \frac{x_{\text{zpf}}^2}{\hbar^2}\hbar^2 G^2 \bar{n}_{\text{cav}}\kappa\left[\frac{1}{(\bar{\Delta}+\Omega)^2+(\kappa/2)^2} - \frac{1}{(\bar{\Delta}-\Omega)^2+(\kappa/2)^2}\right], \tag{C.30}$$

$$= \Gamma_m + g_0^2\bar{a}^2\kappa\left[\frac{1}{(\bar{\Delta}+\Omega)^2+(\kappa/2)^2} - \frac{1}{(\bar{\Delta}-\Omega)^2+(\kappa/2)^2}\right], \tag{C.31}$$

$$= \Gamma_m + A_- - A_+. \tag{C.32}$$

In this previous expression we have defined the average number of intracavity photons as $n_{\text{cav}} \equiv \bar{a}^2$ and $\bar{\Delta} \equiv \Delta + G\bar{x}$ is the static displacement due to the average intracavity pump field. We also introduced the scattering rates

$$A_\pm = g_0^2\bar{a}^2\kappa\frac{1}{(\bar{\Delta}\mp\Omega)^2+(\kappa/2)^2}. \tag{C.33}$$

For optomechanical cooling, $A_\pm$ does not have the exact same definition as in the OMIT derivation (Appendix D), but does represent the Stokes' and anti-Stokes' scattering modes contributing to the cooling/heating of the oscillator. For cooling one would have $A_- > A_+$ and vice-versa for heating. Now with the new convenient definitions of the optomechanical damping as $\Gamma_{\text{opt}} = A_- - A_+$, the symmetrized quantum backaction spectral density is

$$\begin{aligned}\bar{S}_{FF}^{\text{qba}}(\Omega) \approx & \bar{S}_{FF}^{\text{qba}}(\Omega_m) \equiv \frac{S_{FF}^{\text{qba}}(\Omega) - S_{FF}^{\text{qba}}(-\Omega)}{2}, \\ & = m_{\text{eff}}\hbar\Omega_m(A_- + A_+).\end{aligned}$$

The approximation of $\Omega \approx \Omega_M$ was made as a means to linearize the mechanical susceptibility. The approach from here is to evaluate the displacement of the oscillator in terms of average energy and equate that to the average energy of a simple harmonic oscillator (using the equipartition theorem $\langle E\rangle = \langle E_{\text{kin}}\rangle + \langle E_{\text{pot}}\rangle = k_B T_{\text{eff}}$). For small

displacements of the oscillator,

$$\left\langle \delta\hat{x}^2 \right\rangle = \int_{-\infty}^{\infty} |\chi_{\rm eff}(\Omega)|^2 \left( S_{FF}^{\rm th}(\Omega) + S_{FF}^{\rm qba}(\Omega) \right) \frac{d\Omega}{2\pi}, \tag{C.34}$$

$$= 2\int_{0}^{\infty} |\chi_{\rm eff}(\Omega)|^2 \left( \bar{S}_{FF}^{\rm th}(\Omega) + \bar{S}_{FF}^{\rm qba}(\Omega) \right) \frac{d\Omega}{2\pi}, \tag{C.35}$$

$$= \left[ 2m_{\rm eff}\Gamma_m \left( \bar{n} + \frac{1}{2} \right) \hbar\Omega_m + \hbar m_{\rm eff}(A_- + A_+) \right] \int_{-\infty}^{\infty} |\chi_{\rm eff}(\Omega)|^2 \frac{d\Omega}{2\pi}, \tag{C.36}$$

$$= \frac{\left(\bar{n}_m + \frac{1}{2}\right)\hbar}{m_{\rm eff}\Omega_m} \left( \frac{\Gamma_m}{\Gamma_{\rm eff}} \right) + \frac{\hbar}{2m_{\rm eff}\Omega_m} \left( \frac{A_- + A_+}{\Gamma_{\rm eff}} \right). \tag{C.37}$$

In this integral, the effective mechanical susceptibility was found in Chapter 3.3 [42] to be

$$\chi_{\rm eff}(\Omega) = m_{\rm eff}^{-1} \left[ \left( \Omega_m^2 + \frac{\kappa_{\rm dba}(\Omega)}{m_{\rm eff}} \right) - \Omega^2 - i\left(\Gamma_m + \Gamma_{\rm dba}(\Omega)\right)\Omega \right]^{-1}.$$

Since $\langle E \rangle = m_{\rm eff}\Omega_m^2 \langle \delta\hat{x}^2 \rangle = \hbar\Omega_m \left(\bar{n} + \frac{1}{2}\right)$, we can write down the average phonon occupation

$$m_{\rm eff}\Omega_m^2 \left[ \frac{\left(\bar{n}_m + \frac{1}{2}\right)\hbar}{m_{\rm eff}\Omega_m} \left( \frac{\Gamma_m}{\Gamma_{\rm eff}} \right) + \frac{\hbar}{2m_{\rm eff}\Omega_m} \left( \frac{A_- + A_+}{\Gamma_{\rm eff}} \right) \right] = \hbar\Omega_m \left( \bar{n} + \frac{1}{2} \right), \tag{C.38}$$

$$\Gamma_m \left( \bar{n}_m + \frac{1}{2} \right) + \frac{A_- + A_+}{2} = \bar{n}\Gamma_{\rm eff} + \frac{1}{2}\Gamma_{\rm eff}, \tag{C.39}$$

$$\bar{n} = \frac{\bar{n}_m\Gamma_m + A_+}{\Gamma_{\rm eff}}. \tag{C.40}$$

For clarification, the term $\bar{n}_m$ as $\bar{n}_{\rm th}$ has been written slightly differently to make clear the Bose-Einstein distribution $\bar{n}_{\rm th} = (e^{\frac{\hbar\Omega_m}{k_B T}} - 1)^{-1}$. We re-express this equation for the steady-state thermal occupancy to represent a contribution to both normal damping and optomechanical damping:

$$\bar{n} = \frac{\bar{n}_{\rm th}\Gamma_m + A_+}{\Gamma_{\rm m} + \Gamma_{\rm opt}}, \tag{C.41}$$

$$= \frac{\bar{n}_{\rm th}\Gamma_m + \frac{x_{\rm zpf}^2}{\hbar^2} S_{FF}^{\rm qba}(-\Omega)}{\Gamma_{\rm m} + \Gamma_{\rm opt}}, \tag{C.42}$$

$$= \frac{\bar{n}_{\rm th}\Gamma_m + \bar{n}_{\rm c}\Gamma_{\rm opt}}{\Gamma_{\rm m} + \Gamma_{\rm opt}}. \tag{C.43}$$

This expression is essentially a weighted average of the mechanical and cavity phonon

occupancy. In the limit that $\Gamma_{\text{opt}} \gg \Gamma_m$, one can see that the mechanical occupation approaches the cavity occupancy. For a microwave cavity resonant at 10 GHz at a temperature of $T = 50$ mK, this corresponds to a cavity occupancy of roughly $n_c \approx 0.1$. Going back to Eq. (C.40), we can approximate the majority of the optomechanical cooling (for significant cooling) as arising from the sideband asymmetry rather than the intrinsic mechanical damping, i.e. $\Gamma_{\text{eff}} \gg \bar{n}_m \Gamma_m$. This approximation should make intuitive sense in that without the optomechanical cooling, none of the interesting physics occurs. Let us now derive the minimum achievable phonon occupancy for a single cavity under the influence of optomechanical cooling:

$$\bar{n}_{\min}(\bar{\Delta}) \approx \frac{A_+}{\Gamma_{\text{opt}}} = \frac{g_0^2 \bar{a}^2 \kappa \frac{1}{(\bar{\Delta}-\Omega_m)^2+(\kappa/2)^2}}{g_0^2 \bar{a}^2 \kappa \frac{1}{(\bar{\Delta}+\Omega_m)^2+(\kappa/2)^2} - g_0^2 \bar{a}^2 \kappa \frac{1}{(\bar{\Delta}-\Omega_m)^2+(\kappa/2)^2}}, \tag{C.44}$$

$$= \frac{(\bar{\Delta}+\Omega_m)^2 + (\kappa/2)^2}{(\bar{\Delta}-\Omega_m)^2 - (\bar{\Delta}+\Omega_m)^2}, \tag{C.45}$$

$$= -\frac{(\bar{\Delta}+\Omega_m)^2 + (\kappa/2)^2}{4\bar{\Delta}\Omega_m}. \tag{C.46}$$

To minimize the occupation number, we evaluate $\frac{d\bar{n}_{\min}}{d\bar{\Delta}} = 0$:

$$\frac{d\bar{n}_{\min}}{d\bar{\Delta}} = -\frac{1}{4\Omega_m}\left[\frac{2(\bar{\Delta}+\Omega_m)}{\bar{\Delta}} + \frac{(\bar{\Delta}+\Omega_m)^2 + \left(\frac{\kappa}{2}\right)^2}{\bar{\Delta}^2}\right] = 0, \tag{C.47}$$

$$\bar{\Delta} = \pm\sqrt{\Omega_m^2 + \left(\frac{\kappa}{2}\right)^2}. \tag{C.48}$$

In order to identify the correct solution, one takes the second derivative to determine concavity of the function:

$$\frac{d^2\bar{n}_{\min}}{d\bar{\Delta}^2} = \frac{d}{d\bar{\Delta}}\left\{-\frac{1}{4\Omega_m}\left[\frac{2(\bar{\Delta}+\Omega_m)}{\bar{\Delta}} + \frac{(\bar{\Delta}+\Omega_m)^2 + \left(\frac{\kappa}{2}\right)^2}{\bar{\Delta}^2}\right]\right\},$$

$$= -\frac{(\bar{\Delta}+\Omega_m)^2 + \left(\frac{\kappa}{2}\right)^2}{2\Omega_m\bar{\Delta}^3} + \frac{1}{2\bar{\Delta}^2}.$$

In order for this second derivative expression to be positive, therefore demonstrating a minimum, the negative solution for $\bar{\Delta}$ must be chosen due to the first term $-\frac{C}{\bar{\Delta}^3}$, where $C$ is a constant. So,

$$\bar{\Delta}_{\text{optimal}} = -\sqrt{\Omega_m^2 + \left(\frac{\kappa}{2}\right)^2}. \tag{C.49}$$

Using this expression, we continue with the evaluation of the minimum phonon occupancy:

$$\bar{n}_{\min}(\bar{\Delta}_{\text{optimal}}) = -\frac{\bar{\Delta}^2 + 2\bar{\Delta}\Omega_m + \Omega_m^2 + (\kappa/2)^2}{4\bar{\Delta}\Omega_m}, \tag{C.50}$$

$$= \frac{\Omega_m^2 + (\kappa/2)^2}{2\Omega_m\sqrt{\Omega_m^2 + \left(\frac{\kappa}{2}\right)^2}} - \frac{1}{2}, \tag{C.51}$$

$$= \frac{1}{2}\left(\sqrt{1 + \left(\frac{\kappa}{2\Omega_m}\right)^2} - 1\right). \tag{C.52}$$

If we are to assume we are within the resolved sideband regime such that $\Omega_m \gg \kappa$, then the expression can be reduced even further with the taylor expansion relation $(1+x)^\alpha = \sum_{n=0}^{\infty}\binom{\alpha}{n}x^n$, where $\binom{\alpha}{n} = \frac{\alpha!}{(\alpha-n)!n!}$:

$$\bar{n}_{\min}(\bar{\Delta}_{\text{optimal}}) \simeq \frac{1}{2}\left(1 + \frac{1}{2}\left(\frac{\kappa}{2\Omega_m}\right)^2 - 1\right) = \frac{\kappa^2}{16\Omega_m^2}. \tag{C.53}$$

In the same reasoning for a "bad" cavity with $\kappa \gg \Omega_m$ the minimum phonon occupancy due to optomechanical cooling is:

$$\bar{n}_{\min}(\bar{\Delta}_{\text{optimal}}) \simeq \frac{\kappa}{4\Omega_m}. \tag{C.54}$$

# Appendix D

# Optomechanically-Induced Transparency

Optomechanically-induced transparency (OMIT) is a phenomenon similar to EIT [101] in which a two-photon resonance condition gives rise to a window of transparency in the middle of an absorption spectrum. This can also be used to prevent transmission in the midst of a transmission measurement. The basic principle is that the weak probe and strong pump drive the mechanical oscillator at the beat frequency, which destructively interferes with the probe photons. OMIT has been proposed as a means to delaying, slowing light, and storing light for memory purposes [7]. We continue with some of the derivations done earlier in Chapter 3.3b,c, the two equations we now have are:

$$\dot{\delta a} = \left(i\bar{\Delta} - \frac{\kappa}{2}\right)\delta a + iG\bar{a}\delta x + \sqrt{\eta_c \kappa}\delta a_{\text{in}}, \tag{D.1}$$

$$\ddot{\delta x} + \Gamma_m \dot{\delta x} + \Omega_m^2 \delta x = \frac{\hbar G}{m_{\text{eff}}}\bar{a}(\delta a + \delta a^\dagger). \tag{D.2}$$

In order to solve these equations we will now "identify all operators with their expectation values since the drive fields are weak, but classically coherent" (i.e. $y(t) = \langle y(t) \rangle$). We assume an ansatz of the form

$$\delta a = A^- e^{-i\Omega t} + A^+ e^{+i\Omega t}, \tag{D.3a}$$

$$\delta a^* = (A^+)^* e^{-i\Omega t} + (A^-)^* e^{+i\Omega t}, \tag{D.3b}$$

$$\delta x = X e^{-i\Omega t} + X^* e^{+i\Omega t}. \tag{D.3c}$$

The variable $\Omega \equiv \omega_p - \omega_\ell$ represents detuning from the probe frequency (which should be centered upon the static cavity resonance frequency). For $+\Omega$, this implies the

anti-Stokes scattering mode (hence amplitude $A^-$) and vice-versa. I will derive two of the six equations that arrive from these solutions (only three are needed). Three equations arise from the frequencies at the probe ($e^{-i\Omega t}$) and the other sideband ($e^{i\Omega t}$). Inserting Eqs. D.3a and D.3c into Eq. D.1 and introducing $\delta a_{\text{in}} = a_p e^{-i\Omega t}$ and taking only the $e^{-i\Omega t}$ terms,

$$-i\Omega A^- e^{-i\Omega t} = \Big(i\bar{\Delta} - \frac{\kappa}{2}\Big)A^- e^{-i\Omega t} + iG\bar{a}Xe^{-i\Omega t} + \sqrt{\eta_c\kappa}a_p e^{-i\Omega t},$$
$$(-i(\bar{\Delta}+\Omega) + \kappa/2)A^- = iG\bar{a}X + \sqrt{\eta_c\kappa}a_p.$$

We also need to expand Eq. D.2,

$$-\Omega^2 X - i\Omega\Gamma_m X + \Omega_m^2 X = \frac{\hbar G\bar{a}}{m_{\text{eff}}}\Big((A^-) + (A^+)^*\Big),$$
$$\chi^{-1}X = \hbar G\bar{a}\Big((A^-) + (A^+)^*\Big).$$

The mechanical susceptibility is introduced at this point and familiarly defined as $\chi \equiv [m_{\text{eff}}(\Omega_m^2 - \Omega^2 - i\Omega\Gamma_m)]^{-1}$. Going through a similar derivation with the ansatz in Eq. D.3b and combining with the two previous equations we have:

$$(-i(\bar{\Delta}+\Omega) + \kappa/2)A^- = iG\bar{a}X + \sqrt{\eta_c\kappa}a_p, \tag{D.4}$$
$$(+i(\bar{\Delta}-\Omega) + \kappa/2)(A^+)^* = -iG\bar{a}X, \tag{D.5}$$
$$\chi^{-1}X = \hbar G\bar{a}\Big(A^- + (A^+)^*\Big). \tag{D.6}$$

Plug Eq. (D.5) into (D.6),

$$\chi^{-1}X = \hbar G\bar{a}\left(A^- + \frac{iG\bar{a}X}{i(\bar{\Delta}-\Omega)+\kappa/2)}\right),$$
$$(1 + if(\Omega))X = \hbar G\bar{a}\chi A^-.$$

We have defined (yet again) a new term only to make the math easier for writing, $f(\Omega) \equiv \frac{\hbar G^2\bar{a}^2\chi}{i(\bar{\Delta}-\Omega)+\kappa/2}$. Now insert Eq. (D.4) (in terms of $X$) into the last expression,

$$\frac{1+if(\Omega)}{iG\bar{a}}\Big[(-i(\bar{\Delta}+\Omega)+\kappa/2)A^- - \sqrt{\eta_c\kappa}a_p\Big] = \hbar G\bar{a}\chi A^-,$$
$$A^- = \frac{(1+if(\Omega))}{-i(\bar{\Delta}+\Omega)+\kappa/2+2\bar{\Delta}f(\Omega)}\sqrt{\eta_c\kappa}a_p.$$

If we are to consider the transmission of the probe amplitude signal, we need to utilize input-output theory [102]. The standard input-output relation of signals entering and

leaving a cavity is written as

$$a_{\rm out}(t) = a_{\rm in}(t) - \sqrt{\eta_c\kappa}a(t),$$
$$a_{\rm out}(t) = (a_{\rm in} - \sqrt{\eta_c\kappa}\bar{a})e^{-i\omega_c t} + (a_p - \sqrt{\eta_c\kappa}A^-)e^{-i(\omega_c+\Omega)t} - \sqrt{\eta_c\kappa}A^+e^{-i(\omega_c-\Omega)t}.$$

In the second line we have inserted the previous ansatz in full form as $a(t) = \bar{a} + A^-e^{-i\Omega t} + A^+e^{+i\Omega t}$. Looking at the exponential terms one can conclude the physical origin for each term. The first term in the output signal is the strong drive field, the second term is the probe field (input) and anti-Stokes scattering mode, and the last term is only the Stokes scattering mode because there is no input field at that frequency. The transmission of the probe field is the ratio of output signal to input signal at the probe frequency, then

$$t_p = \frac{a_{\rm p,out}}{a_{\rm p,in}}, \tag{D.7}$$
$$= 1 - \frac{\sqrt{\eta_c\kappa}A^-}{a_p}, \tag{D.8}$$
$$= 1 - \frac{(1 + if(\Omega))}{-i(\bar{\Delta} + \Omega) + \kappa/2 + 2\bar{\Delta}f(\Omega)}\eta_c\kappa. \tag{D.9}$$

The equations can be re-expressed if we "linearize" the mechanical susceptibility by introducing the variable $\Delta' = \Omega - \Omega_m$. By linearizing $\chi$, we assume the quantity $\Delta'$ is small and therefore $\Omega \approx \Omega_m$ simplifying the equation:

$$m_{\rm eff}(\Omega_m^2 - \Omega^2 - i\Gamma_m\Omega) = m_{\rm eff}\big[(\Omega_m + \Omega)(\Omega_m - \Omega) - i\Omega\Gamma_m\big],$$
$$= -m_{\rm eff}\Omega_m(2\Delta' + i\Gamma_m),$$

where we approximated that $\Delta'^2 \approx 0$. Therefore, we can now go back to Eqs. D.4, D.5, D.6 and obtain new expressions for the anti-Stokes scattering mode. In addition to the above simplification, we assume the system is within the resolved sideband regime $\Omega_m \gg \kappa$ and (in that case) the Stokes scattering mode is far off-resonance ($A^+ \approx 0$). Using this information,

$$(-i(\bar{\Delta} + \Delta' + \Omega_m) + \kappa/2)A^- = -iG\bar{a}X + \sqrt{\eta_c\kappa}a_p, \tag{D.10}$$
$$m_{\rm eff}\Omega_m(-2\Delta' - i\Gamma_m)X = -\hbar G\bar{a}A^-, \tag{D.11}$$

where we have our new equations. Now solve for the anti-Stokes field amplitude,

$$A^-(-i(\bar{\Delta}+\Delta'+\Omega_m)+\kappa/2) = -iG\bar{a}\frac{-\hbar G\bar{a}A^-}{m_{\text{eff}}\Omega_m(-2\Delta'-i\Gamma_m)} + \sqrt{\eta_c\kappa}a_p,$$
$$A^- = \frac{m_{\text{eff}}\Omega_m(-2\Delta'-i\Gamma_m)\sqrt{\eta_c\kappa}a_p}{m_{\text{eff}}\Omega_m(-2\Delta'-i\Gamma_m)(-i(\bar{\Delta}+\Delta'+\Omega_m)+\kappa/2)-i\hbar G^2\bar{a}^2},$$
$$A^- = \frac{\sqrt{\eta_c\kappa}a_p}{-i(\bar{\Delta}+\Delta'+\Omega_m)+\kappa/2+\frac{g_0^2\bar{a}^2}{(-i\Delta'+\Gamma_m/2)}},$$

where we have introduced $g_0 \equiv Gx_{\text{zpf}}$ and $x_{\text{zpf}} \equiv \sqrt{\frac{\hbar}{2m_{\text{eff}}\Omega_m}}$. If we detune the laser to be resonant with the static-shifted cavity resonance ($\bar{\Delta} = -\Omega_m$), then the anti-Stokes scattering mode (the probe field) is

$$A^- = \frac{\sqrt{\eta_c\kappa}a_p}{-i\Delta'+\kappa/2+\frac{g_0^2\bar{a}^2}{-i\Delta'+\Gamma_m/2}}. \tag{D.12}$$

The transmission of the probe field can be found again through the use of equation (D.9). The amplitude of the transmission signal is found via $|t_p|^2$. In order to simplify the expression further, we shall introduce a weak coupling approximation ($g \equiv g_0\alpha, \Gamma_m \ll \kappa$) as well as $i\Delta' + \kappa/2 \approx \kappa/2$. Therefore, rewriting the last expression,

$$A^- = \frac{\sqrt{\eta_c\kappa}a_p}{\kappa/2+\frac{g_0^2\bar{a}^2}{-i\Delta'+\Gamma_m/2}} \cdot \frac{2(-i\Delta'+\Gamma_m/2)}{2(-i\Delta'+\Gamma_m/2)},$$
$$= \frac{4(-i\Delta'+\Gamma_m/2)\sqrt{\eta_c\kappa}a_p}{2\kappa(-i\Delta'+\Gamma_m/2)+4g_0^2\bar{a}^2}.$$

Now, turning back to the transmission of the probe field, the expression is expanded:

$$t_p = 1 - \frac{\sqrt{\eta_c\kappa}A^-}{a_p},$$
$$= 1 - \frac{4\eta_c\kappa(-i\Delta'+\Gamma_m/2)}{2\kappa(-i\Delta'+\Gamma_m/2)+4g_0^2\bar{a}^2},$$
$$= 1 - 2\eta_c + \frac{8\eta_c g_0^2\bar{a}^2}{-2i\Delta'\kappa+\kappa\Gamma_m+4g_0^2\bar{a}^2}.$$

It is now useful to introduce a modified transmission that only takes into account

the spectrum of the probe field:

$$t_p' = \frac{t_p - t_r}{1 - t_r}.$$

Here, $t_r$ is the residual on-resonance transmission with no coupling laser (i.e. $t_r = t_p(\Delta' = 0, g_0\bar{a} = 0)$), which simply yields $t_r = 1 - 2\eta_c$. This means that the numerator corresponds to the total probe transmission (laser on) and the denominator is the total transmission (laser on). Weis et al. [7] mention this expression evaluates to saying that $\eta_c = \frac{1}{2}$ and leads to:

$$t_p' = \frac{4g_0^2\bar{a}^2}{-2i\Delta'\kappa + \kappa\Gamma_m + 4g_0^2\bar{a}^2},$$

with transmission (divide through my $\kappa$) as

$$|t_p'|^2 = \frac{16g_0^4\bar{a}^4/\kappa^2}{\underbrace{\left(\Gamma_m + 4g_0^2\bar{a}^2/\kappa\right)^2}_{\Gamma_{\text{OMIT}}} + (2\Delta')^2}.$$

The peak-value on-resonance ($\Delta' = 0$) transmission is:

$$|t_p'(\Delta' = 0)|^2 = \frac{16g_0^4\bar{a}^4/\kappa^2}{\left(\Gamma_m + 4g_0^2\bar{a}^2/\kappa\right)^2}. \tag{D.13}$$

For final simplifications, the optomechanical cooperativity is defined $C = C_0\bar{a}^2$, where $C_0 \equiv \frac{4g_0^2}{\kappa\Gamma_m}$ is the single photon cooperativity. Using this information the final OMIT expressions for the transparency window and transmission are:

$$\Gamma_{\text{OMIT}} = \Gamma_m(1 + C), \tag{D.14}$$

$$|t_p'(\Delta' = 0)|^2 = \left(\frac{C}{1 + C}\right)^2. \tag{D.15}$$

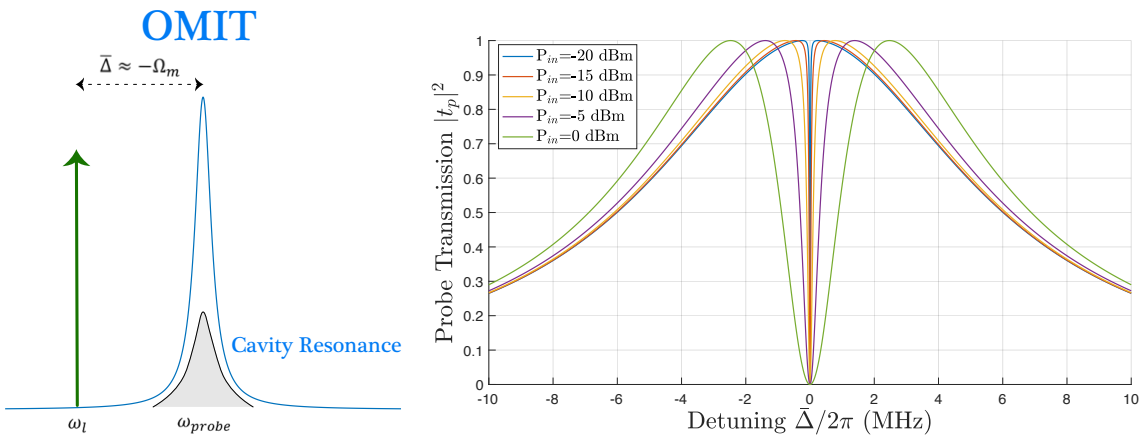


Figure D.1: Experimental approach (left) to observing OMIT. A stationary pump (denoted $\omega_\ell$) is placed approximately one mechanical frequency away and destructively interferes with the sweeping probe signal that gives rise to the graph on the right. Various pump powers can give rise to stronger transparency dips. Chosen parameters are within experimental feasibility using a re-entrant cavity and thin-film membrane with $G = 2$ GHz/$\mu$m, $m_{\text{eff}} = 100$ ng, $\Omega_m/2\pi = 100$ kHz, $\Gamma_m/2\pi = 1$ Hz, $\omega_0/2\pi = 3.5$ GHz.

# Appendix E

# Coupled Cavities

In this section we present the problem of two coupled cavities with one cavity connected to a mechanical oscillator. This derivation has been adapted from some theoretical papers proposing coupled cavity systems to enhance optomechanics [95–97, 103–105]. The motivation for this scheme is that a low-$Q$ cavity with a mechanical mode coupled to a high-$Q$ cavity will experience larger optomechanical effects than a single low-$Q$ optomechanical cavity. Let the reader note that this derivation considers any abstract geometry and therefore the notation is slightly different here regarding $g_0 = \frac{d\omega}{dx} x_{\mathrm{zpf}}$, which ultimately, does not have any meaningful difference because the negative sign can be absorbed by the derivative. We start with the Hamiltonian for two coupled cavities (denoted $J$) with one cavity coupled to a mechanical oscillator ($g_0$):

$$H = \underbrace{\hbar\omega_1 a_1^\dagger a_1 + \hbar\omega_2 a_2^\dagger a_2 + \hbar\Omega_m b^\dagger b}_{H_{\mathrm{free}}} + \underbrace{\hbar g_0 a_1^\dagger a_1 (b^\dagger + b)}_{H_{o-m}} + \underbrace{\hbar J a_1^\dagger a_2 + \hbar J^* a_2^\dagger a_1}_{H_{o-o}} \tag{E.1}$$

$$+ \underbrace{i\hbar\left(\Omega_1^* e^{i\omega_{\mathrm{in}}t} a_1 + \Omega_1 e^{-i\omega_{\mathrm{in}}t} a_1^\dagger\right) + i\hbar\left(\Omega_2^* e^{i\omega_{\mathrm{in}}t} a_2 + \Omega_2 e^{-i\omega_{\mathrm{in}}t} a_2^\dagger\right)}_{H_{\mathrm{drive}}}, \tag{E.2}$$

where $\Omega_i = \sqrt{\frac{\kappa_{i,ex} P_i}{\hbar\omega_{\mathrm{in}}}}$. The terms above represent (in order) the photons in each each, the phonons in the mechanical oscillator, the optomechanical coupling, the photon-photon coupling between cavities, and the driving laser. In the rotating frame at the laser driving frequency $a_{\mathrm{in}} = a_{\mathrm{in}} e^{i\omega_{\mathrm{in}}t}$ we can re-write the Hamiltonian in terms of the detuning:

$$\begin{aligned} H = &-\hbar\Delta_1 a_1^\dagger a_1 - \hbar\Delta_2 a_2^\dagger a_2 + \hbar\Omega_m b^\dagger b + \hbar g_0 a_1^\dagger a_1 (b^\dagger + b) + \hbar J a_1^\dagger a_2 + \hbar J^* a_2^\dagger a_1 \\ &+ i\hbar\left(\Omega_1^* a_1 + \Omega_1 a_1^\dagger\right) + i\hbar\left(\Omega_2^* a_2 + \Omega_2 a_2^\dagger\right). \end{aligned}$$

We have written the detunings for the $i^{th}$ cavity according to $\Delta_i = \omega_{\text{in}} - \omega_i$. Going through the standard approach of obtaining the Langevin equations via $\dot{a}_i = -\frac{i}{\hbar}[a, H]$ and introducing cavity loss and noise terms we write down,

$$\dot{a}_1 = \left(i\Delta_1 - \frac{\kappa_1}{2}\right) a_1 - ig_0 a_1(b^\dagger + b) - iJa_2 + \Omega_1 - \sqrt{\kappa_1}a_{\text{in},1}, \tag{E.3}$$

$$\dot{a}_2 = \left(i\Delta_2 - \frac{\kappa_2}{2}\right) a_2 - iJ^* a_1 + \Omega_2 - \sqrt{\kappa_2}a_{\text{in},2}, \tag{E.4}$$

$$\dot{b} = \left(-i\Omega_m - \frac{\gamma}{2}\right) b - ig_0 a_1^\dagger a_1 - \sqrt{\gamma}b_{\text{in}}. \tag{E.5}$$

Now we use a transformation such that there is a strong drive with some perturbations $a_1 = \alpha_1 + a_1$, $a_2 = \alpha_2 + a_2$, and $b = \beta + b$. By solving for the steady-state case first ($\dot{a} = 0$ and no noise), we can then plug in the solution for the dynamical equation afterwards:

$$\alpha_1 = \frac{iJ\alpha_2 - \Omega_1}{i\Delta_1' - \frac{\kappa_1}{2}},$$
$$\alpha_2 = \frac{iJ^*\alpha_1 - \Omega_2}{i\Delta_2 - \frac{\kappa_2}{2}},$$
$$\beta = \frac{ig_0\alpha_1^*\alpha_1}{-i\Omega_m - \frac{\gamma}{2}},$$

where $\Delta_1' = \Delta_1 - g_0(\beta^\dagger + \beta)$. Then, the dynamical equations become

$$\dot{a}_1 = \left(i\Delta' - \frac{\kappa_1}{2}\right) a_1 - ig_0(\alpha_1 + a_1)(b^\dagger + b) - iJa_2 - \sqrt{\kappa_1}a_{\text{in},1},$$
$$\dot{a}_2 = \left(i\Delta_2 - \frac{\kappa_2}{2}\right) a_2 - iJ^* a_1 - \sqrt{\kappa_2}a_{\text{in},2},$$
$$\dot{b} = \left(-i\Omega_m - \frac{\gamma}{2}\right) b - ig_0\left(\alpha_1^* a_1 + a_1^\dagger \alpha_1\right) - ig_0 a_1^\dagger a_1 - \sqrt{\gamma}b_{\text{in}}.$$

Under strong driving conditions, the nonlinear terms can be ignored $ig_0 a_1(b^\dagger + b)$ and $ig_0 a_1^\dagger a$ because they are considered small. Therefore, the final linearized Langevin equations take the form:

$$\dot{a}_1 = \left(i\Delta' - \frac{\kappa_1}{2}\right) a_1 - ig_0\alpha_1(b^\dagger + b) - iJa_2 - \sqrt{\kappa_1}a_{\text{in},1},$$
$$\dot{a}_2 = \left(i\Delta_2 - \frac{\kappa_2}{2}\right) a_2 - iJ^* a_1 - \sqrt{\kappa_2}a_{\text{in},2},$$
$$\dot{b} = \left(-i\Omega_m - \frac{\gamma}{2}\right) b - ig_0\left(\alpha_1^* a_1 + a_1^\dagger \alpha_1\right) - \sqrt{\gamma}b_{\text{in}}.$$

This form can be also be represented by the linearized Hamiltonian:

$$H_L = -i\hbar\Delta_1' a_1^\dagger a_1 - i\hbar\Delta_2 a_2^\dagger a_2 + \hbar g_0\left(\alpha_1 a_1^\dagger + \alpha_1^* a_1\right)(b^\dagger + b) + \hbar\left(J a_1^\dagger a_2 + J^* a_2^\dagger a_1\right).$$

The linearized optical force acting on the membrane can be derived from the linearized Hamiltonian:

$$F = -\frac{\partial H}{\partial x} = -\hbar G|a|^2, \tag{E.6}$$

$$= -\frac{\hbar g_0}{x_{zp}}(\alpha_1^* + a_1^\dagger)(\alpha_1 + a_1), \tag{E.7}$$

$$= -\frac{\hbar g_0}{x_{zp}}(\alpha_1^* a_1 + \alpha_1 a_1^\dagger), \tag{E.8}$$

$$= -\frac{\hbar}{x_{zp}}(g^* a_1 + g a_1^\dagger). \tag{E.9}$$

The multi-photon optomechanical coupling $g \equiv g_0\alpha$ has now been introduced. Now we will switch to the frequency domain via a Fourier transform ($F[\dot{a}(t)] = -i\omega a(\omega)$). The equations of motion can be re-written now (first for $a_2$):

$$a_2(\omega) = \frac{-iJ^* a_1(\omega) - \sqrt{\kappa_2}a_{\text{in},2}(\omega)}{-i(\omega + \Delta_2) + \frac{\kappa_2}{2}}, \tag{E.10}$$

$$= \chi_2(\omega)\left(-iJ^* a_1(\omega) - \sqrt{\kappa_2}a_{\text{in},2}(\omega)\right). \tag{E.11}$$

I have defined the cavity susceptibility for the $j$th cavity as $\chi_j(\omega) \equiv \left[-i(\omega + \Delta_j) + \frac{\kappa_j}{2}\right]^{-1}$. Using this information, we dive further into the math with the equation for $a_1(\omega)$:

$$-i\omega a_1(\omega) - \left(i\Delta_1' - \frac{\kappa_1}{2}\right)a_1(\omega) = -ig(b^\dagger(\omega) + b(\omega))$$
$$-iJ\left[\chi_2\left(-iJ^* a_1(\omega) - \sqrt{\kappa_2}a_{\text{in},2}(\omega)\right)\right] - \sqrt{\kappa_1}a_{\text{in},1}(\omega),$$
$$a_1(\omega) = \chi_1\left[-ig(b^\dagger(\omega) + b(\omega)) - iJ\chi_2(-iJ^* a_1(\omega) - \sqrt{\kappa_2}a_{\text{in},2}(\omega)) - \sqrt{\kappa_1}a_{\text{in},1}(\omega)\right],$$
$$\left(\chi_2|J|^2 + \frac{1}{\chi_1}\right)a_1 = -ig(b^\dagger(\omega) + b(\omega)) + iJ\chi_2\sqrt{\kappa_2}a_{\text{in},2}(\omega) - \sqrt{\kappa_1}a_{\text{in},1}(\omega),$$
$$a_1(\omega) = \chi\left[-ig(b^\dagger(\omega) + b(\omega)) + iJ\chi_2\sqrt{\kappa_2}a_{\text{in},2}(\omega) - \sqrt{\kappa_1}a_{\text{in},1}(\omega)\right].$$

The variable $\chi \equiv \left[\frac{1}{\chi_1} + |J|^2\chi_2\right]^{-1}$ has been defined to simplify the equations. Now, we can approach the equations for the mechanical mode. The roadmap of this derivation is to obtain all the expressions for the cavity and mechanical modes,

then solve for the quantum noise force power spectral density. The authors introduce the mechanical susceptibility in a similar manner to the cavity susceptibility $\chi_m(\omega) \equiv \left[-i(\omega - \Omega_m) + \frac{\gamma}{2}\right]^{-1}$ (rather than using mechanical equations of motion) and also has the property $[\chi(\omega)]^* = \chi^*(-\omega)$. We write the down the mechanical mode in the frequency domain (only keeping mechanical modes $b$ and not $b^\dagger$):

$$\begin{aligned} b(\omega) &= \chi_m \left[-ig^* a_1(\omega) - iga_1^\dagger(\omega) - \sqrt{\gamma} b_{\text{in}}(\omega)\right], \\ &= \chi_m \Big\{ -ig^*\chi \left[-igb + iJ\chi_2\sqrt{\kappa_2}a_{\text{in},2} - \sqrt{\kappa_1}a_{\text{in},1}\right] \\ &\qquad -ig\chi^* \left[ig^* b^\dagger - iJ^*\chi_2^*\sqrt{\kappa_2}a_{\text{in},2}^\dagger - \sqrt{\kappa_1}a_{\text{in},1}^\dagger\right] \Big\}, \\ = \chi_m \Big\{ &-|g|^2\chi(\omega)b + g^*(-\omega)J\chi(\omega)\chi_2(\omega)\sqrt{\kappa_2}a_{\text{in},2} + ig^*(-\omega)\chi(\omega)\sqrt{\kappa_1}a_{\text{in},1} \\ &+|g|^2\chi^*(-\omega)b - g\chi^*(-\omega)J^*(-\omega)\chi_2^*(-\omega)\sqrt{\kappa_2}a_{\text{in},2}^\dagger + ig\chi^*(-\omega)\sqrt{\kappa_1}a_{\text{in},1}^\dagger - \sqrt{\gamma}b_{\text{in}} \Big\}. \end{aligned}$$

Before this gets uglier, let's define some terms. Looking at the $\sqrt{\kappa_2}$ terms and assuming $J$ is real ($J^* = J$), let

$$A_2 \equiv J\left[g^*(-\omega)\chi(\omega)\chi_2(\omega)a_{\text{in},2} - g\chi^*(-\omega)\chi_2^*(-\omega)a_{\text{in},2}^\dagger\right]\sqrt{\kappa_2}. \tag{E.12}$$

Likewise, looking at the $\sqrt{\kappa_1}$ terms, we let

$$A_1 \equiv g^*(-\omega)\chi(\omega)a_{\text{in},1} + g\chi^*(-\omega)a_{\text{in},1}^\dagger. \tag{E.13}$$

Therefore, the mechanical mode is condensed in the following manner:

$$b(\omega) = \chi_m\left\{|g|^2\chi^*(-\omega)b(\omega) - |g|^2\chi(\omega)b(\omega) + \sqrt{\kappa_2}A_2 + i\sqrt{\kappa_1}A_1 - \sqrt{\gamma}b_{\text{in}}(\omega)\right\}.$$

Now we define a familiar term in the optomechanical community known as the "optomechanical self-energy":

$$\Sigma \equiv -i|g|^2\left(\chi(\omega) - \chi^*(-\omega)\right). \tag{E.14}$$

Continuing with the algebra and expanding the notation of the mechanical susceptibility:

$$\left(-i(\omega-\Omega_m)+\frac{\gamma}{2}+i\Sigma\right)b(\omega)=\sqrt{\kappa_2}A_2+i\sqrt{\kappa_1}A_1-\sqrt{\gamma}b_{\rm in},$$
$$b(\omega)=\frac{\sqrt{\gamma}b_{\rm in}(\omega)-i\sqrt{\kappa_1}A_1(\omega)-\sqrt{\kappa_2}A_2(\omega)}{i\omega-i(\Omega_m+\Sigma)-\frac{\gamma}{2}}.$$

Now let us turn our attention to the quantum noise force power spectral density given by

$$S_{FF}(\omega)=\int d\tau e^{i\omega\tau}\left\langle F(t+\tau)F(t)\right\rangle. \tag{E.15}$$

First, we note the following commutation relationships, which will help in analyzing the integral.

$$\left\langle a_{\rm in,1}(t)a^\dagger_{\rm in,1}(t')\right\rangle=\left\langle a_{\rm in,2}(t)a^\dagger_{\rm in,2}(t')\right\rangle=\delta(t-t'), \tag{E.16}$$
$$\left\langle a^\dagger_{\rm in,1}(t)a_{\rm in,1}(t')\right\rangle=\left\langle a^\dagger_{\rm in,2}(t)a_{\rm in,2}(t')\right\rangle=0, \tag{E.17}$$
$$\left\langle b_{\rm in}(t)b^\dagger_{\rm in}(t')\right\rangle=(n_{\rm th}+1)\delta(t-t'), \tag{E.18}$$
$$\left\langle b^\dagger_{\rm in}(t)b_{\rm in}(t')\right\rangle=n_{\rm th}\delta(t-t'). \tag{E.19}$$

These relations can be understood fairly well when considering an empty cavity $\left\langle a^\dagger a\right\rangle=0$. The general commutation relation reveals $[a,a^\dagger]=1$, which leads to $aa^\dagger=a^\dagger a+1$. Therefore, one can see where the extra factor comes from for an empty cavity and as well as the mechanical oscillator, which has a nonzero initial phonon occupation. For now, we assume a weak mechanical coupling to the optomechanical system so that the mechanical operators drop out of the equations. In addition, we only be keep the nonzero terms:

$$\begin{aligned}S_{FF}(\omega)&=\int_{-\infty}^{\infty}\left\langle F(\omega)F(\omega')\right\rangle\frac{d\omega'}{2\pi},\\&=\frac{1}{x_{\rm zp}^2}\int_{-\infty}^{\infty}\left\langle\left\{|g|^2|\chi(\omega)|^2|J|^2|\chi_2(\omega)|^2\kappa_2 a_{\rm in,2}(\omega)a^\dagger_{\rm in,2}(-\omega')\right.\right.\\&\qquad\left.\left.+|g|^2|\chi(\omega)|^2\kappa_1 a_{\rm in,1}(\omega)a^\dagger_{\rm in,1}(-\omega')\right\}\right\rangle\frac{d\omega}{2\pi},\\&=\frac{|g\chi|^2}{x_{\rm zp}^2}\left[\kappa_1+\kappa_2\left|J\chi_2(\omega)\right|^2\right].\end{aligned}$$

Now we shall obtain expressions that link the double cavity system to an effective

single cavity. This is basically saying we need the derive the interaction between the mechanical mode and high-$Q$ mode, known as the "Dark Mode." We begin with the time-domain equations:

$$\dot{a}_1(t) = \left(i\Delta_1' - \frac{\kappa_1}{2}\right) a_1(t) - ig_0\alpha_1\left(b^\dagger(t) + b(t)\right) - iJa_2(t) - \sqrt{\kappa_1}a_{\text{in},1}. \tag{E.20}$$

An integrating factor $u$ is chosen to solve the differential equation $u = e^{-\int\left(i\Delta_1' - \frac{\kappa_1}{2}\right)dt} = e^{-\left(i\Delta_1' - \frac{\kappa_1}{2}\right)t}$. Multiply through the entire equation for $a_1(t)$ by $u$ and then one recognizes the LHS as a single derivative, then integrate:

$$\begin{aligned}
\int_0^t \frac{d}{d\tau}\left[a_1(\tau)e^{-\left(i\Delta_1' - \frac{\kappa_1}{2}\right)\tau}\right]d\tau &= \int_0^t \Big[ - ig_0\alpha_1\left(b^\dagger(\tau) + b(\tau)\right) \\
&\quad - iJa_2(\tau) - \sqrt{\kappa_1}a_{\text{in},1}(\tau)\Big]e^{-\left(i\Delta_1' - \frac{\kappa_1}{2}\right)\tau}d\tau, \\
a_1(t) = a_1(0)e^{\left(i\Delta_1' - \frac{\kappa_1}{2}\right)t} &+ e^{\left(i\Delta_1' - \frac{\kappa_1}{2}\right)t}\int_0^t \Big[ - ig_0\alpha_1\left(b^\dagger(\tau) + b(\tau)\right) \\
&\quad - iJa_2(\tau) - \sqrt{\kappa_1}a_{\text{in},1}(\tau)\Big]e^{-\left(i\Delta_1' - \frac{\kappa_1}{2}\right)\tau}d\tau.
\end{aligned}$$

The same derivation can be used for the second cavity and the mechanical mode to obtain

$$a_2(t) = a_2(0)e^{\left(i\Delta_2 - \frac{\kappa_2}{2}\right)t} + \underbrace{e^{\left(i\Delta_2 - \frac{\kappa_2}{2}\right)t}\int_0^t d\tau\left[-iJ^*a_1(\tau) - \sqrt{\kappa_2}a_{\text{in},2}(\tau)\right]e^{-\left(i\Delta_2 - \frac{\kappa_2}{2}\right)\tau}}_{A_{\text{in},2}(t)}, \tag{E.21}$$

$$b(t) = b(0)e^{\left(-i\Omega_m - \frac{\gamma}{2}\right)t} + \underbrace{e^{\left(-i\Omega_m - \frac{\gamma}{2}\right)t}\int_0^t d\tau\left[-ig^*a_1(\tau) - iga_1^\dagger(\tau) - \sqrt{\gamma}b_{\text{in}}(\tau)\right]e^{\left(i\Omega_m + \frac{\gamma}{2}\right)\tau}}_{B_{\text{in}}(t)}, \tag{E.22}$$

where we have identified $A_{\text{in},2}(t)$ and $B_{\text{in}}(t)$ as additional noise terms. Now, we insert

the expressions in to $a_1(t)$ for an awful equation:

$$\begin{aligned} a_1(t) = a_1(0)e^{\left(i\Delta_1' - \frac{\kappa_1}{2}\right)t} + e^{\left(i\Delta_1' - \frac{\kappa_1}{2}\right)t}\int_0^t d\tau \Big\{ &- ig\left[b(0)e^{\left(-i\Omega_m - \frac{\gamma}{2}\right)\tau} + B_{\text{in}}(\tau)\right] \\ &- ig\left[b^\dagger(0)e^{\left(i\Omega_m + \frac{\gamma}{2}\right)\tau} + B_{\text{in}}^\dagger(\tau)\right] - iJ\left[a_2(0)e^{\left(i\Delta_2 - \frac{\kappa_2}{2}\right)t} + A_{\text{in},2}(\tau)\right] \\ &- \sqrt{\kappa_1}a_{\text{in},1}(\tau)\Big\} e^{\left(-i\Delta_1 + \frac{\kappa_1}{2}\right)\tau}. \end{aligned}$$

We shall now assume $\Delta_1 \gg \Delta_2$, $\kappa_1 \gg \kappa_2, \gamma$, which allows us to say the other terms have negligible contribution within the integral and can be effectively pulled out as constants.

$$\begin{aligned} a_1(t) &= a_1(0)e^{\left(i\Delta_1 - \frac{\kappa_1}{2}\right)t} + e^{\left(i\Delta_1 - \frac{\kappa_1}{2}\right)t}\left[ - ig\left(b^\dagger(t) + b(t)\right) - iJa_2(t) - \sqrt{\kappa_1}a_{\text{in},1}(t)\right] \\ &\times \left[\frac{1}{-i\Delta_1' + \frac{\kappa_1}{2}}e^{\left(-i\Delta_1' + \frac{\kappa_1}{2}\right)t} - \frac{1}{-i\Delta_1' + \frac{\kappa_1}{2}}\right], \\ &= a_1(0)e^{\left(i\Delta_1 - \frac{\kappa_1}{2}\right)t} + \left(\frac{1}{-i\Delta_1' + \frac{\kappa_1}{2}}\right)\left[ - ig\left(b^\dagger(t) + b(t)\right) - iJa_2(t) - \sqrt{\kappa_1}a_{\text{in},1}(t)\right] \\ &\underbrace{- \left(\frac{e^{\left(i\Delta_1 - \frac{\kappa_1}{2}\right)t}}{-i\Delta_1' + \frac{\kappa_1}{2}}\right)\left[ - ig\left(b^\dagger(t) + b(t)\right) - iJa_2(t) - \sqrt{\kappa_1}a_{\text{in},1}(t)\right]}_{\text{Decays Exponentially}}, \\ &\approx a_1(0)e^{\left(i\Delta_1 - \frac{\kappa_1}{2}\right)t} + \frac{-ig\left(b^\dagger(t) + b(t)\right)}{-i\Delta_1' + \frac{\kappa_1}{2}} - \frac{iJa_2(t)}{-i\Delta_1' + \frac{\kappa_1}{2}} + A_{\text{in},1}(t). \end{aligned}$$

One of the terms was ignored because it decays exponentially with the pre-factor of $\propto e^{-\kappa/2}$. In addition the noise term is represented by $A_{\text{in},1}$. This can be plugged into the expression for $\dot{a}_2(t)$:

$$\dot{a}_2(t) = \left(i\Delta_2 - \frac{\kappa_2}{2}\right)a_2(t) - iJ^*\left[\frac{-ig\left(b^\dagger(t) + b(t)\right)}{-i\Delta_1 + \frac{\kappa_1}{2}} - \frac{iJa_2(t)}{-i\Delta_1 + \frac{\kappa_1}{2}}\right. \tag{E.23}$$

$$\left. + a_1(0)e^{\left(i\Delta_1 - \frac{\kappa_1}{2}\right)t} + A_{\text{in},1}(t)\right] - \sqrt{\kappa_2}a_{\text{in},2}(t). \tag{E.24}$$

We can now identify the effective parameters by grouping $a_2$ and mechanical terms

and comparing with the single cavity case:

$$i\Delta_2 - \frac{i\Delta_1'|J|^2}{\Delta_1'^2 + \left(\frac{\kappa_1}{2}\right)^2} - \frac{\kappa_2}{2} - \frac{\kappa_1}{2}\frac{|J|^2}{\Delta_1'^2 + \left(\frac{\kappa_1}{2}\right)^2} \Leftrightarrow i\underbrace{(\Delta_2 - \eta^2\Delta_1')}_{\equiv\Delta_{\text{eff}}} - \frac{1}{2}\underbrace{(\kappa_2 + \eta^2\kappa_1)}_{\equiv\kappa_{\text{eff}}},$$
$$\left|\frac{J^* g}{i\Delta_1 - \frac{\kappa_1}{2}}\right| \Leftrightarrow |g_{\text{eff}}|.$$

The coupling term is defined:

$$\eta \equiv \frac{|J|}{\left(\Delta_1'^2 + \left(\frac{\kappa_1}{2}\right)^2\right)^{1/2}}, \tag{E.25}$$

which leads to $|g^{\text{eff}}| = \eta g$. Notice that for $\Delta_1' \gg \kappa_1 \rightarrow \eta \approx \left|\frac{J}{\Delta_1'}\right|$. This result leads to the effective quantum noise force power spectral density

$$S_{FF}^{\text{eff}}(\omega) = \frac{\kappa_{\text{eff}}|g_{\text{eff}}\chi_{\text{eff}}(\omega)|^2}{x_{\text{zp}}^2}, \tag{E.26}$$

where the effective susceptibility has been defined $\chi_{\text{eff}}(\omega) = \left[-i(\omega + \Delta_{\text{eff}}) + \frac{\kappa_{\text{eff}}}{2}\right]^{-1}$. Likewise, the effective optomechanical damping rate is expressed as

$$\Gamma_{\text{eff}} = \frac{4|g_{\text{eff}}|^2}{\kappa_{\text{eff}}}. \tag{E.27}$$

# Bibliography


[1] Johannes Kepler. 1619. de cometis libelli tres.

[2] The thing - great seal bug, June 2019.

[3] B ISECOM. *Hacking Exposed Linux: Linux Security Secrets and Solutions*. McGraw-Hill Pub., 2008.

[4] Benjamin P Abbott, Richard Abbott, TD Abbott, MR Abernathy, Fausto Acernese, Kendall Ackley, Carl Adams, Thomas Adams, Paolo Addesso, RX Adhikari, et al. Observation of gravitational waves from a binary black hole merger. *Physical review letters*, 116(6):061102, 2016.

[5] JD Teufel, Tobias Donner, Dale Li, JW Harlow, MS Allman, Katarina Cicak, AJ Sirois, Jed D Whittaker, KW Lehnert, and Raymond W Simmonds. Sideband cooling of micromechanical motion to the quantum ground state. *Nature*, 475(7356):359, 2011.

[6] Marc-Antoine Lemonde, Nicolas Didier, and Aashish A Clerk. Enhanced nonlinear interactions in quantum optomechanics via mechanical amplification. *Nature communications*, 7:11338, 2016.

[7] Stefan Weis, Rémi Rivière, Samuel Deléglise, Emanuel Gavartin, Olivier Arcizet, Albert Schliesser, and Tobias J Kippenberg. Optomechanically induced transparency. *Science*, 330(6010):1520–1523, 2010.

[8] Reed W Andrews, Robert W Peterson, Tom P Purdy, Katarina Cicak, Raymond W Simmonds, Cindy A Regal, and Konrad W Lehnert. Bidirectional and efficient conversion between microwave and optical light. *Nature Physics*, 10(4):321, 2014.

[9] Tolga Bagci, Anders Simonsen, Silvan Schmid, Luis G Villanueva, Emil Zeuthen, Jürgen Appel, Jacob M Taylor, A Sørensen, Koji Usami, Albert Schliesser, et al. Optical detection of radio waves through a nanomechanical transducer. *Nature*, 507(7490):81, 2014.

[10] Nathan Rafaël Bernier, Laszlo Daniel Toth, A Koottandavida, Marie Adrienne Ioannou, Daniel Malz, Andreas Nunnenkamp, AK Feofanov, and TJ Kippenberg. Nonreciprocal reconfigurable microwave optomechanical circuit. *Nature Communications*, 8(1):604, 2017.

[11] Martijn A Cohen, Daniel Bothner, Yaroslav M Blanter, and Gary A Steele. Optomechanical microwave amplification without mechanical amplification. *arXiv preprint arXiv:1812.05459*, 2018.

[12] Markus Aspelmeyer, Pierre Meystre, and Keith Schwab. Quantum optomechanics. *Physics Today*, 65(7):29–35, 2012.

[13] Mingyun Yuan, Martijn A Cohen, and Gary A Steele. Silicon nitride membrane resonators at millikelvin temperatures with quality factors exceeding 108. *Applied Physics Letters*, 107(26):263501, 2015.

[14] Mingyun Yuan, Vibhor Singh, Yaroslav M Blanter, and Gary A Steele. Large cooperativity and microkelvin cooling with a three-dimensional optomechanical cavity. *Nature communications*, 6:8491, 2015.

[15] Matthew Reagor, Wolfgang Pfaff, Christopher Axline, Reinier W Heeres, Nissim Ofek, Katrina Sliwa, Eric Holland, Chen Wang, Jacob Blumoff, Kevin Chou, et al. Quantum memory with millisecond coherence in circuit qed. *Physical Review B*, 94(1):014506, 2016.

[16] LD Tóth, NR Bernier, AK Feofanov, and TJ Kippenberg. A maser based on dynamical backaction on microwave light. *Physics Letters A*, 2017.

[17] Mohammad-Ali Miri and Andrea Alù. Coupled cavity optomechanical metawaveguides. *JOSA B*, 34(7):D68–D76, 2017.

[18] Christiaan Bekker, Rachpon Kalra, Christopher Baker, and Warwick P Bowen. Injection locking of an electro-optomechanical device. *Optica*, 4(10):1196–1204, 2017.

[19] D Lee, M Underwood, D Mason, AB Shkarin, SW Hoch, and JGE Harris. Multimode optomechanical dynamics in a cavity with avoided crossings. *Nature communications*, 6:6232, 2015.

[20] Patrick A Truitt, Jared B Hertzberg, CC Huang, Kamil L Ekinci, and Keith C Schwab. Efficient and sensitive capacitive readout of nanomechanical resonator arrays. *Nano letters*, 7(1):120–126, 2007.

[21] Michael Metcalfe. Applications of cavity optomechanics. *Applied Physics Reviews*, 1(3):031105, 2014.

[22] V Arbet-Engels, Cristoforo Benvenuti, S Calatroni, Pierre Darriulat, MA Peck, A-M Valente, and CA Van't Hof. Superconducting niobium cavities, a case for the film technology. *Nuclear Instruments and Methods in Physics Research Section A: Accelerators, Spectrometers, Detectors and Associated Equipment*, 463(1-2):1–8, 2001.

[23] Stefan Kuhr, Sébastien Gleyzes, Christine Guerlin, Julien Bernu, U Busk Hoff, Samuel Deléglise, Stefano Osnaghi, Michel Brune, J-M Raimond, Serge Haroche, et al. Ultrahigh finesse fabry-pérot superconducting resonator. *Applied Physics Letters*, 90(16):164101, 2007.

[24] Alexander Romanenko, Anna Grassellino, O Melnychuk, and DA Sergatskov. Dependence of the residual surface resistance of superconducting radio frequency cavities on the cooling dynamics around t c. *Journal of Applied Physics*, 115(18):184903, 2014.

[25] A Romanenko, A Grassellino, AC Crawford, DA Sergatskov, and O Melnychuk. Ultra-high quality factors in superconducting niobium cavities in ambient magnetic fields up to 190 mg. *Applied Physics Letters*, 105(23):234103, 2014.

[26] Atsushi Noguchi, Rekishu Yamazaki, Manabu Ataka, Hiroyuki Fujita, Yutaka Tabuchi, Toyofumi Ishikawa, Koji Usami, and Yasunobu Nakamura. Strong coupling in multimode quantum electromechanics. *arXiv preprint arXiv:1602.01554*, 2016.

[27] Yeghishe Tsaturyan, Andreas Barg, Eugene S Polzik, and Albert Schliesser. Ultracoherent nanomechanical resonators via soft clamping and dissipation dilution. *Nature Nanotechnology*, 12(8):776, 2017.

[28] Amir H Ghadimi, Sergey A Fedorov, Nils J Engelsen, Mohammad J Bereyhi, Ryan Schilling, Dalziel J Wilson, and Tobias J Kippenberg. Elastic strain engineering for ultralow mechanical dissipation. *Science*, 360(6390):764–768, 2018.

[29] Luis A Martinez, Alessandro R Castelli, William Delmas, Jay E Sharping, and Raymond Chiao. Electromagnetic coupling to centimeter-scale mechanical membrane resonators via rf cylindrical cavities. *New Journal of Physics*, 18(11):113015, 2016.

[30] Markus Aspelmeyer, Tobias J Kippenberg, and Florian Marquardt. Cavity optomechanics. *Reviews of Modern Physics*, 86(4):1391, 2014.

[31] Albert Schliesser, Pascal Del'Haye, Nima Nooshi, KJ Vahala, and TJ Kippenberg. Radiation pressure cooling of a micromechanical oscillator using dynamical backaction. *Physical Review Letters*, 97(24):243905, 2006.

[32] Albert Schliesser, Rémi Rivière, Georg Anetsberger, Olivier Arcizet, and Tobias J Kippenberg. Resolved-sideband cooling of a micromechanical oscillator. *Nature Physics*, 4(5):415, 2008.

[33] David M Pozar. *Microwave engineering*. John Wiley & Sons, 2009.

[34] Hasan Padamsee, Jens Knobloch, Tom Hays, et al. *RF superconductivity for accelerators*, volume 2011. Wiley Online Library, 2008.

[35] Tobias J Kippenberg and Kerry J Vahala. Cavity opto-mechanics. *Optics express*, 15(25):17172–17205, 2007.

[36] Jeremy Bourhill, Vincent Castel, Alexandre Manchec, and Gwendal Cochet. Spectroscopy of magnetic materials for universal characterisation of cavity-magnon polariton coupling strength. *arXiv preprint arXiv:1910.08333*, 2019.

[37] John Bardeen, Leon N Cooper, and John Robert Schrieffer. Theory of superconductivity. *Physical review*, 108(5):1175, 1957.

[38] Jean-Michel Le Floch, Yahoui Fan, Michel Aubourg, Dominique Cros, NC Carvalho, Q Shan, J Bourhill, EN Ivanov, Georges Humbert, Valérie Madrangeas, et al. Rigorous analysis of highly tunable cylindrical transverse magnetic mode re-entrant cavities. *Review of Scientific Instruments*, 84(12):125114, 2013.

[39] Y. Fan, Z. Zhang, N. C. Carvalho, J. Le Floch, Q. Shan, and M. E. Tobar. Investigation of higher order reentrant modes of a cylindrical reentrant-ring cavity resonator. *IEEE Transactions on Microwave Theory and Techniques*, 62(8):1657–1662, Aug 2014.

[40] Kazuo Fujisawa. General treatment of klystron resonant cavities. *IRE Transactions on Microwave Theory and Techniques*, 6(4):344–358, 1958.

[41] Qiang Li, Tao Wang, Yikai Su, Min Yan, and Min Qiu. Coupled mode theory analysis of mode-splitting in coupled cavity system. *Optics express*, 18(8):8367–8382, 2010.

[42] Rémi Rivière. *Cavity optomechanics with silica toroidal microresonators down to low phonon occupancy*. PhD thesis, lmu, 2011.

[43] BD Hauer, C Doolin, KSD Beach, and JP Davis. A general procedure for thermomechanical calibration of nano/micro-mechanical resonators. *Annals of Physics*, 339:181–207, 2013.

[44] Albert Schliesser and Tobias J Kippenberg. Cavity optomechanics with whispering-gallery mode optical micro-resonators. In *Advances In Atomic, Molecular, and Optical Physics*, volume 58, pages 207–323. Elsevier, 2010.

[45] Hendrik Schütz. Quantum optomechanics at room temperature. Technical report, EPFL, 2017.

[46] Jacob M Pate, Luis A Martinez, Johnathon J Thompson, Raymond Y Chiao, and Jay E Sharping. Electrostatic tuning of mechanical and microwave resonances in 3d superconducting radio frequency cavities. *AIP Advances*, 8(11):115223, 2018.

[47] Keith Schwab, J Steinhauer, JC Davis, and Richard E Packard. Fabrication of a silicon-based superfluid oscillator. *Journal of microelectromechanical systems*, 5(3):180–186, 1996.

[48] Keith Schwab, JC Davis, and RE Packard. A microfabricated superfluid 4 he "rf squid". *Czechoslovak Journal of Physics*, 46(5):2739–2740, 1996.

[49] Tomasz Starecki. Analog front-end circuitry in piezoelectric and microphone detection of photoacoustic signals. *International Journal of Thermophysics*, 35(11):2124–2139, 2014.

[50] Mohamed H Awida, Donato Passarelli, Paolo Berrutti, Ivan Gonin, Sergei Kazakov, Timergali Khabiboulline, Jeremiah Holzabauer, Thomas Nicol, Joseph Ozelis, Mattia Parise, et al. Development of low $\beta$ single-spoke resonators for the front end of the proton improvement plan-ii at fermilab. *IEEE Transactions on Nuclear Science*, 64(9):2450–2464, 2017.

[51] Jeremiah Holzbauer, Yuriy Pischalnikov, Warren Schappert, Jae-Chul Yun, et al. Performance of srf cavity tuners at lcls ii prototype cryomodule at fnal. In *Proc. LINAC*, 2016.

[52] Jeremiah Holzbauer, Crispin Contreras-Martinez, Yuriy Pischalnikov, Warren Schappert, and Jae-Chul Yun. Production tuner testing for lcls-ii cryomodule production. In *9th Int. Particle Accelerator Conf.(IPAC'18), Vancouver, BC, Canada, April 29-May 4, 2018*, pages 2678–2680. JACOW Publishing, Geneva, Switzerland, 2018.

[53] Muhammad Shoaib, Nor Hisham, Noohul Basheer, and Mohammad Tariq. Frequency and displacement analysis of electrostatic cantilever-based mems sensor. *Analog Integrated Circuits and Signal Processing*, 88(1):1–11, 2016.

[54] Hendrick BG Casimir. On the attraction between two perfectly conducting plates. In *Proc. Kon. Ned. Akad. Wet.*, volume 51, page 793, 1948.

[55] AO Sushkov, WJ Kim, DAR Dalvit, and SK Lamoreaux. Observation of the thermal Casimir force. *Nature Physics*, 7(3):230, 2011.

[56] Giacomo Bressi, Giovanni Carugno, Roberto Onofrio, and Giuseppe Ruoso. Measurement of the Casimir force between parallel metallic surfaces. *Physical Review Letters*, 88(4):041804, 2002.

[57] Alejandro W Rodriguez, Federico Capasso, and Steven G Johnson. The Casimir effect in microstructured geometries. *Nature Photonics*, 5(4):211, 2011.

[58] Jianping Zou, Z Marcet, Alejandro W Rodriguez, MT Homer Reid, AP McCauley, II Kravchenko, T Lu, Y Bao, SG Johnson, and HB Chan. Casimir forces on a silicon micromechanical chip. *Nature Communications*, 4:1845, 2013.

[59] Christopher M Wilson, Göran Johansson, Arsalan Pourkabirian, Michael Simoen, J Robert Johansson, Tim Duty, F Nori, and Per Delsing. Observation of the dynamical Casimir effect in a superconducting circuit. *Nature*, 479(7373):376, 2011.

[60] David AT Somers, Joseph L Garrett, Kevin J Palm, and Jeremy N Munday. Measurement of the Casimir torque. *Nature*, 564(7736):386, 2018.

[61] GL Klimchitskaya, U Mohideen, and VM Mostepanenko. The Casimir force between real materials: Experiment and theory. *Reviews of Modern Physics*, 81(4):1827, 2009.

[62] John Michael Obrecht, RJ Wild, M Antezza, LP Pitaevskii, S Stringari, and Eric A Cornell. Measurement of the temperature dependence of the Casimir-Polder force. *Physical Review Letters*, 98(6):063201, 2007.

[63] Alexander Stange, Matthias Imboden, Josh Javor, Lawrence K Barrett, and David J Bishop. Building a Casimir metrology platform with a commercial mems sensor. *Microsystems & nanoengineering*, 5(1):14, 2019.

[64] Steven K Lamoreaux. The Casimir force: background, experiments, and applications. *Reports on progress in Physics*, 68(1):201, 2004.

[65] Xi-fang Liu, Yong Li, and H Jing. Casimir switch: steering optical transparency with vacuum forces. *Scientific Reports*, 6:27102, 2016.

[66] M Imboden, J Morrison, DK Campbell, and DJ Bishop. Design of a Casimir-driven parametric amplifier. *Journal of Applied Physics*, 116(13):134504, 2014.

[67] Nicholas Rivera, Liang Jie Wong, John D Joannopoulos, Marin Soljačić, and Ido Kaminer. Light emission based on nanophotonic vacuum forces. *Nature Physics*, pages 1–6, 2019.

[68] Thomas Corbitt, Christopher Wipf, Timothy Bodiya, David Ottaway, Daniel Sigg, Nicolas Smith, Stanley Whitcomb, and Nergis Mavalvala. Optical dilution and feedback cooling of a gram-scale oscillator to 6.9 mk. *Physical Review Letters*, 99(16):160801, 2007.

[69] Michael E Tobar, Clayton R Locke, Eugene N Ivanov, Ik Siong Heng, and David G Blair. Accurate calibration technique for a resonant-mass gravitational wave detector. *Review of Scientific Instruments*, 71(11):4282–4285, 2000.

[70] D. G. Blair, E. N. Ivanov, M. E. Tobar, P. J. Turner, F. van Kann, and I. S. Heng. High sensitivity gravitational wave antenna with parametric transducer readout. *Physical Review Letters*, 74(11):1908–1911, 1995.

[71] J. J. Barroso, P. J. Castro, O. D. Aguiar, and L. A. Carneiro. Reentrant cavities as electromechanical transducers. *Review of Scientific Instruments*, 75(4):1000–1005, 2019/01/10 2004.

[72] N. C. Carvalho, Y. Fan, J-M. Le Floch, and M. E. Tobar. Piezoelectric voltage coupled reentrant cavity resonator. *Review of Scientific Instruments*, 85(10):104705, 2014.

[73] Maxim Goryachev and Michael E Tobar. The 3d split-ring cavity lattice: a new metastructure for engineering arrays of coupled microwave harmonic oscillators. *New Journal of Physics*, 17(2):023003, 2015.

[74] N. C. Carvalho, Y. Fan, and M. E. Tobar. Piezoelectric tunable microwave superconducting cavity. *Review of Scientific Instruments*, 87(9):094702, 2016.

[75] T. J. Clark, V. Vadakkumbatt, F. Souris, H. Ramp, and J. P. Davis. Cryogenic microwave filter cavity with a tunability greater than 5 GHz. *Review of Scientific Instruments*, 89(11):114704, 2018.

[76] Mahmood Bagheri, Menno Poot, Mo Li, Wolfram PH Pernice, and Hong X Tang. Dynamic manipulation of nanomechanical resonators in the high-amplitude regime and non-volatile mechanical memory operation. *Nature Nanotechnology*, 6(11):726, 2011.

[77] Quirin P Unterreithmeier, Eva M Weig, and Jörg P Kotthaus. Universal transduction scheme for nanomechanical systems based on dielectric forces. *Nature*, 458(7241):1001, 2009.

[78] HB Chan, VA Aksyuk, RN Kleiman, DJ Bishop, and Federico Capasso. Nonlinear micromechanical Casimir oscillator. *Physical Review Letters*, 87(21):211801, 2001.

[79] Eugene Simon Polzik, Albert Schliesser, Silvan Schmid, Anders Sondberg Sorensen, Jacob M Taylor, Koji Usami, Tolga Bagci, Anders Simonsen, Luis Guillermo Villanueva, Emil Zeuthen, et al. Optical detector and amplifier for rf-detection having a position dependent capacitor with a displaceable membrane, May 23 2017. US Patent 9,660,721.

[80] M. Goryachev and M.E. Tobar. Microwave frequency magnetic field manipulation systems and methods and associated application instruments, apparatus and system. Patent: AU2014903143, 12 August 12 August 2014.

[81] Maxim Goryachev, Warrick G. Farr, Daniel L. Creedon, Yaohui Fan, Mikhail Kostylev, and Michael E. Tobar. High-cooperativity cavity qed with magnons at microwave frequencies. *Physical Review Applied*, 2(5):054002–, 11 2014.

[82] Nikita Kostylev, Maxim Goryachev, and Michael E. Tobar. Superstrong coupling of a microwave cavity to yttrium iron garnet magnons. *Applied Physics Letters*, 108(6):062402, 2016.

[83] Daniel L. Creedon, Jean-Michel Le Floch, Maxim Goryachev, Warrick G. Farr, Stefania Castelletto, and Michael E. Tobar. Strong coupling between $p1$ diamond impurity centers and a three-dimensional lumped photonic microwave cavity. *Phys. Rev. B*, 91:140408, Apr 2015.

[84] Jeffrey F Rhoads, Steven W Shaw, and Kimberly L Turner. Nonlinear dynamics and its applications in micro-and nanoresonators. In *ASME 2008 Dynamic Systems and Control Conference*, pages 1509–1538. American Society of Mechanical Engineers Digital Collection, 2009.

[85] Pu Huang, Jingwei Zhou, Liang Zhang, Dong Hou, Shaochun Lin, Wen Deng, Chao Meng, Changkui Duan, Chenyong Ju, Xiao Zheng, et al. Generating giant

and tunable nonlinearity in a macroscopic mechanical resonator from a single chemical bond. *Nature Communications*, 7:11517, 2016.

[86] Philippe Brax, Carsten van de Bruck, Anne-Christine Davis, David F Mota, and Douglas Shaw. Detecting chameleons through Casimir force measurements. *Physical Review D*, 76(12):124034, 2007.

[87] Attaallah Almasi, Philippe Brax, Davide Iannuzzi, and René IP Sedmik. Force sensor for chameleon and Casimir force experiments with parallel-plate configuration. *Physical Review D*, 91(10):102002, 2015.

[88] Serge Galliou, Maxim Goryachev, Roger Bourquin, Philippe Abbé, Jean Pierre Aubry, and Michael E Tobar. Extremely low loss phonon-trapping cryogenic acoustic cavities for future physical experiments. *Scientific reports*, 3:2132, 2013.

[89] JD Teufel, Dale Li, MS Allman, K Cicak, AJ Sirois, JD Whittaker, and RW Simmonds. Circuit cavity electromechanics in the strong-coupling regime. *Nature*, 471(7337):204–208, 2011.

[90] Martijn A Cohen, Mingyun Yuan, Bas WA de Jong, Ewout Beukers, Sal J Bosman, and Gary A Steele. A split-cavity design for the incorporation of a dc bias in a 3d microwave cavity. *Applied Physics Letters*, 110(17):172601, 2017.

[91] GA Peterson, S Kotler, F Lecocq, K Cicak, XY Jin, RW Simmonds, J Aumentado, and JD Teufel. Ultrastrong parametric coupling between a superconducting cavity and a mechanical resonator. *Physical Review Letters*, 123(24):247701, 2019.

[92] CR Locke, ME Tobar, EN Ivanov, and DG Blair. Parametric interaction of the electric and acoustic fields in a sapphire monocrystal transducer with a microwave readout. *Journal of applied physics*, 84(12):6523–6527, 1998.

[93] BD Cuthbertson, ME Tobar, EN Ivanov, and DG Blair. Parametric backaction effects in a high-q cyrogenic sapphire transducer. *Review of Scientific Instruments*, 67(7):2435–2442, 1996.

[94] Jeremy Bourhill, Eugene Ivanov, and ME Tobar. Precision measurement of a low-loss cylindrical dumbbell-shaped sapphire mechanical oscillator using radiation pressure. *Physical Review A*, 92(2):023817, 2015.

[95] Jin-Shan Feng, Lei Tan, Huai-Qiang Gu, and Wu-Ming Liu. Auxiliary-cavity-assisted ground-state cooling of an optically levitated nanosphere in the unresolved-sideband regime. *Physical Review A*, 96(6):063818, 2017.

[96] Yong-Chun Liu, Yun-Feng Xiao, Xingsheng Luan, Qihuang Gong, and Chee Wei Wong. Coupled cavities for motional ground-state cooling and strong optomechanical coupling. *Physical Review A*, 91(3):033818, 2015.

[97] Jun-Ya Yang, Dong-Yang Wang, Cheng-Hua Bai, Si-Yu Guan, Xiao-Yuan Gao, Ai-Dong Zhu, and Hong-Fu Wang. Ground-state cooling of mechanical oscillator via quadratic optomechanical coupling with two coupled optical cavities. *Optics express*, 27(16):22855–22867, 2019.

[98] Alexander Grey Krause. *Acceleration Sensing, Feedback Cooling, and Nonlinear Dynamics with Nanoscale Cavity-Optomechanical Devices*. 2015.

[99] Reed W Andrews. Quantum signal processing with mechanical oscillators. 2015.

[100] Charles G. Torre. Quantum mechanics, spring 2007 lecture slides.

[101] Stephen E Harris. Electromagnetically induced transparency. In *Quantum Electronics and Laser Science Conference*, page QTuB1. Optical Society of America, 1997.

[102] Crispin Gardiner and Peter Zoller. *Quantum noise: a handbook of Markovian and non-Markovian quantum stochastic methods with applications to quantum optics*, volume 56. Springer Science; Business Media, 2004.

[103] Claudiu Genes, Helmut Ritsch, and Ddavid Vitali. Micromechanical oscillator ground-state cooling via resonant intracavity optical gain or absorption. *Physical Review A*, 80(6):061803, 2009.

[104] Dong-Yang Wang, Cheng-Hua Bai, Hong-Fu Wang, Ai-Dong Zhu, and Shou Zhang. Steady-state mechanical squeezing in a double-cavity optomechanical system. *Scientific reports*, 6:38559, 2016.

[105] Xi Chen, Yong-Chun Liu, Pai Peng, Yanyan Zhi, and Yun-Feng Xiao. Cooling of macroscopic mechanical resonators in hybrid atom-optomechanical systems. *Physical Review A*, 92(3):033841, 2015.

[106] Texas Instruments. Noise analysis in operational amplifier circuits. *Application Report, SLVA043B*, 2007.

[107] TJ Kippenberg M. Aspelmeyer and F. Marquardt. *Cavity Optomechanics*. Springer Berlin Heidelberg, Berlin, Heidelberg, 2014.

[108] Jerry B Marion. *Classical dynamics of particles and systems*. Academic Press, 2013.

[109] Amir H Safavi-Naeini, TP Mayer Alegre, Jasper Chan, Matt Eichenfield, Martin Winger, Qiang Lin, Jeffrey T Hill, DE Chang, and Oskar Painter. Electromagnetically induced transparency and slow light with optomechanics. *Nature*, 472(7341):69–73, 2011.

[110] CW Gardiner and MJ Collett. Input and output in damped quantum systems: Quantum stochastic differential equations and the master equation. *Physical Review A*, 31(6):3761, 1985.

[111] David Chandler. Introduction to modern statistical mechanics. 1, 1987.

[112] Aashish A Clerk, Michel H Devoret, Steven M Girvin, Florian Marquardt, and Robert J Schoelkopf. Introduction to quantum noise, measurement, and amplification. *Reviews of Modern Physics*, 82(2):1155, 2010.

[113] Jonathan Keeling. Light-matter interactions and quantum optics., 2014.

[114] JD Teufel, T Donner, MA Castellanos-Beltran, JW Harlow, and KW Lehnert. Nanomechanical motion measured with an imprecision below that at the standard quantum limit. *Nature nanotechnology*, 4(12):820–823, 2009.

[115] B Abbott, R Abbott, R Adhikari, P Ajith, Bruce Allen, G Allen, R Amin, SB Anderson, WG Anderson, MA Arain, et al. Observation of a kilogram-scale oscillator near its quantum ground state. *New Journal of Physics*, 11(7):073032, 2009.

[116] GW Ford and M Kac. On the quantum langevin equation. *Journal of statistical physics*, 46(5-6):803–810, 1987.

[117] M Karuza, C Biancofiore, M Bawaj, C Molinelli, M Galassi, R Natali, P Tombesi, G Di Giuseppe, and D Vitali. Optomechanically induced transparency in a membrane-in-the-middle setup at room temperature. *Physical Review A*, 88(1):013804, 2013.

[118] Gerard J. Milburn Warwick P. Bowen. *Quantum Optomechanics*. CRC Press, 2016.

[119] R Victor Jones. The interaction of radiation and matter: Quantum theory. May 2000.

[120] Chunhua Dong, Victor Fiore, Mark C Kuzyk, and Hailin Wang. Transient optomechanically induced transparency in a silica microsphere. *Physical Review A*, 87(5):055802, 2013.

[121] JJ Barroso, PJ Castro, OD Aguiar, and LA Carneiro. Reentrant cavities as electromechanical transducers. *Review of scientific instruments*, 75(4):1000–1005, 2004.

[122] Jens Knobloch. Basic concepts of measurements made on superconducting rf cavities. Technical report, 1991.

[123] Ahmet AkkoÇ. *Design and Implementation of a Microwave Cavity Resonator for Modulated Backscattered Wave*. PhD thesis, Middle East Technical University, 2015.

[124] G Ciovati, G Myneni, F Stevie, P Maheshwari, and D Griffis. High field q slope and the baking effect: Review of recent experimental results and new data on nb heat treatments. *Physical Review Special Topics-Accelerators and Beams*, 13(2):022002, 2010.

[125] Xiaoguang Liu, Linda PB Katehi, William J Chappell, and Dimitrios Peroulis. High-$q$ tunable microwave cavity resonators and filters using soi-based rf mems tuners. *Journal of Microelectromechanical Systems*, 19(4):774–784, 2010.

[126] Shun Yanai, Vibhor Singh, Mingyun Yuan, MF Gely, SJ Bosman, and GA Steele. Mechanical dissipation in more superconducting metal drums. *Applied Physics Letters*, 110(8):083103, 2017.

[127] Xiu Gu, Anton Frisk Kockum, Adam Miranowicz, Yu-xi Liu, and Franco Nori. Microwave photonics with superconducting quantum circuits. *Physics Reports*, 2017.

[128] Amro M Elshurafa, Kareem Khirallah, Hani H Tawfik, Ahmed Emira, Ahmed KS Abdel Aziz, and Sherif M Sedky. Nonlinear dynamics of spring softening and hardening in folded-mems comb drive resonators. *Journal of Microelectromechanical Systems*, 20(4):943–958, 2011.

[129] Hanhee Paik, DI Schuster, Lev S Bishop, G Kirchmair, G Catelani, AP Sears, BR Johnson, MJ Reagor, L Frunzio, LI Glazman, et al. Observation of high coherence in josephson junction qubits measured in a three-dimensional circuit qed architecture. *Physical Review Letters*, 107(24):240501, 2011.

[130] CE Reece, PJ Reiner, and AC Melissinos. Parametric converters for detection of small harmonic displacements. *Nuclear Instruments and Methods in Physics Research Section A: Accelerators, Spectrometers, Detectors and Associated Equipment*, 245(2-3):299–315, 1986.

[131] N C. Carvalho, Y Fan, and ME Tobar. Piezoelectric tunable microwave superconducting cavity. *Review of Scientific Instruments*, 87(9):094702, 2016.

[132] E Mykkänen, JS Lehtinen, A Kemppinen, C Krause, D Drung, J Nissilä, and AJ Manninen. Reducing current noise in cryogenic experiments by vacuum-insulated cables. *Review of Scientific Instruments*, 87(10):105111, 2016.

[133] VS Ilchenko, PS Volikov, VL Velichansky, F Treussart, V Lefevre-Seguin, J-M Raimond, and S Haroche. Strain-tunable high-q optical microsphere resonator. *Optics communications*, 145(1-6):86–90, 1998.

[134] LA De Lorenzo and KC Schwab. Superfluid optomechanics: coupling of a superfluid to a superconducting condensate. *New Journal of Physics*, 16(11):113020, 2014.

[135] H Rokhsari, TJ Kippenberg, T Carmon, and KJ Vahala. Theoretical and experimental study of radiation pressure-induced mechanical oscillations (parametric instability) in optical microcavities. *IEEE journal of selected topics in Quantum Electronics*, 12(1):96–107, 2006.

[136] F Souris, H Christiani, and JP Davis. Tuning a 3d microwave cavity via superfluid helium at millikelvin temperatures. *Applied Physics Letters*, 111(17):172601, 2017.

[137] Rachpon Kalra, Arne Laucht, Juan Pablo Dehollain, Daniel Bar, Solomon Freer, Stephanie Simmons, Juha T Muhonen, and Andrea Morello. Vibration-induced electrical noise in a cryogen-free dilution refrigerator: Characterization, mitigation, and impact on qubit coherence. *Review of Scientific Instruments*, 87(7):073905, 2016.

[138] Remi Riviere, Samuel Deleglise, Stefan Weis, Emanuel Gavartin, Olivier Arcizet, Albert Schliesser, and Tobias J Kippenberg. Optomechanical sideband cooling of a micromechanical oscillator close to the quantum ground state. *Physical Review A*, 83(6):063835, 2011.

[139] F Michael Serry, Dirk Walliser, and G Jordan Maclay. The anharmonic casimir oscillator (aco)-the Casimir effect in a model microelectromechanical system. *Journal of Microelectromechanical Systems*, 4(4):193–205, 1995.

[140] M. Goryachev and M. E. Tobar. Creating tuneable microwave media from a two-dimensional lattice of re-entrant posts. *Journal of Applied Physics*, 118(20):204504, 2015.

[141] James M Lehto Miller, Azadeh Ansari, David B Heinz, Yunhan Chen, Ian B Flader, Dongsuk D Shin, L Guillermo Villanueva, and Thomas W Kenny. Effective quality factor tuning mechanisms in micromechanical resonators. *Applied Physics Reviews*, 5(4):041307, 2018.

[142] Maxim Goryachev, Stuart Watt, Jeremy Bourhill, Mikhail Kostylev, and Michael E. Tobar. Cavity magnon polaritons with lithium ferrite and three-dimensional microwave resonators at millikelvin temperatures. *Phys. Rev. B*, 97:155129, Apr 2018.

[143] Siyu Chen, Weidong Yang, Jie Song, and Fenglin Guo. A new mechanism of energy dissipation in nanomechanical resonators due to the Casimir force. *Journal of Applied Physics*, 126(4):044502, 2019.

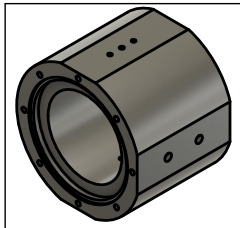

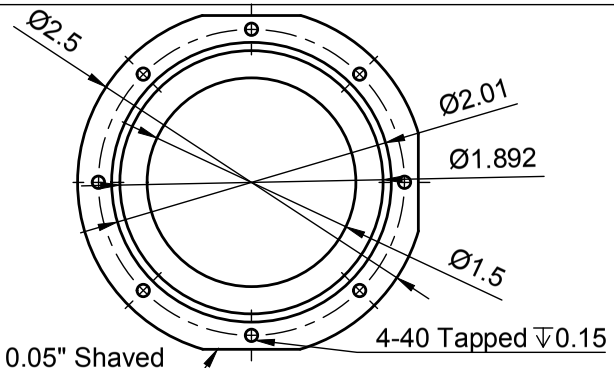


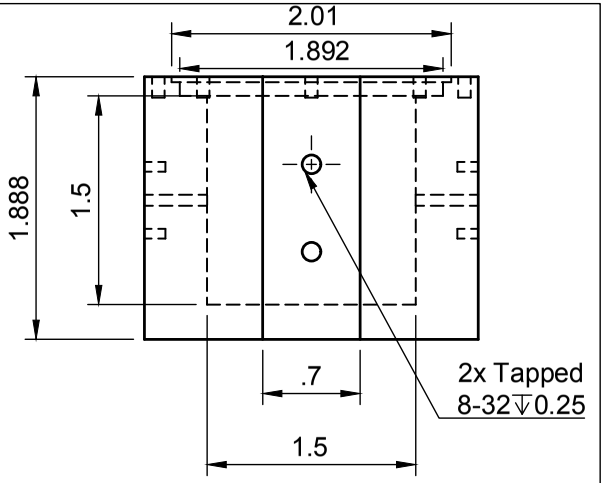


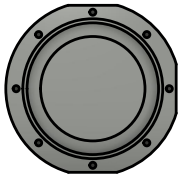

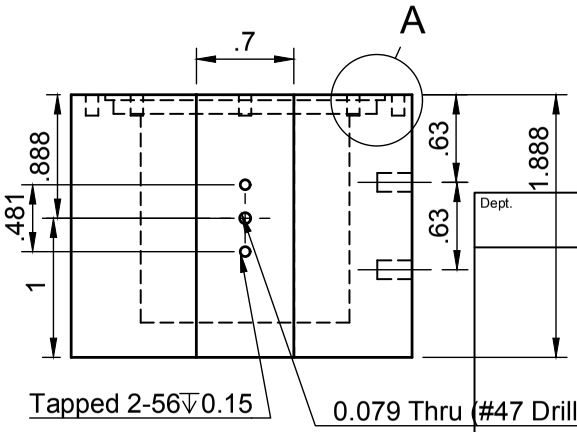


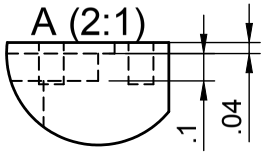


| | | | |
|---|---|---|---|
| Dept. | Technical reference | Created by: Jacob Pate 4/26/18 | Approved by |
| | | Document type | Document status |
| | | Title: SRFCavity Membrane with Air Gap units are inches | DWG No. |
| | | | Rev. / Date of issue / Sheet: 1/1 |

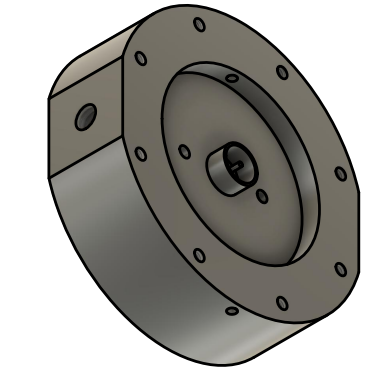

A-A (1:1)

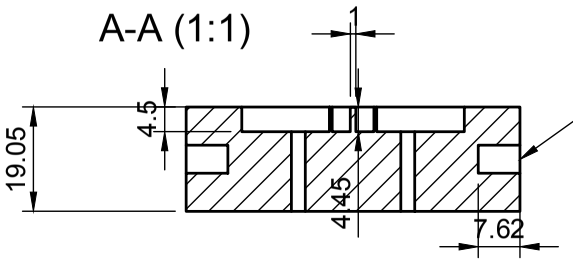


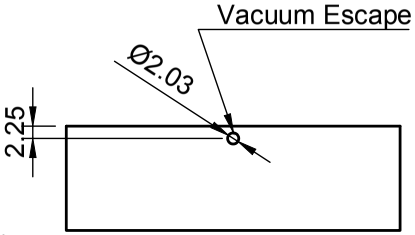


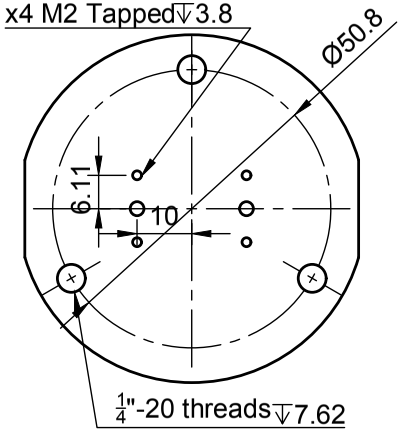


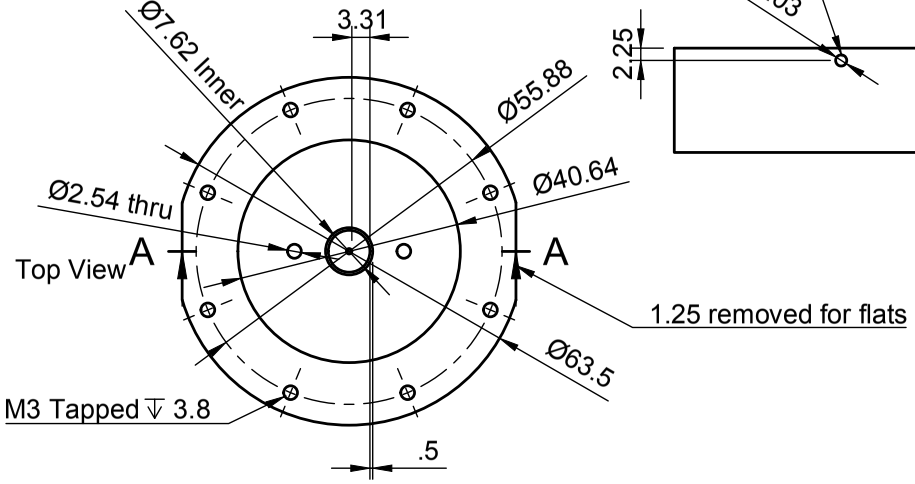


| Dept. | Technical reference | Created by | Approved by |
|---|---|---|---|
| | | Jacob Pate 11/29/19 | |
| Units are mm. Center post with diameter 1mm, height 4.45 mm should give resonance about 4 GHz for gap of 50 um. | | Document type | Document status |
| | | Title: RingCavity | DWG No. |
| | | | Rev. / Date of issue / Sheet: 1/1 |